UNIVERSITY OF IOANNINA
SCHOOL OF SCIENCE
DEPARTMENT OF PHYSICS

Studies of quantum chromodynamics and measurement of the strong coupling constant with jets from the CMS experiment at the LHC

Giannis Flouris

PhD Thesis

IOANNINA 2016

ΠΑΝΕΠΙΣΤΗΜΙΟ ΙΩΑΝΝΙΝΩΝ
ΣΧΟΛΗ ΘΕΤΙΚΩΝ ΕΠΙΣΤΗΜΩΝ
ΤΜΗΜΑ ΦΥΣΙΚΗΣ

Μελέτες της κβαντικής χρωμοδυναμικής και μέτρηση της σταθεράς σύζευξης των ισχυρών αλληλεπιδράσεων με πίδακες σωματίων στο πείραμα CMS του LHC

Γιάννης Φλουρής

ΔΙΔΑΚΤΟΡΙΚΗ ΔΙΑΤΡΙΒΗ

ΙΩΑΝΝΙΝΑ 2016

Τριμελής Συμβουλευτική Επιτροπή
Αναπληρωτής Καθηγητής Παναγιώτης Κόκκας
Καθηγητής Κωνσταντίνος Φουντάς
Επίκουρη Καθηγήτρια Νίκη Σαουλίδου

Επταμελής Εξεταστική Επιτροπή
Αναπληρωτής Καθηγητής Παναγιώτης Κόκκας
Καθηγητής Κωνσταντίνος Φουντάς
Επίκουρη Καθηγήτρια Νίκη Σαουλίδου
Αναπληρωτής Καθηγητής Ιωάννης Παπαδόπουλος
Επίκουρος Καθηγητής Ιωάννης Στρόλογγας
Επίκουρος Καθηγητής Κωνσταντίνος Κουσουρής
Αναπληρωτής Καθηγητής Νικόλαος Μάνθος

Three-member Advisory Committee
Associate Professor Panagiotis Kokkas
Professor Constantinos Foudas
Assistant Professor Niki Saoulidou

Seven-member Assessment Committee
Associate Professor Panagiotis Kokkas
Professor Constantinos Foudas
Assistant Professor Niki Saoulidou
Assistant Professor Ioannis Papadopoulos
Assistant Professor John Strologas
Assistant Professor Konstantinos Kousouris
Associate Professor Nikolaos Manthos

Ευχαριστίες

Περίληψη

Η παρούσα διατριβή ασχολείται με την πειραματική επιβεβαίωση της διαταρακτικής Κβαντικής Χρωμοδυναμικής όπως περιγράφεται από το Καθιερωμένο Πρότυπο. Η διατριβή αποτελείται από τρεις αναλύσεις με πίδακες σωματιδίων στην τελική κατάσταση. Τα δεδομένα συλλέχθηκαν από το πείραμα ΎΜΣ κατά την διάρκεια συγκρούσεων προτονίων-προτονίων στον επιταχυντή ΛΗΎ.

Η πρώτη ανάλυση μετράει την σταθερά ισχυρής αλληλεπίδρασης, α_s, από την ολική διαφορική ενεργό διατομή πιδάκων. Τα δεδομένα συλλέχθηκαν από συγκρούσεις προτονίων-προτονίων σε ενέργεια κέντρου μάζας 7 TeV, και αντιστοιχούν σε ολοκληρωμένη φωτεινότητα 5.0 fb^{-1}. Η τιμή της σταθεράς στη μάζα του μποζονίου Z, βρέθηκε να είναι $\alpha_s(M_Z) = 0.1185 \pm 0.0019(exp)^{+0.0037}_{-0.0060}(theo)$ και είναι σε συμφωνία με τον παγκόσμιο μέσο όρο. Επίσης μελετήθηκε η ασυμπτωτική φύση της σταθεράς και φαίνεται να είναι σε συμφωνία με τους θεωρητικούς υπολογισμούς.

Η δεύτερη ανάλυση μετράει την σταθερά ισχυρής αλληλεπίδρασης, ας, από τον λόγο της ενεργής διατομής 3 προς 2 πιδάκων σωματιδίων. Τα δεδομένα συλλέχθηκαν από συγκρούσεις πρωτονίων- πρωτονίων σε ενέργεια κέντρου μάζας 7 TeV, και αντιστοιχούν σε ολοκληρωμένη φωτεινότητα 5.0 fb^{-1}. Η τιμή της σταθεράς στη μάζα του μποζονίου Z, βρέθηκε να είναι $\alpha_s(M_Z) = 0.1148 \pm 0.0014(exp.) \pm 0.0018(PDF) \pm 0.0050(theory)$, συγκρίνοντας την πειραματική μέτρηση και τη θεωρία στην περιοχή, $0.42 < \langle p_{T1,2} \rangle < 1.39$ TeV. Αυτή η μέτρηση αποτελεί την πρώτη μέτρηση της σταθεράς ισχυρής αλληλεπίδρασης σε κλίμακα πέραν των 0.6 TeV. Από αυτή την ανάλυση δεν φάνηκε καμία απόκλιση από την θεωρία.

Η τρίτη ανάλυση μετράει τις αποσυσχετίσεις των αζιμουθιακών γωνιών ανάμεσα στους δύο πίδακες με την μεγαλύτερη εγκάρσια ορμή. Η μέτρηση πραγματοποιήθηκε σε εφτά περιοχές οι οποίες ορίζονται από το μέγεθος της εγκάρσιας ορμής του πίδακα με την μεγαλύτερη εγκάρσια ορμή σε ένα γεγονός. Τα δεδομένα συλλέχθηκαν από συγκρούσεις πρωτονίων-πρωτονίων σε ενέργεια κέντρου μάζας 8 TeV, και αντιστοιχούν σε ολοκληρωμένη φωτεινότητα 19.7 fb^{-1}. Οι αζιμουθιακές αποσυσχετίσεις προκύπτουν από την

εκπομπή επιπλέον πιδάκων και εξαρτώνται από την τοπολογία των γεγονότων με πολλαπλούς πίδακες. Τα αποτελέσματα συγκρίνονται με προβλέψεις από τη διαταρακτική Κβαντική Χρωμοδυναμική και προσομοιώσεις γεγονότων από γεννήτορες Monte Carlo. Από τις συγκρίσεις φαίνεται ότι οι γεννήτορες γεγονότων με δύο παρτόνια στην τελική κατάσταση αδυνατούν να περιγράψουν την μέτρηση. Καλύτερη συμφωνία επιτυγχάνεται όταν χρησιμοποιήθηκαν θεωρητικά εργαλεία τα οποία παράγουν τουλάχιστον τρία παρτόνια. Αυτή η παρατήρηση καταδεικνύει την ανάγκη για την βελτίωση των υπολογισμών πολλαπλών πιδάκων.

Abstract

This dissertation studies the experimental verification of the perturbative Quantum Chromodynamics (pQCD) as it is described within the theoretical framework of the Standard Model (SM). The dissertation consists of three analyses with jets in the final state. The data were recorded by the CMS Experiment at the LHC during proton-proton collisions.

The first analysis measured the strong coupling constant, α_s, from the inclusive jet cross section. The data were collected during proton-proton collisions at the centre-of-mass energy of 7 TeV, corresponding to an integrated luminosity of $5.0\,fb^{-1}$. The value of strong coupling at the mass of the Z boson was found to be $\alpha_s(M_Z) = 0.1185 \pm 0.0019(exp)^{+0.0037}_{-0.0060}(theo)$ is in agreement with the world average. The running of the strong coupling was also studied and is found to be consistent with the predictions of pQCD.

The second analysis measured the strong coupling constant, α_s, from the ratio of the inclusive $3-$jet cross section to the inclusive $2-$jet cross section. The data sample was collected during 2011 during proton-proton collisions at centre-of-mass energy of 7 TeV, corresponding to an integrated luminosity of 5.0 fb^{-1}. The strong coupling constant at the scale of the Z boson mass is determined to be $\alpha_s(MZ) = 0.1148 \pm 0.0014(exp.) \pm 0.0018(PDF) \pm 0.0050(theory)$, by comparing the ratio in the range $0.42 < \langle p_{\mathrm{T1,2}} \rangle < 1.39\ TeV$ to the predictions of pQCD. This is the first determination of $\alpha_s(MZ)$ from measurements at momentum scales beyond 0.6 TeV. No deviation from the expected behavior is observed.

The third analysis measured the decorrelation of azimuthal angles between the two jets with the largest transverse momenta and it is presented for seven regions of leading jet transverse momentum up to 2.2TeV. The data sample was collected during proton-proton collisions with the CMS experiment at a centre-of-mass energy of 8 TeV corresponding to an integrated luminosity of $19.7\,fb^{-1}$. The dijet azimuthal decorrelation is caused by the radiation of additional jets and probes the dynamics of multijet production. The results are compared to next-to-leading-order (NLO) predictions of pQCD, and to simulations using Monte Carlo event generators. Event

generators with only two outgoing high transverse momentum partons fail to describe the measurement while better agreement is achieved when at least three outgoing partons are complemented through either NLO predictions or parton showers. This observation emphasizes the need to improve predictions for multijet production.

Σύνοψη

Η Φυσική Στοιχειωδών Σωματιδίων είναι η επιστήμη που επιδιώκει την κατανόηση της φύσης στην πιο στοιχειώδη της μορφή. Η Φυσική Στοιχειωδών Σωματιδίων ξεκίνησε σαν φιλοσοφική αναζήτηση από τους αρχαίους Έλληνες (Λεύκιππο, Δημόκριτο κλ) και Ινδούς (Κανάντα) φιλοσόφους. Το ανθρώπινο είδος πάντα έψαχνε την προέλευση του κόσμου και την σύσταση της ύλης. Πρακτικά η συνεισφορά των αρχαίων φιλοσόφων είναι μηδενική στην μοντέρνα Φυσική αλλά δεν θα μπορούσαμε να αποβλέψουμε την συνεισφορά των σαν τροφή για σκέψη στους σύγχρονους ανθρώπους.

Σήμερα η Φυσική Στοιχειωδών Σωματιδίων είναι μια αυστηρά δομημένη επιστήμη η οποία εκφράζεται μέσω της μαθηματικής γλώσσας και μετράται από περίπλοκα πειράματα. Ο Μεγάλος Αδρονικός Επιταχυντής (LHC) , επιταχυντής πρωτονίων, ο οποίος βρίσκεται στα Γαλλο-Ελβετικά σύνορα έχει στόχο σε γενικές γραμμές τον ίδιο με 2500 χρόνια πριν. Ο στόχος είναι η διεύρυνση της γνώσης μας σε ένα υπέρτατο βαθμό όπου όλες οι φυσικές διαδικασίες που λαμβάνουν χώρα στο σύμπαν να μπορούν να εξηγηθούν με την λογική.

Αυτή η διατριβή περιγράφει την έρευνα που εκπονήθηκε χρησιμοποιώντας δεδομένα από το πείραμα CMS του LHC. Η διατριβή είναι δομημένη σε εφτά κεφάλαια, το πρώτο είναι μια μικρή εισαγωγή, το Κεφάλαιο 2 και 3 περιγράφουν τον επιταχυντή LHC και τον ανιχνευτή του πειράματος CMS αντίστοιχα. Το Κεφάλαιο 4 περιγράφει το Καθιερωμένο Πρότυπο δίνοντας ιδιαίτερη έμφαση στην Κβαντική Χρωμοδυναμική. Στο Κεφάλαιο 5 περιγράφονται οι τεχνικές ανακατασκευής γεγονότων και διόρθωσης της ενέργειας των σωματιδίων που χρησιμοποιήθηκαν στις αναλύσεις. Τέλος τα Κεφάλαια 7 και 8 περιγράφουν τις αναλύσεις και το Κεφάλαιο 9 συνοψίζει τα αποτελέσματα.

Ο Μεγάλος Αδρονικός Επιταχυντής είναι ένας επιταχυντής πρωτονίων και έχει σχεδιαστεί για συγκρούσεις πρωτονίων σε ενέργεια κέντρου μάζας $\sqrt{s} = 14$ TeV. Ο LHC είναι κυκλικός επιταχυντής τοποθετημένος σε τούνελ μήκους $26.7\ km$ στο $CERN$. Στον LHC λειτουργούν διάφορα πειράματα φυσικής υψηλών ενεργειών. Τα δεδομένα που χρησιμοποιήθηκαν στις αναλύσεις που περιγράφονται σε αυτή τη διατριβή συλλέχθηκαν από το πείραμα CMS. Στο Κεφάλαιο 3 περιγράφεται αναλυτικότερα η διάταξη του ανιχνευτή και τα επί

μέρους στοιχεία του.

Το CMS είναι ένα πείραμα γενικού σκοπού το οποίο καταγράφει συγκρούσεις πρωτονίων-πρωτονίων οι οποίες λαμβάνουν χώρα στον LHC. Ο ανιχευτής του CMS αποτελείται από τους ακόλουθους υπο-ανιχνευτές: τον ανιχνευτή τροχιών πυριτίου, το ηλεκτρομαγνητικό καλορίμετρο, το αδρονικό καλορίμετρο και τους ανιχνευτές μιονίων. Οι υπο-ανιχνευτές βρίσκονται σε μαγνητικό πεδίο, 3.8 T, που παράγεται από το υπεραγώγιμο σωληνοειδές. Ο μεγάλος ρυθμός συγκρούσεων στον LHC απαιτεί ανιχνευτές και ηλεκτρονικά με καλή χρονική διακριτική ικανότητα και αντοχή στην ακτινοβολία. Επίσης για να μπορεί να ανταπεξέλθει στο απαιτητικό πρόγραμμα φυσικής ο ανιχνευτής πρέπει να αναγνωρίζει όσο το δυνατόν καλύτερα τα λεπτόνια και τους πίδακες σωματιδίων. Επίσης η καλή διακριτική ικανότητα στην εγκάρσια ορμή των σωματιδίων και την ελλείπουσα ενέργεια σε ένα γεγονός είναι απαραίτητα στοιχεία του ανιχνευτή.

Η Φυσική Στοιχειωδών Σωματιδίων ασχολείται με την κατανόηση της φύσης εξηγώντας τα θεμελιώδη στοιχεία που την απαρτίζουν. Το πιο πλήρες θεωρητικό μοντέλο που εξηγεί τα στοιχειώδη σωματίδια και τις αλληλεπιδράσεις τους ονομάζεται Καθιερωμένο Πρότυπο (ΚΠ). Το ΚΠ περιγράφει τα σωματίδια και τις αλληλεπιδράσεις τους. Συμπεριλαμβάνει τις ηλεκτρομαγνητικές, ισχυρές και ασθενείς αλληλεπιδράσεις. Η βαρυτικές δυνάμεις δεν συμπεριλαμβάνονται στο πλαίσιο του ΚΠ.

Σύμφωνα με το ΚΠ το ορατό Σύμπαν αποτελείται από φερμιόνια, έξι κουάρκς και έξι λεπτόνια, τα οποία φαίνονται στον πίνακα 1. Οι αλληλεπιδράσεις λαμβάνουν χώρα από ανταλλαγές μποζονίων. Οι φορείς των ηλεκτρομαγνητικών αλληλεπιδράσεων είναι τα φωτόνια, των ισχυρών τα γκλουόνια και των ασθενών τρία ανυσματικά μποζόνια, Z^0 και $W^\pm$. Οι φορείς των αλληλεπιδράσεων φαίνονται στον πίνακα 2. Το Μινιμαλιστικό ΚΠ περιέχει επιπλέον τέσσερα βαθμωτά πεδία, δύο φορτισμένα και δύο ουδέτερα. Τρία εξ᾽ αυτών, τα δύο αφόρτιστα και το ένα ουδέτερο, έχουν 'απορροφηθεί' από τα ανυσματικά μποζόνια, το εναπομείναν είναι το πεδίο Χίγκς.

Πίνακας 1: Τα στοιχειώδη σωματίδια του ΚΠ.

Σωματίδια	Γεύση	Φορτίο
Λεπτόνια	$e\ \mu\ \tau$	-1
	$\nu_e\ \nu_\mu\ \nu_\tau$	0
Κουάρκ	$u\ c\ t$	$+\frac{2}{3}$
	$d\ s\ b$	$-\frac{1}{3}$

Το ΚΠ είναι μια θεωρία πεδίου η οποία χρησιμοποιεί την Λαγκρατζιανή

Πίνακας 2: Οι φορείς αλληλεπίδρασης του ΚΠ.

Αλληλεπίδραση	Σωματίδιο	Σπιν	Σχετική Δύναμη
Ισχυρή	g, γκλουόνια	1	$\mathcal{O}(1)$
Ηλεκτρομαγνητική	γ, φωτόνια	1	$\mathcal{O}(10^{-2})$
Ασθενής	W, Z	± 1	$\mathcal{O}(10^{-7})$

διατύπωση ώστε να περιγράψει τα πεδία και τις αλληλεπιδράσεις τους. Οι Λαγκρατζιανές μπορούν να περιέχουν αυθαίρετο αριθμό βαθμών ελευθερίας αρκεί να είναι αμετάβλητες κάτω από τοπικούς μετασχηματισμούς. Οι Λαγκρατζιανές στην κβαντική θεωρία πεδίου λαμβάνονται σαν αξιωματικές εξισώσεις, σε αντίθεση με την κλασσική μηχανική, με τον μοναδικό περιορισμό οτι πρέπει να αναπαράγουν τις εξισώσεις πεδίου. Μπορούν να πολλαπλασιαστούν αυθαίρετα με ένα βαθμωτό παράγοντα ή να τους προστεθεί ένας παράγοντας αρκεί να αναπαράγονται οι εξισώσεις των πεδίων μετά την εφαρμογή των εξισώσεων *Euler − Lagrange*.

Η παρούσα διατριβή ασχολείται με την πειραματική επιβεβαίωση της Κβαντικής Χρωμοδυναμικής, του τομέα του ΚΠ που εξηγεί τις ισχυρές αλληλεπιδράσεις. Τα Κεφάλαια 6 και 7 περιγράφουν τις μετρήσεις που έγιναν χρησιμοποιώντας δεδομένα που λήφθηκαν από το πείραμα CMS προερχόμενα από συγκρούσεις πρωτονίων-πρωτονίων σε ενέργεια κέντρου μάζας $\sqrt{s} = 7$ TeV και $\sqrt{s} = 8$ TeV.

Η πρώτη μέτρηση που περιγράφεται σε αυτήν τη διατριβή είναι η μέτρηση της σταθεράς ισχυρής αλληλεπίδρασης στα $\sqrt{s} = 7$ TeV χρησιμοποιώντας πίδακες σωματιδίων. Σε αυτή την ανάλυση μετρήθηκε η σταθερά ισχυρής αλληλεπίδρασης, α_S σε ενέργεια ίση με την μάζα του ανυσματικού μποζονίου Z και μελετήθηκε η συμπεριφορά της σταθεράς σε διάφορες ενέργειες. Τα γεγονότα συλλέχθησαν κατά τις συγκρούσεις πρωτονίων σε κέντρο μάζας $\sqrt{s} = 7$ TeV κατά το 2011 και αντιστοιχούν σε ολοκληρωμένη φωτεινότητα 5.0 fb^{-1}. Οι πίδακες ανακατασκευάστηκαν με την μέθοδο Particle Flow και για την συσσωμάτωση των σωματιδίων χρησιμοποιήθηκε ο αλγόριθμος anti$-k_{\mathrm{T}}$ με ακτίνα 0.7. Η ανάλυση κατέγραψε πίδακες με ελάχιστη εγκάρσια ορμή $p_T = 114$ GeV σε πέντε περιοχές ωκύτητας με πλάτος $\Delta y = 0.5$ μέχρι $|y| < 2.5$. Μελετήθηκε η διπλή διαφορική ενεργός διατομή συναρτήσει της εγκάρσιας ορμής και της ωκύτητας. Η διπλή διαφορική ενεργός διατομή ορίζεται ως:

$$\frac{d^2\sigma}{dp_{\mathrm{T}}dy} = \frac{1}{\epsilon\mathcal{L}_{int}}\frac{N_{jets}}{\Delta p_{\mathrm{T}}(2\Delta|y|)} \tag{1}$$

όπου ϵ είναι μια διόρθωση λόγω μικρών πειραματικών ανεπαρκειών, $\mathcal{L}_{int}$ είναι

η ολοκληρωμένη φωτεινότητα του δείγματος, N_{jets} ο αριθμός των πιδάκων στο κάθε βήμα, Δp_T και $\Delta|y|$ είναι το πλάτος των βημάτων της εγκάρσιας ορμής και της ωκύτητας. Η μέτρηση σε σύγκριση με υπολογισμούς από τον γεννήτορα γεγονότων POWHEG+PYTHIA6 συμπληρωμένους με διορθώσεις λόγω ηλεκτρασθενών αλληλεπιδράσεων φαίνεται στο σχήμα 1.
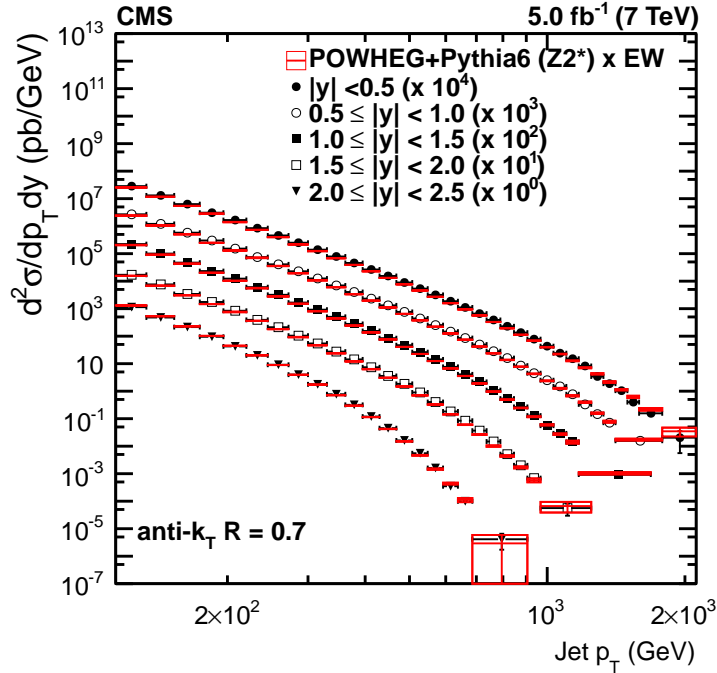

Σχήμα 1:   Η μέτρηση της διπλής διαφορικής ενεργού διατομής σε σύγκριση με υπολογισμος από τον γεννήτορα γεγονότων POWHEG+PYTHIA6 συμπληρμένους με διορθώσεις λόγω ηλεκτρασθενών αλληλεπιδράσεων.

Στη συνέχεια έγιναν υπολογισμοί χρησιμοποιώντας το υπολογιστικό πακέτο NLOJET++ μέσα από το FASTNLO. Οι υπολογισμοί βασίζονται στην θεωρία της διαταρακτικής κβαντικής χρωμόδυναμικής (ΚΧΔ) σε δεύτερη τάξη. Χρησιμοποιήθηκαν διαφορετικά Parton Distribution Functions (PDF) (ABM11, CT10, NNPDF2.1, MSTW2008) και οι υπολογισμοί έγιναν για διάφορες τιμές της σταθεράς ισχυρής αλληλεπίδρασης. Αυτοί οι υπολογισμοί έδειξαν ότι η διπλή διαφορική ενεργός διατομή των πιδάκων είναι ένα μέγεθος το οποίο διαφοροποιείται σημαντικά με την αλλαγή της σταθερας α_S.

Στο σχήμα 2 φαίνεται ο λόγος των πειραματικών δεδομένων με την θεωρία για διάφορα PDFs. Πέραν του $ABM11$ παρατηρείται ότι η θεωρία περιγράφει τα πειραματικά δεδομένα. Στο σχήμα 3 φαίνεται ο λόγος των πειραματικών δεδομένων με την θεωρία για διάφορες τιμές του $\alpha_S(M_Z)$. Παρατηρείται ότι η

τιμή της διπλής διαφορικής ενεργού διατομής είναι ευαίσθητη στην αλλαγή της τιμής του $\alpha_S(M_Z)$, συνεπώς είναι μια κατάλληλη μεταβλητή για την εξαγωγή της σταθεράς ισχυρής αλληλεπίδρασης από τα δεδομένα.
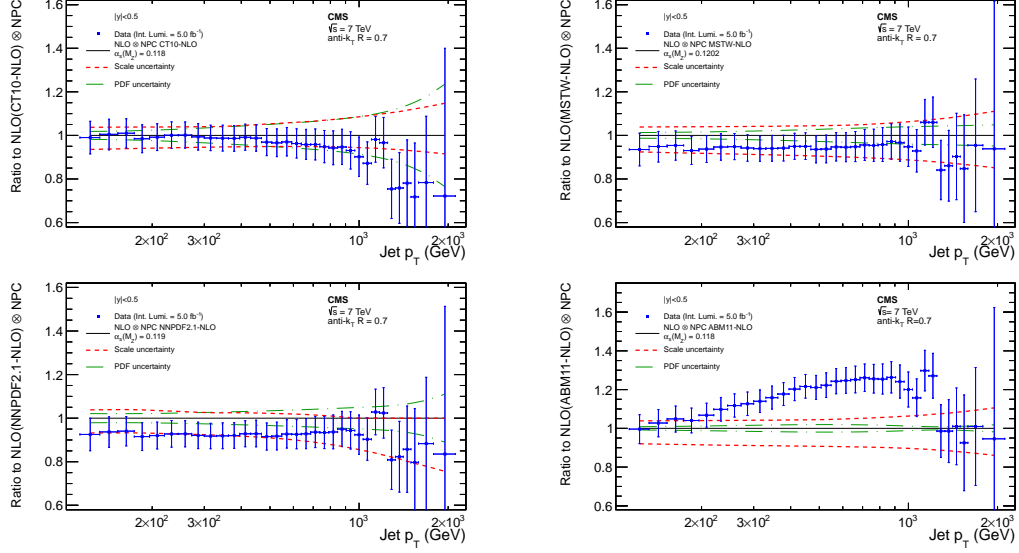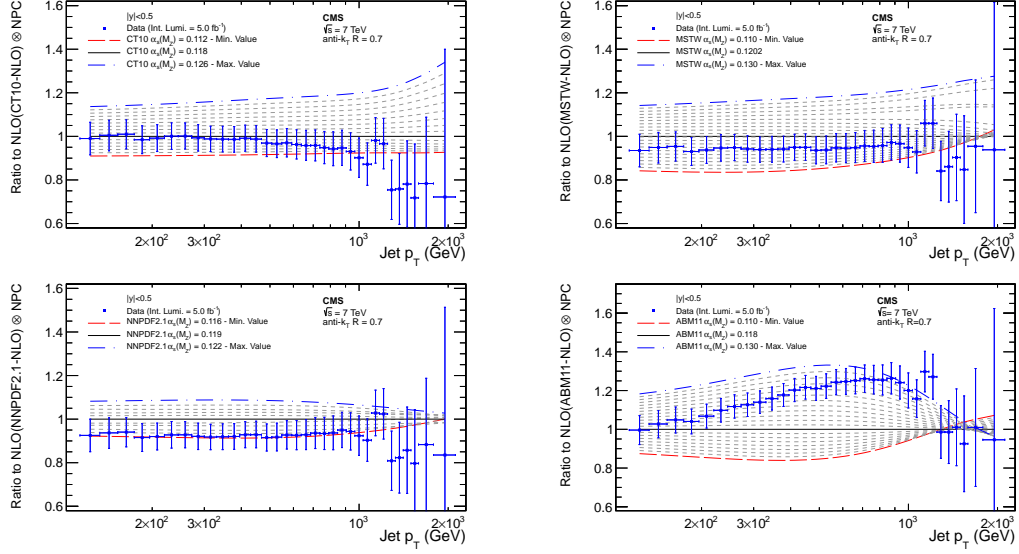

Σχήμα 2: Λόγος πειραματικών μετρήσεων με θεωρητικούς υπολογισμούς χρησιμοποιώντας τέσσερα διαφορετικά PDFs για την περιοχή $|y| < 0.5$.

Τα δεδομένα προσαρμόστηκαν στην θεωρία χρησιμοποιώντας την μέθοδο χ^2 και εξήχθη η σταθερά ισχυρής αλληλεπίδρασης, χρησιμοποιώντας το $CT10-NLO$. Το αποτέλεσμα είναι το ακόλουθο:

$$\alpha_S(M_Z) = 0.1185 \pm 0.0019\,(\text{exp.}) \pm 0.0028\,(\text{PDF}) \pm 0.0004\,(\text{NP})^{+0.0053}_{-0.0024}\,(\text{scale})$$
$$= 0.1185^{+0.0063}_{-0.0042}\,,$$

$$(2)$$

Η επόμενη μέτρηση η οποία περιγράφεται επίσης στο Κεφάλαιο 6 είναι η μέτρηση της σταθεράς ισχυρής αλληλεπίδρασης χρησιμοποιώντας τον λόγο της ενεργούς διατομής τριών πιδάκων προς την ενεργό διατομή δύο πιδάκων. Ο λόγος R_{32} μετρήθηκε συναρτήσει του μέσου όρου των εγκάρσιων ορμών των δύο πρώτων πιδάκων. Στην ανάλυση λήφθηκαν υπόψιν πίδακες με $p_T > 150 GeV$ και $|y| < 2.5$. Για την ανακατασκευή των σωματιδίων χρησιμοποιήθηκε η μέθοδος Particle Flow και για την συσσωμάτωση των σωματιδίων σε πίδακες χρησιμοποιήθηκε ο αλγόριθμος anti$-k_T$ με ακτίνα 0.7. Η θεωρία υπολογίστηκε χρησιμοποιώντας το υπολογιστικό πακέτο NLOJET++ μέσα από το FASTNLO.
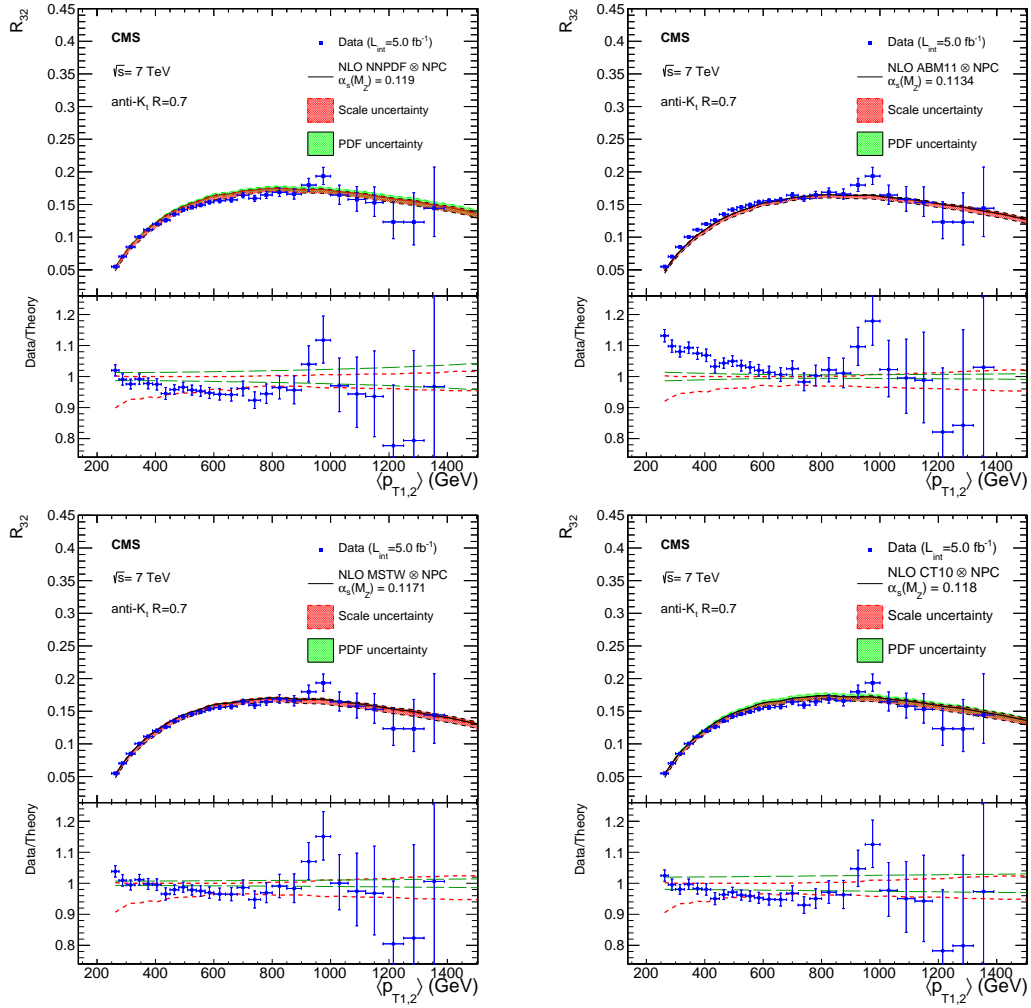
Σχήμα 3: Λόγος πειραματικών μετρήσεων με υπολογισμούς χρησιμοποιώντας τέσσερα διαφορετικά PDFs για την περιοχή |y| < 0.5 για εύρος τιμών του $\alpha_S(M_Z)$. Οι διακεχομένες γραμμές δείχνουν τους υπολογισμούς για διάφορες τιμές του $\alpha_S(M_Z)$ σε βήματα του 0.001.

Στο σχήμα 4 φαίνεται η μέτρηση του λόγου R_{32} συγκρινόμενη με την θεωρία η οποία υπολογίστηκε για διάφορα PDFs. Στο κάτω μέρος των γραφημάτων φαίνεται ο λόγος των δεδομένων ως προς την θεωρία. Στο σχήμα 5 φαίνεται η μέτρηση του λόγου R_{32} συγκρινόμενη με την θεωρία για διάφορες τιμές του $\alpha_S(M_Z)$. Πέραν του $ABM11$ φαίνεται ότι η τιμή του R_{32} είναι ευαίσθητη στην αλλαγή του $\alpha_S(M_Z)$.

Με την μέθοδο χ^2 τα δεδομένα προσαρμόστηκαν στις θεωρητικές τιμές. Χρησιμοποιώντας το $NNPDF2.1 - NNLO$ η τιμή της σταθεράς ισχυρής αλληλεπίδρασης βρέθηκε να είναι:

$$\alpha_s(M_Z) = 0.1148 \pm 0.0014(exp.) \pm 0.0018(PDF) \pm 0.0050(theory) \qquad (3)$$

Οι μετρήσεις της σταθεράς ισχυρής αλληλεπίδρασης (εξίσωση 2 και 3) είναι απόλυτα συμβατές με τον παγκόσμιο μέσο ο οποίος είναι, $\alpha_S(M_Z) = 0.1185 \pm 0.0006$. Επίσης σημειώνουμε ότι και στις δύο μετρήσεις κυριαρχούν οι θεωρητικές αβεβαιότητες.

Σχήμα 4: Στο πάνω μέρος της κάθε εικόνας φαίνεται η σύγκριση των πειραματικών μετρήσεων με θεωρητικούς υπολογισμούς χρησιμοποιώντας τέσσερα διαφορετικά PDFs. Στο κάτω μέρος της κάθε εικόνας εικονίζεται ο λόγος πειραματικών μετρήσεων με την θεωρία.
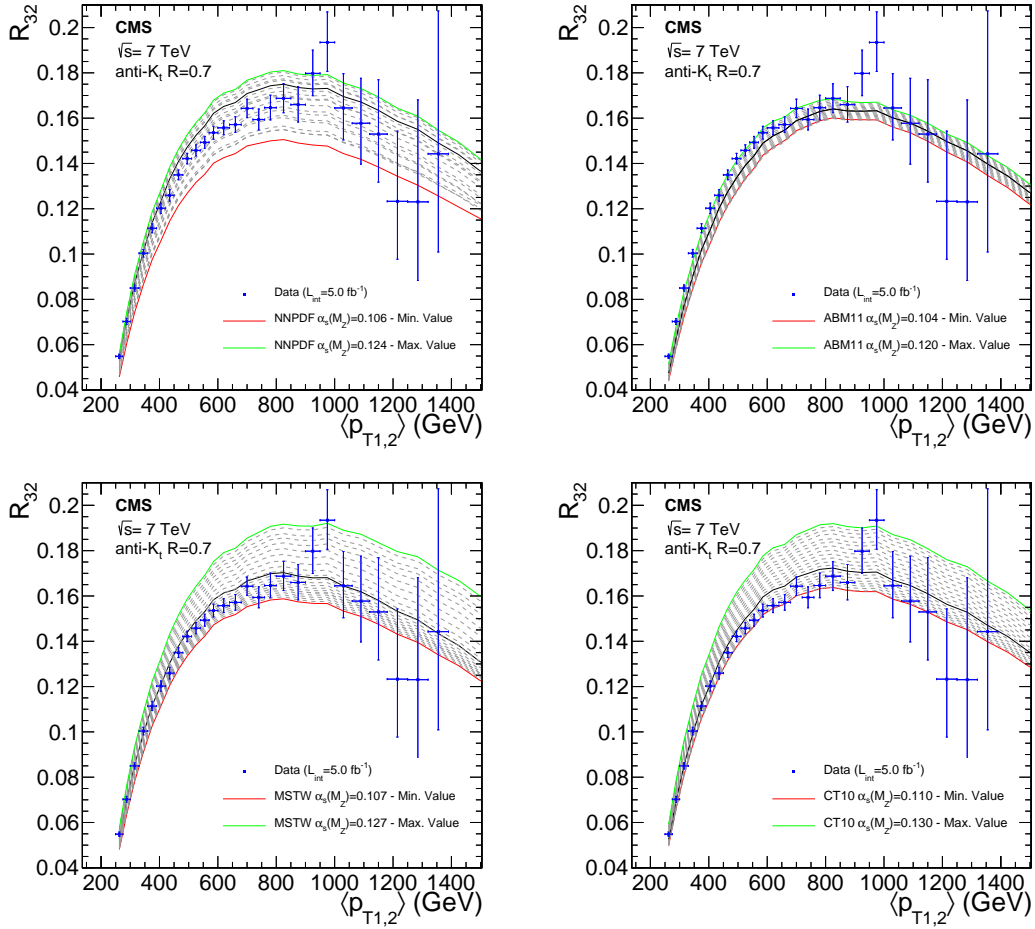
Σχήμα 5: Σύγκριση πειραματικών μετρήσεων με θεωρητικούς υπολογισμούς χρησιμοποιώντας τέσσερα διαφορετικά PDFs για ένα εύρος τιμών του $\alpha_S(M_Z)$. Οι διακεχομένες γραμμές δείχνουν τους υπολογισμούς για διάφορες τιμές του $\alpha_S(M_Z)$ σε βήματα του 0.001.

Στο Κεφάλαιο 7 περιγράφεται η μέτρηση των αζιμουθιακών αποσυσχετισμών δύο πιδάκων. Σε αυτή την ανάλυση μετρήθηκε η κανονικοποιημένη διαφορική ενεργός διατομή των δύο πιδάκων με την μεγαλύτερη εγκάρσια ορμή, ως συνάρτηση της αζιμουθιακής γωνίας, $\Delta\phi_{Dijet}$. Τα δεδομένα συλλέχθηκαν από συγκρούσεις πρωτονίων στο κέντρο μάζας, $\sqrt{s} = 8$ TeV και αντιστοιχούν σε ολοκληρωμένη φωτεινότητα 19.7 fb^{-1}. Οι μετρήσεις έχουν συγκριθεί με υπολογισμούς δεύτερης τάξης στην διαταραχτική θεωρία ΚΧΔ και με προσομοιώσεις Monte Carlo.

Η μέτρηση πραγματοποιήθηκε σε εφτά περιοχές της ορμής του κυρίαρχου πίδακα p_T^{max}. Η μεγαλύτερη ορμή πιδάκων που καταγράφηκε στα γεγονότα είναι $p_T = 2.2$ TeV. Για την ανακατασκευή των σωματιδίων χρησιμοποιήθηκε η μέθοδος Particle Flow και για την συσσωμάτωση των σωματιδίων σε πίδακες χρησιμοποιήθηκε ο αλγόριθμος anti$-k_{\mathrm{T}}$ με ακτίνα 0.7.

Στην ΚΧΔ σε πρώτη τάξη LO (Leading Order) τα δύο παρτόνια στην τελική κατάσταση παράγονται σε ένα εγκάρσιο επίπεδο. Σε αυτή την περίπτωση η αζιμουθιακή γωνία μεταξύ των δύο πιδάκων, $\Delta\phi_{\mathrm{Dijet}} = \phi_{\mathrm{jet1}} - \phi_{\mathrm{jet2}}$, ισούται με π. Μη διαταραχτίκα φαινόμενα όπως είναι οι αλληλεπιδράσεις πολλαπλών παρτονίων ή ο αδρονισμός διαταράσουν ελαφρά αυτόν το συσχετισμό. Η παραγωγή όμως ενός τρίτου πίδακα οδηγεί στον αποσυσχετισμό της αζιμουθιακής γωνίας. Η μικρότερη εφικτή γωνία με τοπολογία τριών πιδάκων είναι $\Delta\phi_{\mathrm{Dijet}} = 2\pi/3$. Η εκπομπή τέταρτου ή και περισσοτέρων πιδάκων οδηγεί σε γωνίες μικρότερες, μέχρι το μηδέν. Η μέτρηση αυτή μελετάει γεγονότα με πολλαπλούς πίδακες μετρώντας μόνο τις γωνίες και τις ορμές των δύο πρώτων πιδάκων. Στο σχήμα 6 φαίνεται η κανονικοποιήμενη ενεργός διατομή συναρτήσει του $\Delta\phi_{\mathrm{Dijet}}$ για τις εφτά περιοχές $p_{\mathrm{T}}^{\mathrm{max}}$. Τα δεδομένα συγκρίνονται με θεωρητικούς υπολογισμούς βασισμένους στο υπολογιστικό πακέτο NLOJET++, που χρησιμοποιεί το C10-NLO PDF. Στο σχήμα 7 εικονίζεται ο λόγος της μέτρησης προς την θεωρία χρησιμοποιώντας πέντε διαφορετικά PDF. Στο σχήμα 8 φαίνεται η μέτρηση συγκρινόμενη με τα αποτελέσματα που προέκυψαν από τις προσομοιώσεις Monte Carlo χρησιμοποιώντας πέντε διαφορετικούς γεννήτορες γεγονότων. Στο σχήμα 9 εικονίζεται ο λόγος των προσομειώσεων προς τα δεδομένα.

Οι υπολογισμοί δεύτερης τάξης στην διαταραχτική θεωρία ΚΧΔ έχουν ως αποτέλεσμα την παραγωγή τεσσάρων παρτονίων. Για την περιοχή $\Delta\phi_{\mathrm{Dijet}} > 2\pi/3$ ο υπολογισμός είναι NLO ενώ για την περιοχή $\Delta\phi_{\mathrm{Dijet}} < 2\pi/3$ LO. Οι υπολογισμοί σε NLO περιγράφουν τα δεδομένα στην περιοχή $\Delta\phi_{\mathrm{Dijet}} > 5\pi/6$, αλλά αποκλίνουν σημαντικά κάτω από αυτή την περιοχή. Το ίδιο μοτίβο παρατηρείται στην LO περιοχή όπου η θεωρία περιγράφει τα δεδομένα στην περιοχή $\Delta\phi_{\mathrm{Dijet}} \approx 2\pi/3$ ενώ κάτω από αυτή την περιοχή η θεωρία αποκλίνει.

Συγκρίνοντας τα δεδομένα με διάφορους γεννήτορες γεγονότων παρατηρείται ότι ανάμεσα στους LO γεννήτορες ο PYTHIA8 δίνει την

καλύτερη συμφωνία. Ο γεννήτορας POWHEG παρόλο που υπολογίζει ενεργές διατομές σε NLO έχει την ίδια συμφωνία με τα δεδομένα όπως οι LO γεννήτορες. Ο γεννήτορας MADGRAPH δίνει την καλύτερη συμφωνία και αυτό έγκειται στο γεγονός ότι μπορεί να προσομοίωσει μέχρι τέσσερα παρτόνια καθώς επίσης είναι συνδεδεμένος με τον PYTHIA6 για προσομοιώσεις παρτονικών καταιονισμών. Η ανάλυση φανερώνει την ανάγκη για βελτιώση των θεωρητικών υπολογισμών των γεγονότων με πολλαπλούς πιδάκες.
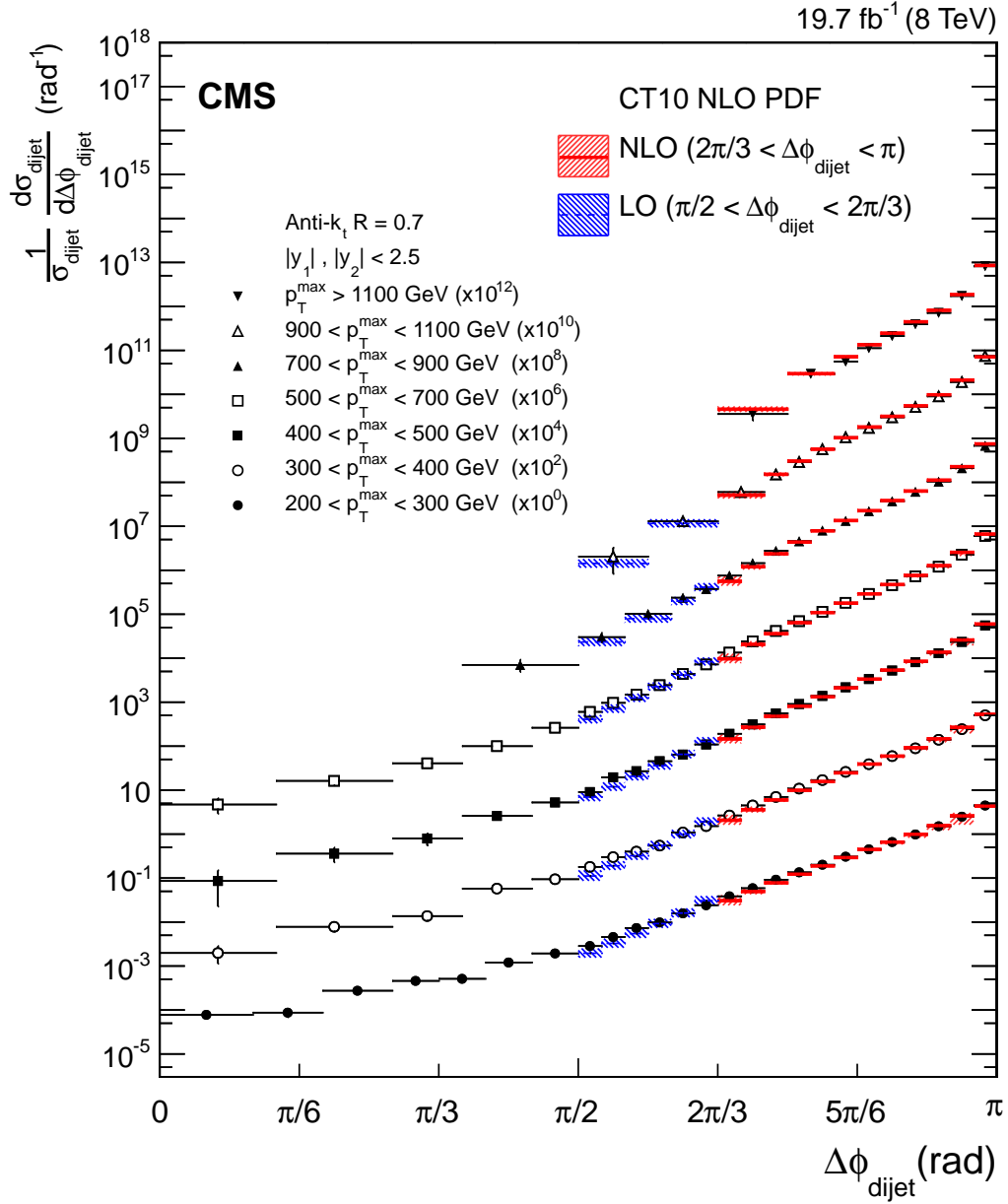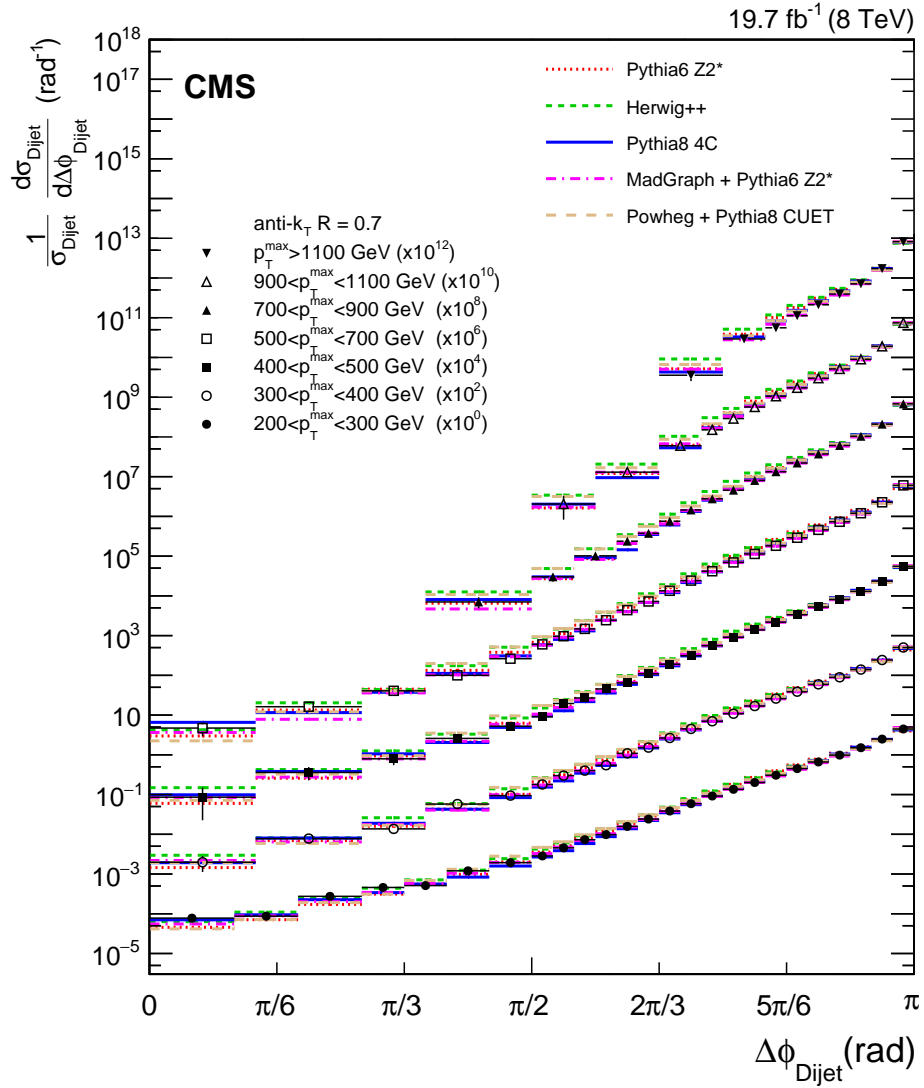
Σχήμα 6: Η κανονικοποιήμενη ενεργός διατομή συναρτήσει του $\Delta\phi_{\text{Dijet}}$ για τις εφτά περιοχές $p_{\text{T}}^{\max}$. Τα δεδομένα συγκρίνονται με θεωρητικούς υπολογισμούς που χρησιμοποιούν το C10-NLO PDF

.
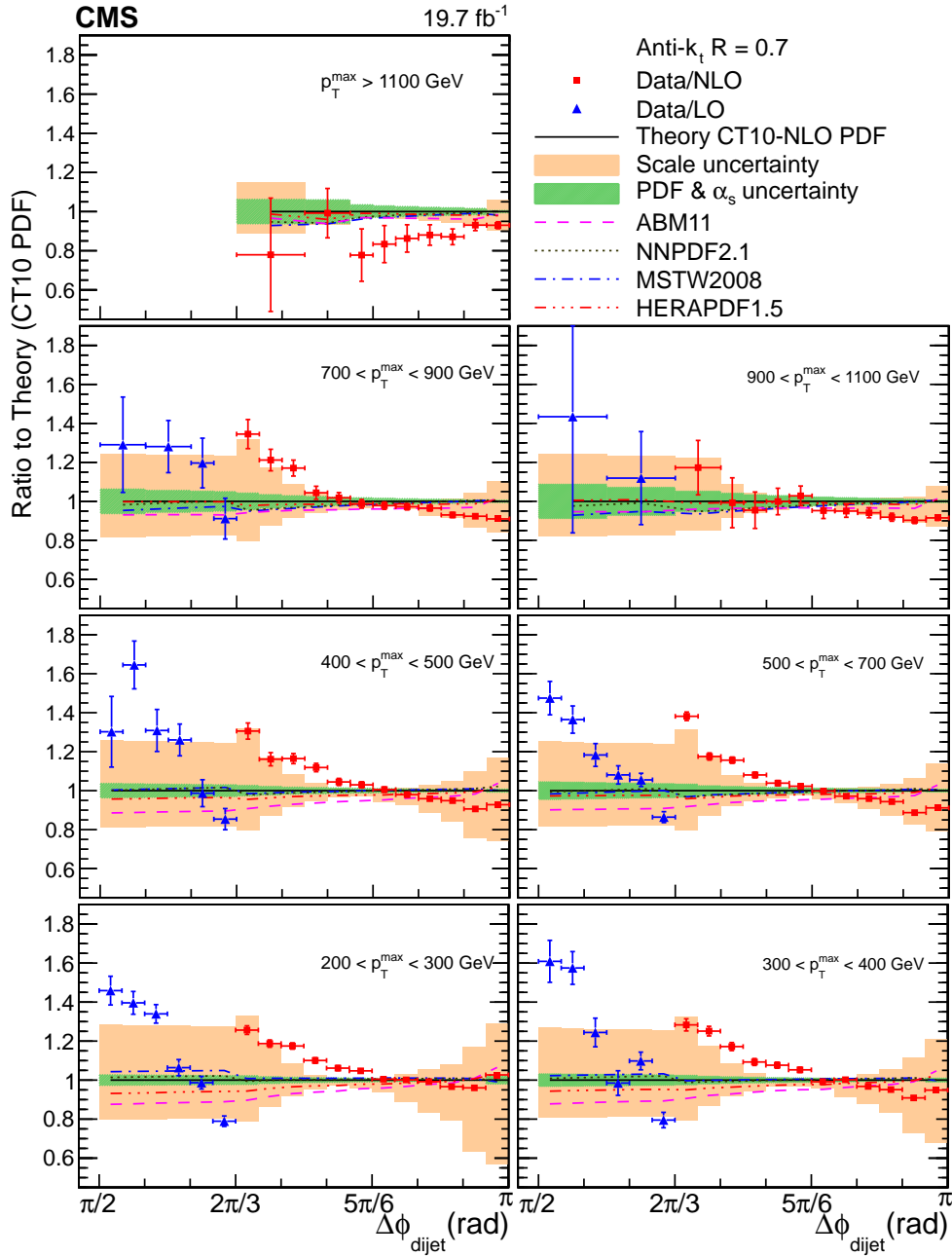
Σχήμα 7: Ο λόγος της κανονικοποιημένης ενεργούς διατομής χρησιμοποιώντας πέντε διαφορετικά PDFs. Οι γραμμές των σφαλμάτων στα πειραματικά σημεία δείχνουν την συνολική αβεβαιότητα (στατιστική και συστηματική). Οι αβεβαιότητες των θεωρητικών υπολογισμών φαίνονται ως σκιασμένες περιοχές.

Σχήμα 8: Κανονικοποιήμενη ενεργός διατομή συναρτήσει του $\Delta\phi_{\mathrm{Dijet}}$ για εφτά περιοχές $p_{\mathrm{T}}^{\max}$ συγκρινόμενη με υπολογισμού από τους γεννήτορες, PYTHIA6, , PYTHIA8, MADGRAPH+PYTHIA6 και POWHEG+PYTHIA8
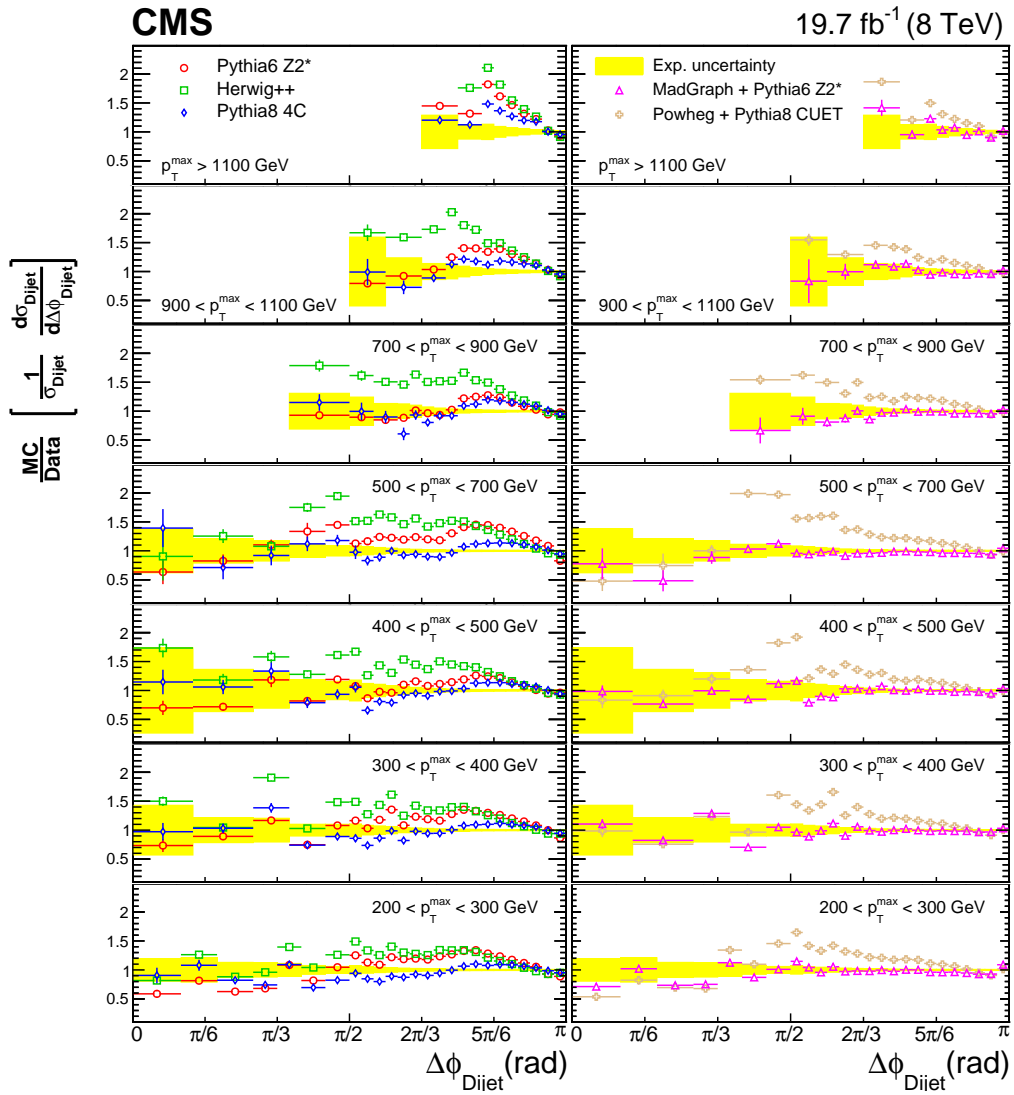
Σχήμα 9: Ο λόγος των προσομειώσεων προς τα δεδομένα συναρτήσει του $\Delta\phi_{\mathrm{Dijet}}$ για εφτά περιοχές $p_{\mathrm{T}}^{\mathrm{max}}$.

Contents

Figures

Tables

1   Introduction

Particle physics is the science that is aiming to describe nature to its elementary form. Particle physics started as a philosophical quest of ancient Greek (Leukipus, Democritus etc) and Indian (Kanada) philosophers. The human mankind has always been wondering about the origin of the cosmos and the ultimate blocks of matter. Ancient's philosophers contribution to modern particle physics is practically zero but we cannot overlook that their ideas gave food for thought to modern physicists.

Nowadays particle physics is a strict science described by the mathematical language and probed by complex experiments. The large hadron collider (LHC), a proton-proton collider, placed at Franco-Swiss borders at the European Laboratory for Particle Physics (CERN) is the biggest experiment in the history of human mankind. Its ultimate purpose does not differ from the ancients philosophers, 2500 years ago. The goal is to extend the human mankind's knowledge to a supreme level, where all physical processes taking place in our universe are understood and explained by logic.

This thesis describes the research performed using data from the compact muon solenoid (CMS) detector which is placed at the LHC collider. The thesis is structured in seven chapters, besides the Introduction. In Chapter 2 and Chapter 3, the LHC and CMS experiments are briefly described. In Chapter 4 the theoretical framework of particle physics called Standard Model (SM) is described with emphasis to Quantum Chromodynamics (QCD). Chapter 5 describes the event reconstruction and energy correction techniques used in the analyses. Chapters 5 and 7 describe the analyses at 7 and $8TeV$ respectively. Finally Chapter 8 sums up the results derived from the analyses.

2   The Large Hadron Collider

The Large Hardon Collider (LHC) is a proton-proton collider designed to probe physics with centre of mass up to $\sqrt{s} = 14 TeV$. LHC is a two ring hadron accelerator installed in the $26.7 km$ tunnel at CERN, where Large Electron Positron (LEP) was installed. The primary aim of the LHC is to search the the nature of electroweak symmetry and the discovery of the Higgs boson, and to reveal physics beyond the Standard Model (BSM). The LHC has two general purpose experiments CMS[1] and ATLAS[2] that cross-check each other. There four more experiments; ALICE[3], LHCb[4], TOTEM[5], and LHCf[6].

The LHC is a promising project for discoveries and high precision measurements not only because of its high energy but also for the high rate of number of events, N_{event}, generated in each collision

$$N_{event} = L\sigma_{event} \tag{1}$$

where σ is the cross section for the event under study and L the machine's luminosity. The luminosity is defined as

$$L = \frac{1}{\sigma}\frac{dN}{dt} \tag{2}$$

where the integrated luminosity, is the integral of L over time. The LHC design luminosity is $L = 10^{34} cm^2 s^{-1}$. The machine luminosity is a value that depends only on the beam parameters and in can be expressed as:

$$L = \frac{N_b^2 n_b f_{rev} \gamma_r}{4\pi\epsilon_n\beta^*}F \tag{3}$$

where N_b is the number of particles per bunch, n_b the number of bunches per beam, f_{rev} the revolution frequency, γ_r the relativistic gamma factor, ϵ_n the normalized transverse beam emittance, β^* the beta function at the collision point, and F the geometric reduction factor due to the crossing angle at the interaction point (IP).

The total integrated luminosity delivered by the LHC and the one recorded by the CMS are summarized in Table 1 and figure 1 show the 2012 data of integrated luminosity versus time.

Table 1: The integrated luminosity delivered by the LHC and recorded by the CMS.

Year	$\sqrt{s}(TeV)$	$\mathcal{L}_{LHC}(fb^{-1})$	$\mathcal{L}_{CMS}(fb^{-1})$
2010	7	0.442	0.408
2011	7	6.13	5.55
2012	8	23.30	21.79

The acceleration of two counter rotating bunches of protons requires opposite magnetic fields in each ring. The LHC uses superconducting NbTi Rutherford cables cooled at 1.9K using super-fluid helium and operate at 8 Tesla. The LHC ring is consisted by 1232 superconducting dipole magnets that are used to direct the beam and 392 quadrupole magnets that are used to collimate the beams.

The acceleration of the proton bunches is achieved gradually through a complex of smaller accelerators. The injection chains starts from a linear accelerator LINAC2 which accelerates protons at $50 MeV$ and subsequently injects them to proton synchrotron booster (PSB). PSB increases the protons energy to $1.4 GeV$ and injects them into Proton Synchrotron (PS) which
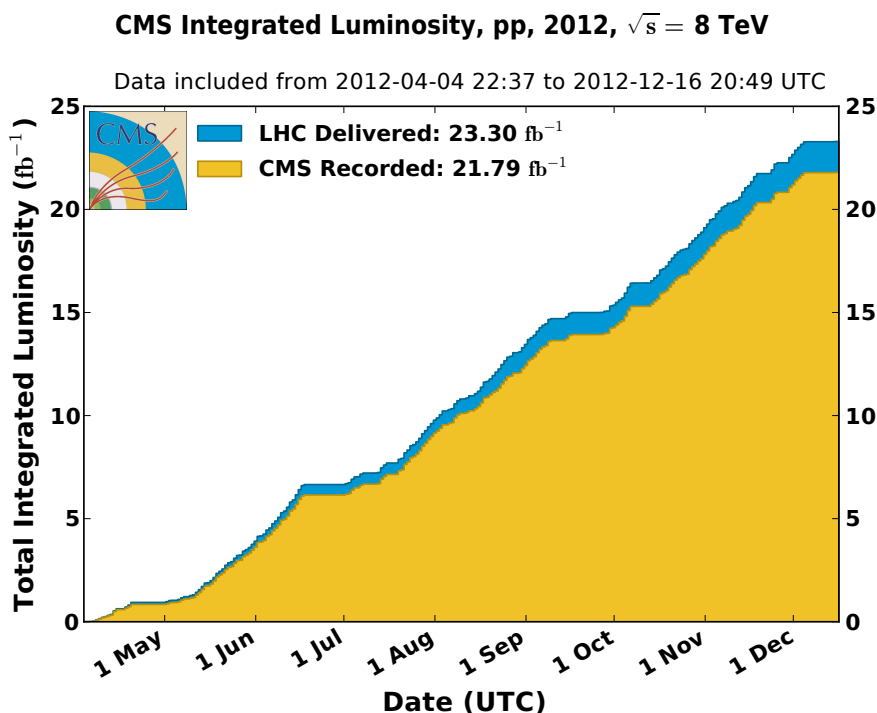
Figure 1: The integrated luminosity delivered by the LHC and recorded by the CMS during 2012.

accelerates protons up to $25 GeV$. PS then injects protons to Super Proton Synchroton (SPS) which finally increase protons energy to 450 GeV before injecting them to LHC. The complex of the accelerators is illustrated in figure2. The minimum injection time of LHC is $16 mins$ and the acceleration time from $450 GeV$ to $7 TeV$ in the LHC is $20 mins$.

The LHC captures, accelerates and stores the injected beam using a superconducting cavity system working at 400.8 MHz. The LHC is design to accelerate 2082 bunches, each containing $\approx 1.15 \times 10^{11}$ protons, separated by 25 ns. The separation though during the three year of run is, 150ns during 2010, 75/50 ns during 2011, and 50 during 2012.
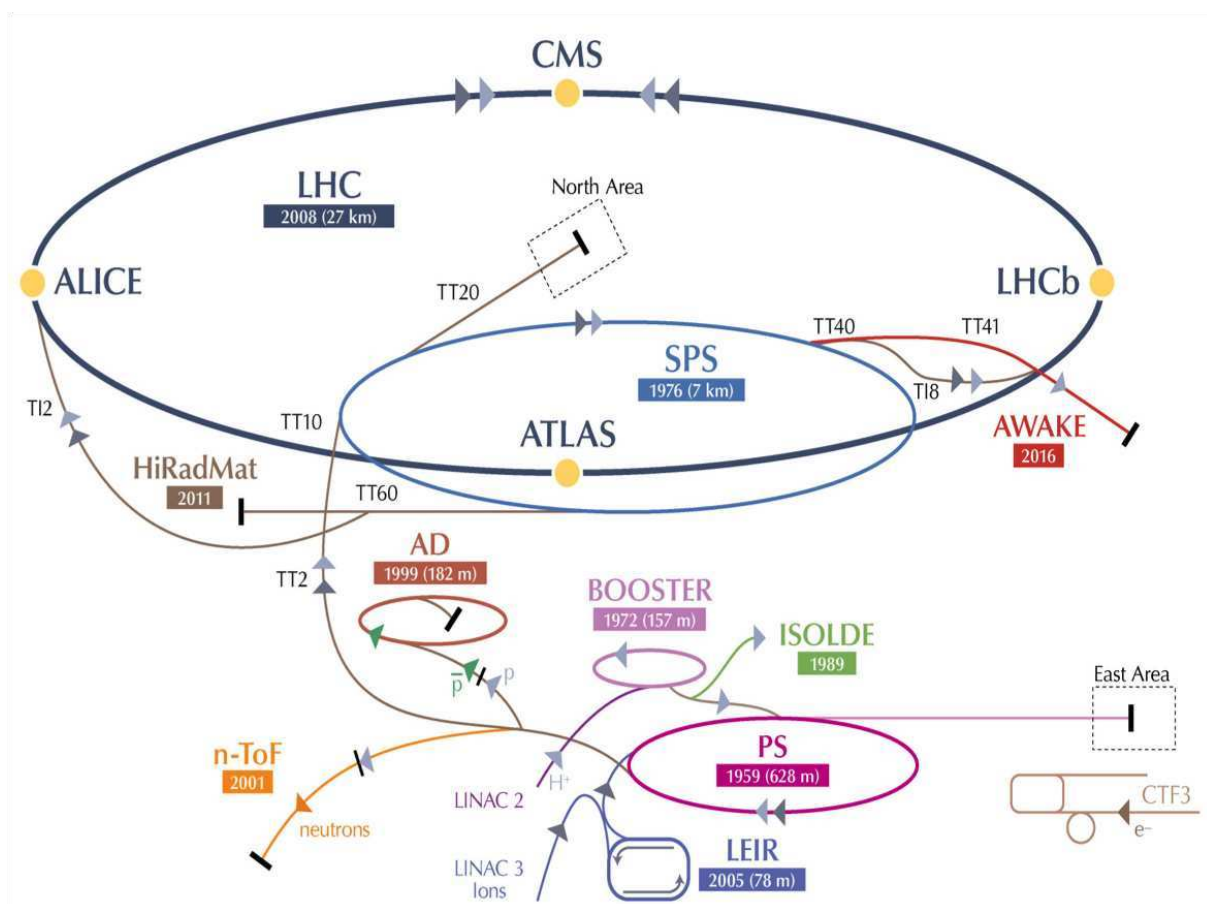
Figure 2: CERN's accelerator complex.

3   The Compact Muon Solenoid

The Compact Muon Solenoid (CMS) is one of the general purpose detectors recording collisions from LHC. It has a cylindrical shape, with dimensions 21-m long, 15-m wide and 15-m high and it placed 100-m underground near the village Cessy in France. The CMS detector consists of a set of sub-detectors placed in layers, see figure 3 layers of sub-detectors, silicon tracker, electromagnetic calorimeter (ECAL), hardonic calorimeter (HCAL), and muon detectors and the 4 Tesla superconducting solenoid.
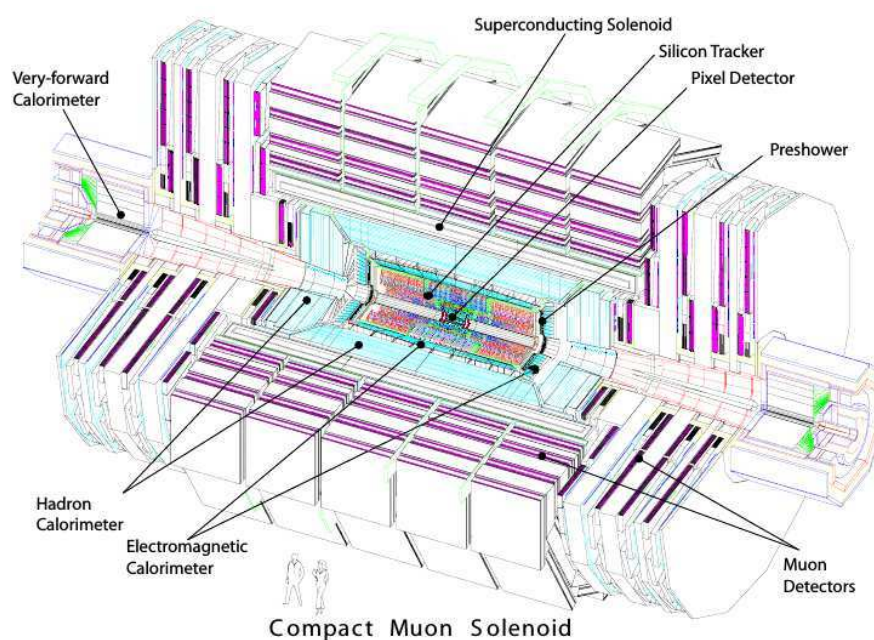
Figure 3: A perspective view of the CMS detector.

The large luminosity of LHC requires detectors and electronics with good time resolution and hardness in radiation. In order to cope to the demanding physics program CMS has to follow the following requirements. Good lepton and jet identification and momentum resolution. Also good diphoton and dielectron mass resolution is essential as well as good missing transverse energy resolution.

The coordinate system used by CMS has its origin centered at the nominal collision point, the y-axis pointing vertically upward, the $x-$axis pointing radially inward toward the center of the LHC, and the z-axis point along the counter-clockwise beam direction. The azimuthal angle is denoted as ϕ and it is measured from the $x-$axis in the $x-y$ plane. The polar angle denoted as θ is measured from the z-axis but it is rarely used; instead pseudorapitidy is used which is defined as $\eta = -lntan(\theta/2)$.

The chapter is describing the basic concepts and functionalities of the sub-detectors and triggering system. A complete description of the detector can be found in[1].

3.1   Superconducting magnet

The large bending power is crucial in order to make possible the precision momentum measurements of charged particles. The magnetic field is provided by the superconducting magnet which is designed to reach 4-T field and 12Tm bending power. The magnet is 13-m long, 6-

minner-diameter and it is placed between the HCAL and the muon detectors. The magnetic field is returned through an iron yoke and geometrically fully covers the muon detectors. An artistic view of the superconducting solenoid is shown in Fig. 4.
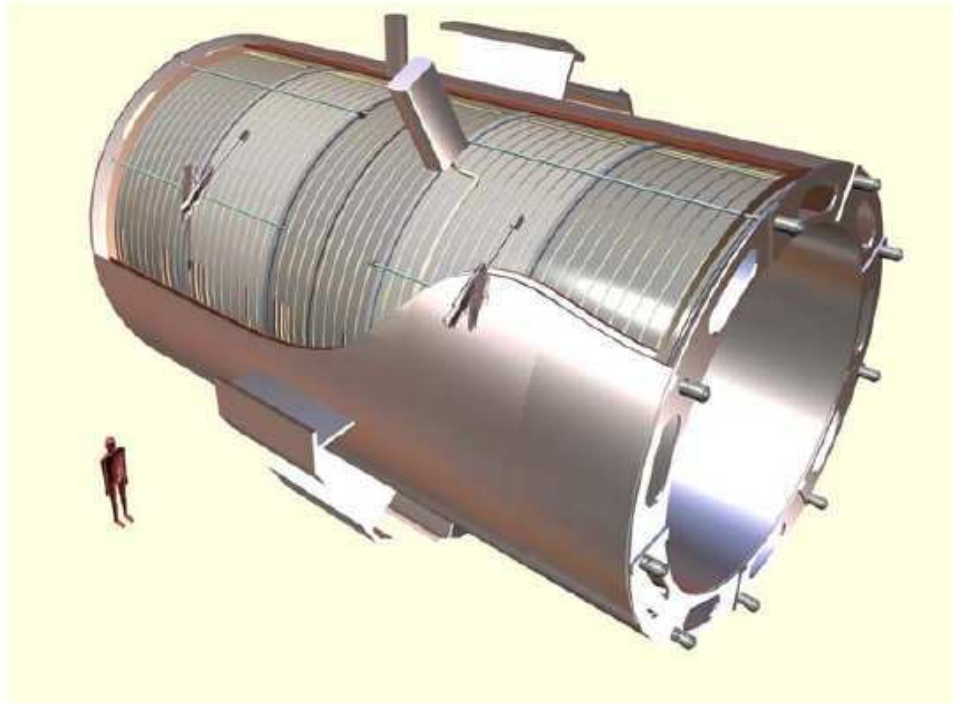
Figure 4: The superconducting solenoid, an artistic view.

The iron yoke weights 10 000-t and it consists of 5 wheels and 2 endcaps. The conductor is made from NbTi Rutherford-type cable which is mechanically reinforced with an aluminium alloy. The helium refrigerator is used to cool down to 4.6 K the solenoid.

3.2 Inner tracking system

The inner tracking system of CMS is the detector closest to the beam, with length 5.8 m long and diameter 2.5 m. The task of this sub-detector is to provide precise measurements of charged particles coming from collisions as well as reconstruction of secondary vertices. At the full luminosity run of LHC about 1000 particles every $20ns$ will permeate the tracker; therefore high granularity and fast response is required.

Figure 5 shows schematically how the sub-detectors are placed. At $r = 4.4, 7.3$ and $10.2cm$ the cylindrical layers of hybrid pixel detector modules are placed. The Tracker Inner Barrel and Disks (TIB/TID) cover the region up to $r = 55cm$ and are consisted of 4 barrel layers plus 3 disks at each end. The Tracker Outer Barrel (TOB)surrounds the TIB/TID covering a region up to $r = 116cm$ and consists of 6 barrel layers. The TOB cover an area in z-axis between $\pm118cm$, beyond that region the Tracker EndCaps (TEC+ and TEC-) covers the region $124cm < |z| < 282cm$ and $22.5cm < |r| < 113.5cm$. Each TEC is composed of 9 disks. The inner tracking system is covering an area up to $|\eta| < 2.5$.

The radiation length, X_0, of the CMS tracker increases from $0.4X_0$ at $\eta \approx 0$ to about $1.8X_0$ at $\eta \approx 1.4$, beyond that it reduces to about $1 x_0$ at $\eta \approx 2.5$

The measurement of a charged particle in a magnetic field is achieved by measuring the sagita(s) and the length(L) of the track, as shown in figure 6.
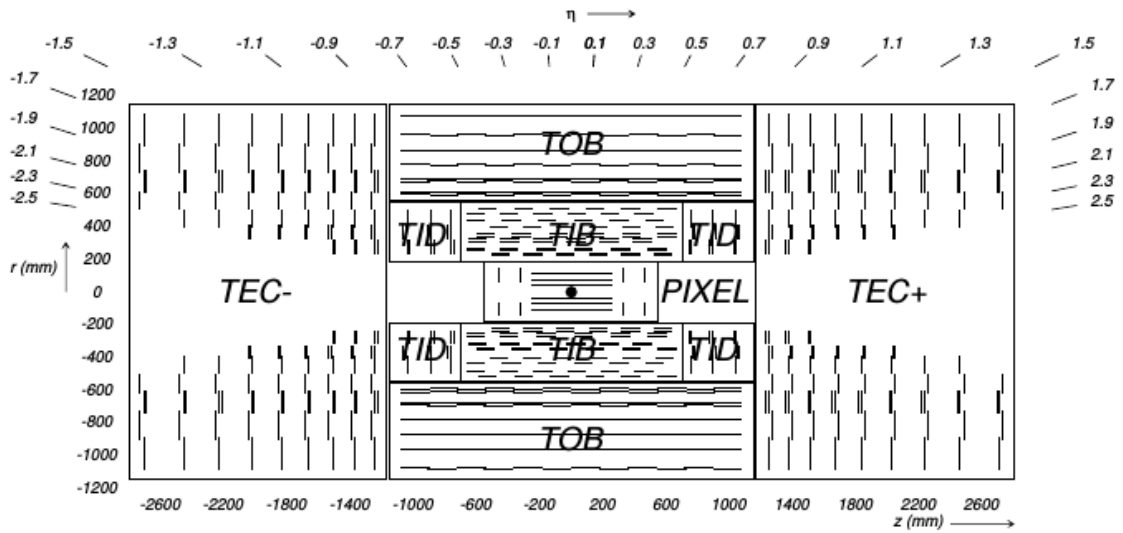
Figure 5: Section in $r - z$ plane of the tracker system of CMS.
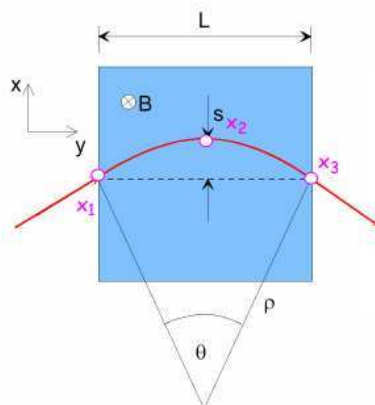
Figure 6: Charged particle in magnetic field.

The momentum in units of GeV is given by:

$$p(GeV) = 0.3 \cdot B(Tesla) \cdot R(m) \tag{4}$$

The momentum in terms of sagita and length can be written as:

$$p(GeV) = \frac{0.3}{8} \frac{L^2 B}{s} \tag{5}$$

The resolution of the momentum measurement for high p_T isolated tracks and the muon momentum in combination with the muons chambers is shown in the left and right part of figure 7 respectively. The high p_T isolated track's momentum resolution is better than $\frac{\delta p_T}{p_T} \approx (15 \cdot p_T \oplus 0.5)\%$ in the region $|\eta| < 1.6$ and is degrading for as $|\eta|$ approaches 2.5.
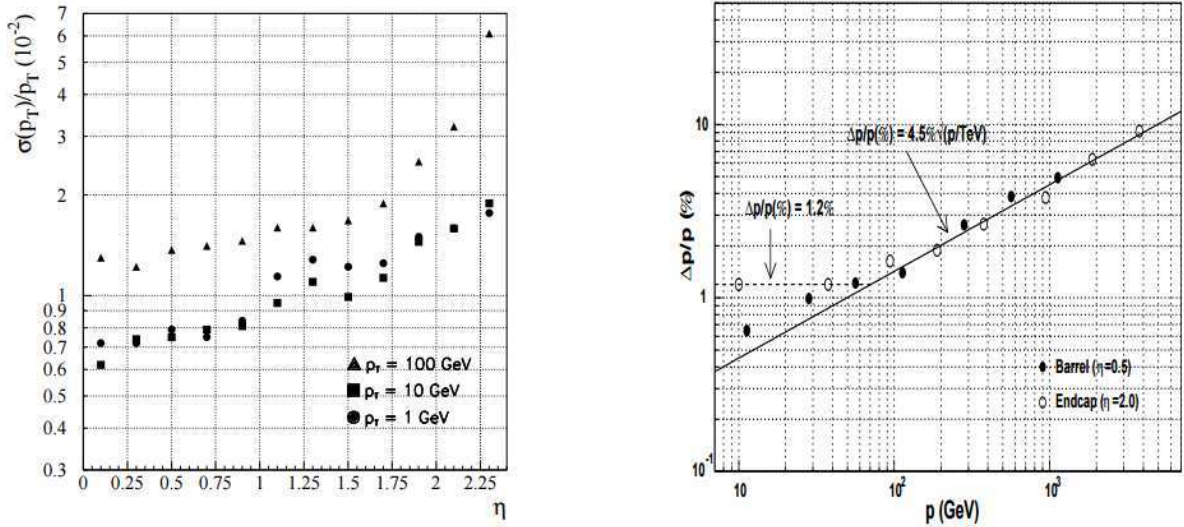
Figure 7: Left: high p_T isolated tracks resolution as a function of η. Right: Combination of tracker and muon chambers resolution a a function of p_T.

3.3 Electromagnetic calorimeter

The electromagnetic calorimeter(ECAL) of CMS consists of the central barrel and two endcaps. The central barrel carries 61200 lead tungstate ($P_b WO_4$) while 7324 crystals are mounted in each of the two endcaps. ECAL's endcaps are also equipped with a preshower detector. Avalanche photodiodes (APDs) and vacuum phototriodes are used as photodetectors (VPTs) in barrel and endcaps respectively.

The selection of the high density materials was based on the need of radiation resistance and fine granularity, which are crucial characteristics for the LHC environment. The high density ($8.28 g/cm^3$), short radiation length ($0.89 cm$) and small Moliére radius ($2.2 cm$) and the scintillation decay time which is close to the LHC bunch crossing (80% of the light is emitted in $25 ns$) renders the crystals a proper choice. The $P_b WO_4$ crystals led to a compact calorimeter with high granularity and hardness in radiation.

The barrel part of the ECAL (EB) covers a pseudorapidity range $|\eta| < 1.479$ while the endcaps (EE) cover a pseudorapidity range $1.479 < |\eta| < 3.0$. Figure 8 shows the pseudorapidity coverage of each part.
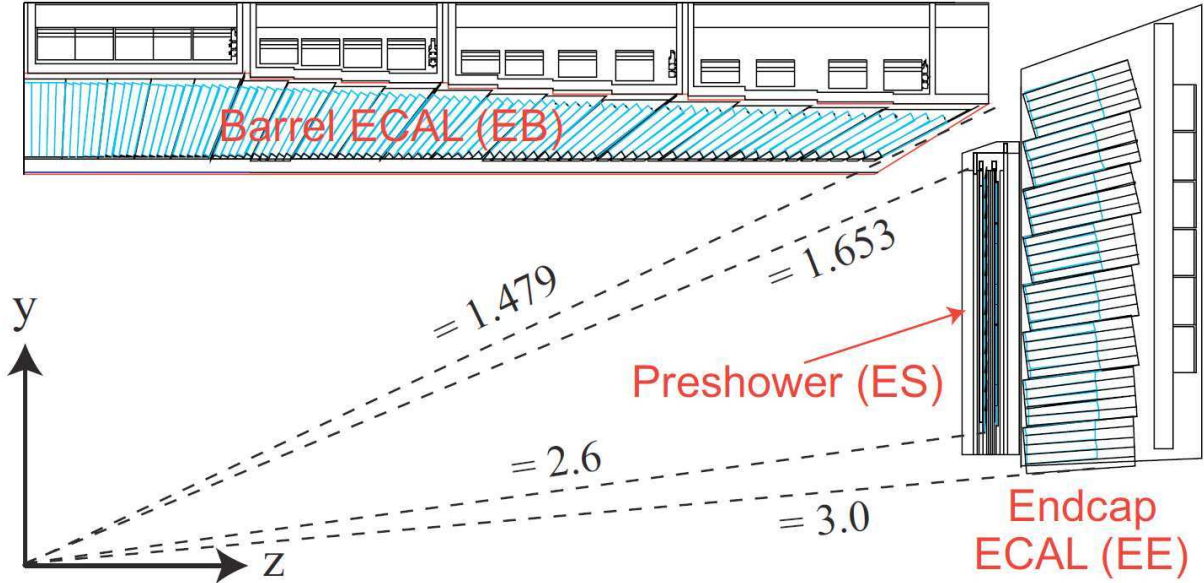
Figure 8: ECAL coverage in various η regions.

The barrel crystal cross-section is approximately 0.0174×0.0174 in $\eta - \phi$ which corresponds to $22 \times 22mm^2$ at the front and $26 \times 26mm^2$ in the rear face. The crystal are formed in that way in order to fit together and leave no gaps; they are also aligned to the nominal interaction vertex with an angle of $3°$ for the same reason. The crystal length is $230mm$ which corresponds to $25.8X_0$. Figure 9 shows schematically how crystals are placed and oriented. The readout of the scintillating light is carried out by APDs with an active area of $5mm^2$; where a pair is mounted in each crystal. They operate at a high gain of 50 since the light yield of crystals is small.

The endcap crystals front cross-section is 28.62×28.62 while the rear face cross-section is 30×30. The length of the crystals is $220mm$ which translates to $24.7X_0$. Each endcap holds 7324 identical crystals grouped in units of 5×5 (superclusters SC). VPTs are used to read out the scintillating light in the case of the endcaps. Each VPT has diameter or $22mm$ and is attached to the back of every crystal; working with mean gain of 10.2 (at zero field).

The preshower detector covers the region $1.653 < |\eta| < 2.6$, it is utilized to identify neutral pions and electrons against minimum ionizing particles (MIP). Preshower is a two layer detector consisting of a lead radiator tha initiates the electromagnetic showers from incoming photons/electrons and silicon strip sensors placed after the radiator. Silicon strip sensors measure the deposited energy and the transverse shower profile. The total thickness of the preshower is $20cm$, which corresponds to $2X_0$ (before the first sensor plane) plus $1X_0$ (before reaching the second plane).

The energy resolution of the ECAL is can be parametrizes as:

$$\left(\frac{\sigma}{E}\right)^2 = \left(\frac{S}{\sqrt{E}}\right)^2 + \left(\frac{N}{E}\right)^2 + C^2 \qquad (6)$$

Where S is the stochastic term depending on event-to-event fluctuation in the lateral shower containment, a photostatistic contibution and fluctuations in energy depositions in the preshower absorber with respect to the final measurement. N is the noise factor depending on electronics noise, digitization nois, and pileup noise. Finaly, C is the constant term depending on the non-uniformity of the longitudinal light collection, intercalibration errors, and leakage of energy
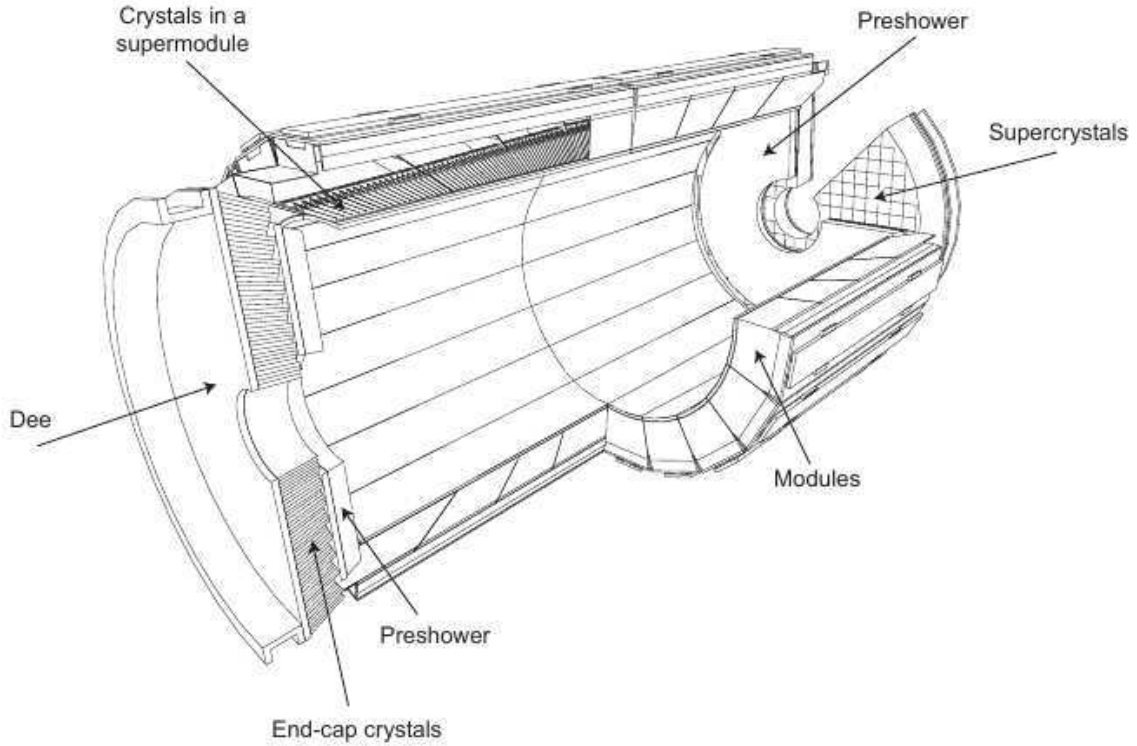
Figure 9: Schematic of ECAL crystals orientation.

from the back of the crystal. Measurements during the test beam showed that the SNC terms are the following:

- Barrel - $S = 2.8\%$, $N = 12\%$, and $C = 0.30\%$
- Endcaps - $S = 5.5\%$, $N = 12\%$, and $C = 0.30\%$

3.4   Hadron calorimeter

The hadron calorimeter (HCAL) barrel and endcaps are contained between the ECAL and the inner part of the solenoid, $1.77m < r < 2.95m$, a fact that constrains the total amount of absorbing material. Outside the solenoid the outer hadron calorimeter (HO, tail catcher) is placed. HCAL covers the region $|\eta| < 3.0$, beyond that there is the forward hadron calorimeter which goes up to $|\eta| < 5.2$. Figure 10 shows the eta coverage of barrel (HB), endcap (HE), outer (HO) and forward (HF) calorimeters.

The HB is a sampling calorimeter covering the region $|\eta| < 1.3$ and it consists of 36 identical azimuthal wedges which form two half-barrels. The absorber consists of a $40mm$ front steel plate, eight $50.5mm$ brass plates, and $75mm$ steel back plate. The absorber thickness is 5.82 interaction length, λ_I, at 90° increasing as $1/sin\theta$; ECAL adds about 1.1 of λ_I. The 70000 plastic scintillators are segmented in $\Delta\eta \times \Delta\phi = 0.087 \times 0.087$.

The HE covers the area $1.3 < |\eta| < 3$ which is the 13.2% of the solid angle and is a region that contains about 34% of the final state particles. The absorber consists of brass plates $79mm$ with $9mm$ gap to accommodate the scintillators; including ECAL is about $10\lambda_I$. The scintillators are segmented in $\Delta\eta \times \Delta\phi = 0.17 \times 0.17$.

The HO is a detector extending the HCAL to the outer part of the solenoid because the stopping
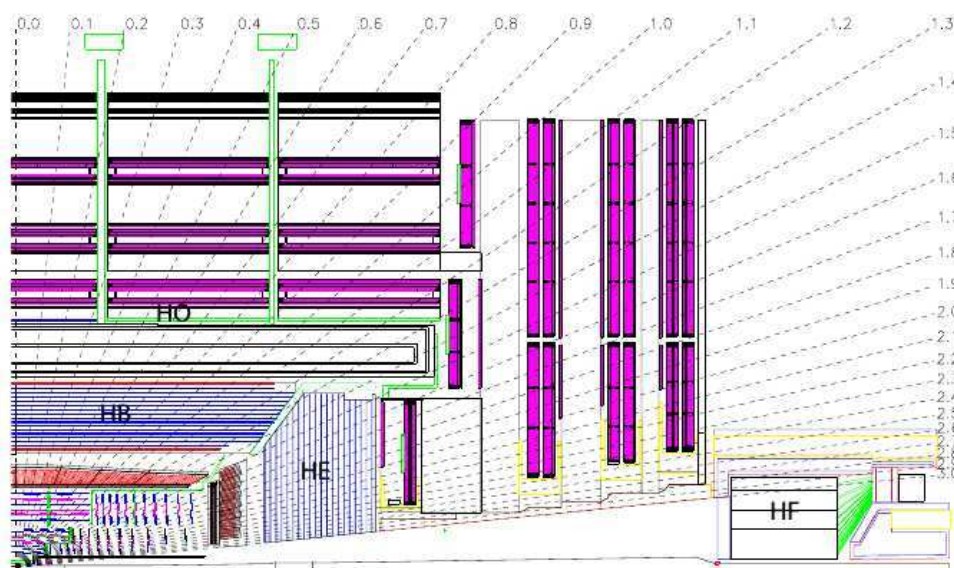
Figure 10: Longitudinal view of CMS showing HCAL.

power of EB and HB is not sufficient to catch all hadron showers. HO utilizes the stopping power of the solenoid coil which adds $1.4/sin\theta$ interaction lengths. At $\eta = 0$, HB has the minimal absorber depth, therefore two layers of HO scintillators are placed; while everywhere else a singe scintillator is placed. The total depth of HCAL is extended to a minimum of $11.8\lambda_I$. The energy resolution of HCAL with and without HO is shown in figure 11 , where single pion MC used.
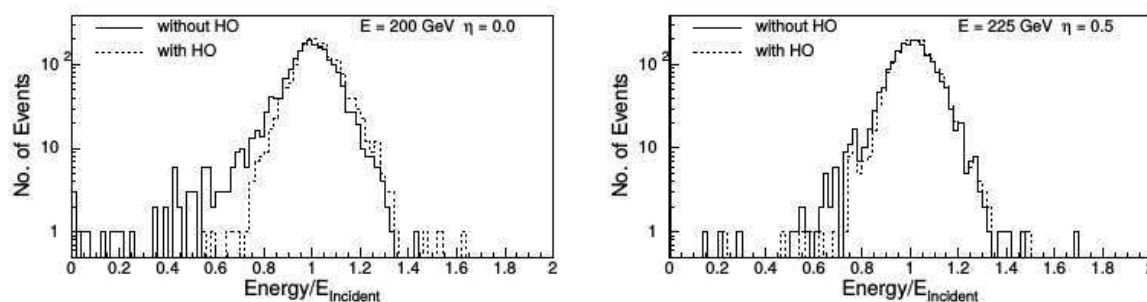
Figure 11: Measured energy over incident energy of single pions with and without HO.

The HF is the most forward detector of HCAL extending the HCAL's reach up to $\eta = 5$. At this region HF is designed in such a way that in 10 years of LHC operation will survive a radiation dose of $\approx 10 MGy$. at these extreme conditions. This was the principal reason why Cherenkov detectors with quartz fibre were selected. The HF is a cylindrical steel structure with radius of $130.0 cm$ and it is located $11.2m$ from the interaction point (IP). The fibres are are placed parallel to the beam line and they form towers of $\Delta\eta \times \Delta\phi = 0.175 \times 0.175$.

3.5   The muon system

Muon detection is considered to be one of the most crucial tasks, as is implied by the name of the CMS. Final states containing muon are important for Higgs discovery, suppersymmetry (SUSY) and other beyond the standard model (BSM) searches. Muons are minimum ioniz-ing particles suffering less by radiative losses in the detector material compared to electrons. CMS muon system covers the pseudorapidity region $|\eta| < 2.4$ and consists of three types of

gaseous detectors: the barrel drift tube (DT) chambers, the cathode strip chambers (CSC), and the resistive plate chambers (RPC).

3.5.1   Drift tube system

The DT chambers cover the pseudorapidity region $|\eta| < 1.2$. It consists of 4 stations and 5 wheels. Figure 12 shows the chambers of one wheel noted as MB1, MB2, MB3, and MB4. The first 3 stations contain 8 chambers each in sets of 4, separated as much as possible to achive the best angular resolution. A DT chamber is made of 3 or 2 superlayers (SL) each made of 4 layers of rectangular drift cells. The transverse dimension of the drift cell (fig. 13) is $21mm$ and it is filled with a gas mixture of $85\%Ar + 15\%CO_2$ resulting a drift time of $380ns$. The length of the wire within the drift cell is $\approx 2.4m$.
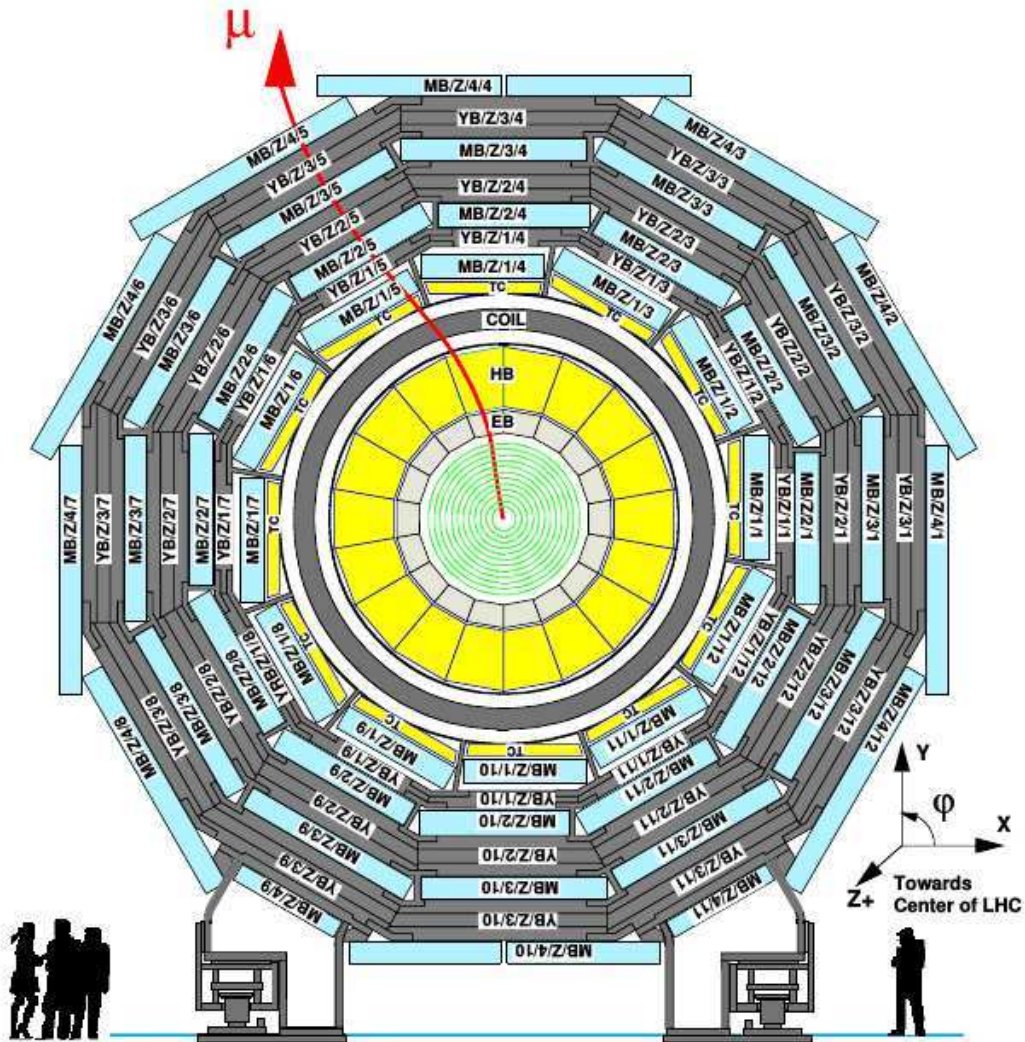
Figure 12: Slice of the CMS detector showing the DT chambers.

The wires in the two outer SLs give track measurements in the $r - \phi$ plane since they are placed parallel to the beam, while in the inner SL the wires are measuring the z position since they are placed orthogonal to the beam line. The third SL is not present in MB4.
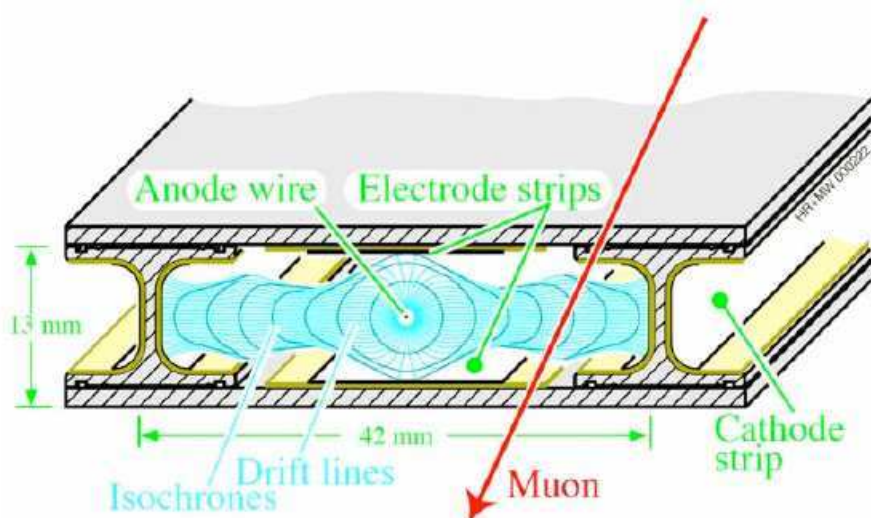
Figure 13: Transverse perspective of the DT cell.

3.5.2   Cathode strip chambers

The endcap muon system of CMS consists of 468 trapezoidal cathode strip chamers (CSC) covering either 10° or 20° inf ϕ each. As shown in figure 14 all chambers, except for the ME1/3 ring, overlap in order to provide contiguous ϕ coverage.
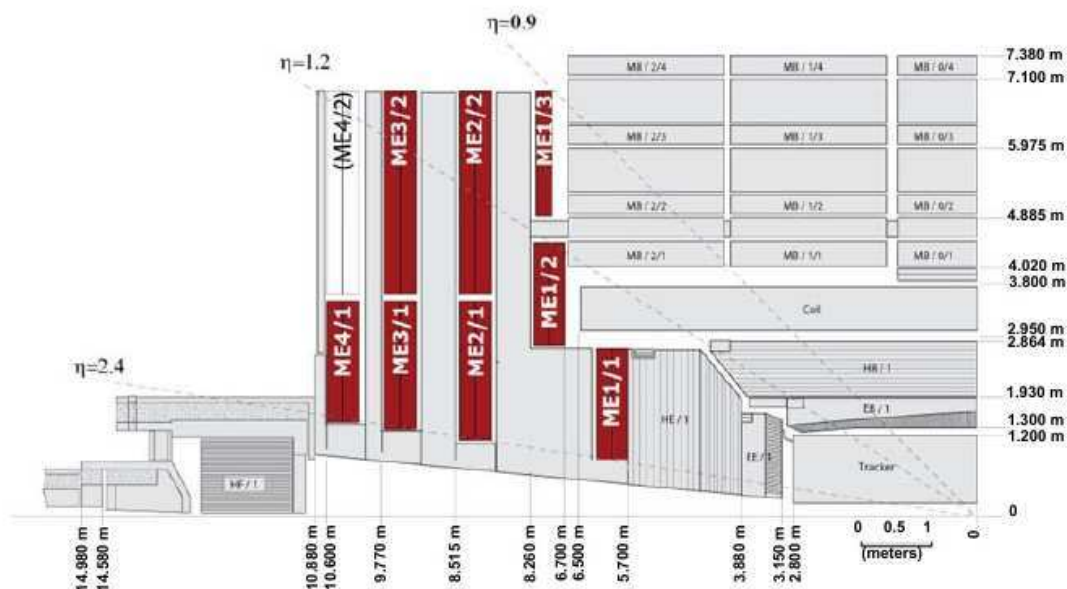
Figure 14: CSC coverage at the endcap region.

The CSCs are multiwire proportional chambers consisting of 6 anode wire planes inserted between 7 cathode panels with strips, shown in figure 15. The largest chambers are $3.4 \times 1.5 m^2$; in total they cover an area of about $5000 m^2$. CSCs can operate in non-uniform magnetic field at high rates and they do not require precise gas, temperature, or pressure control. The performance requirements are: reliability and low-maintenance, at least 99% efficiency per chamber for finding track stubs at L1-trigger, at least 92% probability per chamber to identify the correct
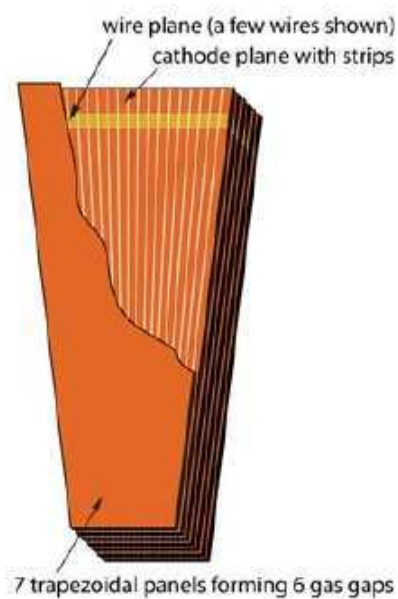
Figure 15: CSC panel.

bunch crossings, about $2mm$ resolution in $r - \phi$ at L1-trigger, and about $75\mu m$ offline resolution for ME1/1(2) and about $150\mu m$ for all others.

3.5.3   Resistive Plate Chamber System

Resistive plate chambers (RPC) are gaseous parallel-plate detectors with time resolution less than $25ns$. Therefore RPCs can be used for a fast response trigger system. RPCs consist of two gaps referred as upper and lower gap operating in avalanche mode with strips in between that pick-up and read out the signal, as shown in figure 16.
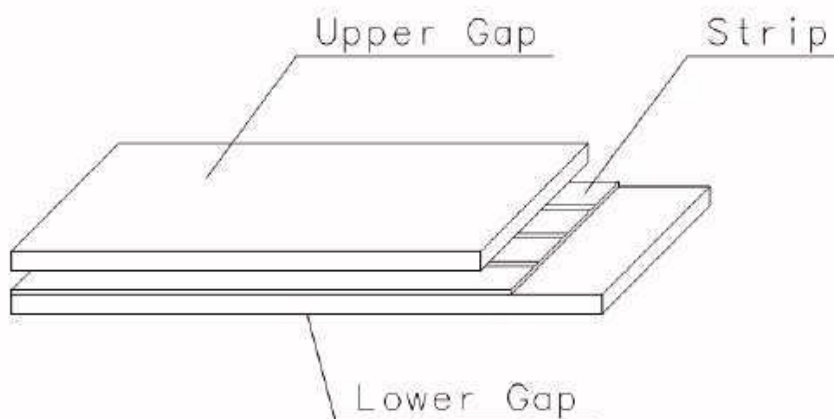
Figure 16: RPC upper and lower gap.

RPC chambers are placed in barrel as well as in the endcap, 6 layers of RPCs are placed in the barrel iron yoke and 4 layers in the barrel covering an area $|\eta| < 2.1$. In first and second muon

stations (in barrel) two RPC chamber are placed while one RPC chamber is placed in stations 2 and 3. The redundancy in the first two allows the trigger to operate even with low$-p_T$ muons.

Muons traversing the detector in the range $|\eta| < 1.2$ crosses RPCs and DT chambers, in the range $1.2 < |\eta| < 2.4$ crosses RPCs and CSCs, and in the endcap-barrel overlap region can leave in any sub-detector.

3.6 The Trigger System

The LHC is designed to collied proton beams at $25ns$, corresponding to frequency of $40MHz$. It is impossible to store such an amount of data and process them, thus a rate reduction has to be achieved during the run at detector level. Consequently a sophisticated and fast system is required to achieve the rate reduction. The trigger system which is responsible for rate reduction it consists of two systems; the L1-trigger which rejects events with logic implemented in hardware during the run (online) and the high level trigger (HLT) which reduces the rate further using algorithms running on PCs farm. The L1 trigger is design to reduce the rate at $100kHz$, which practically the rate is reduced near $30kHz$.

3.6.1 L1 Trigger system

The L1 trigger has local, regional, and global components. The Local Triggers, or Trigger Primitive Generators (TPG), are the front-end electronics connected to the sub-detectors (crystals, chambers etc.). The Regional Triggers collect the trigger primitives from TPGs, combine them and use pattern logic to determine ranked and sorted trigger objects such as electron or muon candidates. The rank determines the confidence attributed to the L1 parameter and it is based on energy or momentum and quality. The Global Triggers, Global Calorimeter (GCT) and Global Muon (GMT) determine the highest-rank objects and send them to Global Trigger(GT). The GT finally decides whether to reject or record the event for further evaluation by the HLT. The architecture of the L1 trigger is shown in figure 17

3.6.2 Calorimeter Trigger

The Calorimeter Trigger consists of calorimeter TPG, RCT, and GCT. The calorimeters are subdivided in trigger towers for trigger purposes. The transverse energies measured by ECAL crystals or the HCAL read-out towers are summed to give the trigger tower E_T and attach the correct bunch crossing. The trigger towers in the region $|\eta| < 1.74$ are covering an area $\eta \times \phi = 0.087 \times 0.087$. Then the RCT receives and processes the trigger primitives determines electron/photon candidates and transverse energy sums per calorimeter region. Also information concerning muon is determined such as MIP and isolation bit. The GCT determines jets, the total transverse energy, the missing transverse energy, jet counts, and H_T. It also provides the highest-rank isolated and non-isolated e/γ candidates.

3.6.3 Muon Trigger

The muon trigger combines information from all three muon systems, the DT, the CSC and the RPC. The barrel DT chambers provide information in track segments in the $\phi-$ and $\eta-$projection. The endcap CSCs provide $3-$dimensional track segments and finally the RPC chambers provide candidates base on regional hit patterns. DT and CSCs identify muon candidate, determine their p_T, location and quality and sort them by rank. They both deliver up to four muon to the GMT. The RPC identifies muon candidates, their p_T and ϕ and delivers four muons from barrel and four from the end-caps to the GMT. All systems provide information concerning the bunch crossing.
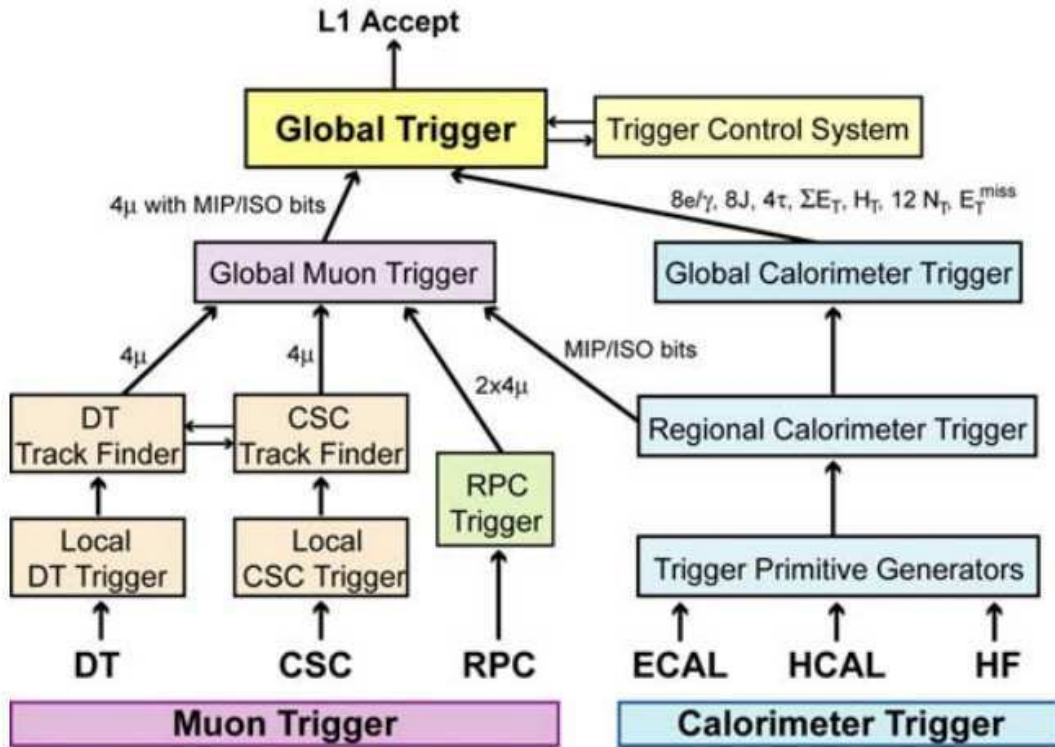
Figure 17: Architecture of L1 Trigger.

Finally GMT receives information from all three systems concerning their p_T, η, ϕ and quality code. It also receives isolation and MIPs bit from GC. By matching information from all system GMT sends the best candidates to the GT.

3.6.4   Global Trigger

The Global Trigger collects information GMT and GCT in order to reject or accept an event. Up to four objects, representing particles and jets, are ranked and sorted. The Global Trigger Logic (GTL) which is the core of GT performs the algorithmic calculations that are using particles p_T threshold, jet multiplicities etc. In total 128 algorithms can be implemented in GTL, results of the algorithms are sent if form of one bit per algorithm to the Final Decision Logic (FDL). Additional steps are followed concerning timing and the results are send to the data acquisition (DAQ) for read-out.

3.7   HLT Trigger system

High level trigger[7] is performed offline in a multi-processor computer farm and it has access to the complete information of the detector. Algorithms are more sophisticated because of the information available and the computing power available. The HLT trigger aims to reduce the rate at the order of $100Hz$. It reconstructs and selects events in two steps that correspond to Level-2 and Level-3 trigger systems. Level-2 trigger uses information only from the calorimeter and muon detectors while the Level-3 trigger uses reconstruction from the entire detector.

4 Theory

Particle physics is the field that tries to understand the basic constituents of nature. The theoretical framework that describes the elementary particles and their interactions is called Standard Model (SM). This chapter will give a short introduction to SM, Quantum Chromodynamics which are part of SM, and the theoretical software tools used.

The beginning of particle physics can be arbitrarily pinpointed by the discovery of the electron, in 1897, by J.J. Thomson. Rutherford, Geiger, and Marsden, in 1908, conducted experiments by colliding alpha particles in gold foil probing the structure of atom. These are the two most prominent experiments of modern particle physics; followed by hundreds of others that each of them contributed to the knowledge we have today. Each experiment either confirmed predictive theories or opened a window for new theories; the most complete theory we have today describing the subatomic world is called the Standard Model (SM) and it is shortly described in this section.

4.1 Standard Model

4.2 Introduction

The Standard Model of elementary particle physics is the theoretical model based on the Quantum Field Theory (QFT) that describes the particles and the forces they exchanging. Namely it describes the electromagnetic, the weak, and the strong force with all particles accompanying them. In spite the fact that SM is providing successful predictions for various experiments it does not incorporate the gravitational force. It also contains a large number of empirical variables that cannot be predicted, thus it is a model that is always evolving and it is not yet completed.

According to SM the visible universe consists of fermions ($\frac{1}{2}$−spin particles), six quarks and six leptons, listed in table 2. The interactions are exchanges of integral spin particles, bosons. Electromagnetic interactions are carried out via photon exchange, γ, strong interactions via gluons and weak interactions via the three vector bosons, Z^0 and $W^\pm$, listed in table 3. The Minimal Standard Model (MSM) also contains four scalar fields, two charged and two neutral. The three of them ,one neutral and two charged, are 'absorbed' by the vector bosons while the fourth is the Higgs field.

Table 2: The fundamental particles of SM.

Particles	Flavour	Charge
leptons	$e\ \mu\ \tau$	-1
	$\nu_e\ \nu_\mu\ \nu_\tau$	0
quarks	$u\ c\ t$	$+\frac{2}{3}$
	$d\ s\ b$	$-\frac{1}{3}$

Table 3: Carriers of force in SM.

Interaction	Particle	Spin	Strength (relative)
Strong	$g, gluons$	1	$\mathcal{O}(1)$
Electromagnetic	$\gamma, Photon$	1	$\mathcal{O}(10^{-2})$
Weak	W, Z	± 1	$\mathcal{O}(10^{-7})$

Standard Model is a gauge theory utilizing the Lagrangian formulation in order to describe fields and its interactions. Symmetries also play a crucial rule in the theoretical formulation of SM, the next subsection is an overview of Lagrangian mechanics and symmetries.

4.3   Lagrangian mechanics and Symmetries

Standard Model is a gauge theory, where gauge refers to the arbitrarily degrees of freedom one can assign to the Lagrangian. These additions of degrees of freedom are called transformations, that in order to be acceptable in the theory have to be local invariant. Local invariance ensures that the Lagrangian gives the same results regardless the degrees of freedom.

Lagrangian formalism is based on the least action principle, where action is defined by the integral of the Lagrangian density over time. In particle physics the Lagrangian density is expressed as a function of the fields ϕ_i and the derivatives of the four components of space-time. The action is written as:

$$S = \int_{t_i}^{t_f} \mathcal{L}(\phi_i, \partial\phi_{i_\mu}) \tag{7}$$

The least action principle states that under small variations the action remains unchanged:

$$\delta S = 0 \tag{8}$$

$$\delta \int_{t_i}^{t_f} \mathcal{L}(\phi_i, \partial\phi_{i_\mu}) = 0 \tag{9}$$

By taking 9 one can derive the Euler-Lagrange equation:

$$\frac{d}{dt}\left(\frac{\partial\mathcal{L}}{\partial(\partial\phi_{i_\mu})}\right) = \frac{\partial\mathcal{L}}{\partial\phi_i} \tag{10}$$

which is the equation of motion of the physical system.

In quantum field theory Lagrangians are taken as axiomatic equations, unlike classical mechanics, with the only constrain to reproduce the field equations. The Lagrangians can be multiplied by a scale factor or an arbitrary factor can be added to them but they should result the same field equations after applying the Euler-Lagrange equations.

4.3.1   Quantum Electrodynamics

Starting from the Dirac Lagrangian, which describes particles and antiparticles of spin $\frac{1}{2}$, one can derive that it is invariant under global phase transformations

$$\psi \to e^{i\theta}\psi \tag{11}$$

where ψ is the spinor filed, but the same does not apply for local phase transformations

$$\psi \to e^{i\theta(x)}\psi \tag{12}$$

where derivatives of $\theta(x)$ remain after the application of Euler-Lagrange equation. In order to compensate this contributions an additional field term is added. The proof and detailed explanation of this procedure can be found in textbooks [8][9][10], of elementary particle physics or quantum field theory.

After the extra term the result is the Lagrangian of Quantum Electrodynamics (QED)

$$\mathcal{L} = [i\hbar c\bar{\psi}\gamma^\mu\partial_\mu\psi - mc^2\bar{\psi}\psi] - \frac{1}{16\pi}F^{\mu\nu}F_{\mu\nu} - (q\bar{\psi}\gamma^\mu\psi)A_\mu \tag{13}$$

The first part of the equation describes electrons and positrons interacting via photons, the second the electromagnetic fields and the final one is the photon created by the particles' current

$$J^\mu = cq(\bar{\psi}\gamma^\mu\psi) \tag{14}$$

The invariance under the local transformation presented above is the so-called local gauge invariance, and it can also be written in terms of matrices

$$\psi \rightarrow U\psi \tag{15}$$

where $U = e^{i\theta}$ is a unitary matrix, $UU^\dagger = 1$.

4.3.2 Quantum Chromodynamics

Matrices 1×1 are classified under the $U(1)$ group and the symmetry is called $U(1)$ gauge symmetry. Yang and Mills extended this idea to a higher non-Abelian theory by introducing 2×2 matrices, local $SU(2)$ transformation. The resulting Lagrangian of Yang-Mills theory has no practical application since the $SU(2)$ group implies a system with two particles with spin$-\frac{1}{2}$. Nonetheless, they delivered a model able to extend theories to higher symmetry groups.

Quantum chromodynamics is a non-Abelian theory based on the Yang-Mills theoretical tools in the context of $SU(3)$ group theory, that represent the color-charge of quarks. The $SU(3)$ group is needed since quarks carry three different types of color, red, green, and blue. Starting with the Dirac Lagrangian

$$\mathcal{L} = i\hbar c\bar{\psi}\gamma^\mu\partial_\mu\psi - mc^2\bar{\psi}\psi \tag{16}$$

where ψ is a three-component column vector

$$\psi = \begin{bmatrix} \psi_r \\ \psi_b \\ \psi_g \end{bmatrix} \tag{17}$$

$$\psi \rightarrow S\psi \tag{18}$$

whith $S \equiv e^{iq\lambda\cdot\phi(x)/\hbar c}$. By applying this transformation to the Lagrangian and adding factors in order to keep invariant the result, the complete Lagrangian of the Quantum Chromodynamics (QCD) is:

$$\mathcal{L} = [i\hbar c\bar{\psi}\gamma^\mu\partial_\mu\psi - mc^2\bar{\psi}\psi] - \frac{1}{16\pi}F^{\mu\nu}F_{\mu\nu} - (q\bar{\psi}\gamma^\mu\lambda\psi)\cdot A_\mu \tag{19}$$

4.3.3 The Higgs Mechanism

The final part to complete the Standard Model from the gauge theory point of the point is to derive the Lagrangian that incorporates the weak interactions. The Proca equation though that it is used to describe the spin-1 particles was modified by setting the mass term to zero in order to describe the photon and gluons. The W and Z bosons though are not massless and this breaks the symmetry if the Proca equation is used, so a more subtle way is needed here. This was done by exploiting the spontaneous symmetry breaking and the Higgs mechanism.

By taking the Lagrangian

$$\mathcal{L} = \frac{1}{2}(\partial_\mu \phi)(\partial^\mu \phi) + e^{-(\alpha\phi)^2} \tag{20}$$

where $\alpha \in \mathbb{R}$, expanding the second term to

$$e^{-(\alpha\phi)^2} = 1 - \alpha^2\phi^2 + \frac{1}{2}\alpha^4\phi^4... \tag{21}$$

and comparing to equation 13 we see that the Lagrangian describes a particle of mass $m = \sqrt{2}\alpha\hbar/c$. In order to ensure that that the Lagrangian has a local minimum we rewrite it as

$$\mathcal{L} = \frac{1}{2}(\partial_\mu \phi)(\partial^\mu \phi) + \frac{1}{2}\mu^2\phi^2 - \frac{1}{4}\lambda^2\phi^4 \tag{22}$$

where λ is real. Then a problem arises, the μ has to be real since it represents a mass term but the sign is wrong and it has to be imaginary which makes no sense. Then by utilizing classical Lagrangian notation where $\mathcal{L} = \mathcal{T} - \mathcal{U}$, we minimize the $\mathcal{U} = -\frac{1}{2}\mu^2\phi^2 + \frac{1}{4}\lambda^2\phi^4$. The minima is found to be $\pm\mu/\lambda$.

By introducing a new variable $\eta \equiv \phi \pm \mu/\lambda$ the Lagrangian can be re-written as

$$\mathcal{L} = \frac{1}{2}(\partial_\mu \eta)(\partial^\mu \eta) - \mu^2\eta^2 \pm \mu\lambda\eta^3 - \frac{1}{4}\lambda^2\eta^4 + \frac{1}{4}(\mu^2/\lambda)^2 \tag{23}$$

where the mass sign has been corrected and the equation describes a particle with $m = \sqrt{2}\mu\hbar/c$. Now if we look back to the equation 22 we see that it is even in ϕ while the reformed equation 23 is odd in ϕ, the symmetry is broken, this is the so-called spontaneous symmetry breaking. The symmetry presented above is discrete symmetry since it has two distinct minima, for a continuous symmetry the equation has to be written as

$$\mathcal{L} = \frac{1}{2}(\partial_\mu \phi_1)(\partial^\mu \phi_1) + \frac{1}{2}(\partial_\mu \phi_2)(\partial^\mu \phi)_2 + \frac{1}{2}\mu^2(\phi_1^2 + \phi_2^2) - \frac{1}{4}\lambda^2(\phi_1^2 + \phi_1^2)^2 \tag{24}$$

where the last two terms are the 'potential energy' with the minima $\phi_1^2 + \phi_2^2 = \mu^2/\lambda^2$. It is convenient to chose one ground state $\phi_{1_{min}} = \mu/\lambda, \phi_{2_{min}} = 0$ and by following the same procedure as before we introduce two new fields $\eta \equiv \phi_1 - \mu/\lambda, \xi \equiv \phi_2$. The resulting Lagrangian after replacing these fields is

$$\mathcal{L} = \left[\frac{1}{2}(\partial_\mu \eta)(\partial^\mu \eta) - \mu^2 \eta^2\right] + \left[\frac{1}{2}(\partial_\mu \xi)(\partial^\mu \xi)\right] - \left[\mu\lambda(\eta^3 + \eta\xi^2) + \frac{\lambda^2}{4}(\eta^4 + \xi^4 + 2\eta^2\xi^2)\right] + \frac{\mu^4}{4\lambda^2}$$

(25)

The first bracket represents a massive field (η), the second one a massles field (ξ), and the third five couplings. Goldstone's theorem shows that the massless field is a result of the continuous spontaneous symmetry breaking.

By combining the two fields in one complex $\phi \equiv \phi_1 + i\phi_2$, the Lagrangian can be written as

$$\mathcal{L} = \frac{1}{2}(\partial_\mu \phi)^*(\partial^\mu \phi) + \frac{1}{2}\mu^2(\phi^*\phi) - \frac{1}{4}\lambda^2(\phi^*\phi)^2$$

(26)

Then by applying local gauge transformation $\phi \rightarrow e^{i\theta(x)}\phi$, replacing the covariant derivative $\mathcal{D}_m = \partial_\mu + i\frac{q}{\hbar c}A_\mu$, and define the new fields $\eta \equiv \phi_1 - \mu/\lambda$, $\xi \equiv \phi_2$ the Lagrangian transforms as

$$\mathcal{L} = \left[\frac{1}{2}(\partial_\mu \eta)(\partial^\mu \eta) - \mu^2 \eta^2\right] +$$
$$\left[-\frac{1}{16\pi}F^{\mu\nu}F_{\mu\nu} + \frac{1}{2}(\frac{q}{\hbar c}\frac{\mu}{\lambda})^2 A_\mu A^\mu\right] +$$
$$\left[\frac{\mu}{\lambda}(\frac{q}{\hbar c})^2 \eta(A_\mu A^\mu) - \lambda\mu\eta^3 - \frac{1}{4}\lambda^2\eta^4\right] + (\frac{\mu^2}{2\lambda})^2$$

(27)

where $\mu = \frac{1}{2\sqrt{\pi}}\left(\frac{\lambda c^2}{q}\right)m_A$.

By choosing this gauge the Goldstone bosons are eliminitated and the equation describes one massive scalar particle (η the Higgs boson) and a massive gauge field A^μ. The method present above that eliminates massless bosons, is the Higgs mechanism.

4.4   Quantum Chromodynamics

The following section gives a historical overview on QCD, the eightfold way, the quark model and how QCD is formed today. Also a more detailed insight on the Lagrangian formulation is given. Finally the running of the strong coupling constant and the parton density functions (PDF) is described.

4.5   Introduction

Murray Gell-Mann, in 1961, introduced the Eightfold Way, the periodic table of particle physics. The Eightfold Way is a model classifying hadrons into patterns according to their charge and and strangeness. Since strange quarks were not introduced back then, the strangeness were assigned to hadrons decaying relatively slowly.

Figure 18 shows how baryons were classified. Despite the fact that the model predicted hadrons that were not observed yet, it begged an answer on why these patterns classify and predict hadrons. Gell-Mann[11] and Zweig[12], in 1964, independently proposed the quark model, the model that suggested that hadrons are not fundamental but entities composed of quarks; as Gell-Mann named the constituents of hadrons. The model had two composition rules, every baryon is composed of three quarks and every meson is composed of two quarks.
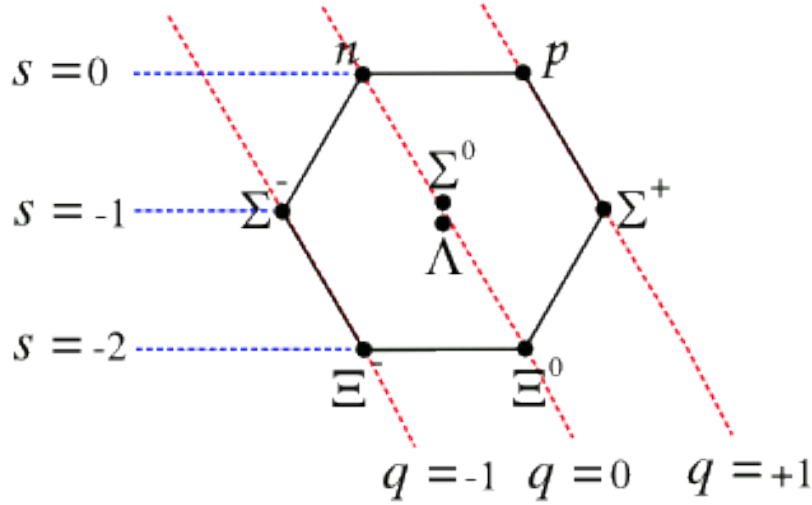
Figure 18: Eightfold Baryons.

The model successfully predicted the existence of the known baryons and the structure of the proton but it had two embarrassing inconsistencies. One would expect that since baryons are composited from quarks then signatures of isolated quarks should appear in experiments. The second inconsistency was the violation of the Pauli's principle, e.g how could three particles of spin$-\frac{1}{2}$ exist in the same system? The solution came in 1964 by O. W. Greenberg [13] who proposed that quarks come in three colors (red, green, blue), and all particles in nature are colorless, where colorless mean that color and anti-color cancel out or that all colors exist equally in a system. Colour is just a playful name for another quantum number, property of particles like spin or electric charge. At the beginning these theories, quark confinement and color hypothesis, looked like desperate ways to save the quark model but latter experiments showed that quarks exist and they come in three colors.

4.6 Experimental Signatures

Signature from quarks and gluons can be seen in high energy colliders (e^+e^-, ep, pp) as jets. Jets are collimated streams of particles resulting from quarks and gluons. Figure 19 shows a first order QCD diagram $qq \rightarrow qq$. Quarks act like free particles right after the collision and the predictions are calculated using the perturbative QCD (pQCD) and then undergo hadronization. Hadronization is a process where quarks emit gluons and vice versa resulting baryons that are interacting with the detector and are identified as jets. Two jet events are signatures of quarks while three and more jet events are signatures of quarks and gluons, a multijet event as it is recorded at CMS detector is shown in figure 20.

The experimental proof of the existence of three coloured quarks comes from the ratio of cross section of hadron production to muon production at electron-positron experiments.

$$R = \frac{\sigma(e^+e^- \rightarrow hadrons)}{\sigma(e^+e^- \rightarrow \mu^+\mu^-)} \tag{28}$$

Hadron cross section are proportional to charge squared but since the numerator includes all combinations of quarks-antiquarks the ratio at leading order becomes

$$R(E) = 3\sum_f Q_f^2 \tag{29}$$
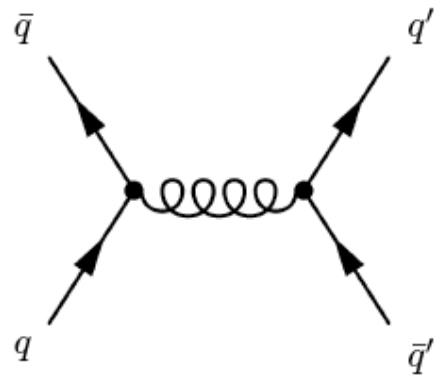
Figure 19: Quark quark interaction.
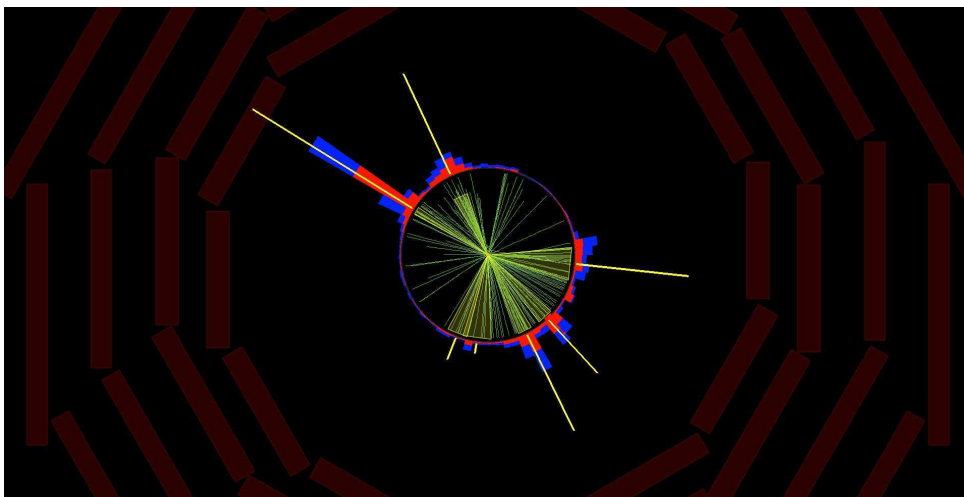
Figure 20: Multijet event CMS.

where f sum over all flavours. It depends on energy since masses of different flavours of quarks vary. Figure 21 shows the ratio at low energies where only u, d, and s quarks contribute resulting

$$R = 3\left[\left(\frac{2}{3}\right)^2 + \left(-\frac{1}{3}\right)^2 + \left(-\frac{1}{3}\right)^2\right] = 2 \tag{30}$$

Besides the peaks that originate from meson resonances the plateau it is described very well by the calculations, either using the naive quark model or a NLO pQCD calculation.
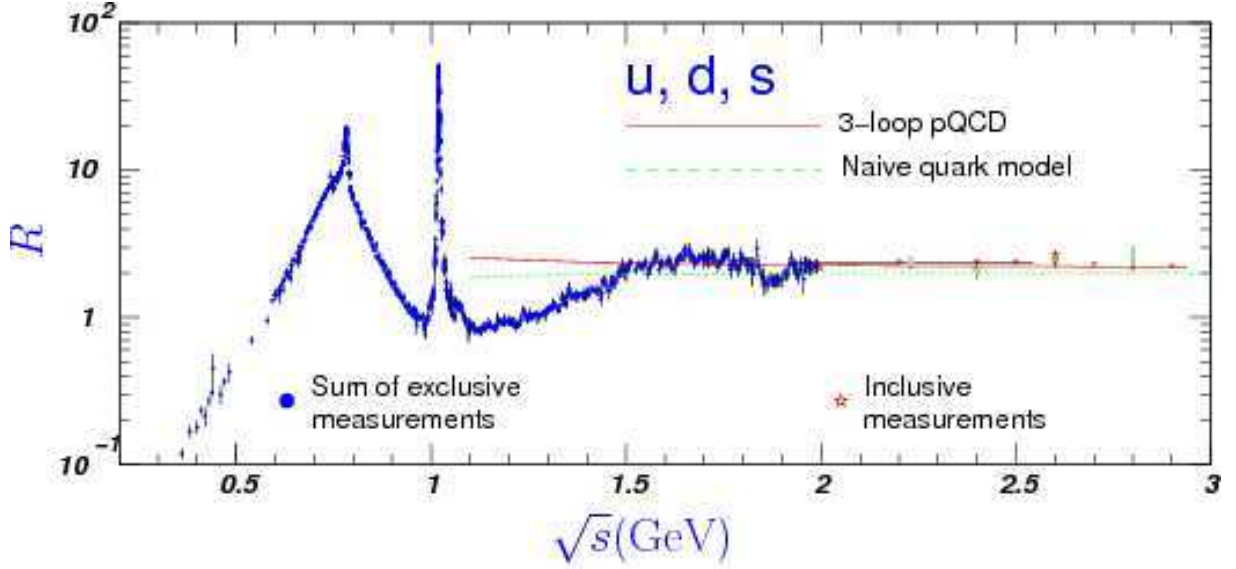
Figure 21: Ratio graph.

4.7 Perturbative QCD

Perturbative QCD is applicable at high energies where the strong coupling constant, α_S, is small and the partons (quarks and gluons) are acting like free particles, this is called the asymptotic freedom. The pQCD calculates only the hard scattering but latter we will see how the factorization theorem can provide calculations for more general observables.

The QCD Lagrangian is written as

$$\mathcal{L} = [i\hbar c\bar{\psi}\gamma^\mu\partial_\mu\psi - mc^2\bar{\psi}\psi] - \frac{1}{16\pi}F^{\mu\nu}F_{\mu\nu} - (q\bar{\psi}\gamma^\mu\lambda\psi)\cdot A_\mu \tag{31}$$

and according to Feynman rules, the free Lagrangian corresponds to the propagator and the interaction terms to vertex factors. Below we see a short list of vertices and propagators and how they contribute to cross sections

where $g_s = \sqrt{4\pi\alpha_s}$.

In QCD we treat the spin$-\frac{1}{2}$ Dirac fields, ψ, as a vector that takes into account color factors as shown in equation 17. The A_μ represent eight gluon (color) fields that are generated from the color current $J_\mu = q\bar{\psi}\gamma^\mu\lambda\psi$. Where λ are the Gell-Mann matrices, eight 3×3 matrices representing color combinations of gluons. The ninth matix that corresponds to a colorless

Table 4: Vertices and propagators.

Propagators	Quarks	$\frac{i(\not{q}+mc)}{q^2-m^2c^2}$
	Gluons	$\frac{-ig_{\mu\nu}\delta^{\alpha\beta}}{q^2}$
Vertices	Quark-Gluon	$\frac{-ig_s}{2}\lambda^\alpha\gamma^\mu$

gluon is experimentally excluded. A colorless gluon could exist free in nature thus it would be easily detectable and rather common. The rows of these matrices correspond to color (r, b, g) while the columns correspond to anti-color $(\bar{r}, \bar{b}, \bar{g})$. The eight matrices are the following:

$$\lambda^n = \begin{pmatrix} r\bar{r} & r\bar{b} & r\bar{g} \\ b\bar{r} & b\bar{b} & b\bar{g} \\ g\bar{r} & g\bar{b} & g\bar{g} \end{pmatrix} \tag{32}$$

$$\lambda^1 = \begin{pmatrix} 0 & 1 & 0 \\ 1 & 0 & 0 \\ 0 & 0 & 0 \end{pmatrix} \lambda^2 = \begin{pmatrix} 0 & 1 & 0 \\ 1 & 0 & 0 \\ 0 & 0 & 0 \end{pmatrix} \tag{33}$$

$$\lambda^3 = \begin{pmatrix} 1 & 0 & 0 \\ 0 & -1 & 0 \\ 0 & 0 & 0 \end{pmatrix} \lambda^4 = \begin{pmatrix} 0 & 0 & 1 \\ 0 & 0 & 0 \\ 1 & 0 & 0 \end{pmatrix} \tag{34}$$

$$\lambda^5 = \begin{pmatrix} 0 & 1 & -i \\ 0 & 0 & 0 \\ i & 0 & 0 \end{pmatrix} \lambda^6 = \begin{pmatrix} 0 & 0 & 0 \\ 0 & 0 & 1 \\ 0 & 1 & 0 \end{pmatrix} \tag{35}$$

$$\lambda^7 = \begin{pmatrix} 0 & 0 & 0 \\ 0 & 0 & -i \\ 0 & i & 0 \end{pmatrix} \lambda^8 = \frac{1}{\sqrt{3}} \begin{pmatrix} 1 & 0 & 0 \\ 0 & 1 & 0 \\ 0 & 0 & -2 \end{pmatrix} \tag{36}$$

The term $\frac{1}{16\pi}F^{\mu\nu}F_{\mu\nu}$ is the free Lagrangian of gluon fields and can be written as

$$F^{\mu\nu}F_{\mu\nu} \equiv \left[\partial^\mu A^\nu - \partial^\nu A^\mu - 2q(A^\mu \times A^\nu)\right] \times \left[\partial_\mu A_\nu - \partial_\nu A_\mu - 2q(A_\mu \times A_\nu)\right] \tag{37}$$

the quadratic terms give rise to the gluon propagator while higher order terms give rise to triple and quadrupole couplings of gluons.

Cross sections of the hard scattering depends on two factors; the phase space available and the amplitude $\mathcal{M}$ of the process. The phase space is a purely kinematic term depending on the available energy, the masses and momentum of the particles involved in the scattering process. The amplitude, $\mathcal{M}$, is calculated using the Feynman rules, for the process $q\bar{q} \to q\bar{q}$ as shown in fig 19, $\mathcal{M} \sim g_s^2$ and the total cross section is $\sigma_{tot} \sim |\mathcal{M}|^2 \sim \alpha_s^2$. While for a $q\bar{q} \to q\bar{q}g$ process the cross section is $\sigma_{tot} \sim \alpha_s^3$.

4.7.1   Asymptotic Freedom

Asymptotic freedom is called the fact that the strong coupling constant vanishes, $\alpha_S \to 0$, at large momentum transfer, $Q^2 \to \infty$; and this is the reason why QCD can be treated as perturbative theory. This behaviour of the strong coupling constant allows quarks at high energies behave like free particles.

In quantum field theory, vacuum is not empty space but is considered as the state with the minimum average energy where virtual particles and anti-particles constantly emerge and annihilate. In QED where the force propagators are photons that do not couple to themselves the particles that fill the vacuum are ee^- pairs. Consequently by placing a charge in such a vacuum causes polarization of the vacuum (charge screening) similarly as a dielectric medium. This polarization causes an effective charge of electrons that depends on the distance of the probe, the smaller the distance the larger the charge.

The running of the QED coupling constant can be written as

$$\alpha(Q^2) = \frac{\alpha(0)}{1 + [\alpha(0)/3\pi]ln(Q^2/m_e^2)} \tag{38}$$

but since in QCD $a_Q = 0$ cannot be used it is needed to specify an arbitrary scale μ^2 that lead to

$$\frac{1}{\alpha(Q^2)} = \frac{1}{\alpha(0)}\frac{1}{3\pi}ln(Q^2/m_e^2)$$
$$\frac{1}{\alpha(\mu^2)} = \frac{1}{\alpha(0)}\frac{1}{3\pi}ln(\mu^2/m_e^2) \tag{39}$$

and by subtracting the two the resulting equation is:

$$\alpha(Q^2) = \frac{\alpha(\mu^2)}{1 + [\alpha(\mu^2)/3\pi]ln(Q^2/m_e^2)} \tag{40}$$

The arbitrary scale μ is called the renormalization scale that renders the running equation independed of $\alpha(0)$.

The running of the coupling constant can be written as a series expansion in powers of α and gives the so-called beta function.

$$\beta(\alpha) = \frac{d\alpha(Q^2)}{dln(Q^2)} = -(\beta_0\alpha^2 + \beta_1\alpha^3 + \cdots) \tag{41}$$

A similar model to QED stands for QCD where quark anti-quark pairs fill the vacuum; however the strong force propagators, gluons, couple to themselves and they also fill the vacuum. Quark-antiquark pairs cause screening of the color charge while gluon-gluon pairs cause anti-screening, and as we will see later anti-screening is the predominant effect; thus the smaller the distance of the probe the smaller the color charge. Figure 22 shows the one loop diagrams with quark-antiquakr and gluon gluon loops.

The running of the strong coupling constant
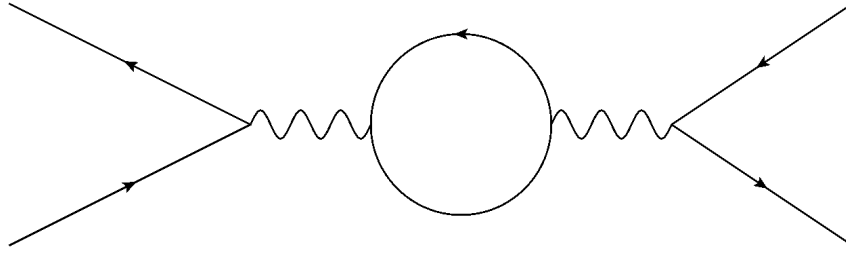
Figure 22: One loop Feynman diagram.

$$\alpha_s(Q^2) = \frac{\alpha_s(\mu^2)}{1 + [\alpha_s(\mu^2)/12\pi](11N_c - 2f)ln(Q^2/\mu^2)}, Q^2 >> \mu^2 \tag{42}$$

where N_c is the number of colors and f the number of flavours in SM. The N_c factor comes from the gluon-gluon loops while the f factor comes from the quark-quark loop, and this shows that in SM where $N_c > n$ the anti-screening is dominant. Consequently the sign of the second term in the denumerator is positive thus the $\alpha_s \rightarrow 0$ for higher transferred momentum Q^2. Let us write the α_S as

$$\frac{1}{\alpha_s(Q^2)} = \frac{1}{\alpha_s(\mu^2)} + \beta_0 ln(\frac{Q^2}{\mu^2}) \equiv \beta_0 ln(\frac{Q^2}{\Lambda^2}) \tag{43}$$

where $\beta_0 = \frac{11N_c - 2n_f}{12\pi}$ and Λ the scale where $\alpha_s(\mu^2)$ becomes infinite, thus the first term of the right hand side of the equation vanishes and the equation becomes

$$\alpha_s(Q^2) = \frac{1}{\beta_0 ln(\frac{Q^2}{\Lambda^2})} \tag{44}$$

The QCD scale parameter, Λ, is rarely used so the running of the strong coupling constant is written as

$$\alpha_s(Q^2) = \frac{\alpha_s(\mu^2)}{1 + \beta_0\alpha_s(\mu^2)ln(Q^2/\mu^2)} \tag{45}$$

The asymptotic freedom as it is mentioned allows the treatment of QCD as a perturbative theory but pQCD predicts cross sections of processes that have quark and gluons at final-state. The probe of quarks and gluons is a jet signature at the detector, so the cross section section calculations of quarks and gluons is not the complete picture. So in order to make pQCD usable we need either observables insensitive to long distance effects or we need to parametrize these long distance effects. The observables insensitive to long distance effects are called infrared safe observables and the parametrization of long distance effects is achieved by utilizing the factorization theorem.

4.7.2 Infrared Safety

Infrared problems are called the singularities appearing due to soft and collinear radiation, where the third parton in $2 \rightarrow 3$ processes merge with an other parton and the process becomes $2 \rightarrow 2$.

The cross section of the $e^+e^- \rightarrow q\bar{q}g$ process is given by

$$\frac{d^2\sigma}{dx_1 dx_2} = \sigma_0 \frac{2\alpha_s}{2\pi} \frac{x_1^2 + x_2^2}{(1 - x_1)(1 - x_2)} \tag{46}$$

In terms of angles of the partons the denumerator can be written as

$$(1 - x_1)(1 - x_2) \sim [x_2 x_3 (1 - cos\theta_{23})][x_3 x_1 (1 - cos\theta_{31})] \tag{47}$$

Index 1 stands for quark, 2 for antiquark and 3 for gluon. Singularities arise in three cases, collinear radiation of qg ($\theta_{31} = 0$), $g\bar{q}$ emitted collinear ($\theta_{32} = 0$), and finally by a soft gluon ($x_3 \rightarrow 0$).

One solution is to construct infrared safe observables that are insensitive to long distance processes. Thrust, sphericity, aplanarity are infrared safe observables but such observables are very limited.

4.7.3   Factorization and Parton Distribution Functions

The pQCD theory is a successful theory that describes quark and gluon interactions but it suffers from singularities that limit its predictions to few variables. There is a theory though that isolates the long distance contributions and factorizes them into the parton distribution functions (PDFs); it is called the factorization theorem.

The cross section of hadron-hadron can be written as

$$\sigma^{hh} = \sum_{ij} \int dx_1 dx_2 f_i(x_1, \mu^2) f_j(x_2, \mu^2) \hat{\sigma}(x_1, x_2, Q^2/\mu^2) \tag{48}$$

where $f(x, \mu)$ are the PDFs, i, j indices run over the quarks flavours, indices 1 and 2 represent hadrons and μ is the factorization scale. Factorization scale is similar to renormalization one, if a parton has transverse momentum larger than μ contributes to the hard matrix elements, otherwise is absorbed in the PDFs.

Before going further into the factorization theorem let's see what are the PDFs and how they are obtained. PDFs cannot be calculated from theory but they are obtained from experiment. Deep inelastic scattering (ep) were the first experiments that provided the PDFs since the transferred momentum can be determined easily by measuring the momentum of the outgoing electron. The drawback of DIS experiments is that the cannot probe gluons inside protons since the emitted photon from electrons does not couple to gluons, so hadron-hadron colliders are the most prominent for measuring the gluon's PDF.

The DIS cross section can be written qualitatively as

$$\sigma^{ep} \sim \sigma_0 \left[W_2 + 2W_1 tan^2 \left(\frac{\theta}{2} \right) \right] \tag{49}$$

where W_i are the structure function of proton measured from DIS experiments. According to Bjorken scaling in the asymptotic limit where $Q \rightarrow \infty$ the structure functions can be parametrized as a function of $x = \frac{Q^2}{2p \cdot q}$, where p is the momentum of the proton and q the transferred momentum. The result is the structure function F_2,

$$F_2(x) = \sum_i e_i^2 x f_i(x) \tag{50}$$

where e_i is the charge of quarks. The Gallan-Gross relation says that in parton model $F_2 = 2xF_1$. Structure functions depend on quark PDF, $u(x), d(x), \bar{s}(x)$... but is convenient to define them as valence and sea distributions.

$$u(x) = u_v(x) + u_s(x) \tag{51}$$
$$d(x) = d_v(x) + d_s(x) \tag{52}$$
$$u_s(x) = \bar{u}_s(x) = d_s(x) = \bar{d}_s(x) = s_s(x) = \bar{s}_s(x) = S(x) \tag{53}$$

where $S(x)$ is the sea quark distribution. By summing all partons the *uud* combination and all the other properties of the proton must be retrieved; the sum rules are:

$$\int_0^1 dx u_v = \int_0^1 dx(u(x) - \bar{u}(x)) = 2 \tag{54}$$

$$\int_0^1 dx d_v = \int_0^1 dx(d(x) - \bar{d}(x)) = 1 \tag{55}$$

$$\int_0^1 dx u_v = \int_0^1 dx(s(x) - \bar{s}(x)) = 0 \tag{56}$$

These summing rules indicate that the net amount of $u-$valence quarks within the proton are two, one $d-$valence quark and no strange quark. A naive approximation would expect that if we sum over all the momenta carried by partons within the proton we could reconstruct the momentum of the proton

$$\sum_i \int_0^1 dx(xp)[q_i(x)] = p \tag{57}$$

where i sums over all quark flavours, p is the momentum of the proton and x is the fraction of the momentum carried by each parton. The first DIS experiments showed that this is not the case and the sum of the equation 57 is approximately $\frac{1}{2}p$. The missing momentum is carried by gluons and in order to obtain the proton momentum one needs to sum the gluons momentum as well

$$\sum_i \int_0^1 dx(xp)[q_i(x)] + \int_0^1 dx(xp)[g(x)] = p \tag{58}$$

Figure 23 shows the PDF of u, d, s and g defined by CT10 PDF set; the various PDF sets and their differences will be described in following sections.

PDFs are process independent, consequently the PDFs obtained by DIS experiments can be used to predict cross sections of hadron-hadron interactions. In order to explain the factorization theorem we will start from DIS processes where Q^2 can be defined accurately and latter expand the theory to hadron-hadron collisions.

The cross section of the process of figure 24 by exploiting the factorization theorem is written as

$$\sigma^{ep} = \sum_j \int dx f_j(x, \mu^2) \hat{\sigma}(x, Q^2/\mu^2) \tag{59}$$
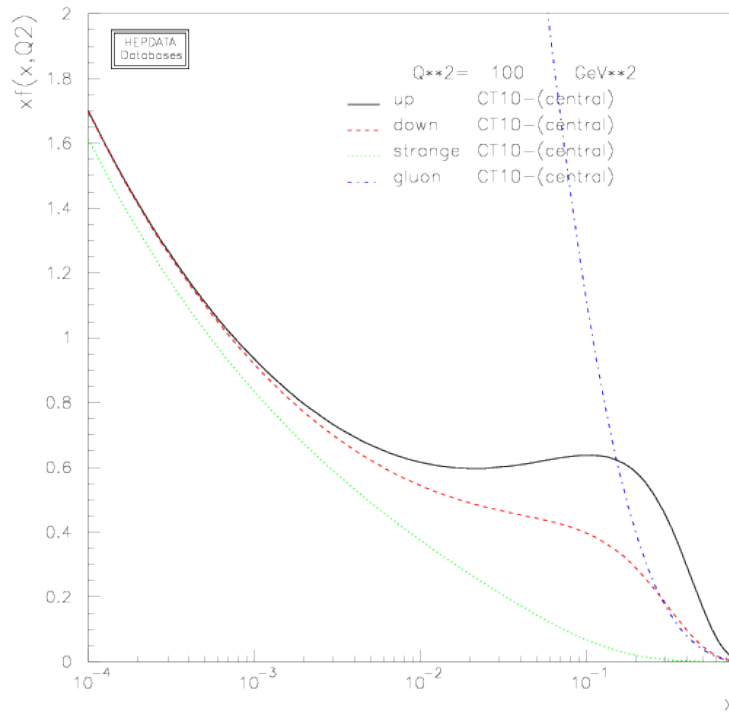
Figure 23: PDF of $u, d, s,$ and g from CT10.
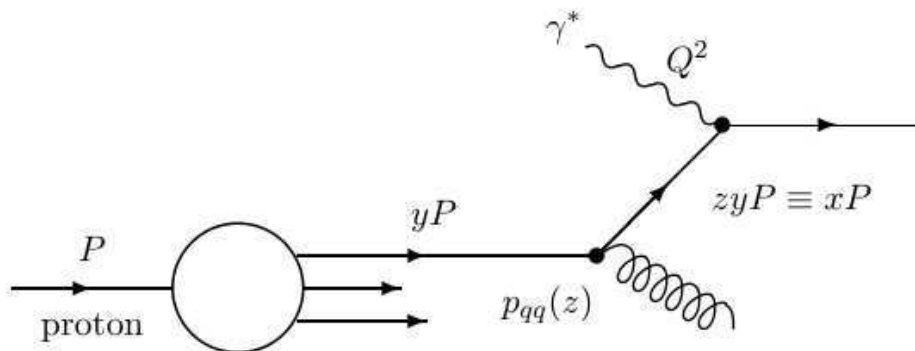
Figure 24: Feynman diagram of deep inelastic scattering process.

The QCD improved parton model takes into account gluons as dynamical entities instead of missing energy. Starting from equation 50 and taking into account the gluon radiation seen in figure 24 it can be re-written as

$$\frac{F_2(x,Q^2)}{x} = \sum_i e_i^2 \int_x^1 \frac{dy}{y} f_i(y) \left[\delta(1 - \frac{x}{y}) + \frac{\alpha_S}{2\pi} P_{qq}(\frac{x}{y}) ln(\frac{Q^2}{m^2}) \right] \tag{60}$$

Where $P_{qq}(\frac{x}{y})$ is the splitting function that gives the probability the emission of a gluon from a parent quark with the daughter quark conserving a fraction of the initial momentum $z = \frac{x}{y}$. For each of the processes $g \to qg, g \to gg$ etc there is a different splitting function listed below at leading order

$$P_{qq}(z) = \frac{4}{3} \left[\frac{1+z^2}{1-z} + \frac{3}{2}\delta(1-z) \right] \tag{61}$$

$$P_{qg}(z) = \frac{1}{2} \left[z^2 + (1-z)^2 \right] \tag{62}$$

$$P_{qg}(z) = \frac{4}{3} \left[\frac{1+(1-z)^2}{z} \right] \tag{63}$$

$$P_{gg}(z) = 6 \left[\frac{z}{1-z} + \frac{1-z}{z}z(1-z) + (\frac{11}{12} - \frac{n_f}{18}\delta(1-z)) \right] \tag{64}$$

Equation 60 depends on a cut off parameter m and it diverges when $m \to 0$, similarly as the running of the coupling constant, it is convenient to introduce an arbitrary parameter μ. Equation 60 gives

$$f(x,Q^2) = \int_x^1 \frac{dy}{y} f(y,\mu^2) \left[\delta(1 - \frac{x}{y}) + \frac{\alpha_S}{2\pi} Pqq(z)ln\frac{Q}{\mu^2} \right] \tag{65}$$

where we introduced the factorization scale, μ, and by taking the derivative of μ and setting equal to zero we get the evolution equation of a quark distribution, the so-called DGLAP evolution equation

$$\mu^2 \frac{\partial f(x,Q^2)}{\partial \mu^2} = \frac{\alpha_S}{2\pi} \int_x^1 \frac{dy}{y} f(y,\mu^2) P_{qq}(z) + \mathcal{O}(\alpha_S^2) \tag{66}$$

In proton proton collisions $pp \to X + all$ where X is can be the leading jet, two pairs of jets or any other triggering particle, Q^2 cannot be measured explicitly. The hard scale Q^2 is then defined by the leading jet p_T, the average of the two leading jets $< p_{T1,2} >$ or the dijet invariant mass M_{jj} with the constraint that the Q^2 is comparable to $\sqrt{s}$. The factorisation theorem then states that the total cross section can be written as 48, where $\hat{\sigma}$ is the cross section of $parton_1 + parton_2 \to X + all$ calculated by the pQCD. The factorization scale, μ, is usually set equal to Q^2.

4.8   Non-Perturbative QCD

The previous section presented the available tools to calculate cross sections up to the parton level. The processes at a collider though are not simple parton-parton interactions and the detectors are recording jets composed of stable particles. The dominant processes that are taken into account to simulate the full process of collision and detection are the parton showering (PS), hadronization and multi-parton interactions (MPI). These processes are based on

empirical models rather in pQCD and non-perturbative(NP) techniques are utilized for their simulation.

4.8.1 Parton Showers

Accelerated quarks lose energy via gluon emission, then gluons themselves split into quarks, this process is called parton showering (PS). Depending on which quark emits the gluons, PS is categorized in initial state radiation (ISR) if the incoming parton emits the gluon and final state radiation (FSR) if the outgoing parton emits the gluon. The outgoing parton loses its energy via gluon emission and quark splitting to the point that the parton's scale falls to some Q_0^2, then the hadronization process occurs.

Parton showers are basically higher order contributions to the hard scattering process but it is not possible to calculate them exactly thus various models parametrize these contributions.

4.8.2 Hadronisation

The confinement described in previous section does not allow coloured particles to exist in nature. Partons from showering reach a low scale Q_0^2 where the strong coupling constant increases then partons are pulled together and form colorless combinations where perturbative calculations fail. This procedure is called hadronization and various models were developed, the most popular are String-Lund model[14][15] utilized by PYTHIA and cluster model utilized by HERWIG.
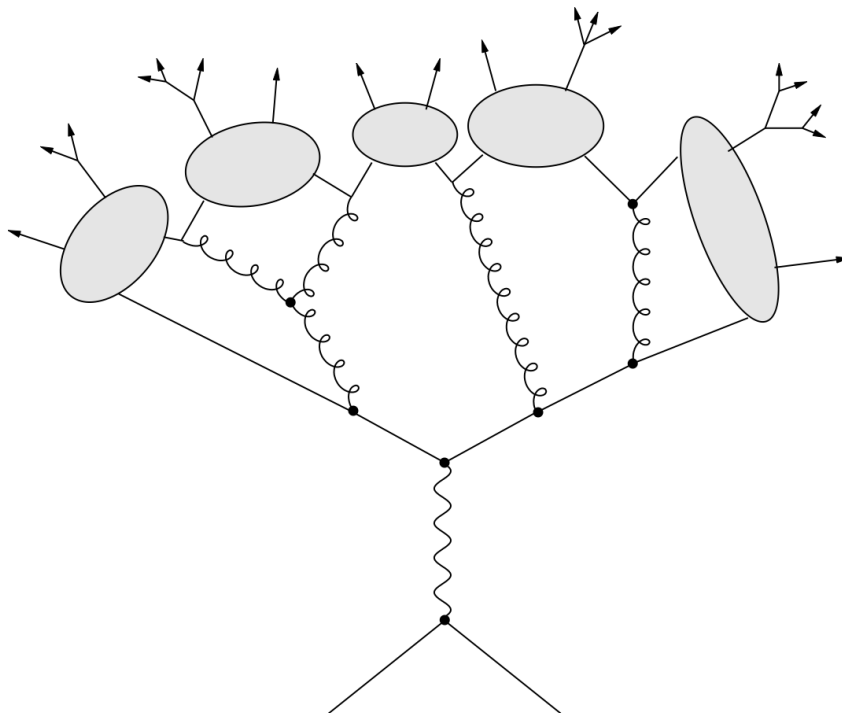
Figure 25: Hadronization.

4.8.3 Underlying Event

In pp experiments where bunches of protons are collided the hard-process is not the only one that has to be taken into account in order to calculate the cross sections. Underlying event processes also occur during the collisions where beam remnants interact via small momentum

transfers. These processes are non-perturbative thus the approximations rely on models or parametrization of data [16].

4.8.4 Non Pertubative Corrections

Monte Carlo generators such as PYTHIA or HERWIG++ contain LO calculations and non perturbative contribution in one framework. NLOJET++ though gives predictions derived only from pQCD calculations. It is known though that non perturbative effects are significant especially at multijet events containing jets with small p_T, thus it is necessary to somehow compensate these effects with a correction applied to the pQCD calculations.

The corrections are calculated using Monte Carlo generators that simulate NP effects. These generators (PYTHIA, HERWIG etc) can simulate events with or without taking into account effects due to NP effects. Thus two samples of events are generated to calculate NP corrections, one with all contributions taken into account (nominal) and one without multi parton interactions and parton showers simulated. The corrections are defined as

$$C_{NP} = \frac{\sigma_{\text{LO+PS+HAD+MPI}}}{\sigma_{\text{LO+PS}}} \tag{67}$$

where C_{NP} is the correction and σ the cross section of the studied observable. Then the pQCD calculations are corrected as:

$$\sigma_{pQCD \otimes NP} = C_{NP} \times \sigma_{pQCD} \tag{68}$$

In order to be unbiased against any underlying assumptions arising from the Monte Carlo generators, two or more generators are used to calculate these corrections. Then the final correction applied to pQCD calculations is the center of the envelope of the two (or more) corrections and the half of the spread among the corrections from the various generators is assigned as the uncertainty of the NP corrections.

4.9 HEP Tools

In high energy physics the calculations and the modelling of the various processes are complicated, for that reason sophisticated software has been developed to deliver predictions for the experiments. This chapter describes shortly the various monte carlo generators and tools that have been used for the predictions included in this thesis.

4.9.1 Monte Carlo Generators

Monte carlo generators are complicated software that simulate the processes taking place at the experiments. These simulations can be factorized in two distinct simulations:

- Event Generator
- Detector Simulation

The event generator simulates the proton proton interaction taking into account the PDF, simulates the initial state radiation, calculates the matrix element of the hard scattering, simulates the parton showers and the hadronization. For this purpose various MC generators were developed with different approaches, they are described below. The fact that these are complicated simulations each analysis has to take into various generators since the high complexity leaves space for bugs or wrong assumptions.

The second part, the detector simulation takes into account the interaction of the particles with the material of the detector. Then the interactions are translated to digital signals simulating the electronics of the detector. The CMS detector is simulated using GEANT4[17].

Consequently a MC simulation can be used directly from the generator level in order to compare with data and extract results independent of the detector or it can be used for detector studies. Below there is a short description of the MC generators used for the analyses described in chapters6 and 7.

4.9.1.1 PYTHIA

Pythia is a multi purpose generator that includes various physical processes, it simulates both the perturbative and non-perturbative processes described on the previous chapter. Two version are widely used, Pythia6 [18] and Pythia8[19], written in Fortran and C++ respectively. Pythia6 can simulate hard QCD processes with two partons at the final state while Pythia8 up to three partons.

Then the using the outgoing partons of the hard scattering the parton showering(PS) takes place. Pythia8 produces PS using the dipole-style p_T ordered evolution that approaches the gluon emission as a dipole radiation using a pair of partons. The parton showering process leads to a simulation that it can produce more than two jets in the final state. Finally the hadronization process is taking place using the Lund string fragmentation framework.

4.9.1.2 HERWIG

Herwig also comes in two version written in Fortran and C++ (Herwig++ [20]). It is a multi purpose generator that simulates two to two processes and the parton shower simulates more jets in the final state. Herwig uses the coherent branching algorithm of [21] using angular ordering of emissions in the PS. Finally for the hadronization Herwig uses the cluster model.

4.9.1.3 MADGRAPH

Madgraph[22] is a multi purpose tree-level generator that can give up to four partons at the final state. The hardonization, parton showering and the rest of the non-perturbative processes are taken into account by interfacing to PYTHIA. The MLM [23] matching procedure is used in order to avoid double counting partons from tree level and parton showers.

4.9.1.4 POWHEG

POWHEG [24] [25] is a framework that provides NLO calculations, in this thesis the dijet [26] calculations has been used which leads to the production of three partons at the final state. Higher jet multiplicities in the events can be done by interfacing POWHEG to generators that provide parton shower simulations, like PYTHIA.

4.9.1.5 NLOJet++

NLOJet++ [27, 28] is a program that calculates LO and NLO jet cross sections at a given renormalisation and factorisation scale and with agiven PDF set. The core library uses the Catani-Seymour general algorithm that calculates jet cross sections in NLO based on the subtraction

method. This calculation does not take into account non-perturbative contributions thus an approximate corrections is applied usually derived by the monte carlo generators descibed above.

4.9.2   FastNLO

FastNLO[29] is a framework that uses calculations from NLOJet++ but it uses some techniques that disentangles the α_S, PDF perturbative coefficients in the calculation. FastNLO produces interpolation tables containing pQCD coefficents for one observable performing the complicated calculations only once. Then it allows to calculate the observable by varying the α_S and PDF in a fast way. It also allows the variation of renormalisation, factorisation scale and the usage of various α_S evolution schemes.

4.9.3   PDF Sets

The parton density functions are an indispensable part of the calculations. PDF sets are delivered by various groups that use different methods to constrain parton density functions. The various groups deliver the PDF sets at a common file format that is treated by LHAPDF[30] software.

The PDF sets contain information in discrete points in x and Q space, while the LHAPDF software is an interpolator that evaluates the PDFs in a continous space. The PDF sets used in the analysis are ABM11, CT10, NNPDF2.1, MSTW2008, and HERAPDF1.5. All groups use data from various experiments besides HERAPDF that uses only HERA DIS data.

The various groups deliver their PDF sets in various $\alpha_S(M_Z)$ values and at differnet order of patron evolution, NLO and NNLO. Different flavor schemes are employed by the groups; all groups besides ABM use a variable flavour scheme, the various charachteristics of the PDF sets are tabulated in table 5.

Table 5: The PDF sets used to compare the data with expectations together with the corresponding number of active flavours N_f, the assumed mass M_Z of the Z boson, and the default values of $\alpha_S(M_Z)$.

Base set	Refs.	N_f	M_Z (GeV)	$\alpha_S(M_Z)$
ABM11	[31]	5	91.174	0.1180
CT10	[32]	≤ 5	91.188	0.1180
HERAPDF1.5	[33]	≤ 5	91.187	0.1176
MSTW2008	[34]	≤ 5	91.1876	0.1202
NNPDF21	[35]	≤ 6	91.2	0.1190

4.9.3.1   Statistical Treatment and PDF uncertainties

The two methods that PDF groups treat the datasets that are used in the determination of the PDF sets are the Hessian method and the Monte Carlo approach. NNPDF uses the Monte Carlo approach while everyone else uses the Hessian method.

Each group follows a different parametrization which introduces different number of free parameters. For the Hessian approach each parameter correspond to two eigenvectors, one in the

positive and one in the negative direction of the eigenvector. NNPDF delivers a Monte Carlo sample of 100 or 1000 replicas of PDFs.

In order to calculate the PDF uncertainties the cross sections are calculated for each eigenvector or replica, using fastNLO. The uncertainties for PDFs that use the Hessian method are calculated using the following formula:

$$(\Delta X_{PDF})^2 = \frac{1}{4} \sum_{k=1}^{d} [X(S_k^+) - X(S_k^-)]^2 \tag{69}$$

where d is the number of eigenvectors and ΔX is the uncertainty of the cross section and $X(S_k^{+-})$ is the predicted cross section for each eigenvector. The uncertainties in CT10 PDF set are computed at 2σ or 90% confidence level C.L., in order to scale these uncertainties down to 1σ the uncertainties are divided by a factor of $\sqrt{2} erf^{-1}(0.9) \approx 1.645$.

The uncertainty of the Monte Carlo PDF (NNPDF2.1) is calculated as the standard deviation of the sample using the following formula:

$$(\Delta X_{PDF})^2 = \frac{1}{(N_{rep} - 1)} \sum_{k=1}^{N_{rep}} [X(q_k) - \langle X(q_k) \rangle]^2 \tag{70}$$

where N_{rep} is the number of replicas ($N_{rep} = 100$ in the analyses of the following chapters), ΔX is the uncertainty of the cross section and $X(q_k)$ is the predicted cross section for each replica.

Each PDF set is delivered in a particular $\alpha_S(M_Z)$ depending on the fits performed by each group, this set is also called as central PDF set. However PDF sets are delivered also in different $\alpha_S(M_Z)$ values. The central one is used for the comparisons with data while the rest for α_S fits. The $\alpha_S(M_Z)$ introduces an additional uncertainty to the calculations. The uncertainty is calculated by re-evaluating the cross section by varying upwards and downwards the $\alpha_S(M_Z)$ by $\delta_{\alpha_S}^{1\sigma}$ (depending on the uncertainty of each PDF):

$$(\Delta X_{\alpha_S})^2 = X(\alpha_S{}^0 \pm \delta_{\alpha_S}^{1\sigma}) - X(\alpha_S{}^0) \tag{71}$$

where $X(\alpha_S{}^0)$ is the cross section with the central PDF and $X(\alpha_S{}^0 + \delta_{\alpha_S}^{1\sigma})$ is the cross section with the shifted $\alpha_S(M_Z)$ by 1σ.

The PDF and $\alpha_S(M_Z)$ uncertainties can be combined by adding them quadratically

$$(\Delta X_{\alpha_S+PDF})^2 = (\Delta X_{\alpha_S})^2 + (\Delta X_{PDF})^2 \tag{72}$$

5 Event Selection and Reconstruction

This chapter describes the methods used to reconstruct the objects, used in the analyses described in the Chapters 6 and 7, such as jets and missing transverse energy (MET). It also describes how jet's energy and MET are corrected.

5.1 Reconstruction

Jets as described in theory chapter do not consist of a single particle thus sophisticated algorithms are employed in order to identify the stream of particles as jets. The particle flow reconstruction technique and the anti$-k_T$ clustering algorithm will be described in this section as these algorithm used in the analyses in the Chapters 6 and 7.

5.1.1 Particle Flow Reconstruction

The Particle Flow (PF) reconstruction algorithm [36] identifies and reconstructs stable particles such as electrons, muons, photons, charged or neutral hadrons from all sub-detectors of CMS and it defines their energy, direction and type. The information of all particles is then used as an input to the algorithm to build jets, MET, taus, to quantify charged lepton isolation, tag b jets etc.

The algorithm starts by identifying muons, then the energy deposits and tracks of the muons are removed from the list of all deposits and tracks detected. Then electron identification and reconstruction follows by combining information from tracker and ECAL, then the information used to build the PF electron is removed from the list. In the next step tighter criteria in track selection is applied in order to reject fake tracks. Then the algorithm uses the rest of the tracks and calorimeters deposits that can give rise to hadrons, photons and rarely muons. Then by linking information from ECAL, HCAL and the trackers the algorithm decides whether there are charged or neutral hadrons or photons.

The optimal combination of all particles is very important for jet reconstruction since a jet, let's say of 500 GeV consists of particles with transverse momentum at the order of ~ 10 GeV.

5.1.2 Clustering Algorithm

Jets cannot be determined by the PF algorithm alone, so an additional algorithm is required to cluster particles into cones within determined borders. The analyses described in the next chapters use the infrared and collinear safe algorithm, anti$-k_T$ [37] as it is implemented by FASTJET [38] package.

The parameters need to be defined in order to construct the algorithm are the distance between particles i and j (d_{ij}) and the distance between particle i and beam (d_{iB}). Those parameters are defined as

$$d_{ij} = min(p_{Ti}^{2p}, p_{Tj}^{2p}) \frac{\Delta_{ij}^2}{R^2} \tag{73}$$

$$d_{iB} = p_{Ti}^{2p} \tag{74}$$

where $\Delta_{ij}^2 = (y_i - y_j)^2 + (\phi_i - \phi_j)^2$, $p_{Ti,j}$, $\phi_{i,j}$, $y_{i,j}$, are respectively the transverse momentum, azimuthal angle an the rapidity of particle i or j. The radius parameter R, is a constant that defines the borders of the cone that defines a jet. The parameter p defines the dependence of the algorithm to the particle's momentum for $k > 1$ the algorithm starts with soft particles, for

$k < 1$ starts this hard particles while $k = 0$ renders the algorithm independent of the energy. The k_T algorithm [39] uses $p = 1$, the Cambridge-Aachen uses $p = 0$ and the anti$-k_T$ uses $p = -1$.

In order to explain the functionality of the algorithm, let us consider two hard particles p_{T2}, p_{T1} and many soft particles. The variable d_{1j} between the hard particle 1 and the soft particles is mainly defined by the hard particle, therefore soft particles tend to cluster with hard ones. If the hard particle has no other hard neighbours within a radius of $2R$ then it will congregate the soft particles and form a perfectly conical jet. The algorithm can form non-conical jets in cases hard particles are neighbouring in a distance $\Delta_{12} < 2R$. The behaviour of the algorithm in the various cases is described in [40].

5.2   Corrections

The calorimeters of the CMS detector has non-uniform and non-linear response in energy deposits by particles. Thus the measured energy of the particles needs correction in order to correspond to the true particle energy. The following section describes how jet and missing transverse energy are corrected.

5.2.1   Jets

CMS follows a factorized approach to jet energy corrections (JEC) [41], meaning that each effect is taken care by a different level of correction. The corrections are applied as scale factor to the four momentum of the jet level by level depending on jet's p_T, η, flavour etc. as shown in figure 26. In analyses of the next chapters L1, L2, L3 and L2L3 corrections were used.

- L1 Pile Up
  This correction is applied to remove additional energy resulting from out of time (pileup) events. These events do not participate in the hard scattering but they can add fake energy to jets.

- L2 Relative Jet Correction This corrections is applied to make the response of the detector flat versus η and is achieved by correcting a jet in arbitrary η to a jet in the central region. The corrections are derived either by using MC or dijet events from data.

- L3 Absolute Jet Correction
  This corrections is applied to make the response of the detector flat versus p_T. After the application of the L2 correction the L3 corrections are derived either by using MC or data (dijets,Z/γ+jets).

- L2L3 Residuals
  After applying the above corrections there is still some discrepancy between MC and data. This discrepancy is compensated by the application of the L2L3 corrections.
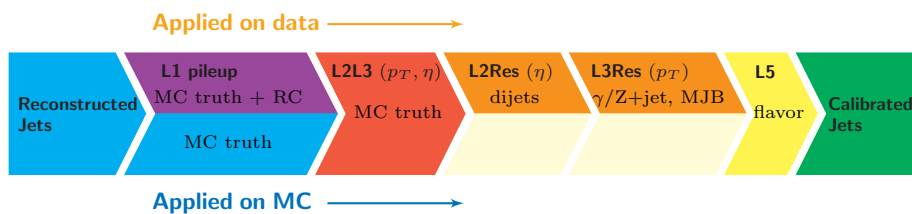
Figure 26: Sequential corrections of jets.

5.3 Missing Transverse Energy

The missing transverse energy is defined as

$$\not{E}_T^{raw} = -\sum_i \vec{p}_{Ti} \tag{75}$$

where index i is summing over all reconstructed particles in the event. It can be factorized in the terms of jets p_T and unclustered particles in order to take advantage of JECs and correct $\not{E}_T$; and it is written as

$$\not{E}_T^{raw} = -\sum_{i,uncl} \vec{p}_{Ti} - \sum_{i,jets} \vec{p}_{Ti}^{raw} \tag{76}$$

The Type-I corrected $\not{E}_T$ that uses JECs to correct jets is defined as:

$$\not{E}_T^{TypeI} = -\sum_{i,uncl} \vec{p}_{Ti} - \sum_{i,jets} \vec{p}_{Ti}^{corr} \tag{77}$$

Raw MET is used in the analyses of the next chapters since it is only used to apply a cut at $\not{E}_T / \sum E_T$.

5.4 Trigger Efficiency

The first step of the analysis is the determination of the trigger paths that collect the data. The triggers L1 and HLT have a nominal value where above that threshold are recording events. The real value though that the triggers start recording data (fire) is not 100% of the nominal. Thus a study is required to measure the value that triggers are 100% efficient.

Some triggers, in order to reduce even further the data taking, are recording only a fraction of the events that pass the L1 and HLT requirements. The suppresion factor is called prescale factor f_p, which indicates the ratio of the events that fired the trigger N_f to the events that have been recorded N_r:

$$f_p = \frac{N_f}{N_r} \tag{78}$$

In the ideal case where two trigger paths, HLT JetX and JetY, are unprescaled ($f_p = 1$) the ratio of the spectrum recorded by the two trigger gives the trigger efficiency ϵ:

$$\epsilon_Y = \frac{Obs(HLTJetY)}{Obs(HLTJetX)} \tag{79}$$

In the case thought that the trigger paths are prescaled, elaborate techniques are needed to measure the value that the triggering is fully efficient. A pseudo-emulation technique is used to measure the trigger efficiency in the analyses described in the following chapters.

The pseudo-emulation technique can be described by the following three steps:

- Fill a histogram with the observable, (i.e. $3-$jet cross section as a function of $\langle p_{T1,2} \rangle$) using an HLT path (i.e. HLT Jet240).

- Access the L1 and HLT objects of the jets that filled the histogram. Check if the objects pass the requirements for the next trigger(i.e HLT Jet370) and fill a histogram with these jets.

- Divide the two, fit with the error function and get the point which the error function reached the 99% of the plateau.

Figure 27 shows the trigger efficiency used for the ratio of 3−jet to 2−jet inclusive cross sections analysis described in 6.2.
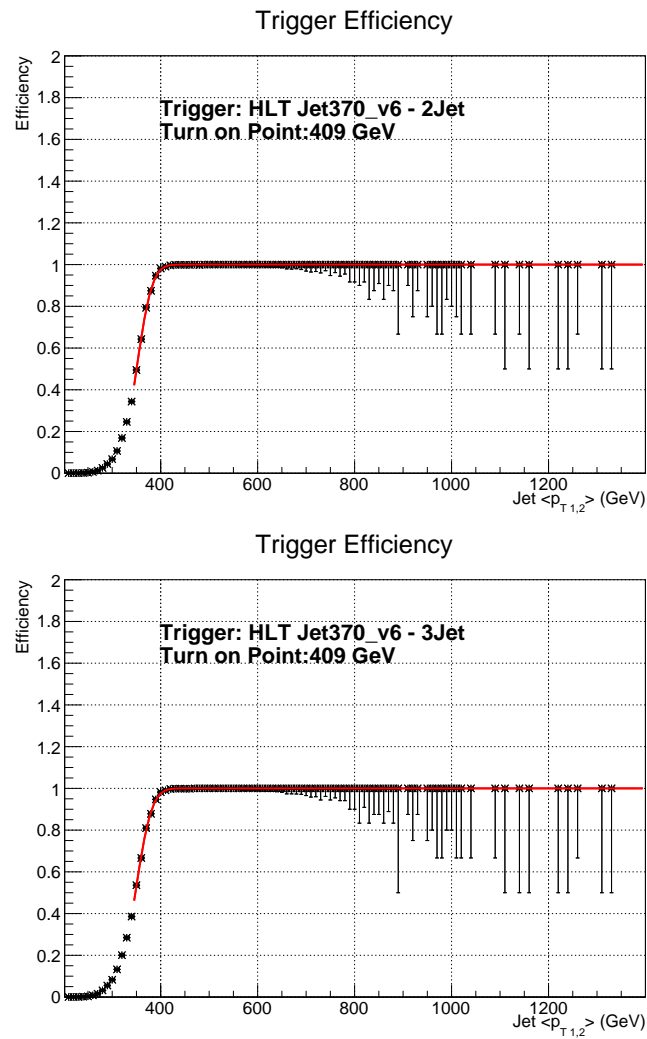
Figure 27: Trigger Efficiency.

6 Analysis at $\sqrt{s} = 7TeV$

This chapter describes the measurement of two observables with jets in final state, both using data from pp interactions at $\sqrt{s} = 7$ TeV. The first measurement, presented in subsection 6.1 is the inclusive jet cross section, as it was published by CMS in [42], an observable proportional to α_S^2. The second measurement, presented in subsection 6.2, is the ratio of the inclusive 3−jet to 2−jet cross sections, an observable proportional to α_S. Both observables are used to extract the strong coupling constant.

6.1 The Inclusive Jet Cross Section Measurement

This subsection describes the extraction of the strong coupling constant, α_S, from the inclusive jet cross section measurement at $\sqrt{s} = 7$ TeV. Subsection 6.1.1 gives a brief description of the measurement. Subsection 6.1.2 describes the theoretical components of the analysis while section 6.1.3 the extraction of the α_S at the mass of vector boson Z.

6.1.1 The Measurment Overview

The events analyzed in the following analysis were collected by the CMS detector at proton-proton collisions at $\sqrt{s} = 7$ TeV in 2011 and correspond to an integrated luminosity 5.0 fb^{-1}. The particles used in the jet clustering were reconstructed using the PF technique and jets were clustered using the anti-k_T algorithm with the radius parameter set at $R = 0.7$. The data were collected using single-jet HLT triggers, the integrated luminosity collected by each trigger path is shown in table 6.

Table 6: The integrated luminosity for each trigger sample considered in this analysis.

HLT p_T threshold (GeV)	60	110	190	240	320
$\mathcal{L}$ (pb^{-1})	0.41	7.3	152	512	4980

In order to suppress non-physical jets it is required that each jet should contain at least two particles, one of which is a charged hadron, and the jet energy fraction carried by neutral hadrons and photons should be less than 90%. The comparison of $\not{E}_T / \sum E_T$ distribution from data and QCD simulation is shown in figure 28, above $\not{E}_T / \sum E_T = 0.3$ the QCD simulation cannot describe data. The region $\not{E}_T / \sum E_T > 0.3$ is discarded from the dataset since is populated from events originating from processes such as Z+jet(s) and W+jet(s).

The double differential cross section that is studied in this section is defined as:

$$\frac{d^2\sigma}{dp_T dy} = \frac{1}{\epsilon \mathcal{L}_{int}} \frac{N_{jets}}{\Delta p_T (2\Delta|y|)} \tag{80}$$

where ϵ is the product of trigger and event selection efficiencies, $\mathcal{L}_{int}$ is the integrated luminosity of the data sample, N_{jets} is the number of jets in the bin, Δp_T and $\Delta|y|$ are the bin widths of transverse momentum and rapidity. The analysis recorder jets with minimum $p_T = 114$ GeV in five rapidity bins of width $\Delta y = 0.5$ up to $|y| < 2.5$.

The inclusive jet p_T spectrum was reconstructed in five exclusive regions by taking into account the efficiency of each trigger path. The spectrum for the innermost rapidity bin, at detector level is shown in figure 29.

The detector-level spectrum suffers from smearing effects due to the finite resolution of the detector thus it cannot be compared with measurements from different experiments or with
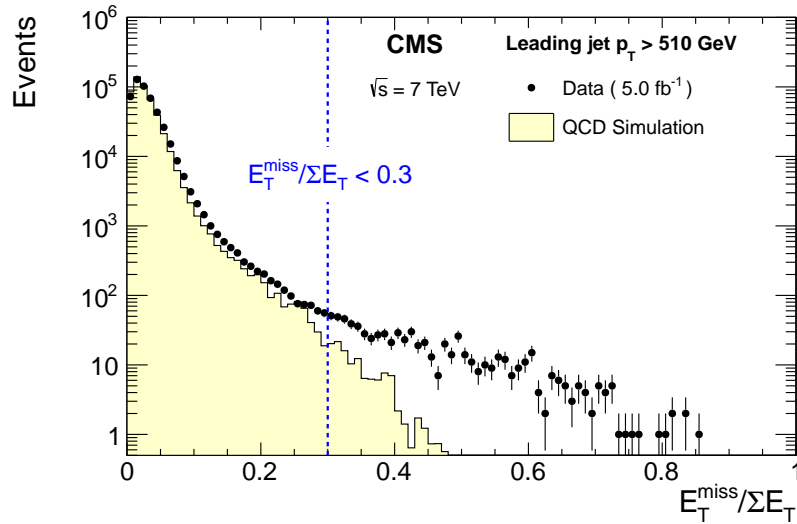
Figure 28: Missing energy over the sum of the energy from data (black points) and QCD simulation (shaded area).
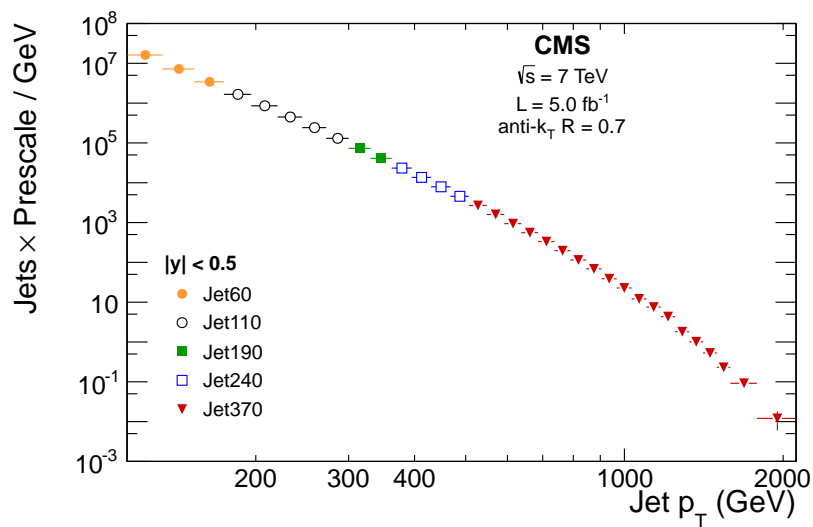
Figure 29: Reconstructed jet p_T spectrum from five trigger paths.

particle-level simulations. In order to remove the smearing effects the unfolding technique has been used as is implemented in the ROOUNFOLD package, using the iterative Bayesian method. The unfolding method takes as input the detector-level spectrum and the migration matrix that maps the generator-level jets to the detector-level jets. The migration matrix is shown in figure 30, the matrix is derived from MC simulations. The output of the unfolding is the particle-level spectrum and the correlation matrix that is used in the chi-squared fit for the extractions of the $\alpha_S(M_Z)$.
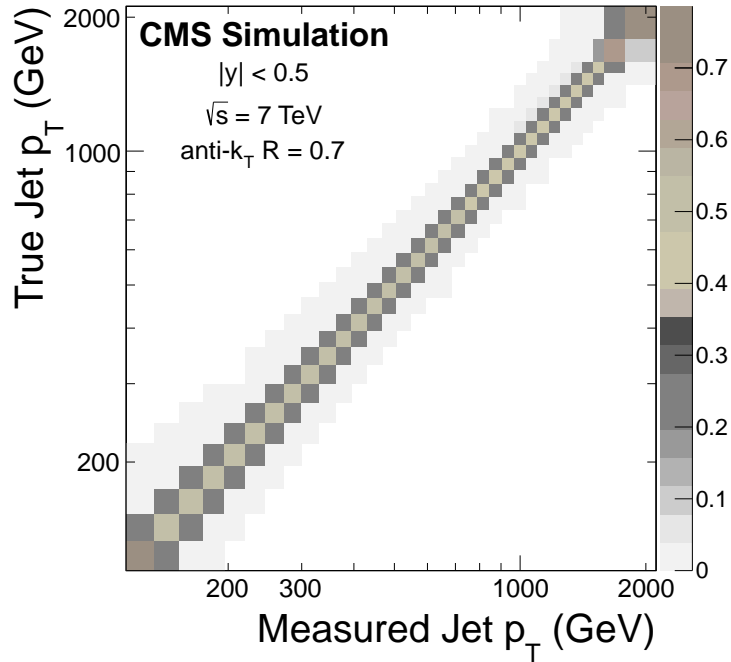
Figure 30: Migration matrix, mapping the generator-level (true) to detector-level (measured) jet p_T.

6.1.1.1   Experimental uncertainties

The main experimental uncertainties originate from the jet energy scale (JES), the unfolding method, and the luminosity. There is also a small uncertainty 1% assigned in jet p_T to take into account small effects due to trigger or jet identification inefficiencies.

The jet-energy calibration procedure and the ways to estimate the JES uncertainty is described in Ref.[43]. The energy of reconstructed jets is corrected as described in subsection 5.2.1. There are 16 important sources of jet energy corrections for this analysis and each one is accompanied by it's uncertainty. The 16 sources are listed below:

- ABSOLUTE: Absolute uncertainty.
  Using data with photon+jet and Z+jet events an absolute calibration of jet energies is performed in the jet p_T range of about 30–600 GeV. Uncertainties in the determination of electromagnetic energies in the ECAL, of the muon momenta from $Z \rightarrow \mu\mu$ decays, and of the corrections for initial- (ISR) and final-state (FSR) radiation are propagated together with the statistical uncertainty to give the absolute JES uncertainty.

- HIGHPTEXTRA: High and low p_T extrapolation uncertainty.

Where an absolute calibration with data is not possible, events are produced with the event generators PYTHIA6 and HERWIG++ and are subsequently processed through the CMS detector simulation based on GEANT4 [44]. Differences in particular in modelling the fragmentation process and the underlying event lead to an extrapolation uncertainty relative to the directly calibrated jet p_T range of about 30–600 GeV.

- SINGLEPION: High and low p_T extrapolation uncertainty.
  This source accounts for a $\pm 3\%$ variation in the single particle response that is propagated to jets using a parameterized fast simulation of the CMS detector [45].

- FLAVOR: Jet flavor related uncertainty.
  Differences in detector response to light, charm, and bottom quark as well as gluon initiated jets relative to the mixture predicted by QCD for the measured processes are evaluated on the basis of simulations with PYTHIA6 and HERWIG++.

- TIME: Uncertainty caused by time dependent detector effects.
  This source considers residual time-dependent variations in the detector conditions such as the endcap ECAL crystal transparency.

- RELATIVE: η-dependent uncertainties coming from the dijet balance method.

  - RELATIVEJER: Caused by the jet p_T resolution (JER).
    These are three separate sources RELATIVEJEREC1, RELATIVEJEREC2, and RELATIVEJERHF, which are assumed to be fully correlated for the endcap with upstream tracking detectors (EC1), the endcap without upstream tracking detectors (EC2), and the hadronic forward calorimeter (HF).
  - RELATIVEFSR: η-dependent uncertainty caused by corrections for final-state radiation.
    The uncertainty is correlated from one region to the other and increases towards HF.
  - RELATIVESTAT[EC2][HF]: Statistical uncertainty in the determination of η-dependent corrections.
    These are two separate sources for the endcap without upstream tracking detectors (EC2), and the hadronic forward calorimeter (HF).

- PILEUP[DATAMC][OOT][PT][BIAS][JETRATE]: Uncertainties for the pile-up corrections.
  These are five separate sources of uncertainty. PILEUPDATAMC parameterizes differences between data and MC events versus η in Zero Bias data. PILEUPOOT estimates residual out-of-time pile-up for prescaled triggers, if MC events are reweighted to unprescaled data. PILEUPPT covers for an offset dependence on jet p_T (due to e.g. zero-suppression effects), when the correction is calibrated for jets in the p_T range of 20—30 GeV. PILEUPBIAS accounts for differences in measured offset from Zero Bias (neutrino gun) MC events and from MC truth in a QCD sample. PILEUPJETRATE covers for observed jet rate variations versus the average number of reconstructed primary vertices in the 2011 single jet triggers after applying L1 corrections.

The 16 sources are mutually uncorrelated and initially reported as fully correlated across p_T and $|y|$. However an unphysical behaviour was observed during the fitting procedure of $\alpha_S(M_Z)$ demanding a more detailed study of the JES correlations. A study performed varying the correlation factors of the various JES sources which showed that the χ^2 and $\alpha_S(M_Z)$ is dramatically increased after applying 100% correlation. This behaviour led to a further examination of the

JES correlations that lead to reduction of the correlation of one source (Single Pion). Instead of the fully correlated across the $|y|$ bins matrix ($C_{SP} = \mathbb{1}$) the partially correlated was used:

$$
C_{SP} = \begin{pmatrix}
1 & 0.5 & 0.5 & 0 & 0 \\
0.5 & 1 & 0.5 & 0 & 0 \\
0.5 & 0.5 & 1 & 0 & 0 \\
0 & 0 & 0 & 1 & 1 \\
0 & 0 & 0 & 1 & 1
\end{pmatrix}
$$

The unfolding method as described in the previous subsection introduces an uncertainty in the measurement. The unfolding uncertainty is estimated to be of the order of $3 - 4\%$ and is fully correlated across p_T and $|y|$ bins.

The uncertainty on the integrated luminosity [46] is flat 2.2%. The uncertainty is directly propagated to cross section as a normalization uncertainty and is fully correlated across p_T and $|y|$ bins.

There is also a small uncertainty 1% assigned in jet p_T to take into account small effects due to trigger or jet identification inefficiencies which is uncorrelated across p_T and bins.

The unfolded measured spectrum compared to dijet calculations at NLO using POWHEG interfaced to PYTHIA6 and corrected with electroweak (EW) corrections [47, 48] is shown in figure 31.
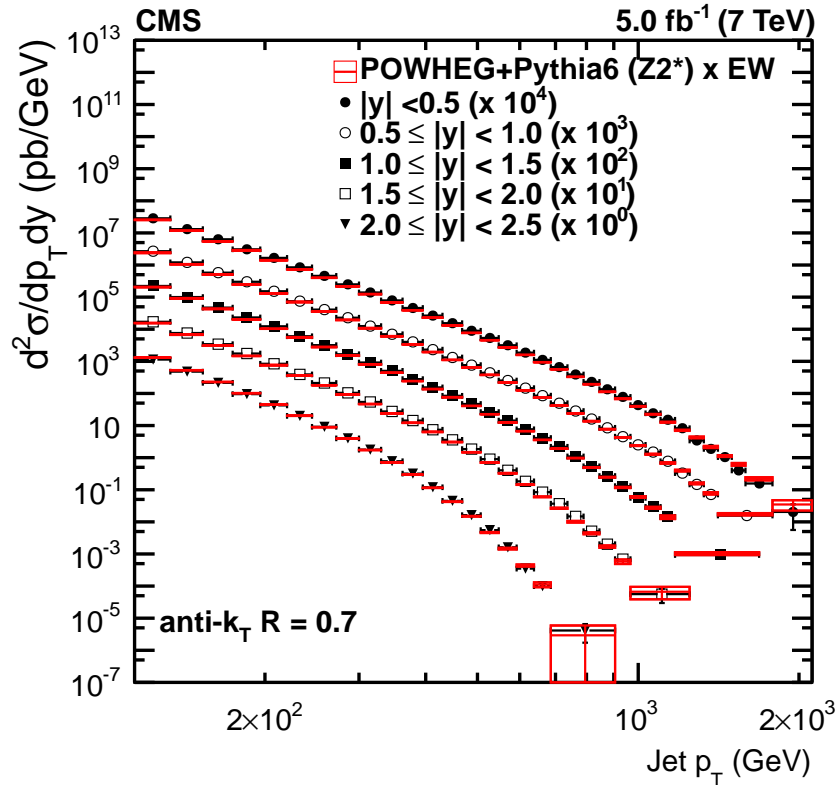
Figure 31: The unfolded differential inclusive jet cross section as a function of p_T in five $|y|$ bins. Theoretical predictions using POWHEG interfaced to PYTHIA6 shown in red. Data points with experimental and systematic uncertainties shown in black points.

6.1.2   Theoretical Components and Comparison with Data

6.1.2.1   Comparison to Theory

The inclusive jet cross sections are compared to dijet next-to-leading order (NLO) calculations. The calculations performed using the NLOJET++ parton generator within the FASTNLO framework. For the calculations four PDF sets were used, ABM11,CT10, MSTW2008, and NNPDF2.1, both at NLO and NNLO. Since NLOJET++ does not simulate MPI and hadronization, in order to compensate the non-perturbative effects theory is corrected with mulitplicative factors, as described in subsection 4.8.4, derived using the monte carlo generators HERWIG++, PYTHIA6 and POWHEG. Figure 32 shows the NP corrections for the innermost and outermost rapidity bins derived from the three MC generators.
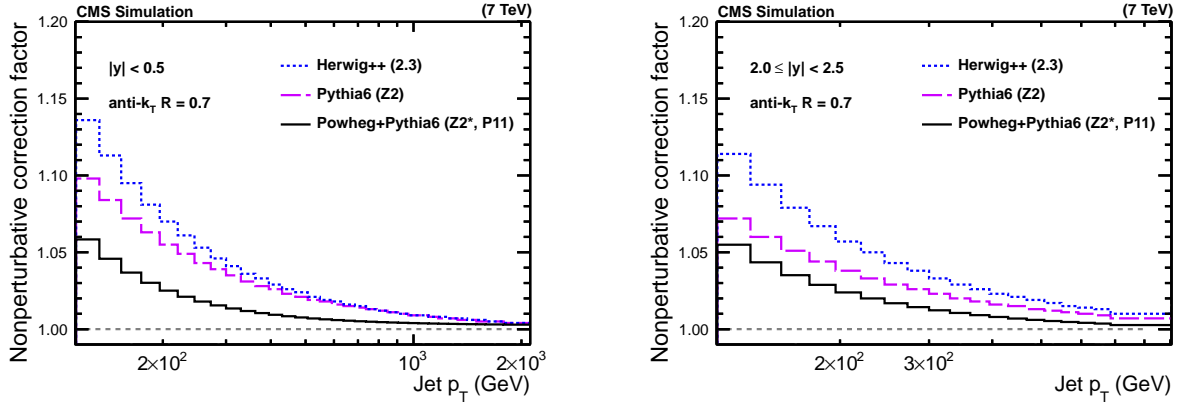
Figure 32: Non pertubative corrections for two $|y|$, derived using HERWIG++, PYTHIA6 and POWHEG.

The final NP corrections that are applied to theory are shown in in figure 33 obtained from the envelope of the three predictions.

Figures 34-41 present the comparison of data to theory, where the blue points (data) are presented with the total uncertainty (both statistical and systematic). The green lines present the PDF uncertainty that has been calculated according to the prescription given by each collaboration which provides the PDF set, also described in subsection 4.9.3. The red line present the scale uncertainty due to renormalization and factorization. The uncertainties due to the renormalization (μ_r) and factorization (μ_f) scales are evaluated by varying the default choice of $\mu_r = \mu_f = \langle p_{T1,2} \rangle$ between $\langle p_{T1,2} \rangle / 2$ and $2\langle p_{T1,2} \rangle$ in the following six combinations $(\mu_r, \mu_f) = (\langle p_{T1,2} \rangle / 2, \langle p_{T1,2} \rangle / 2), (2\langle p_{T1,2} \rangle, 2\langle p_{T1,2} \rangle), (\langle p_{T1,2} \rangle, \langle p_{T1,2} \rangle / 2), (\langle p_{T1,2} \rangle, 2\langle p_{T1,2} \rangle), (\langle p_{T1,2} \rangle / 2, \langle p_{T1,2} \rangle)$ and $(2\langle p_{T1,2} \rangle, \langle p_{T1,2} \rangle)$, the maximum upwards and downwards deviation is considered as the uncertainty. For each PDF set the default $\alpha_S(M_Z)$ value is chosen. A good aggreement is observed between theory and data besides the case were ABM11 is used.
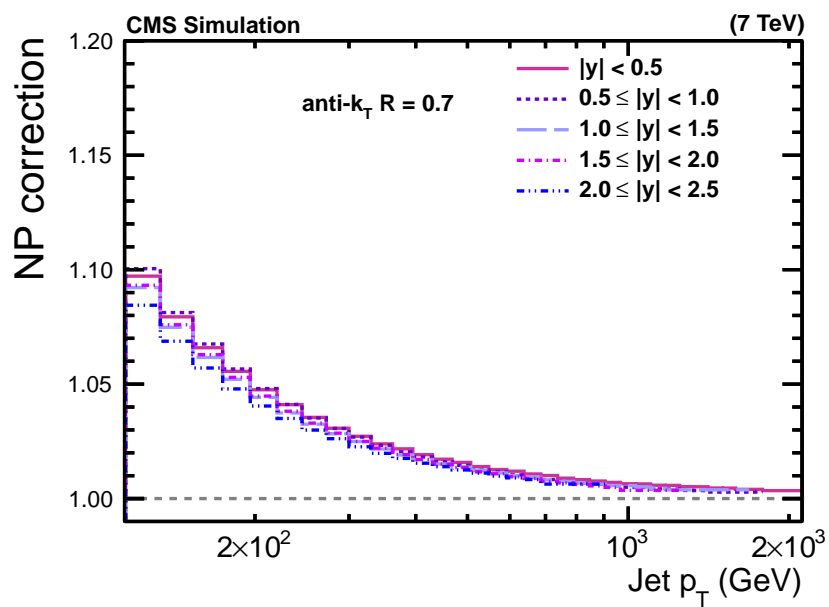
Figure 33: Non pertubative corrections for all $|y|$ bins, derived using the envelope of predictions from HERWIG++, PYTHIA6 and POWHEG.
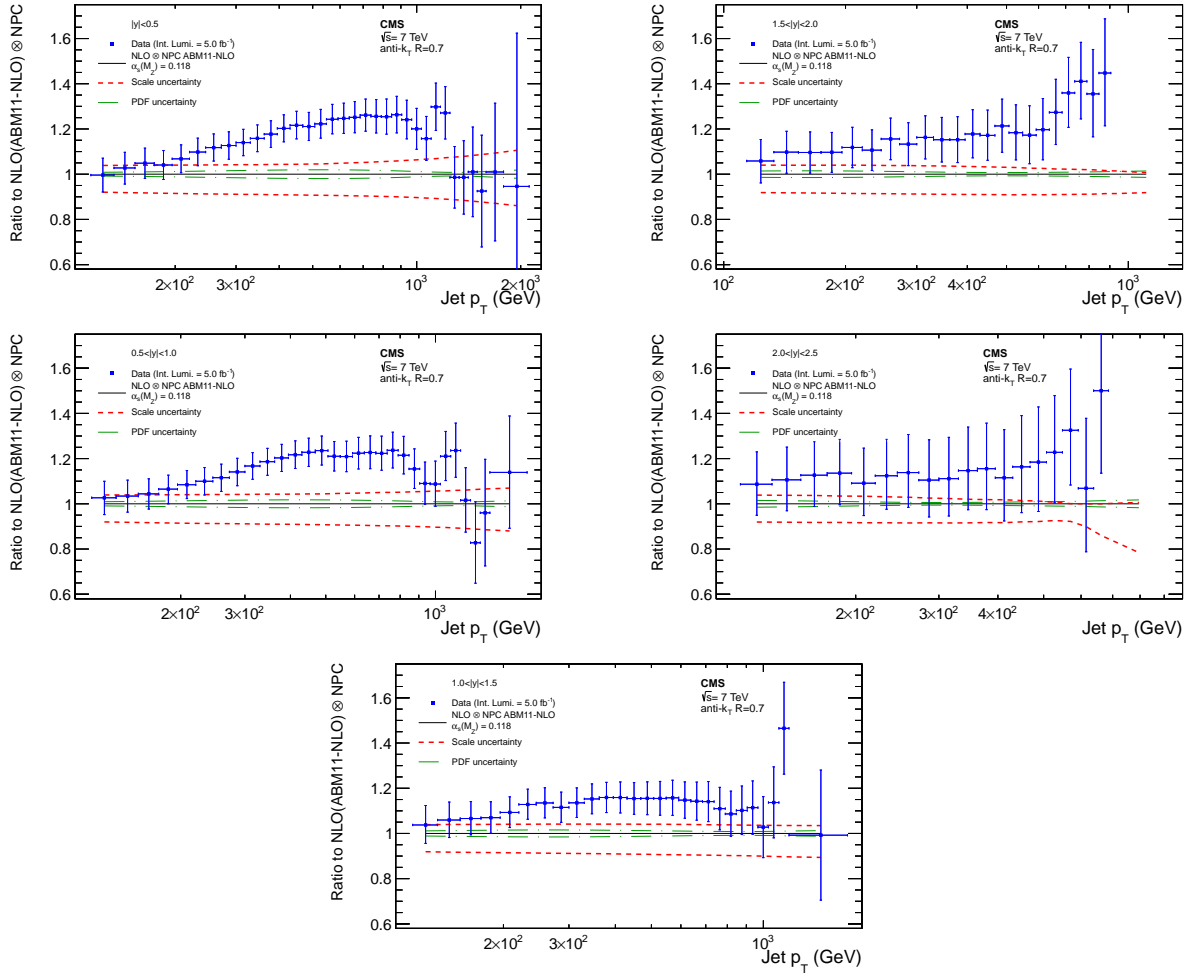
Figure 34: Ratio of the inclusive jet cross section to theory predictions using the **ABM11-NLO PDF** set for the five rapidity bins, where the $\alpha_S(M_Z)$ value is varied in the range 0.110-130 in steps of 0.001. The error bars correspond to the total uncertainty.
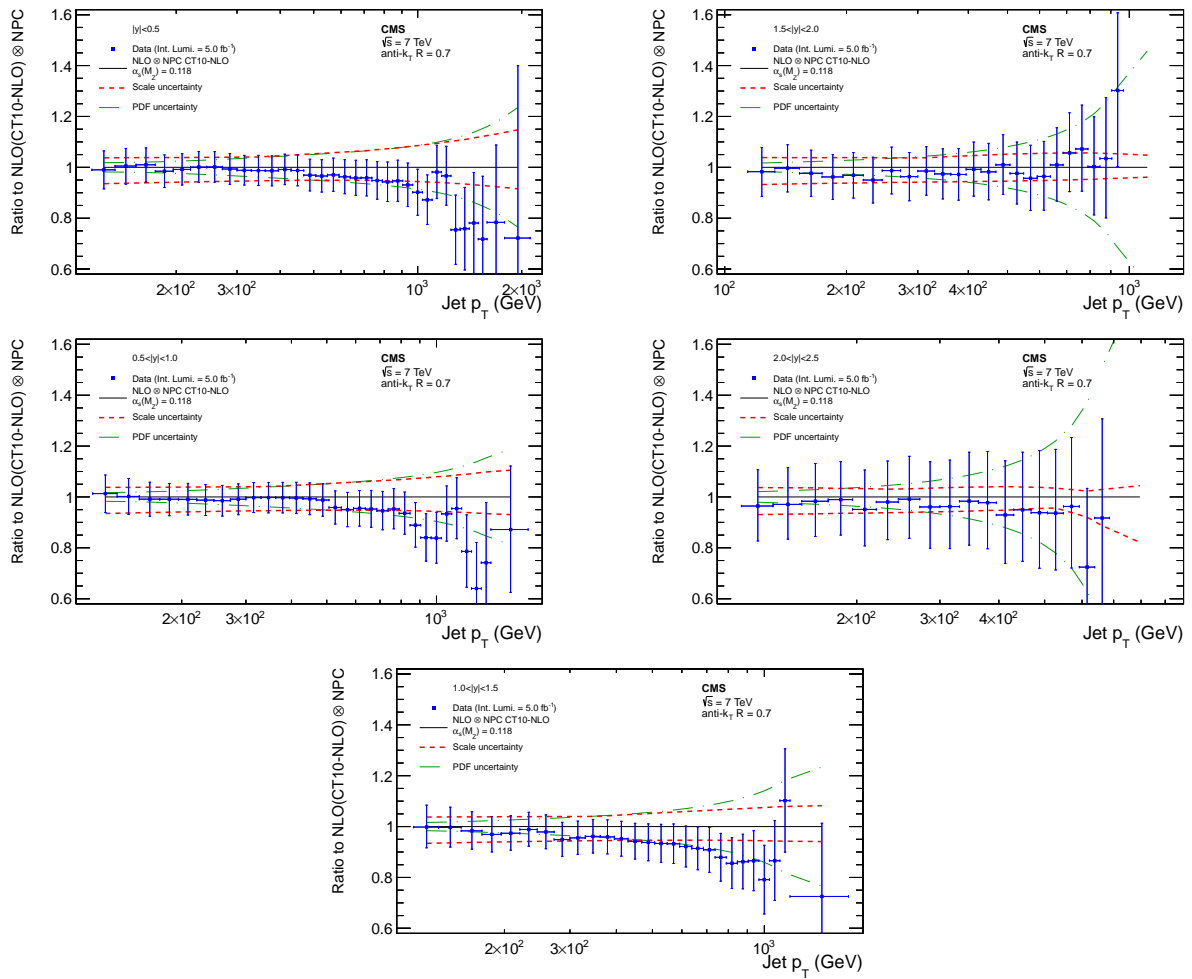
Figure 35: Ratio of the inclusive jet cross section to theory predictions using the **CT10-NLO PDF** set for the five rapidity bins, where the $\alpha_S(M_Z)$ value is varied in the range 0.112-0.126 in steps of 0.001. The error bars correspond to the total uncertainty.
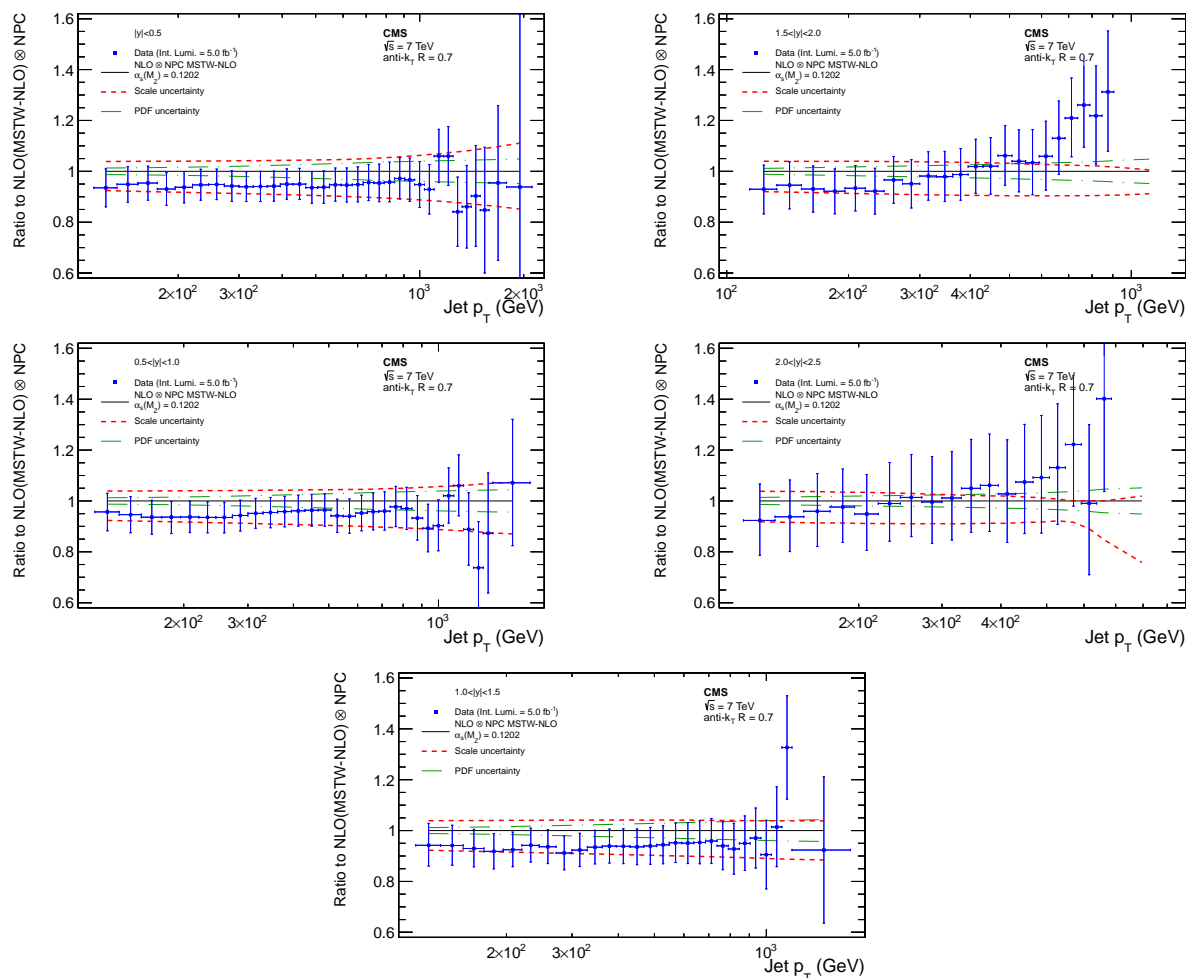
Figure 36: Ratio of the inclusive jet cross section to theory predictions using the **MSTW2008-NLO PDF** set for the five rapidity bins, where the $\alpha_S(M_Z)$ value is varied in the range 0.110-0.130 in steps of 0.001. The error bars correspond to the total uncertainty.
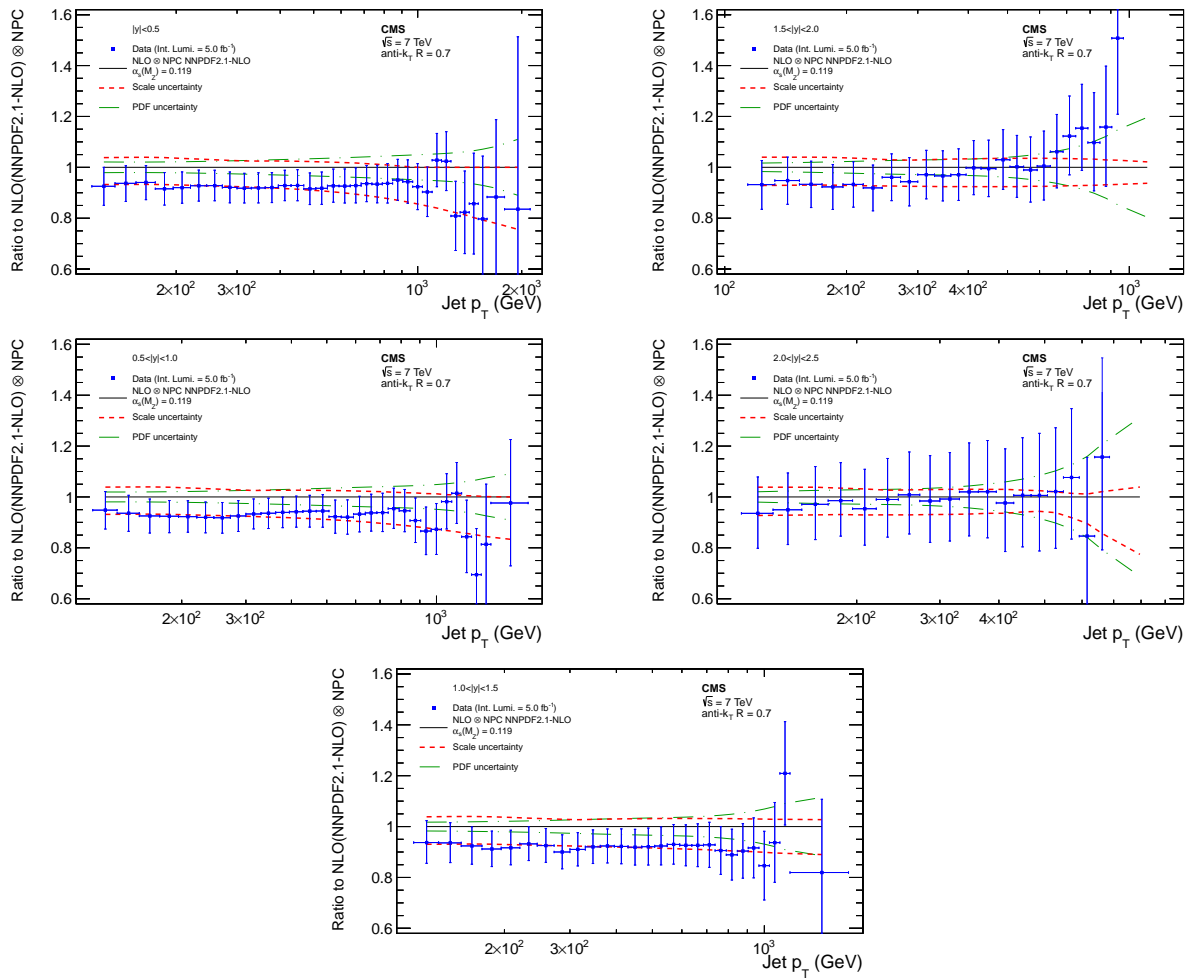
Figure 37: Ratio of the inclusive jet cross section to theory predictions using the **NNPDF2.1-NLO PDF** set for the five rapidity bins, where the $\alpha_S(M_Z)$ value is varied in the range 0.116-0.122 in steps of 0.001. The error bars correspond to the total uncertainty.
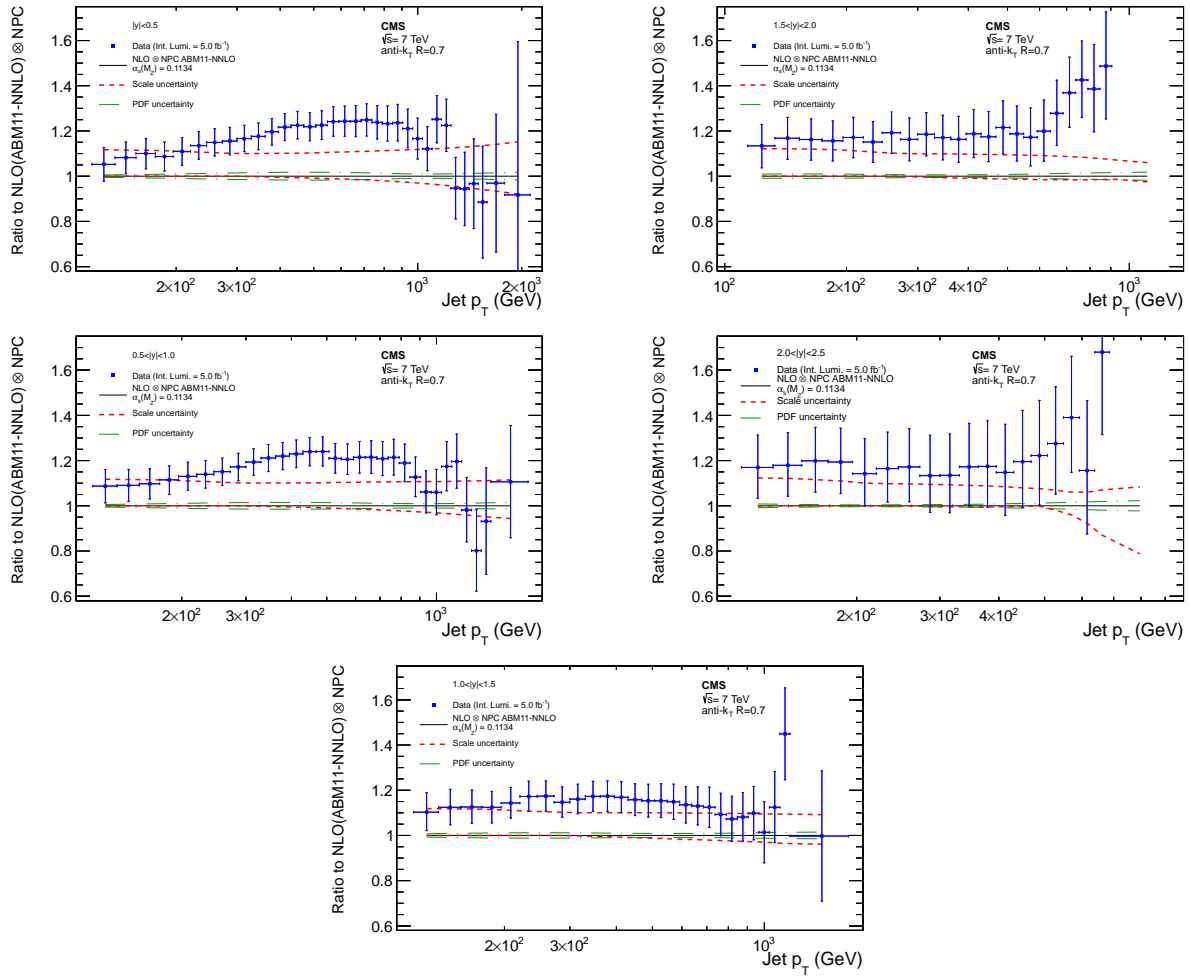
Figure 38: Ratio of the inclusive jet cross section to theory predictions using the **ABM11-NNLO PDF** set for the five rapidity bins, where the $\alpha_S(M_Z)$ value is varied in the range 0.104-120 in steps of 0.001. The error bars correspond to the total uncertainty.
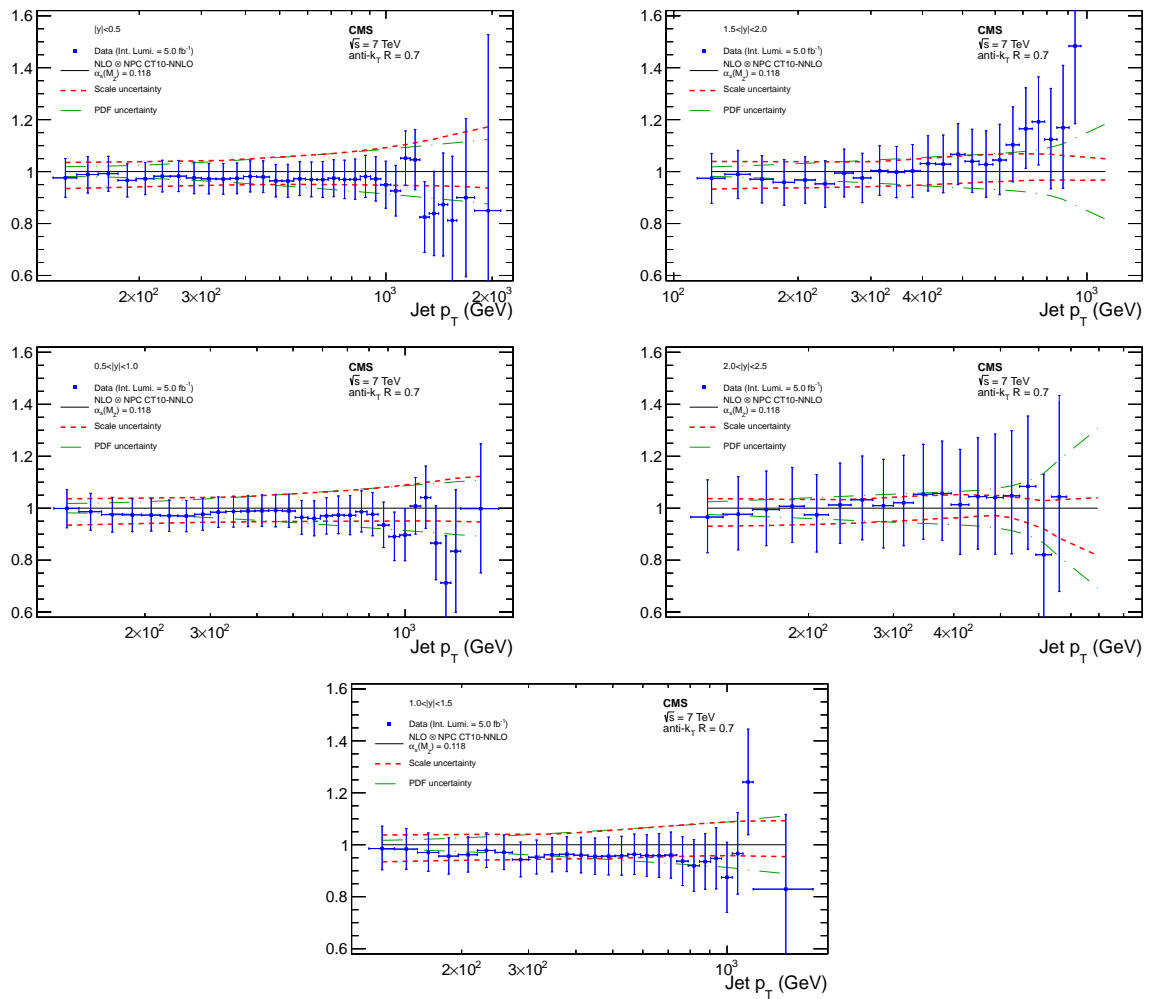
Figure 39: Ratio of the inclusive jet cross section to theory predictions using the **CT10-NNLO PDF** set for the five rapidity bins, where the $\alpha_S(M_Z)$ value is varied in the range 0.110-0.130 in steps of 0.001. The error bars correspond to the total uncertainty.
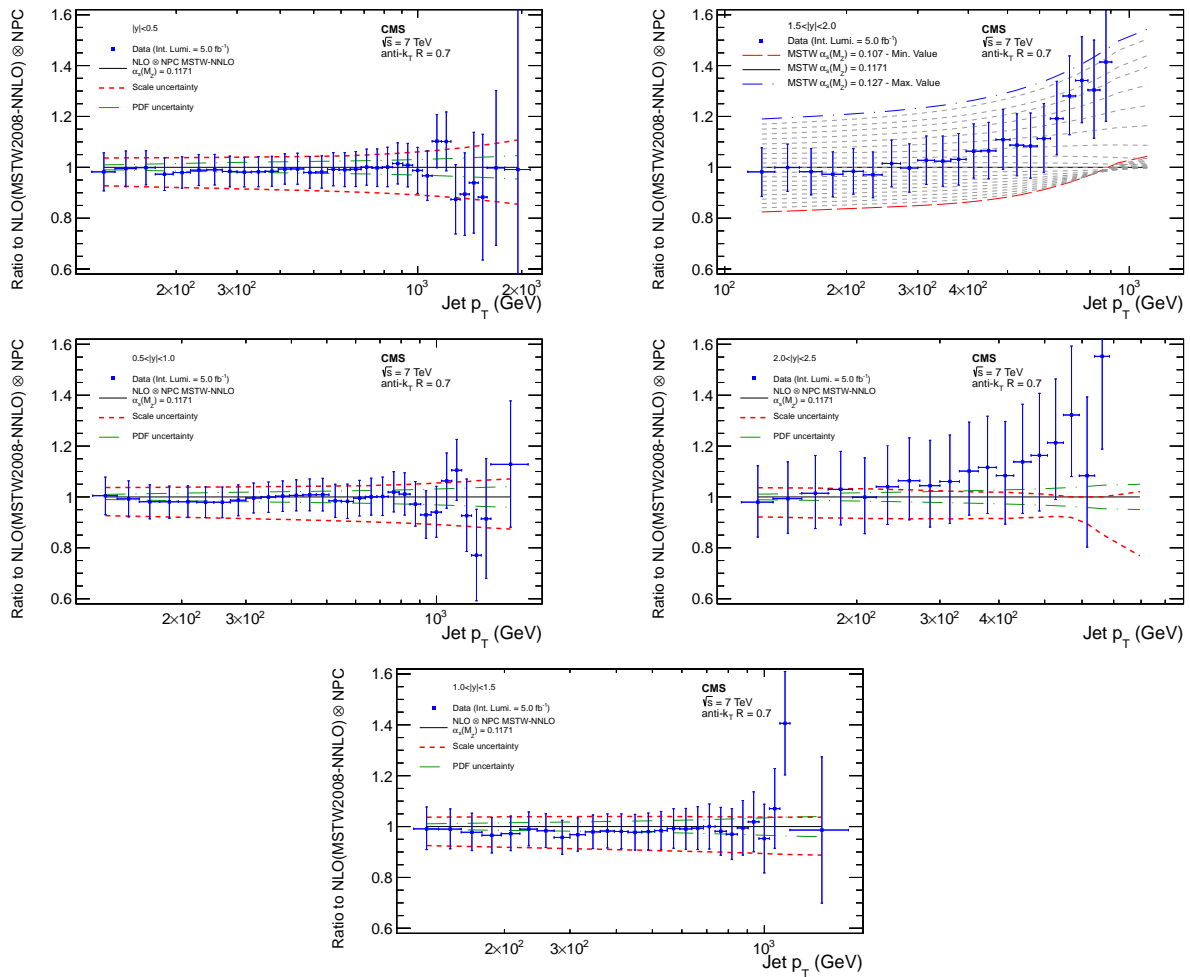
Figure 40: Ratio of the inclusive jet cross section to theory predictions using the **MSTW2008-NNLO PDF** set for the five rapidity bins, where the $\alpha_S(M_Z)$ value is varied in the range 0.107-0.127 in steps of 0.001. The error bars correspond to the total uncertainty.
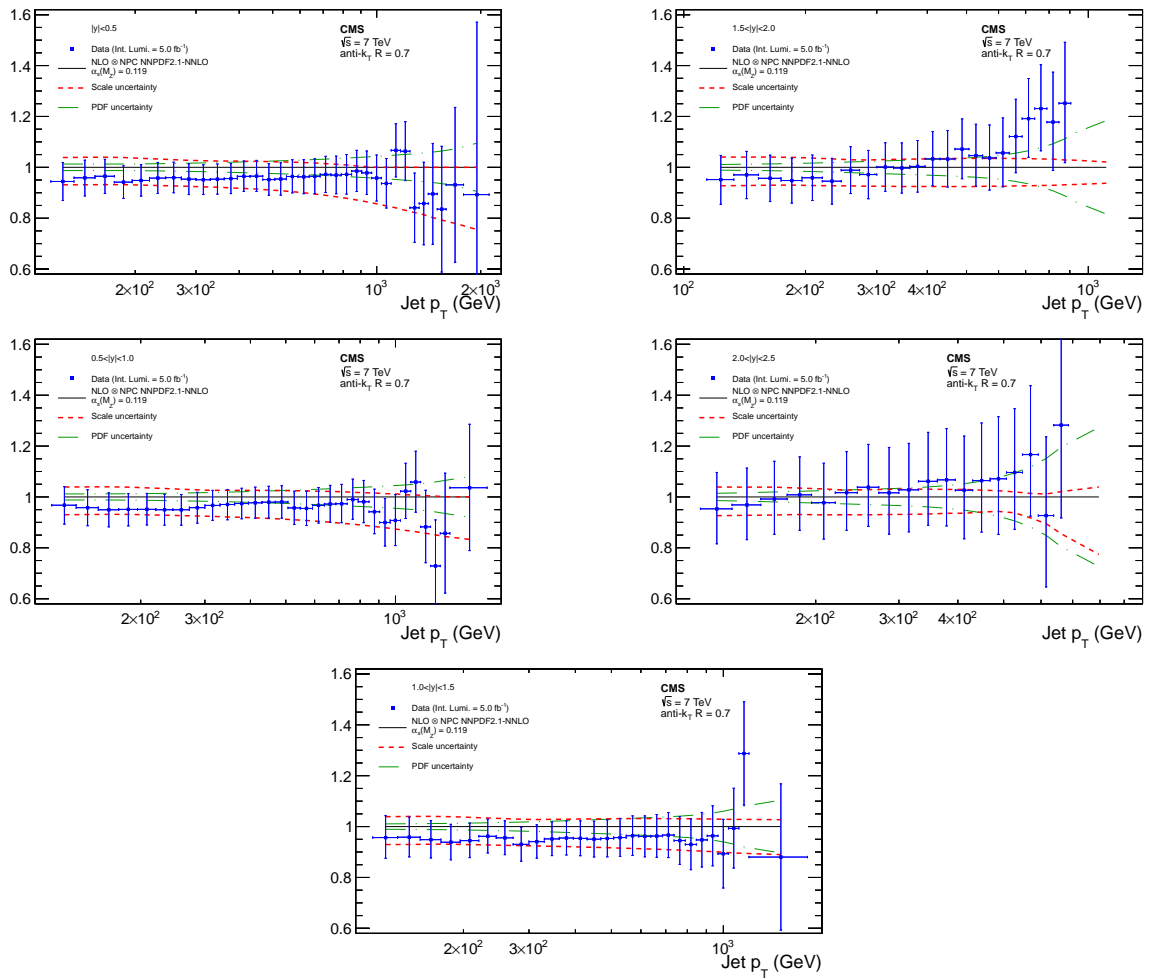
Figure 41: Ratio of the inclusive jet cross section to theory predictions using the **NNPDF2.1-NNLO PDF** set for the five rapidity bins, where the $\alpha_S(M_Z)$ value is varied in the range 0.106-0.124 in steps of 0.001. The error bars correspond to the total uncertainty.

6.1.3   Sensitivity of the inclusive jet cross section to $\alpha_S(M_Z)$

The extraction of the strong coupling constant from data relies on the sensitivity of the measured quantity to variations of α_S. In order to check the sensitivity of the double differential cross section to variations of α_S, calculations performed by varying the α_S in steps of 0.001. Figures 42–45 present the ratio of data to the theory for all variations in $\alpha_S(M_Z)$ available for each PDF set. For this study the ABM11, CT10, MSTW2008 and NNPDF2.1 in NLO and NNLO were used. Besides ABM11 which cannot describe the data, the rest of the PDF sets give a satisfactory description of them and a sufficient sensitivity to the variation of α_S. Therefore the ABM11 PDF set were excluded for the fitting procedure which is described in the next section.
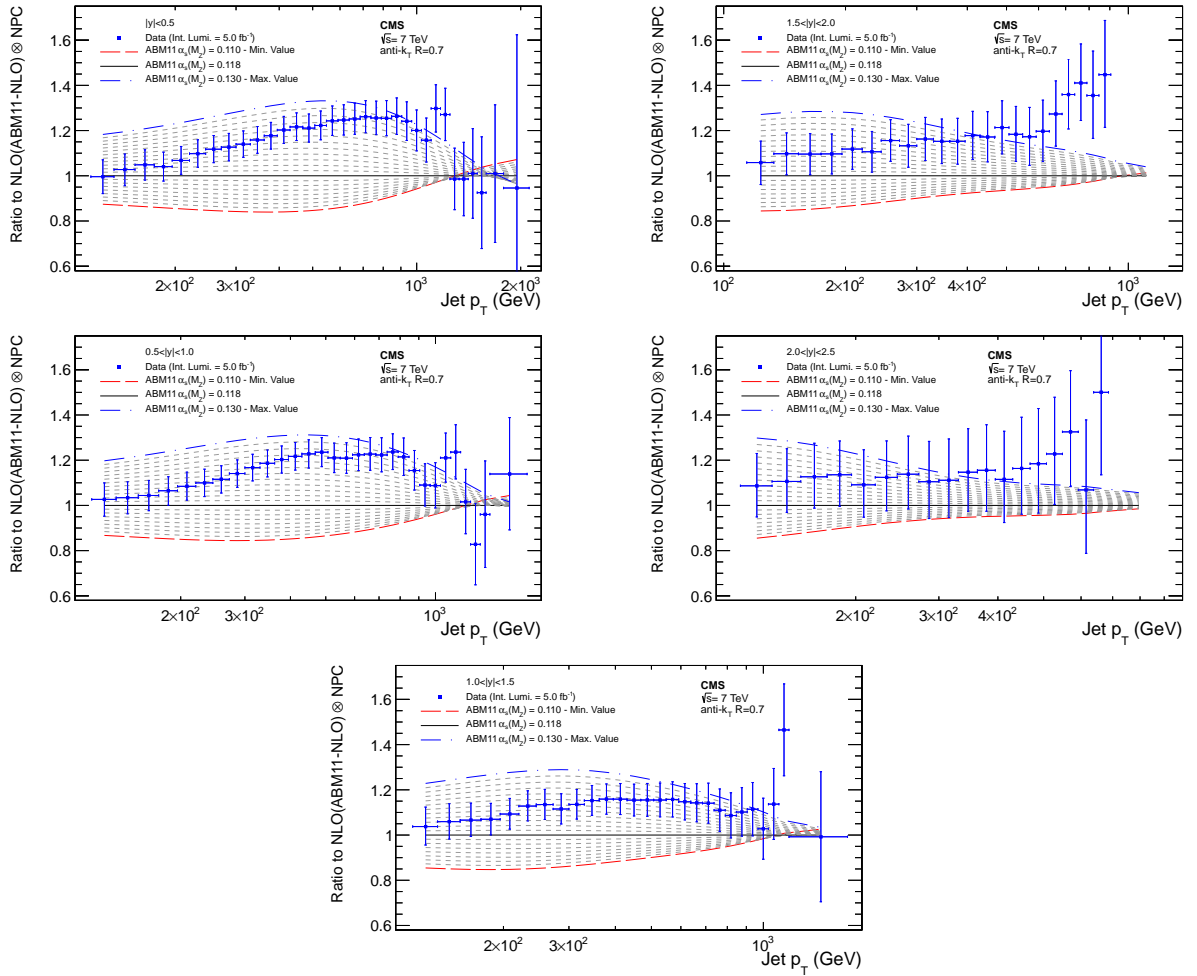
Figure 42: Ratio of the inclusive jet cross section to theory predictions using the **ABM11-NLO PDF** set for the five rapidity bins, where the $\alpha_S(M_Z)$ value is varied in the range 0.110-130 in steps of 0.001. The error bars correspond to the total uncertainty.
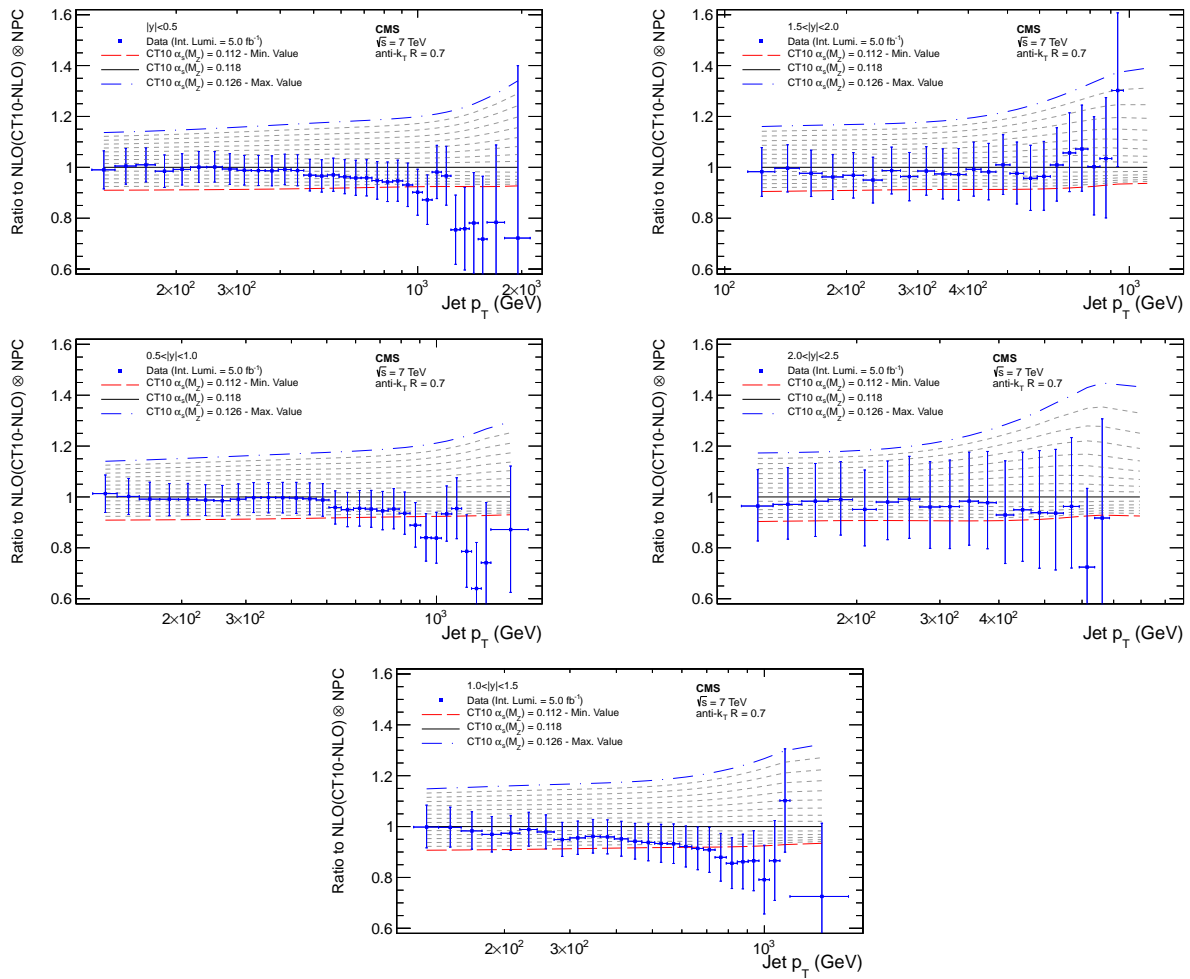
Figure 43: Ratio of the inclusive jet cross section to theory predictions using the **CT10-NLO PDF** set for the five rapidity bins, where the $\alpha_S(M_Z)$ value is varied in the range 0.112-0.126 in steps of 0.001. The error bars correspond to the total uncertainty.
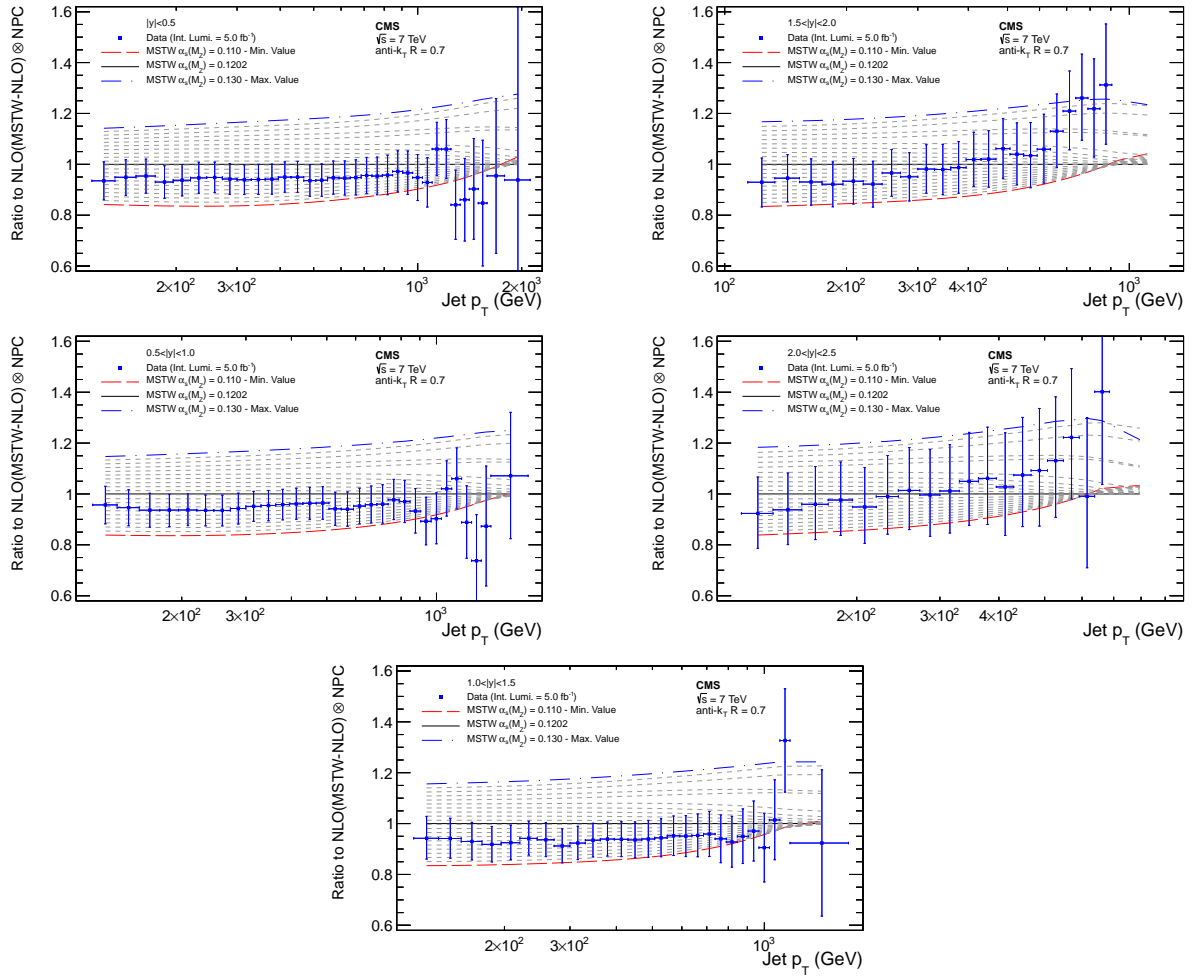
Figure 44: Ratio of the inclusive jet cross section to theory predictions using the **MSTW2008-NLO PDF** set for the five rapidity bins, where the $\alpha_S(M_Z)$ value is varied in the range 0.110-0.130 in steps of 0.001. The error bars correspond to the total uncertainty.
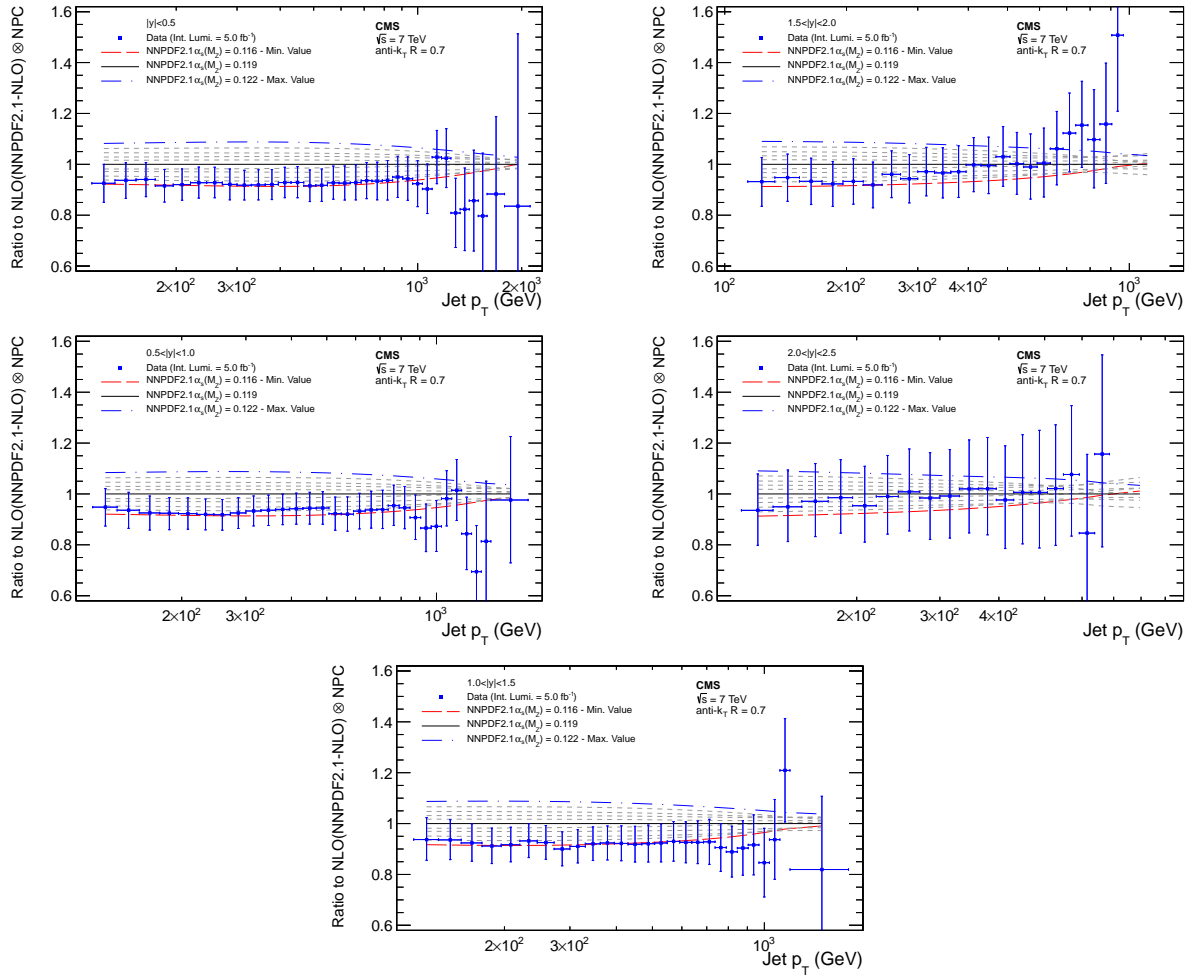
Figure 45: Ratio of the inclusive jet cross section to theory predictions using the **NNPDF2.1-NLO PDF** set for the five rapidity bins, where the $\alpha_S(M_Z)$ value is varied in the range 0.116-0.122 in steps of 0.001. The error bars correspond to the total uncertainty.
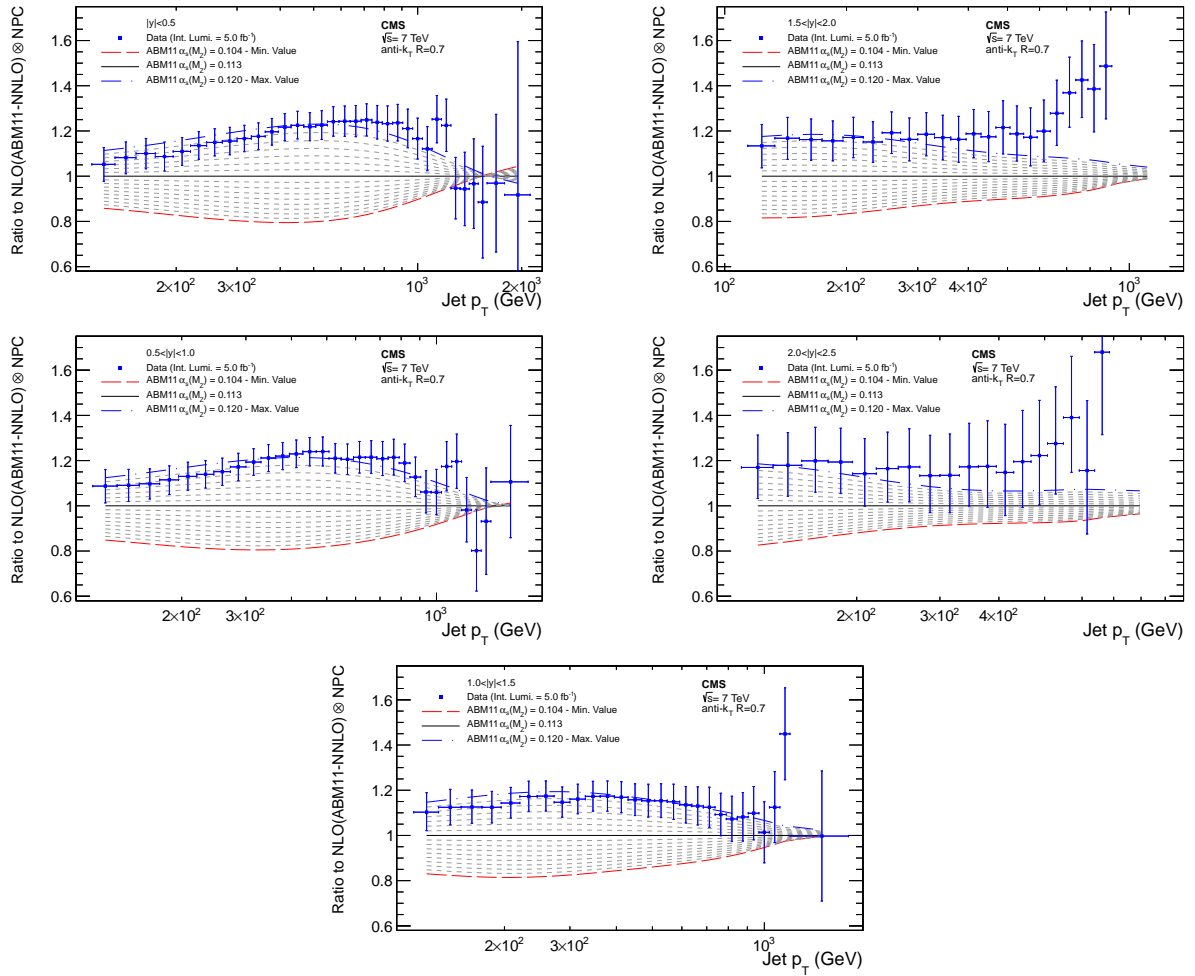
Figure 46: Ratio of the inclusive jet cross section to theory predictions using the **ABM11-NNLO PDF** set for the five rapidity bins, where the $\alpha_S(M_Z)$ value is varied in the range 0.104-120 in steps of 0.001. The error bars correspond to the total uncertainty.
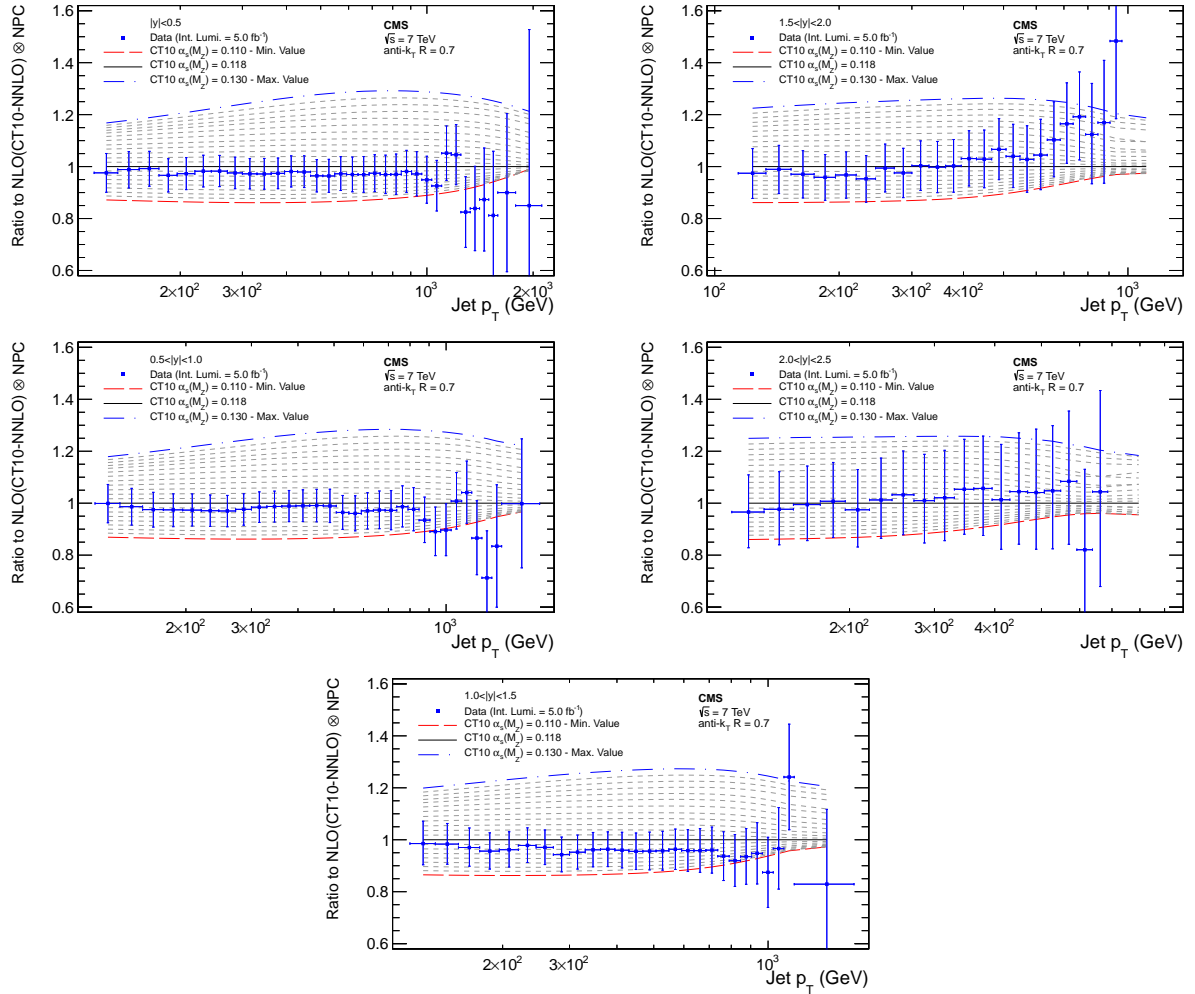
Figure 47: Ratio of the inclusive jet cross section to theory predictions using the **CT10-NNLO PDF** set for the five rapidity bins, where the $\alpha_S(M_Z)$ value is varied in the range 0.110-0.130 in steps of 0.001. The error bars correspond to the total uncertainty.
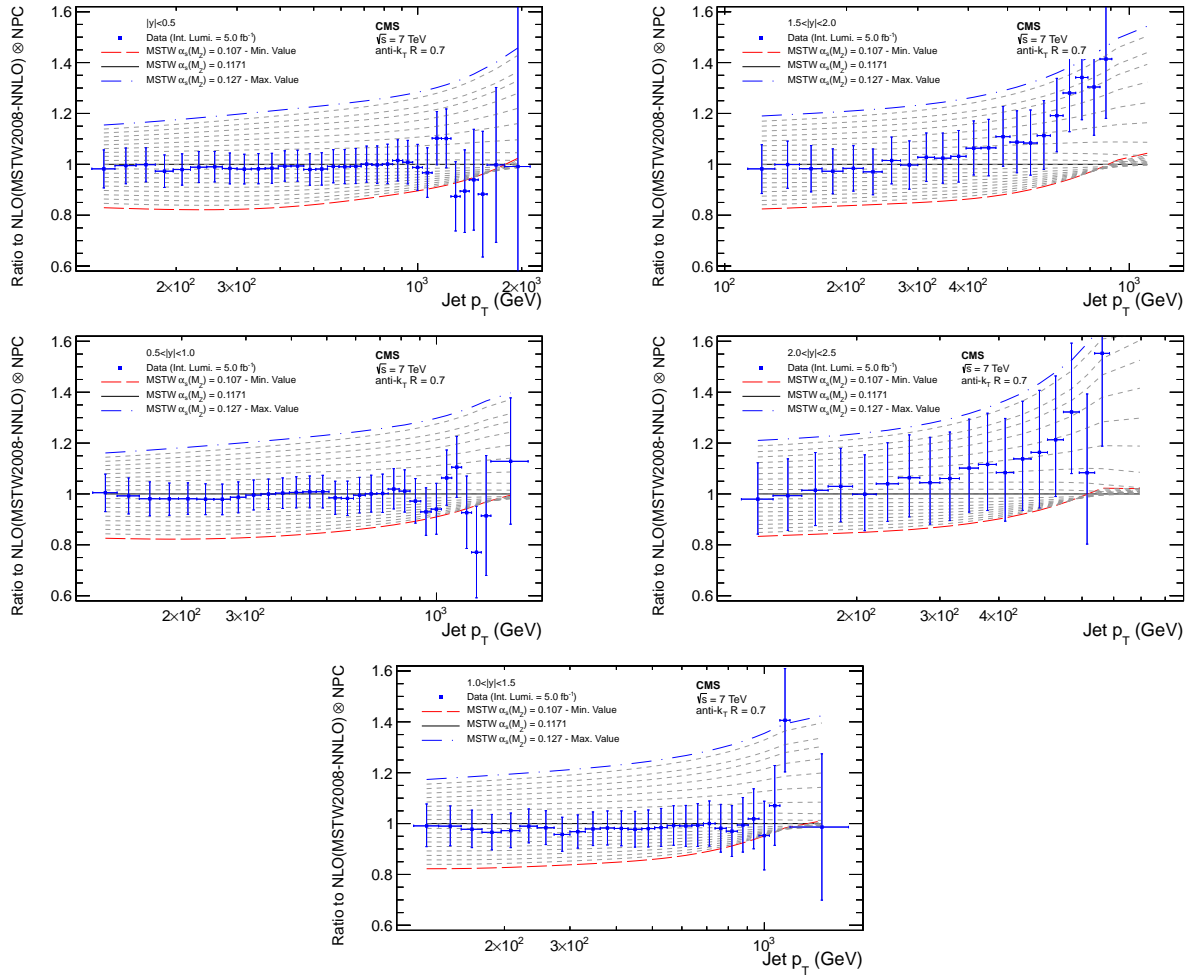
Figure 48: Ratio of the inclusive jet cross section to theory predictions using the **MSTW2008-NNLO PDF** set for the five rapidity bins, where the $\alpha_S(M_Z)$ value is varied in the range 0.107-0.127 in steps of 0.001. The error bars correspond to the total uncertainty.
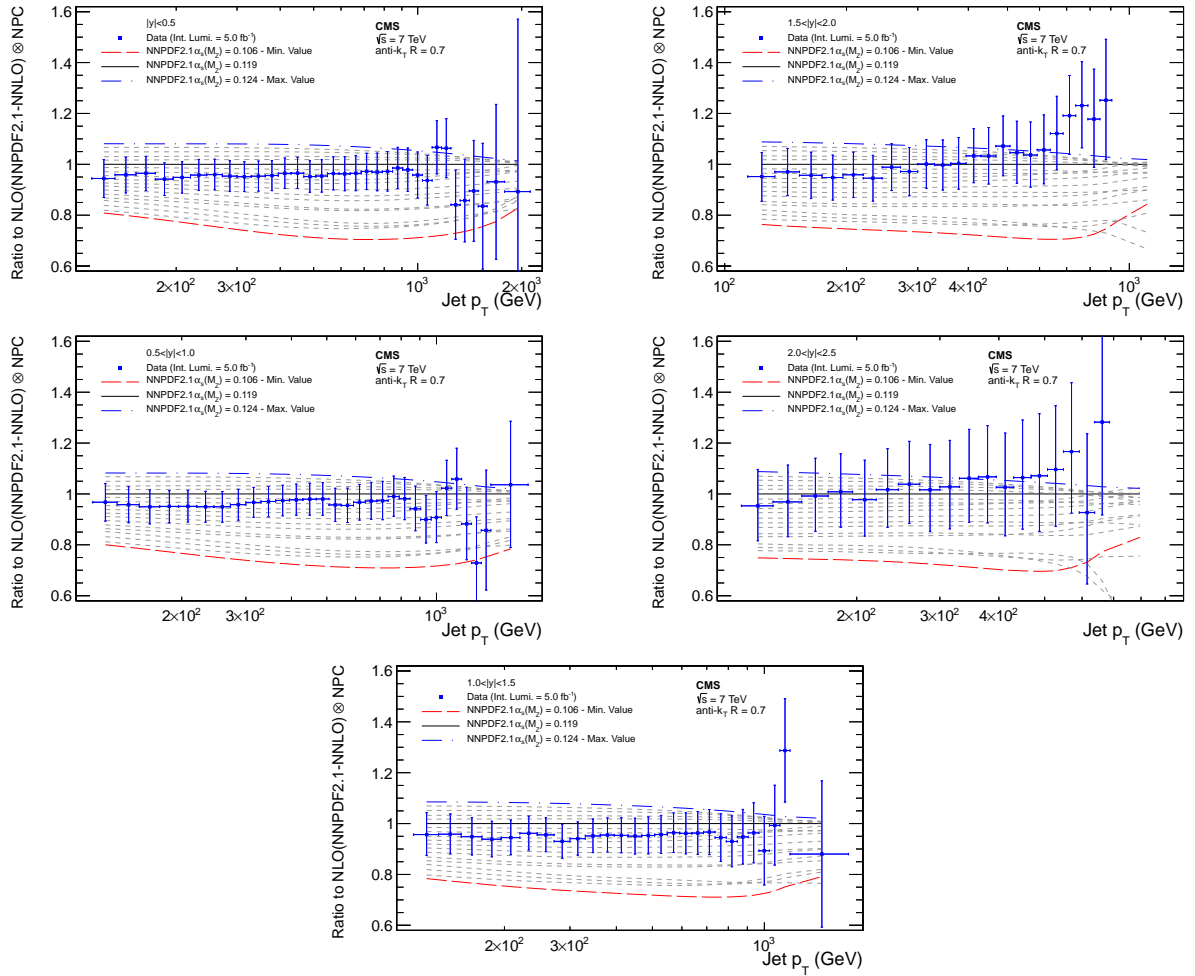
Figure 49: Ratio of the inclusive jet cross section to theory predictions using the **NNPDF2.1-NNLO PDF** set for the five rapidity bins, where the $\alpha_S(M_Z)$ value is varied in the range 0.106-0.124 in steps of 0.001. The error bars correspond to the total uncertainty.

6.1.4 The fitting procedure

The value of $\alpha_S(M_Z)$ is determined by minimizing the χ^2 between the experimental measurement and the theoretical predictions. The χ^2 is defined as

$$\chi^2 = M^T C^{-1} M, \tag{82}$$

where M is the vector of the differences between the data (D^i) and the theoretical values (T^i) in each bin i,

$$M^i = D^i - T^i, \tag{83}$$

and C is the covariance matrix including all uncertainties as described in Ref.[49]. C is defined as

$$C = \text{Cov}^{\text{Stat}} + \sum \text{Cov}^{\text{JES Sources}} + \text{Cov}^{\text{Unfolding}} + \text{Cov}^{\text{Lumi}} + \text{Cov}^{\text{Uncor}} + \text{Cov}^{\text{PDF}}, \tag{84}$$

where:

- Cov^{Stat} is the statistical covariance matrix taking into account the correlations due to unfolding.
- $\text{Cov}^{\text{JES Sources}}$,are the covariance matrices taking into account all Jet Energy Scale (JES) systematic uncertainty sources.
- $\text{Cov}^{\text{Unfolding}}$ is the covariance matrix taking into account the unfolding systematic uncertainty.
- Cov^{Lumi} is the covariance matrix taking into account the luminosity systematic uncertainty.
- $\text{Cov}^{\text{Uncor}}$ is the covariance matrix taking into account all uncorrelated systematic uncertainties such as small trigger and identification inefficiencies, time dependence of the jet p_T resolution and uncertainty on the trigger prescale factor.
- Cov^{PDF} is the covariance matrix taking into account the PDF uncertainties.

All JES sources, the unfolding, and luminosity systematic uncertainties are treated as 100% correlated across the p_T and $|y|$ bins with the exception of one JES source (Single Pion) were the correlation across the $|y|$ bins is treated as:

- 50% correlation in barrel ($|y| < 1.5$)
- 100% correlation in endcap ($1.5 < |y| < 2.5$)
- 0% correlation between barrel and endcap

The JES, unfolding, and luminosity uncertainties are treated as multiplicative to avoid the statistical bias that arises when estimating uncertainties from data[50]. Multiplicative treatment means for each $\alpha_S(M_Z)$ the covariance matrix is calculated using the theoretical spectrum.

The uncertainty on $\alpha_S(M_Z)$ due to the NP uncertainties is evaluated applying the offset method. The theory is varied by the NP uncertainty as $T_{xs} \cdot NP \rightarrow T_{xs} \cdot (NP_{cor} \pm NP_{err})$,the fitting procedure is repeated for these variations and the deviation from the central $\alpha_S(M_Z)$ values is considered as the uncertainty.

The treatment of PDF uncertainties depends on the prescription given by each PDF set. A more detailed description is given in subsection 4.9.3

The uncertainty due to the renormalization and factorization scales is evaluated by applying the offset method, where μ_r and μ_f are varied from the default choice of $\mu_r = \mu_f = p_T$ between $p_T/2$ and $2p_T$ in the following six combinations: $(\mu_r/p_T, \mu_f/p_T) = (1/2, 1/2)$, $(1/2, 1)$, $(1, 1/2)$, $(1, 2)$, $(2, 1)$, and $(2, 2)$. The χ^2 minimization with respect to $\alpha_S(M_Z)$ is repeated for these six combinations. The contribution from the μ_r, μ_f scale variations to the uncertainty is evaluated by considering the maximal upwards and downwards deviation of all six scale combinations from the central result.

6.1.4.1   Fit results for $\alpha_S(M_Z)$ with the CT10-NLO and NNLO PDF sets.

Figure 50 shows the χ^2 minimization with respect to $\alpha_S(M_Z)$ using the CT10-NLO PDF using data from all rapidity bins. Figure 51 shows the χ^2 minimization by varying the scale between $p_T/2$ and $2p_T$ in six combinations. The experimental uncertainties are obtained from the $\alpha_S(M_Z)$ values for which the χ^2 is increased by 1 with respect to the minimum value. Figures 52 and 53 shows the same results using the CT10-NNLO PDF set. In appendix B the results for each rapidity bin are presented.

Table 7 and 8 present the determinations of $\alpha_S(M_Z)$ in bins of rapidity using the CT10-NLO and CT10-NNLO PDF set respectively. In the last row of the table the result of a simultaneous fit of all rapidity bins is shown. In the table the experimental, PDF, NP, and scale uncertainties are also presented separately. The individual contributions of the first three uncertainty sources is evaluated by removing each time one of the uncertainty sources, appearing in Eq. (87), and repeating the χ^2 minimization procedure.

For the two outer rapidity bins ($2.0 < |y| < 2.5$ and $|y| < 2.5$) the CT10-NLO PDF sets for various α_S are not enough to give a full χ^2 parabola. For these cases the HOPPET code used in order to calculate cross sections for lower α_S. This procedure adds an extra uncertainty in the evaluation of $\alpha_S(M_Z)$ noted as "extr" in Table 7. This uncertainty is negligible compared to the experimental one. The description at this procedure can be found in Appendix A.
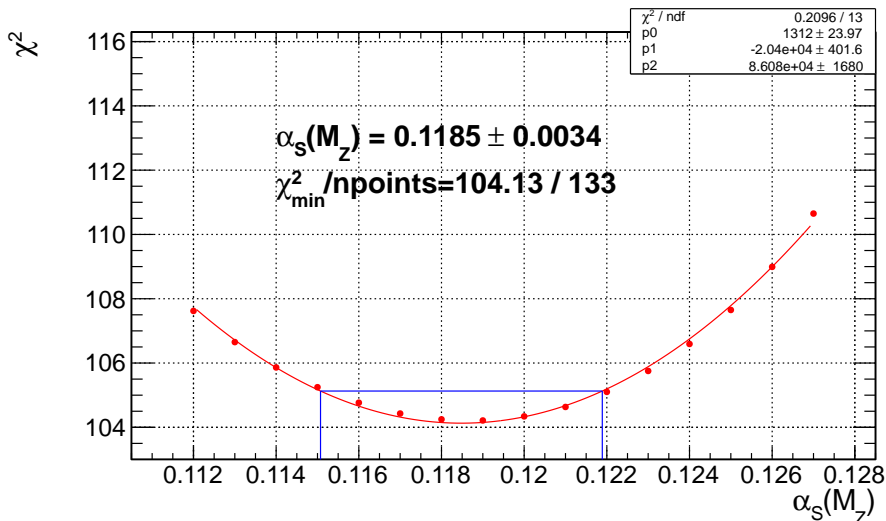
Figure 50: **ALL rapidity bins** $|\mathbf{y}| < \mathbf{2.5}$. The χ^2 minimization with respect to $\alpha_S(M_Z)$ using the **CT10-NLO PDF** set is presented. The experimental uncertainties are obtained from the $\alpha_S(M_Z)$ values for which χ^2 is increased by 1 with respect to the minimum value.
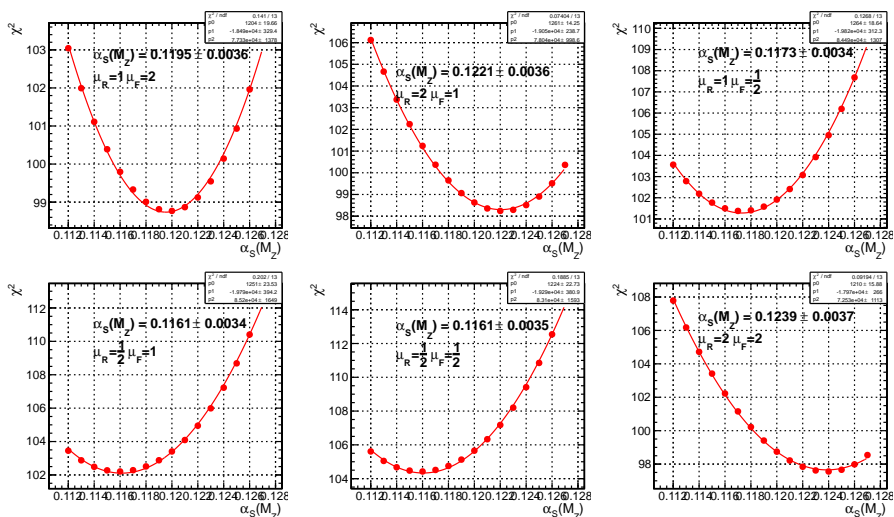
Figure 51: **ALL rapidity bins** $|\mathbf{y}| < \mathbf{2.5}$. The χ^2 minimization by varying the scale between $p_T/2$ and $2p_T$ in six combinations is presented.
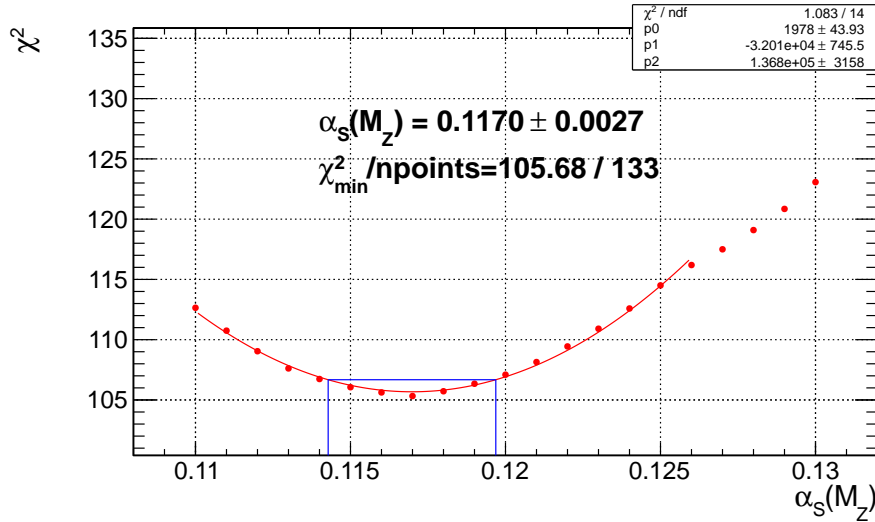
Figure 52: **ALL rapidity bins |y| < 2.5**. The χ^2 minimization with respect to $\alpha_S(M_Z)$ using the **CT10-NNLO PDF** set is presented. The experimental uncertainties are obtained from the $\alpha_S(M_Z)$ values for which χ^2 is increased by 1 with respect to the minimum value.
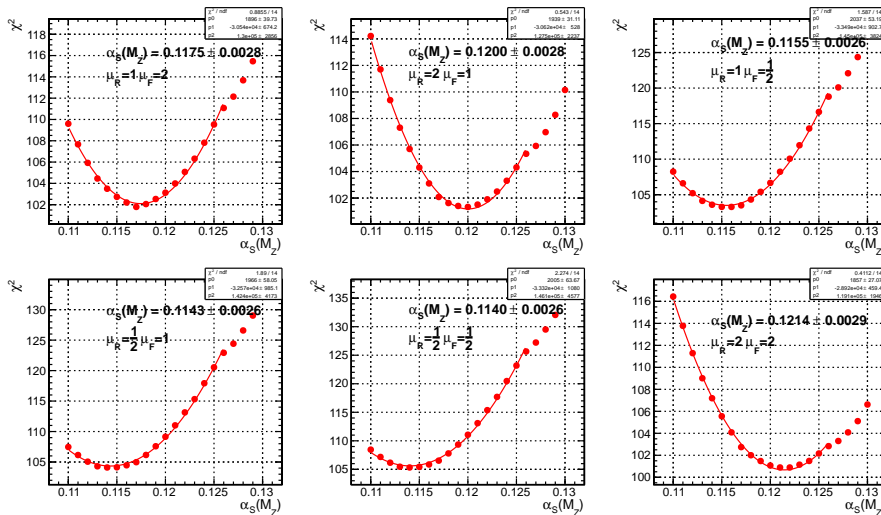
Figure 53: **ALL rapidity bins |y| < 2.5**. The χ^2 minimization by varying the scale between $p_T/2$ and $2p_T$ in six combinations is presented.

Table 7: Determination of $\alpha_S(M_Z)$ in bins of rapidity using the **CT10-NLO** PDF set. The last row presents the result of a simultaneous fit in all rapidity bins.

$|y|$ range	No. of data points	$\alpha_S(M_Z)$	χ^2/n_{dof}
$|y| < 0.5$	33	$0.1189 \pm 0.0024(\text{exp}) \pm 0.0030(\text{PDF})$ $\pm 0.0008(\text{NP})^{+0.0045}_{-0.0027}(\text{scale})$	16.2/32
$0.5 < |y| < 1.0$	30	$0.1182 \pm 0.0024(\text{exp}) \pm 0.0029(\text{PDF})$ $\pm 0.0008(\text{NP})^{+0.0050}_{-0.0025}(\text{scale})$	25.1/29
$1.0 < |y| < 1.5$	27	$0.1165 \pm 0.0027(\text{exp}) \pm 0.0024(\text{PDF})$ $\pm 0.0008(\text{NP})^{+0.0043}_{-0.0020}(\text{scale})$	9.6/26
$1.5 < |y| < 2.0$	24	$0.1146 \pm 0.0035(\text{exp}) \pm 0.0031(\text{PDF})$ $\pm 0.0013(\text{NP}) \pm 0.0004(\text{extr})^{+0.0037}_{-0.0020}(\text{scale})$	20.2/23
$2.0 < |y| < 2.5$	19	$0.1161 \pm 0.0045(\text{exp}) \pm 0.0054(\text{PDF})$ $\pm 0.0015(\text{NP}) \pm 0.0003(\text{extr})^{+0.0034}_{-0.0032}(\text{scale})$	12.6/18
$|y| < 2.5$	133	$0.1185 \pm 0.0019(\text{exp}) \pm 0.0028(\text{PDF})$ $\pm 0.0004(\text{NP})^{+0.0053}_{-0.0024}(\text{scale})$	104.1/132

Table 8: Determination of $\alpha_S(M_Z)$ in bins of rapidity using the **CT10-NNLO** PDF set. The last row presents the result of a simultaneous fit in all rapidity bins.

$|y|$ range	No. of data points	$\alpha_S(M_Z)$	χ^2/n_{dof}
$|y| < 0.5$	33	$0.1180 \pm 0.0017(\text{exp}) \pm 0.0027(\text{PDF})$ $\pm 0.0006(\text{NP})^{+0.0031}_{-0.0026}(\text{scale})$	15.4/32
$0.5 < |y| < 1.0$	30	$0.1176 \pm 0.0016(\text{exp}) \pm 0.0026(\text{PDF})$ $\pm 0.0006(\text{NP})^{+0.0033}_{-0.0023}(\text{scale})$	23.9/29
$1.0 < |y| < 1.5$	27	$0.1169 \pm 0.0019(\text{exp}) \pm 0.0024(\text{PDF})$ $\pm 0.0006(\text{NP})^{+0.0033}_{-0.0019}(\text{scale})$	10.5/26
$1.5 < |y| < 2.0$	24	$0.1133 \pm 0.0023(\text{exp}) \pm 0.0028(\text{PDF})$ $\pm 0.0010(\text{NP})^{+0.0039}_{-0.0029}(\text{scale})$	22.3/23
$2.0 < |y| < 2.5$	19	$0.1172 \pm 0.0044(\text{exp}) \pm 0.0039(\text{PDF})$ $\pm 0.0015(\text{NP})^{+0.0049}_{-0.0060}(\text{scale})$	13.8/18
$|y| < 2.5$	133	$0.1170 \pm 0.0012(\text{exp}) \pm 0.0024(\text{PDF})$ $\pm 0.0004(\text{NP})^{+0.0044}_{-0.0030}(\text{scale})$	105.7/132

6.1.4.2   Fit results for $\alpha_S(M_Z)$ with the MSTW2008-NLO and NNLO PDF sets.

Figure 54 presents the χ^2 minimization with respect to $\alpha_S(M_Z)$ using the MSTW2008-NLO PDF set. The results are presented for each rapidity bin separately and for a simultaneously fit on all rapidity bins (last plot on the right in the bottom).

Table 9 presents the determinations of $\alpha_S(M_Z)$ in bins of rapidity using the MSTW2008-NLO PDF set. In the last row of the table the result of a simultaneous fit of all rapidity bins is shown. The results using the MSTW2008-NNLO PDF set are presented in Table 10 and in Fig. 102.

Within uncertainties all results employing MSTW2008 PDF sets are compatible with the CT10 fits in the previous section. From Fig. 101 clear minima of the χ^2 parabola can be seen except for the rapidity bin $1.5 < |y| < 2.0$ where a minimum is derived from a polynomial extrapolation. The MSTW2008-NLO PDF set therefore was not selected for the central result. Also from Fig. 102 the appearance of a "second" minimum can be noted for the two bins at higher rapidity and in the simultaneous fit of all rapidity bins.

Figure 54: The χ^2 minimization with respect to $\alpha_S(M_Z)$ using the **MSTW2008-NLO PDF** set. The experimental uncertainties are obtained from the $\alpha_S(M_Z)$ values for which χ^2 is increased by 1 with respect to the minimum value. Top left: rapidity $|y| < 0.5$. Top right: rapidity $0.5 < |y| < 1.0$. Middle left: rapidity $1.0 < |y| < 1.5$. Middle right: rapidity $1.5 < |y| < 2.0$. Bottom left: rapidity $2.0 < |y| < 2.5$. Bottom right: all rapidity bins $|y| < 2.5$.
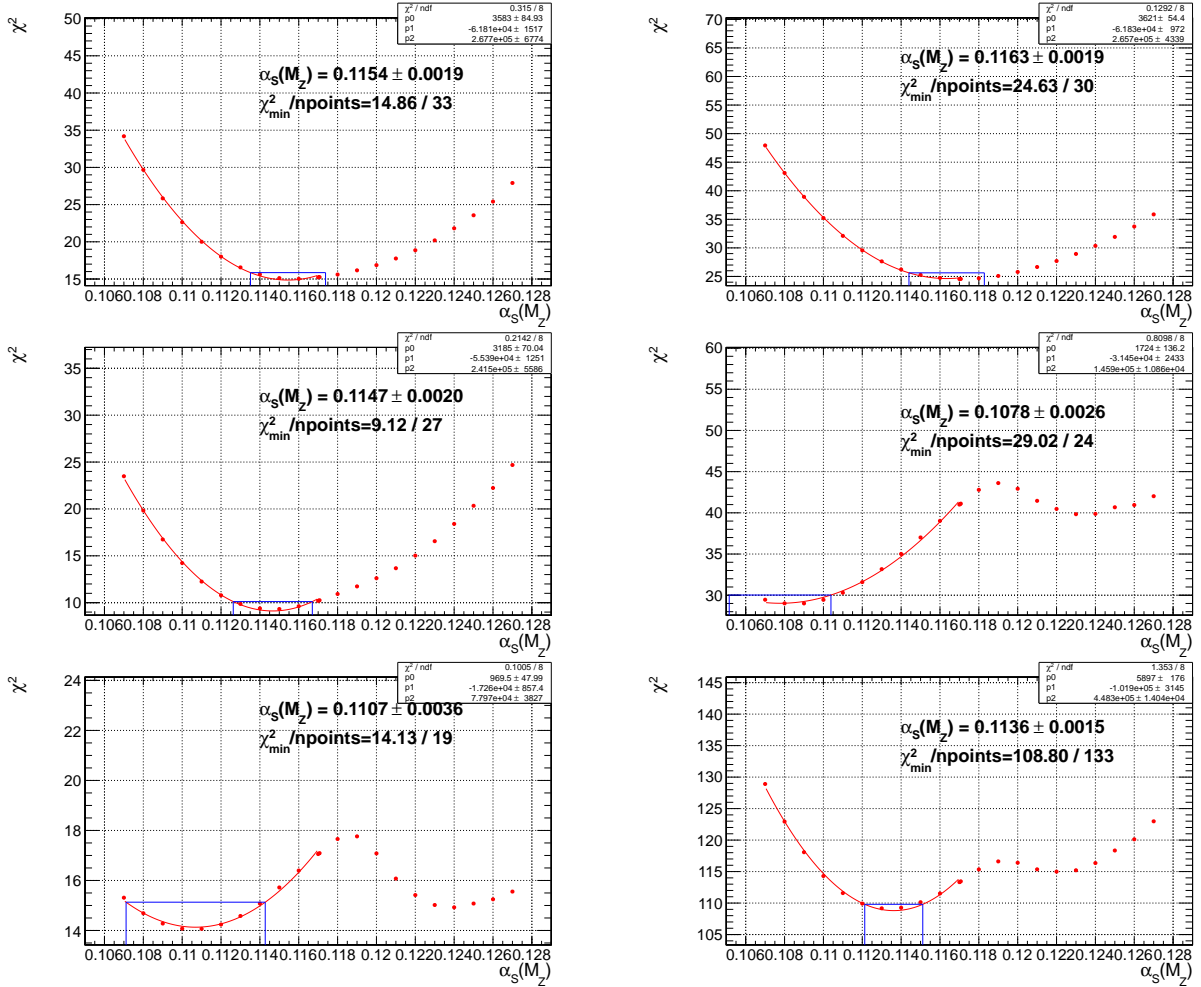
Figure 55: The χ^2 minimization with respect to $\alpha_S(M_Z)$ using the **MSTW2008-NNLO PDF** set. The experimental uncertainties are obtained from the $\alpha_S(M_Z)$ values for which χ^2 is increased by 1 with respect to the minimum value. Top left: rapidity $|y| < 0.5$. Top right: rapidity $0.5 < |y| < 1.0$. Middle left: rapidity $1.0 < |y| < 1.5$. Middle right: rapidity $1.5 < |y| < 2.0$. Bottom left: rapidity $2.0 < |y| < 2.5$. Bottom right: all rapidity bins $|y| < 2.5$.

Table 9: Determination of $\alpha_S(M_Z)$ in bins of rapidity using the **MSTW2008-NLO** PDF set. The last row presents the result of a simultaneous fit in all rapidity bins.

$\lvert y\rvert$ range	No. of points	$\alpha_S(M_Z)$	χ^2/n_{dof}
$\lvert y\rvert < 0.5$	33	$0.1173 \pm 0.0016(\mathrm{exp}) \pm 0.0016(\mathrm{PDF})$ $\pm 0.0001(\mathrm{NP})^{+0.0007}_{-0.0038}(\mathrm{scale})$	15.1/32
$0.5 < \lvert y\rvert < 1.0$	30	$0.1184 \pm 0.0017(\mathrm{exp}) \pm 0.0015(\mathrm{PDF})$ $\pm 0.0002(\mathrm{NP})^{+0.00017}_{-0.0028}(\mathrm{scale})$	23.9/29
$1.0 < \lvert y\rvert < 1.5$	27	$0.1161 \pm 0.0021(\mathrm{exp}) \pm 0.0014(\mathrm{PDF})$ $\pm 0.0003(\mathrm{NP})^{+0.0030}_{-0.0024}(\mathrm{scale})$	10.8/26
$1.5 < \lvert y\rvert < 2.0$	24	$0.1086 \pm 0.0029(\mathrm{exp}) \pm 0.0012(\mathrm{PDF})$ $\pm 0.0009(\mathrm{NP})^{+0.0045}_{-0.0037}(\mathrm{scale})$	26.8/23
$2.0 < \lvert y\rvert < 2.5$	19	$0.1128 \pm 0.0042(\mathrm{exp}) \pm 0.0012(\mathrm{PDF})$ $\pm 0.0012(\mathrm{NP})^{+0.0044}_{-0.0064}(\mathrm{scale})$	13.7/18
$\lvert y\rvert < 2.5$	133	$0.1159 \pm 0.0012(\mathrm{exp}) \pm 0.0014(\mathrm{PDF})$ $\pm 0.0001(\mathrm{NP})^{+0.0024}_{-0.0030}(\mathrm{scale})$	107.9/132

Table 10: Determination of $\alpha_S(M_Z)$ in bins of rapidity using the **MSTW2008-NNLO** PDF set. The last row presents the result of a simultaneous fit in all rapidity bins.

$\lvert y\rvert$ range	No. of points	$\alpha_S(M_Z)$	χ^2/n_{dof}
$\lvert y\rvert < 0.5$	33	$0.1154 \pm 0.0013(\mathrm{exp}) \pm 0.0014(\mathrm{PDF})$ $\pm 0.0001(\mathrm{NP})^{+0.0009}_{-0.0024}(\mathrm{scale})$	14.8/32
$0.5 < \lvert y\rvert < 1.0$	30	$0.1163 \pm 0.0014(\mathrm{exp}) \pm 0.0014(\mathrm{PDF})$ $\pm 0.0001(\mathrm{NP})^{+0.0015}_{-0.0019}(\mathrm{scale})$	24.6/29
$1.0 < \lvert y\rvert < 1.5$	27	$0.1147 \pm 0.0017(\mathrm{exp}) \pm 0.0011(\mathrm{PDF})$ $\pm 0.0002(\mathrm{NP})^{+0.0021}_{-0.0018}(\mathrm{scale})$	9.1/26
$1.5 < \lvert y\rvert < 2.0$	24	$0.1078 \pm 0.0020(\mathrm{exp}) \pm 0.0017(\mathrm{PDF})$ $\pm 0.0006(\mathrm{NP})^{+0.0034}_{-0.0033}(\mathrm{scale})$	29.0/23
$2.0 < \lvert y\rvert < 2.5$	19	$0.1107 \pm 0.0031(\mathrm{exp}) \pm 0.0017(\mathrm{PDF})$ $\pm 0.0008(\mathrm{NP})^{+0.0032}_{-0.0049}(\mathrm{scale})$	14.1/18
$\lvert y\rvert < 2.5$	133	$0.1136 \pm 0.0010(\mathrm{exp}) \pm 0.0011(\mathrm{PDF})$ $\pm 0.0001(\mathrm{NP})^{+0.0019}_{-0.0024}(\mathrm{scale})$	108.8/132

6.1.4.3   Fit results for $\alpha_S(M_Z)$ with the NNPDF2.1-NLO and NNLO PDF sets.

Figure 56 presents the χ^2 minimization with respect to $\alpha_S(M_Z)$ using the NNPDF2.1-NLO PDF set. The results are presented for each rapidity bin separately and for a simultaneously fit on all rapidity bins (last plot on the right in the bottom).

Table 11 presents the determinations of $\alpha_S(M_Z)$ in bins of rapidity using the NNPDF2.1-NLO PDF set. In the last row of the table the result of a simultaneous fit in all rapidity bins is shown. The results using the NNPDF2.1-NNLO PDF set are presented in Table 12 and in figure 57.

Results employing NNPDF2.1 PDF sets are compatible with the previous fits using CT10 or MSTW2008. From Fig. 56 it can be concluded though that the limited lower $\alpha_S(M_Z)$ variations of this PDF set do not allow to clearly identify the minima of the χ^2 parabola, such that again an extrapolation is necessary. This is not the case for the NNPDF2.1 set at NNLO evolution.

As an additional cross check Table 13 and Table 14 report the results using both NNPDF2.1 PDF sets in combination with NLO perturbative coefficients with six active flavours, i.e. $N_f = 6$. The fit results for $\alpha_S(M_Z)$ derived with $N_f = 6$ are ~1% higher than for $N_f = 5$, but are well covered by the NLO scale uncertainties.

Figure 56: The χ^2 minimization with respect to $\alpha_S(M_Z)$ using the **NNPDF2.1-NLO PDF** set. The experimental uncertainties are obtained from the $\alpha_S(M_Z)$ values for which χ^2 is increased by 1 with respect to the minimum value. Top left: rapidity $|y| < 0.5$. Top right: rapidity $0.5 < |y| < 1.0$. Middle left: rapidity $1.0 < |y| < 1.5$. Middle right: rapidity $1.5 < |y| < 2.0$. Bottom left: rapidity $2.0 < |y| < 2.5$. Bottom right: all rapidity bins $|y| < 2.5$.
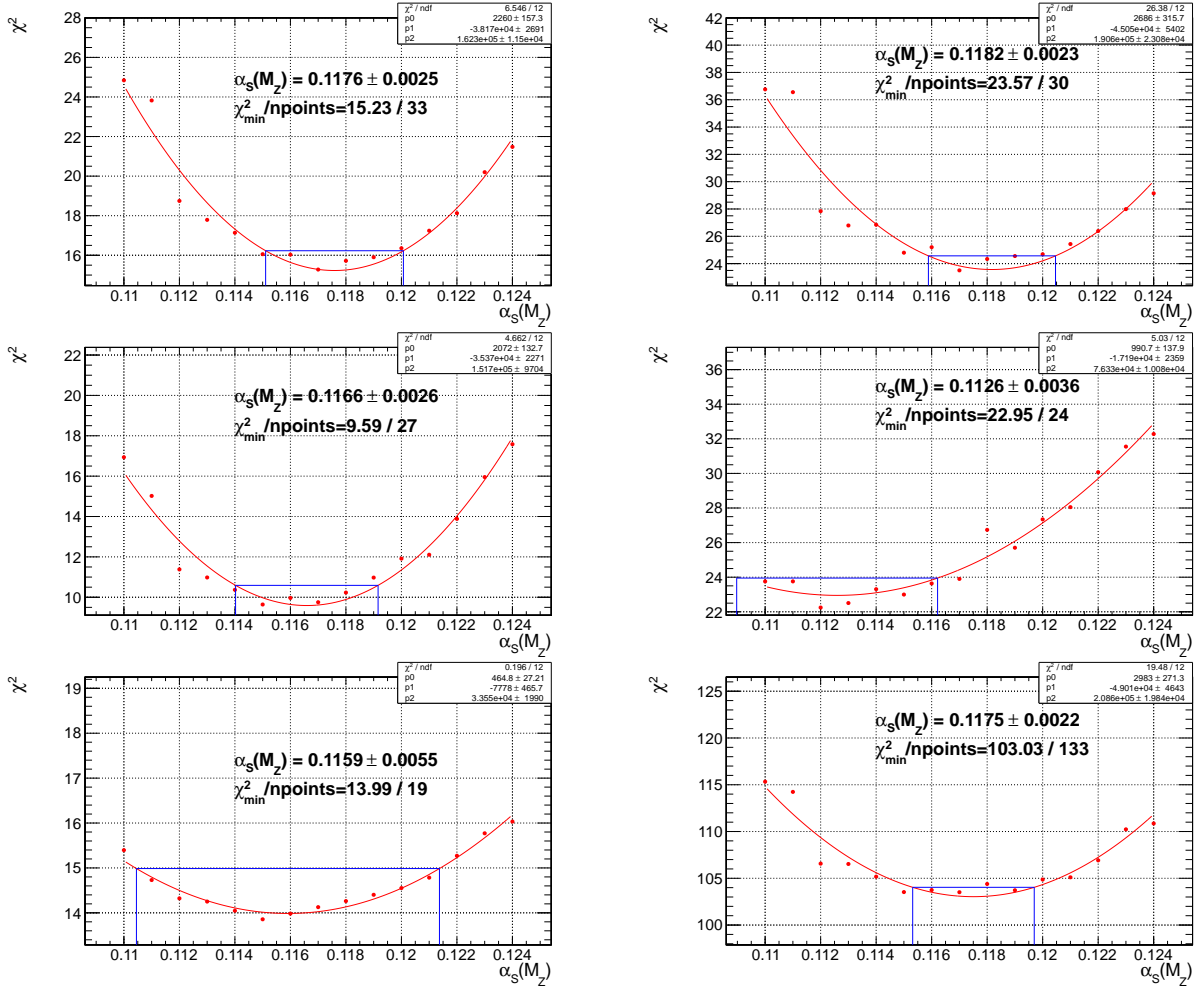
Figure 57: The χ^2 minimization with respect to $\alpha_S(M_Z)$ using the **NNPDF2.1-NNLO PDF** set. The experimental uncertainties are obtained from the $\alpha_S(M_Z)$ values for which χ^2 is increased by 1 with respect to the minimum value. Top left: rapidity $|y| < 0.5$. Top right: rapidity $0.5 < |y| < 1.0$. Middle left: rapidity $1.0 < |y| < 1.5$. Middle right: rapidity $1.5 < |y| < 2.0$. Bottom left: rapidity $2.0 < |y| < 2.5$. Bottom right: all rapidity bins $|y| < 2.5$.

Table 11: Determination of $\alpha_S(M_Z)$ in bins of rapidity using the **NNPDF2.1-NLO** PDF set. The last row presents the result of a simultaneous fit in all rapidity bins.

$|y|$ range	No. of points	$\alpha_S(M_Z)$	χ^2/n_{dof}
$|y| < 0.5$	33	$0.1153 \pm 0.0019(\text{exp}) \pm 0.0024(\text{PDF})$ $\pm 0.0007(\text{NP})^{+0.0017}_{-0.0025}(\text{scale})$	16.1/32
$0.5 < |y| < 1.0$	30	$0.1158 \pm 0.0017(\text{exp}) \pm 0.0023(\text{PDF})$ $\pm 0.0005(\text{NP})^{+0.0022}_{-0.0018}(\text{scale})$	25.0/29
$1.0 < |y| < 1.5$	27	$0.1135 \pm 0.0023(\text{exp}) \pm 0.0024(\text{PDF})$ $\pm 0.0006(\text{NP})^{+0.0035}_{-0.0018}(\text{scale})$	10.8/26
$1.5 < |y| < 2.0$	24	$0.1108 \pm 0.0039(\text{exp}) \pm 0.0021(\text{PDF})$ $\pm 0.0009(\text{NP})^{+0.0050}_{-0.0036}(\text{scale})$	22.5/23
$2.0 < |y| < 2.5$	19	$0.1152 \pm 0.0049(\text{exp}) \pm 0.0043(\text{PDF})$ $\pm 0.0025(\text{NP})^{+0.0040}_{-0.0052}(\text{scale})$	14.0/18
$|y| < 2.5$	133	$0.1150 \pm 0.0014(\text{exp}) \pm 0.0025(\text{PDF})$ $\pm 0.0003(\text{NP})^{+0.0028}_{-0.0026}(\text{scale})$	103.5/132

Table 12: Determination of $\alpha_S(M_Z)$ in bins of rapidity using the **NNPDF NNLO** PDF set. The last row presents the result of a simultaneous fit in all rapidity bins.

| $|y|$ range	No. of points	$\alpha_S(M_Z)$	χ^2/n_{dof}
$|y| < 0.5$	33	$0.1173 \pm 0.0016(\text{exp}) \pm 0.0019(\text{PDF})$ $\pm 0.0001(\text{NP})^{+0.0014}_{-0.0020}(\text{scale})$	15.2/32
$0.5 < |y| < 1.0$	30	$0.1180 \pm 0.0015(\text{exp}) \pm 0.0017(\text{PDF})$ $\pm 0.0002(\text{NP})^{+0.0015}_{-0.0015}(\text{scale})$	23.6/29
$1.0 < |y| < 1.5$	27	$0.1165 \pm 0.0020(\text{exp}) \pm 0.0016(\text{PDF})$ $\pm 0.0001(\text{NP})^{+0.0025}_{-0.0016}(\text{scale})$	9.7/26
$1.5 < |y| < 2.0$	24	$0.1133 \pm 0.0026(\text{exp}) \pm 0.0022(\text{PDF})$ $\pm 0.0005(\text{NP})^{+0.0027}_{-0.0020}(\text{scale})$	22.4/23
$2.0 < |y| < 2.5$	19	$0.1159 \pm 0.0045(\text{exp}) \pm 0.0031(\text{PDF})$ $\pm 0.0012(\text{NP})^{+0.0031}_{-0.0040}(\text{scale})$	14.0/18
$|y| < 2.5$	133	$0.1175 \pm 0.0012(\text{exp}) \pm 0.0018(\text{PDF})$ $\pm 0.0001(\text{NP})^{+0.0020}_{-0.0018}(\text{scale})$	103.0/132

Table 13: Determination of $\alpha_S(M_Z)$ in bins of rapidity using the **NNPDF2.1-NLO** PDF set in combination with perturbative coefficients for $N_f = 6$. The last row presents the result of a simultaneous fit in all rapidity bins.

$|y|$ range	No. of points	$\alpha_S(M_Z)$	χ^2/n_{dof}
$|y| < 0.5$	33	$0.1164 \pm 0.0018(\text{exp}) \pm 0.0024(\text{PDF})$ $\pm 0.0006(\text{NP})^{+0.0014}_{-0.0028}(\text{scale})$	15.9/32
$0.5 < |y| < 1.0$	30	$0.1168 \pm 0.0017(\text{exp}) \pm 0.0023(\text{PDF})$ $\pm 0.0005(\text{NP})^{+0.0019}_{-0.0021}(\text{scale})$	24.5/29
$1.0 < |y| < 1.5$	27	$0.1146 \pm 0.0023(\text{exp}) \pm 0.0024(\text{PDF})$ $\pm 0.0005(\text{NP})^{+0.0033}_{-0.0023}(\text{scale})$	11.1/26
$1.5 < |y| < 2.0$	24	$0.1120 \pm 0.0037(\text{exp}) \pm 0.0021(\text{PDF})$ $\pm 0.0009(\text{NP})^{+0.0043}_{-0.0034}(\text{scale})$	22.6/23
$2.0 < |y| < 2.5$	19	$0.1165 \pm 0.0047(\text{exp}) \pm 0.0042(\text{PDF})$ $\pm 0.0023(\text{NP})^{+0.0035}_{-0.0050}(\text{scale})$	12.2/18
$|y| < 2.5$	133	$0.1158 \pm 0.0014(\text{exp}) \pm 0.0025(\text{PDF})$ $\pm 0.0002(\text{NP})^{+0.0025}_{-0.0027}(\text{scale})$	102.6/132

Table 14: Determination of $\alpha_S(M_Z)$ in bins of rapidity using the **NNPDF NNLO** PDF set in combination with perturbative coefficients for $N_f = 6$. The last row presents the result of a simultaneous fit in all rapidity bins.

$|y|$ range	No. of points	$\alpha_S(M_Z)$	χ^2/n_{dof}
$|y| < 0.5$	33	$0.1181 \pm 0.0016(\text{exp}) \pm 0.0019(\text{PDF})$ $\pm 0.0001(\text{NP})^{+0.0011}_{-0.0025}(\text{scale})$	14.9/32
$0.5 < |y| < 1.0$	30	$0.1187 \pm 0.0015(\text{exp}) \pm 0.0017(\text{PDF})$ $\pm 0.0002(\text{NP})^{+0.0013}_{-0.0018}(\text{scale})$	23.1/29
$1.0 < |y| < 1.5$	27	$0.1171 \pm 0.0020(\text{exp}) \pm 0.0015(\text{PDF})$ $\pm 0.0001(\text{NP})^{+0.0024}_{-0.0019}(\text{scale})$	9.6/26
$1.5 < |y| < 2.0$	24	$0.1142 \pm 0.0026(\text{exp}) \pm 0.0020(\text{PDF})$ $\pm 0.0005(\text{NP})^{+0.0026}_{-0.0021}(\text{scale})$	23.0/23
$2.0 < |y| < 2.5$	19	$0.1168 \pm 0.0044(\text{exp}) \pm 0.0030(\text{PDF})$ $\pm 0.0012(\text{NP})^{+0.0029}_{-0.0037}(\text{scale})$	12.2/18
$|y| < 2.5$	133	$0.1181 \pm 0.0012(\text{exp}) \pm 0.0018(\text{PDF})$ $\pm 0.0001(\text{NP})^{+0.0017}_{-0.0022}(\text{scale})$	101.9/132

6.1.4.4   Comparison of the $\alpha_S(M_Z)$ fit results with the CT10, MSTW2008, and NNPDF2.1 PDF sets.

Table 15 summarizes the determinations of $\alpha_S(M_Z)$ using the CT10, MSTW2008, and NNPDF2.1 PDF sets at NLO and NNLO evolution order. The results reported here are extracted with a simultaneous fit to all rapidity bins. The $\alpha_S(M_Z)$ values are in agreement between the different PDF sets taking into account the various uncertainties.

The final result using the CT10-NLO PDF set is

$$\alpha_S(M_Z) = 0.1185 \pm 0.0019\,(\text{exp.}) \pm 0.0028\,(\text{PDF}) \pm 0.0004\,(\text{NP})^{+0.0053}_{-0.0024}\,(\text{scale})$$
$$= 0.1185^{+0.0063}_{-0.0042}, \tag{85}$$

where experimental, PDF, NP, and scale uncertainties have been added quadratically to give the total uncertainty.

The result is in agreement with the world average value of $\alpha_S(M_Z) = 0.1184 \pm 0.0007$[51], with the Tevatron results[52–54], and recent results obtained with LHC data[42, 55].

Table 15: Determination of $\alpha_S(M_Z)$ using the CT10, MSTW2008, and NNPDF2.1 PDF sets at NLO and NNLO evolution order. The results are obtained by a simultaneous fit to all rapidity bins.

PDF set	$\alpha_S(M_Z)$	χ^2/n_{dof}
CT10-NLO	$0.1185 \pm 0.0019(\text{exp}) \pm 0.0028(\text{PDF})$ $\pm 0.0004(\text{NP})^{+0.0053}_{-0.0024}(\text{scale})$	104.1/132
NNPDF2.1-NLO	$0.1150 \pm 0.0015(\text{exp}) \pm 0.0024(\text{PDF})$ $\pm 0.0003(\text{NP})^{+0.0025}_{-0.0025}(\text{scale})$	103.5/132
MSTW2008-NLO	$0.1159 \pm 0.0012(\text{exp}) \pm 0.0014(\text{PDF})$ $\pm 0.0001(\text{NP})^{+0.0024}_{-0.0030}(\text{scale})$	107.9/132
CT10-NNLO	$0.1170 \pm 0.0012(\text{exp}) \pm 0.0024(\text{PDF})$ $\pm 0.0004(\text{NP})^{+0.0044}_{-0.0030}(\text{scale})$	105.7/132
NNPDF2.1-NNLO	$0.1175 \pm 0.0012(\text{exp}) \pm 0.0019(\text{PDF})$ $\pm 0.0001(\text{NP})^{+0.0018}_{-0.0020}(\text{scale})$	103.0/132
MSTW2008-NNLO	$0.1136 \pm 0.0010(\text{exp}) \pm 0.0011(\text{PDF})$ $\pm 0.0001(\text{NP})^{+0.0019}_{-0.0024}(\text{scale})$	108.8/132

6.1.4.5   Application of alternative NP corrections

All fits up to now have been performed using the nonpertubative correction, defined as the center of the envelope given by PYTHIA6, HERWIG++ and the POWHEG average of tunes Z2* and P11. Half the spread between these three numbers defines the uncertainty.

If alternatively the NP correction factors as derived in[49] using PYTHIA6 and HERWIG++ are applied the results is:

$$\alpha_S(M_Z) = 0.1178 \pm 0.0020(\text{exp}) \pm 0.0029(\text{PDF}) \pm 0.0003(\text{NP}) \tag{86}$$

Fits are also performed in regions of p_T in order to investigate the running of the strong coupling constant. The procedure that has been followed and the values derived by this study are described with the results from R_{32} in section 6.3

6.2   The ratio of 3-jet to 2-jet inclusive cross sections (R_{32})

The following section describes the extraction of the strong coupling constant, α_S, from the ratio of $3-$jet to $2-$jet cross section at $\sqrt{s} = 7$ TeV. Section 6.2.1 gives a brief description of the measurment. Section 6.2.2 describes the theoretical components of the analysis while section 6.2.3 the extraction of the α_S at the mass of vector boson Z.

6.2.1   The R32 Cross Section Measurement Overview

The events presented in the following analysis were collected by the CMS detector at proton-proton collisions at $\sqrt{s} = 7$ TeV in 2011 and correspond to an integrated luminosity $5.0 fb^{-1}$. The particles used in the jet clustering were reconstructed using the PF technique and jets were clustered using the anti-k_T algorithm with the radius parameter set at $R = 0.7$ and $R = 0.5$.

Each event recorded for the analysis is required to have at least one offline-reconstructed primary vertex within the range of $24 cm$, along the beam line, from the nominal interaction point. Each jet is required to consist at least from two particles, one charged hadron and the jet energy fraction from neutral hardrons, photons, muons, and electrons should be less than 90%. These criteria aim to suppress non-physical jets; such as jets from ECAL or HCAL noise.

The R_{32} measurement is the ratio of the inclusive 3-jet cross section to the inclusive 2-jet cross section as a function of the average transverse momenta of the two leading jets, $\langle p_{T1,2} \rangle$. The measured quantity, R_{32}, is corrected for detector effects and unfolded to stable-particle level using the iterative Bayesian method, as is implemented in the ROOUNFOLD package.

In this analysis six different selection scenarios were considered. For the first three scenarios jets were selected to have transverse momentum greater than 50 GeV, rapidity range $|y| < 2.5$ while the third jet to have transverse momentum greater than 15%-25%-35% of the average transverse momentum of the two leading jets. For the last three scenarios jets were selected to have transverse momentum greater than 50-100-150 GeV and be in the rapidity range $|y| < 2.5$. Table 16 summarizes the six different selection scenarios. In all these scenarios events with the first or the second jet $|y| > 2.5$ were rejected. We note here that for this study the anti-k_T clustering algorithm radius parameter was set to R $= 0.5$

Table 16: The six different selection scenarios considered in this analysis.

Scenario	Selection
1	$p_T > 50$ GeV and $p_{T3} > 0.15 \langle p_{T1,2} \rangle$
2	$p_T > 50$ GeV and $p_{T3} > 0.25 \langle p_{T1,2} \rangle$
3	$p_T > 50$ GeV and $p_{T3} > 0.35 \langle p_{T1,2} \rangle$
4	$p_T > 50$ GeV
5	$p_T > 100$ GeV
6	$p_T > 150$ GeV

For the extraction of the α_S the sixth scenario is used were each jet is required to have transverse momentum larger than 150 GeV and $|y| < 2.5$, the high p_T selection renders this analysis insensitive to pile-up. The reasoning for the selection of the particular scenatio is explained in the following paragraphs.

6.2.1.1   Experimental uncertainties
The advantage of the ratio of cross section is that many experimental uncertainties are reduced or totally canceled out. The uncertainty of the integrated luminosity is completely canceled.

The jet four-momentum vector has been corrected with jet energy corrections, which depend on η and p_T, by applying a correction as a multiplicative factor. The multiplicative factor is in general smaller than 1.2, approximately uniform in η, with typical values of 1.1 for jets having $p_T = 100$ GeV and decreasing to 1.0 for higher values of p_T. These corrections are accompanied with an uncertainty (JES) which is estimated to be $2.0 - 2.5\%$, depending on p_T and η. The impact of the systematic JES uncertainty on R_{32} is 1.2%.

The unfolding method also introduces uncertainty to the measurement which arises from three mutually uncorellated sources. The first arises from the insuffiecient knowledge of the parametrisation of the 3-jet and 2-jet spectra that were used to construct the simulated ratio R_{32} used in the unfolding. The slopes were varied by $\pm 10\%$ in order to estimate the uncertainty. The second arises from the insufficient knowledge of the $\langle p_{T1,2} \rangle$ resolution, the uncertainty is estimated by varying the resolution by $\pm 10\%$. Finally the third uncertainty arises from the non-Gausian tails in the $\langle p_{T1,2} \rangle$ resolution; the uncertainty studied by adding non-Gausian tails to the simulation the uncertainty. The total uncertainty due the unfolding method is less than 1%.

6.2.2   Theoretical Components and Comparison with Data

6.2.2.1   Comparison to Theory

The calculations performed using the parton level generator NLOJET++ within the FASTNLO framework using four PDF sets, ABM11, CT10, MSTW2008 and NNPDF2.1. The calculations performed assuming five massless ($N_f = 5$) quark flavors. The PDF sets are delivered in two versions, one using the NLO evolution code while the second one the NNLO evolution code. For practical reasons the NNLO were chosen; the NNLO PDF provide more variations in $\alpha_S(M_Z)$ which allows us to performe the fit. Theoretical calculations are corrected for non-pertubative effects by applying NP corrections derived using PYTHIA6 and HERWIG++. More details of these calculations can be found in subsection 4.8.4.

The studies concerning the selection of the scenario are performed using the anti-k_T = 0.5. Further studies though showed that the anti-k_T =0.5 algorithm yields larger k-factors compared to calculations using anti-k_T = 0.7 and k-factors< 1, as shown in Fig. 58 especially at lowest p_T region. The smaller the k-factors the smaller the difference of the calculation from LO to NLO, it is reasonable to assume that the behaviour is similar to higher orders, thus the anti-k_T = 0.7 is selected for the extraction of the α_S.
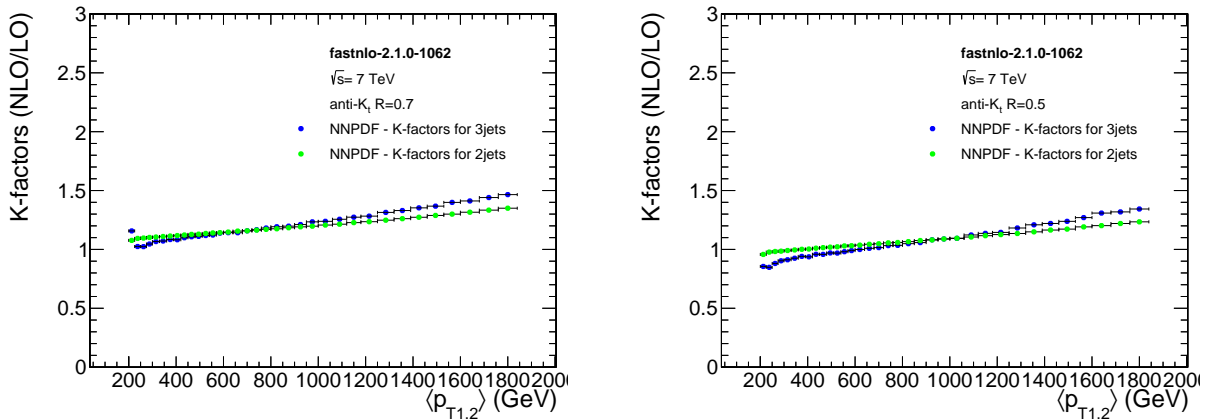
Figure 58: K-Factors NLO/LO for 2-jets and 3-jets cross section.

Fig 59 shows data over NLO theory predictions using the NNPDF2.1 PDF set for anti-k_T radius resolution parameter R $=$ 0.5 and for scenarios with jet $p_T > 100$ GeV (top left) and $p_T > 150$ GeV (top right). Same scenarios below for anti-k_T radius resolution parameter R $=$ 0.7. On the top of each plot, the ratio R_{32} (solid circles) together with the NLO pQCD theoretical prediction (black line), the scale uncertainty (red band) and PDF uncertainty (green band). On the bottom of each plot, the Data/Theory ratio, the scale uncertainty (red dotted lines) and the PDF uncertainty (green dashed lines) bands. From Fig 59 it can be seen that scale uncertainties are significantly smaller when using the anti-$k_T = 0.7$ clustering algorithm that it might be explained from the smaller k-factors of 3$-$jet calculations.

Figure 60 shows the data over NLO theory predictions using the NNPDF2.1 PDF set for scenarios 1 (top left), 2 (top right) and 3 (at the bottom). On the top of each plot, the ratio R_{32} (solid circles) together with the NLO pQCD theoretical prediction (black line), the scale uncertainty (red band) and PDF uncertainty (green band). On the bottom of each plot, the Data/Theory ratio, the scale uncertainty (red dotted lines) and the PDF uncertainty (green dashed lines) bands. Figure 61 shows the same plots for scenarios 4, 5 and 6.

The uncertainties due to the renormalization (μ_r) and factorization (μ_f) scales are evaluated by varying the default choice of $\mu_r = \mu_f = \langle p_{T1,2} \rangle$ between $\langle p_{T1,2} \rangle / 2$ and $2\langle p_{T1,2} \rangle$ in the following six combinations $(\mu_r, \mu_f) = (\langle p_{T1,2} \rangle / 2, \langle p_{T1,2} \rangle / 2)$, $(2\langle p_{T1,2} \rangle, 2\langle p_{T1,2} \rangle)$, $(\langle p_{T1,2} \rangle, \langle p_{T1,2} \rangle / 2)$, $(\langle p_{T1,2} \rangle, 2\langle p_{T1,2} \rangle)$, $(\langle p_{T1,2} \rangle / 2, \langle p_{T1,2} \rangle)$ and $(2\langle p_{T1,2} \rangle, \langle p_{T1,2} \rangle)$.

Fig. 62 shows the behavior of cross sections as a function of μ_r. A variation of μ_r below $\langle p_{T1,2} \rangle / 2$ it would give negative cross sections and a variation above $2\langle p_{T1,2} \rangle$ it would not change the uncertainty significantly. Thus the combinations of the scale variations give a sufficient evaluation of the scale uncertainties.

Within uncertainties, a nice agreement between Data and NLO pQCD theoretical calculations is observed. Figures 60 and 61 also show that scale uncertainties dominate especially at low $\langle p_{T1,2} \rangle$ values.

6.2.3   Determination of $\alpha_S(M_Z)$

In order to check if the ratio R_{32} can be used for the extraction of the strong coupling constant $\alpha_S(M_Z)$ the sensitivity study is needed. The sensitivity study checks whether the theoretical calculations of the observable, in this case R_{32}, is sensitive to $\alpha_S(M_Z)$ variations. The study is performed for all scenarios in order to find the optimum one. Figure 63 shows the data over NLO theory predictions using the NNPDF2.1 PDF set for scenarios 1 (top left), 2 (top right) and 3 (at the bottom). On each plot it is shown, the ratio R_{32} (solid circles) together with the NLO pQCD theoretical predictions (lines) for different values of $\alpha_S(M_Z)$. The value of $\alpha_S(M_Z)$ was varied form 0.106-0.124 in bins of 0.001. Figure 64 shows the same plots but for scenarios 4, 5 and 6.

Figures 63 and 64 show that scenarios (1, 2 and 3) are less sensitive to $\alpha_S(M_Z)$ variations than scenarios (4, 5, and 6) especially in the important region around 1 TeV.

An optimum region to determine $\alpha_S(M_Z)$ is to work at the "plateau" region ($\langle p_{T1,2} \rangle > 400$ GeV) where the sensitivity is high and scale uncertainties become smaller. The most promising scenarios are number 5 and 6. Further studies showed that scenario 6, with $p_T > 150$ GeV, gives better χ^2/n_{dof}, close to one, and smaller scale uncertainties.

Figure 65 shows the comparison of data to theory, for scenario 6, using NNPDF2.1 (upper left), ABM11 (upper right), MSTW (bottom left), and CT10 (bottom right). The data are in
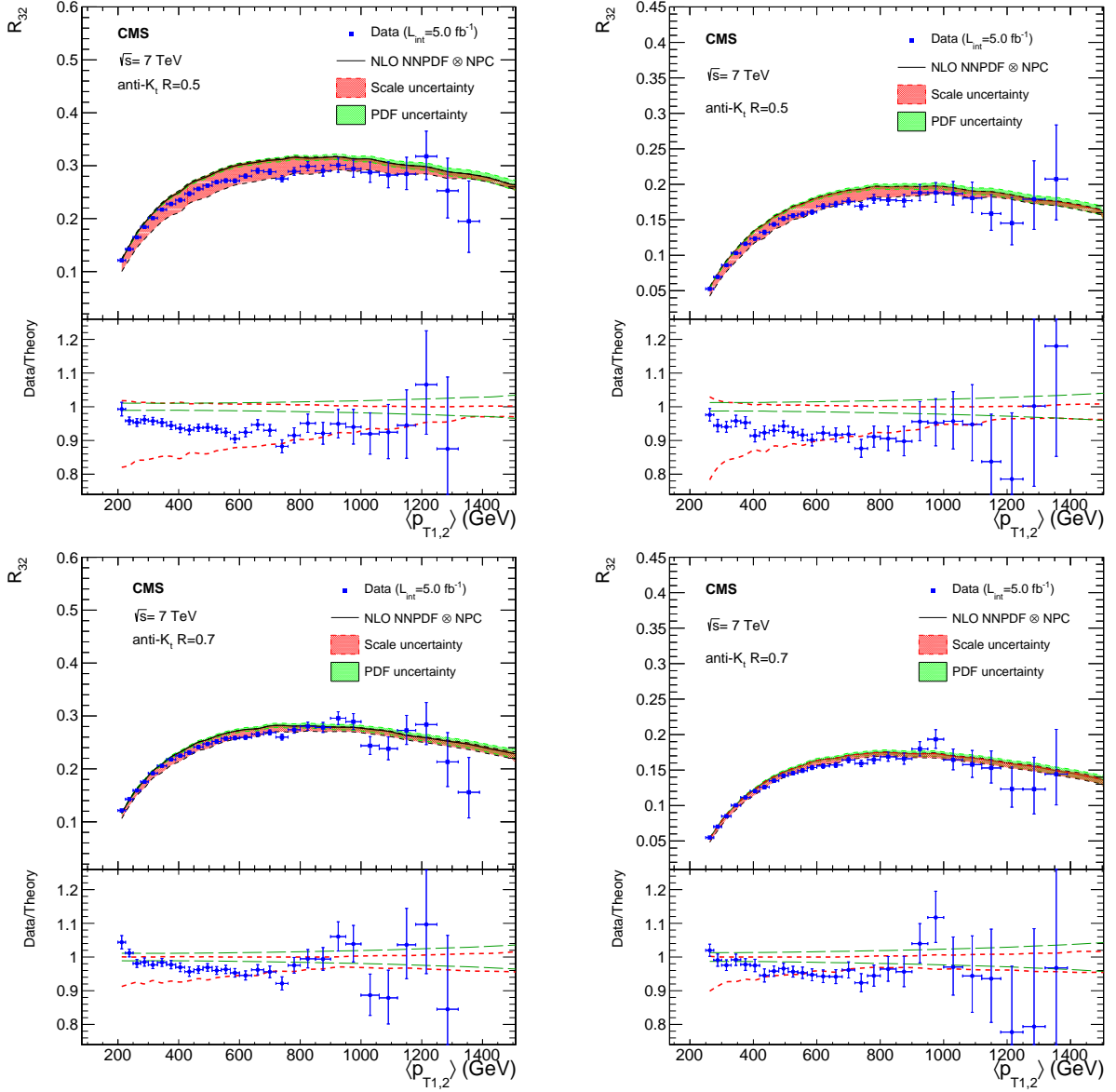
Figure 59: Data over NLO theory predictions using the NNPDF2.1 PDF set for anti-k_T radius resolution parameter R = 0.5 and for scenarios with jet p_T > 100 GeV (top left) and p_T > 150 GeV (top right). Same scenarios bellow for anti-k_T radius resolution parameter R = 0.7. On the top of each plot, the ratio R_{32} (solid circles) together with the NLO pQCD theoretical prediction (black line), the scale uncertainty (red band) and PDF uncertainty (green band). On the bottom of each plot, the Data/Theory ratio, the scale uncertainty (red dotted lines) and the PDF uncertainty (green dashed lines) bands.
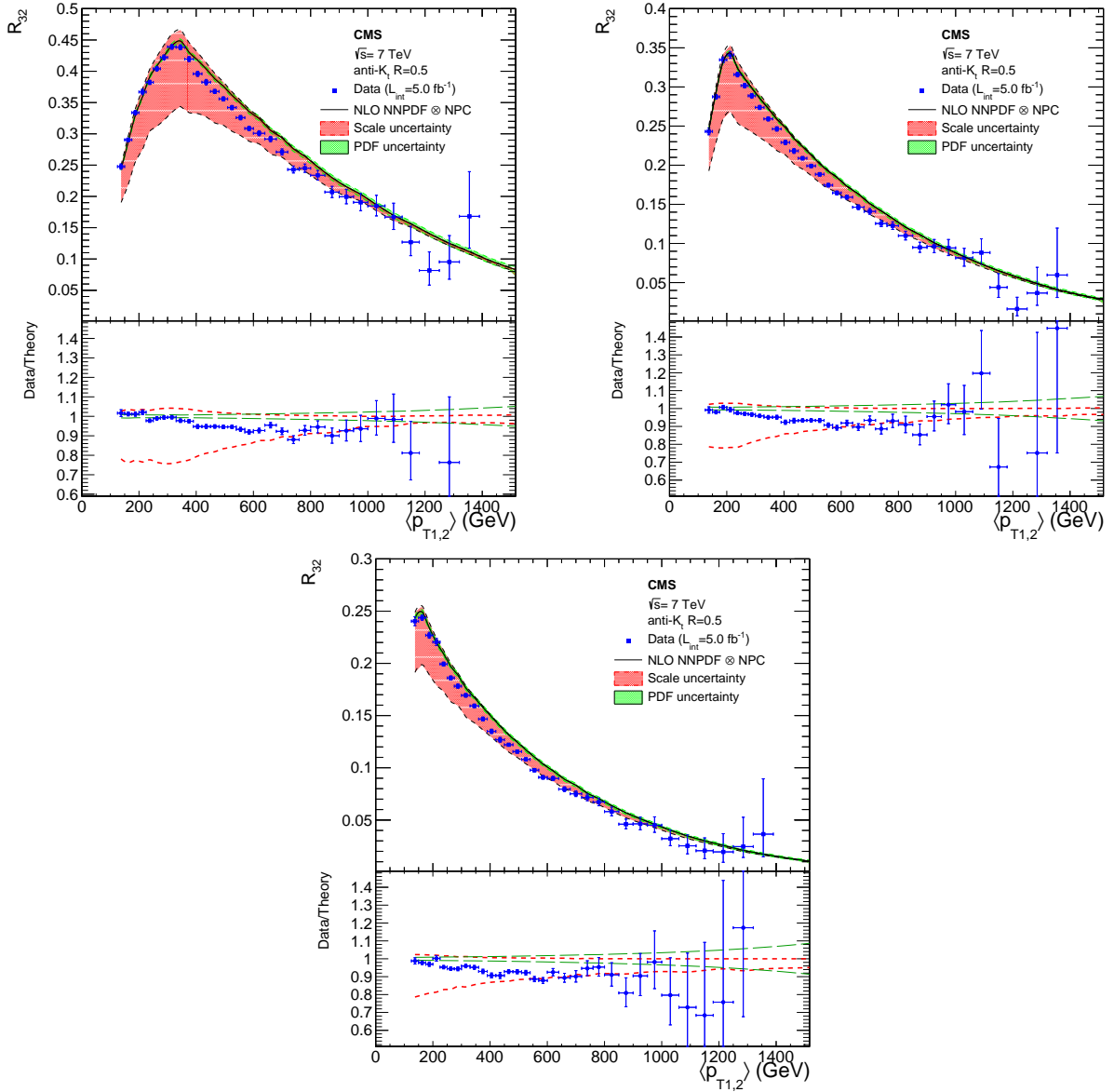
Figure 60: Data over NLO theory predictions using the NNPDF2.1 PDF set for scenarios 1 (top left), 2 (top right) and 3 (at the bottom). On the top of each plot, the ratio R_{32} (solid circles) together with the NLO pQCD theoretical prediction (black line), the scale uncertainty (red band) and PDF uncertainty (green band). On the bottom of each plot, the Data/Theory ratio, the scale uncertainty (red dotted lines) and the PDF uncertainty (green dashed lines) bands.
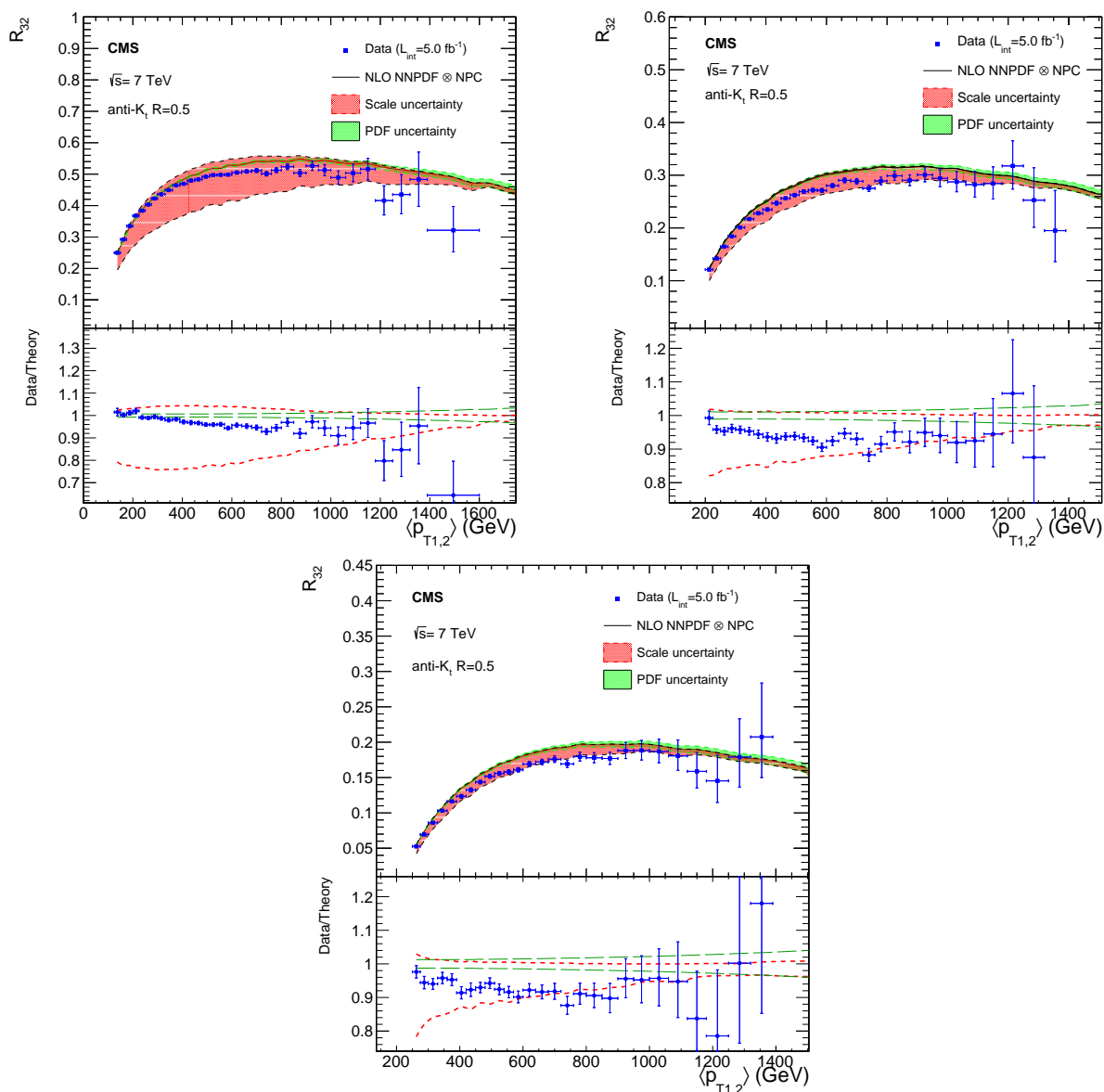
Figure 61: Data over NLO theory predictions using the NNPDF2.1 PDF set for scenarios 4 (top left), 5 (top right) and 6 (at the bottom). On the top of each plot, the ratio R_{32} (solid circles) together with the NLO pQCD theoretical prediction (black line), the scale uncertainty (red band) and PDF uncertainty (green band). On the bottom of each plot, the Data/Theory ratio, the scale uncertainty (red dotted lines) and the PDF uncertainty (green dashed lines) bands.
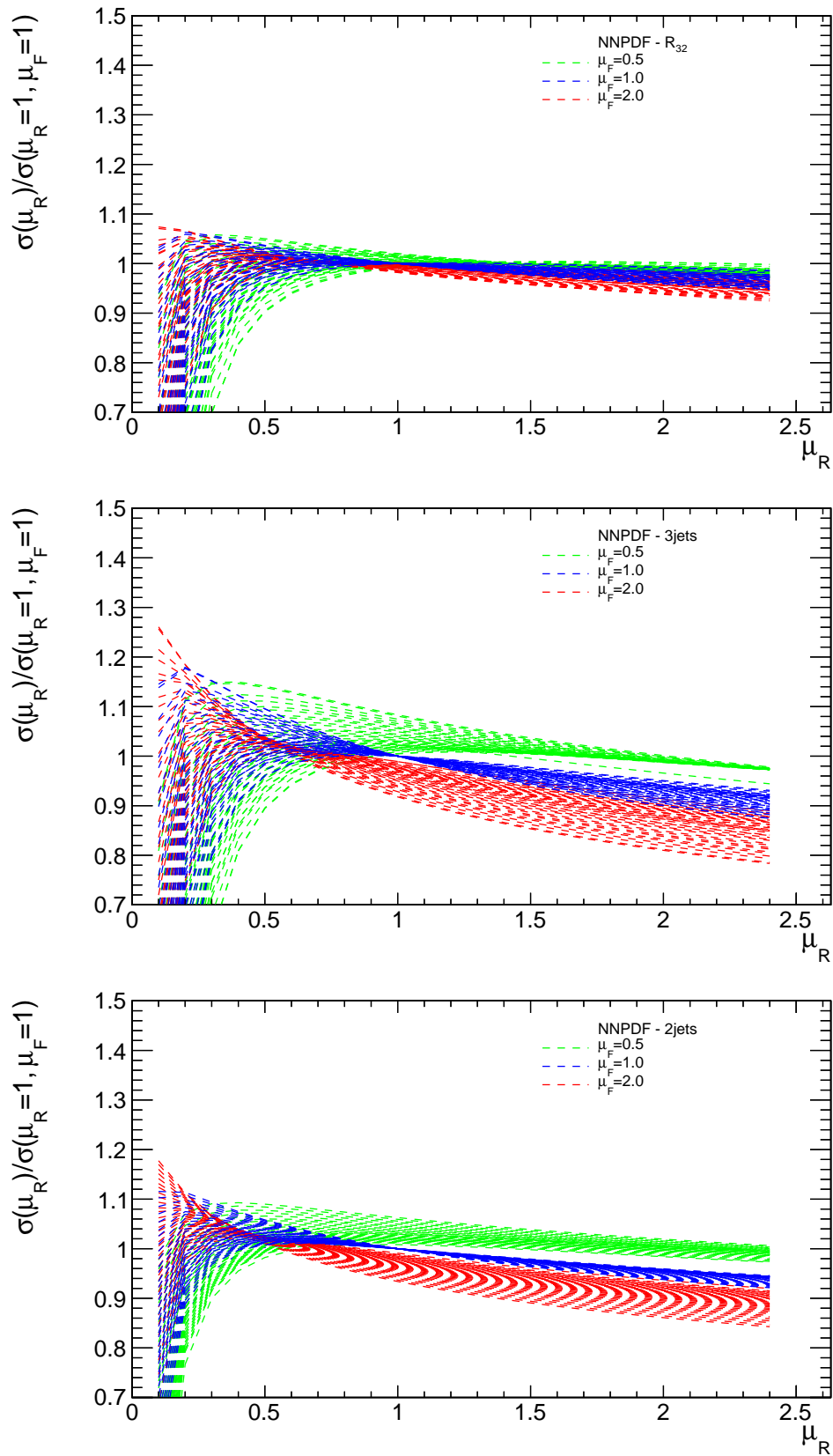
Figure 62: Scale variations of 3-jets cross sections, 2-jets cross sections and R_{32}.

agreement within uncertainties with theoretical predictions derived using CT10, MSTW2008, and NNPDF2.1, throughout the range of the measurement. Calculations derived using ABM11 underestimate the measurement, especially at the low $\langle p_{T1,2} \rangle$ region.

Figure 66 shows the comparison of data to theory using various $\alpha_S(M_Z)$ values. This study shows that R_{32} is sensitive to variations of $\alpha_S(M_Z)$, thus is an appropriate observable for the extraction of α_S. The calculations using ABM11 are not sensitive to $\alpha_S(M_Z)$, consequently ABM11 has been excluded from the χ^2 fit.

For the extraction of the $\alpha_S(M_Z)$ from data a χ^2 fit is performed; the procedure is the same as described in section 6.1.4. For the final result the NNPDF2.1 PDF set was selected since it gives an adequate range of $\alpha_S(M_Z)$ values a fact that qualifies it to extract the $\alpha_S(M_Z)$ and the scale uncertainties. Since the NNPDF2.1 PDF is given as a MC set, the uncertainties on the $\alpha_S(M_Z)$ can be calculated independently of the covariance matrix as a consequence the covariance matrix that is used in the χ^2 fit is written as:

$$C = \text{Cov}^{\text{Stat}} + \sum \text{Cov}^{\text{JES Sources}} + \sum \text{Cov}^{\text{Unfolding Sources}} \tag{87}$$

The NNPDF2.1 is delivered as a MC sample of 100 replicas, the fitting procedure is repeated for each replica resulting 100 values of $\alpha_S(M_Z)$. These values are distributed as a Gausian, the standard deviation of the distribution is considered as the PDF uncertainty.

The final result when using data from $420 - 1390$ GeV is :

$$\alpha_S(M_Z) = 0.1148 \pm 0.0014(exp.) \pm 0.0018(PDF) \pm 0.0050(theory) \tag{88}$$

with $\chi^2/n_{\text{dof}} = 22.0/20$ which indicates the goodness of the fit. Results derived using MSTW2008 and CT10 are in agreement within uncertainties with the result obtained using NNPDF2.1. The results from all the PDF sets are summarized in Table 17.

Table 17: Determination of $\alpha_S(M_Z)$ using the CT10, MSTW2008, and NNPDF2.1 sets.

PDF Sets	$\alpha_S(M_Z)$	χ^2/n_{dof}
CT10-NNLO	$0.1135 \pm 0.0019(\text{exp})$	$21.1/20$
MSTW2008-NNLO	$0.1141 \pm 0.0022(\text{exp})$	$20.6/20$
NNPDF2.1-NNLO	$0.1148 \pm 0.0014(\text{exp})$	$20.0/20$

The experimental uncertainties obtained from the χ^2 fit are not independent of the PDF and that can be seen from the sensitivity figures. A variation of $\Delta\alpha_S(M_Z) = \pm 0.001$ yields a different variation of R_{32} depending to the PDF set, this leads to different experimental uncertainties for each PDF set.

Results are also obtained with NLO PDF sets and are found to be in agreement with the results obtained using the NNLO PDF sets. The results within uncertainties are compatible with the world average value of $\alpha_S(M_Z) = 0.1184 \pm 0.0007$.
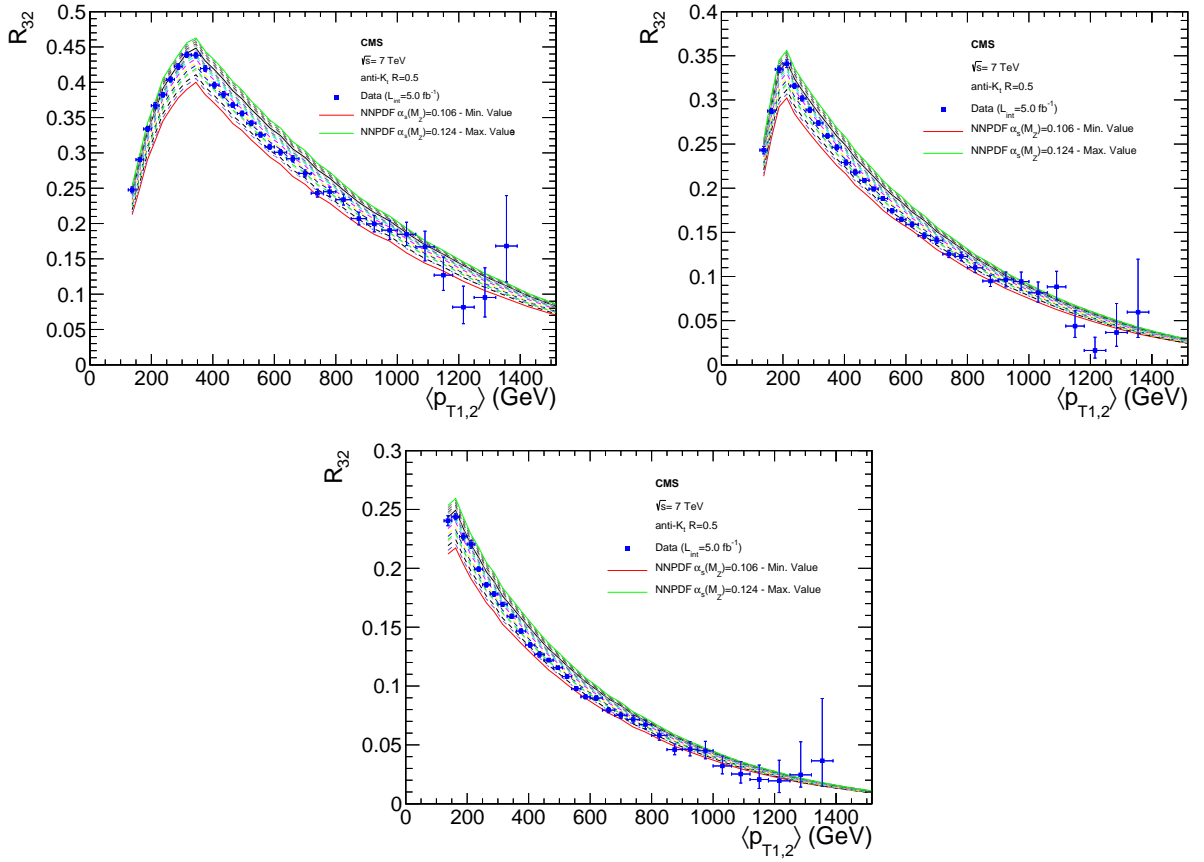
Figure 63: Data over NLO theory predictions using the NNPDF2.1 PDF set for scenarios 1 (top left), 2 (top right) and 3 (at the bottom). On each plot, the ratio R_{32} (solid circles) together with the NLO pQCD theoretical predictions (lines) for different values of $\alpha_S(M_Z)$. The value of $\alpha_S(M_Z)$ was varied form 0.106-0.124 in bins of 0.001.
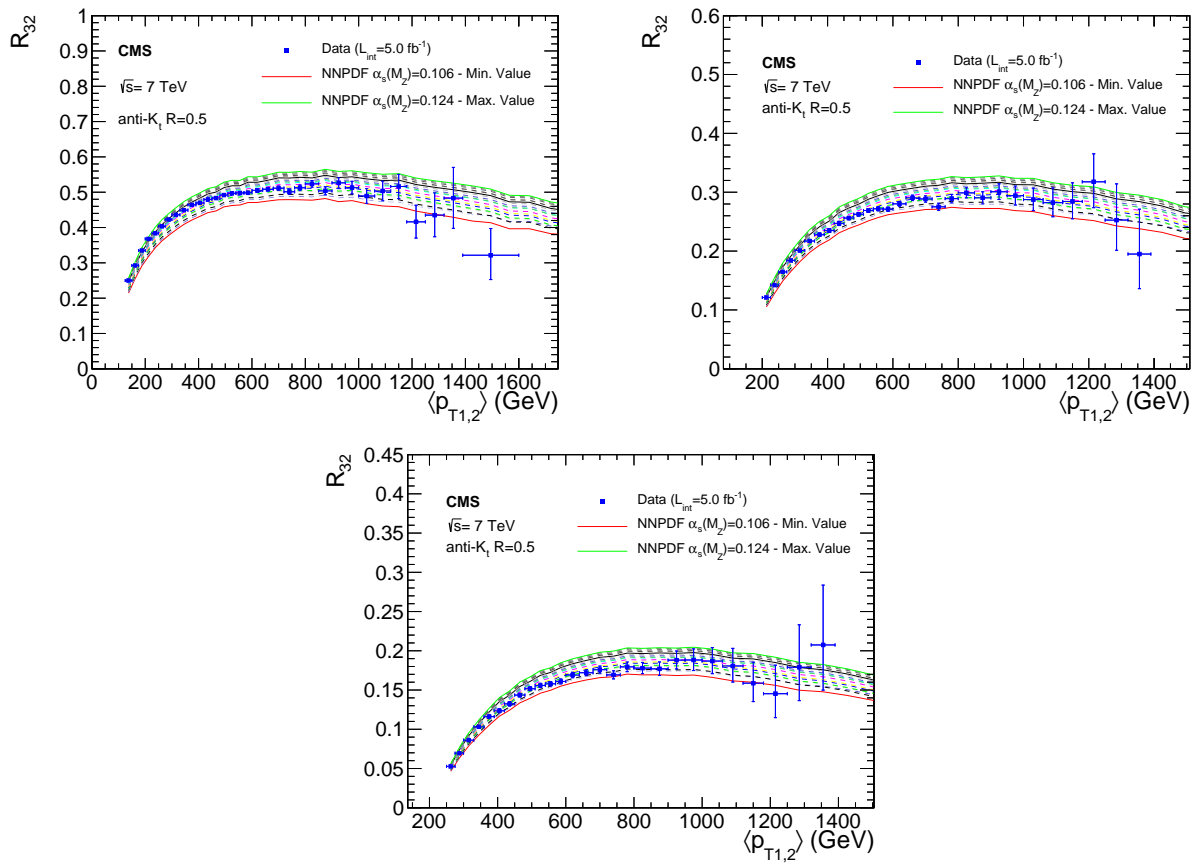
Figure 64: Data over NLO theory predictions using the NNPDF2.1 PDF set for scenarios 4 (top left), 5 (top right) and 6 (at the bottom). On each plot, the ratio R_{32} (solid circles) together with the NLO pQCD theoretical predictions (lines) for different values of $\alpha_S(M_Z)$. The value of $\alpha_S(M_Z)$ was varied form 0.106-0.124 in bins of 0.001.
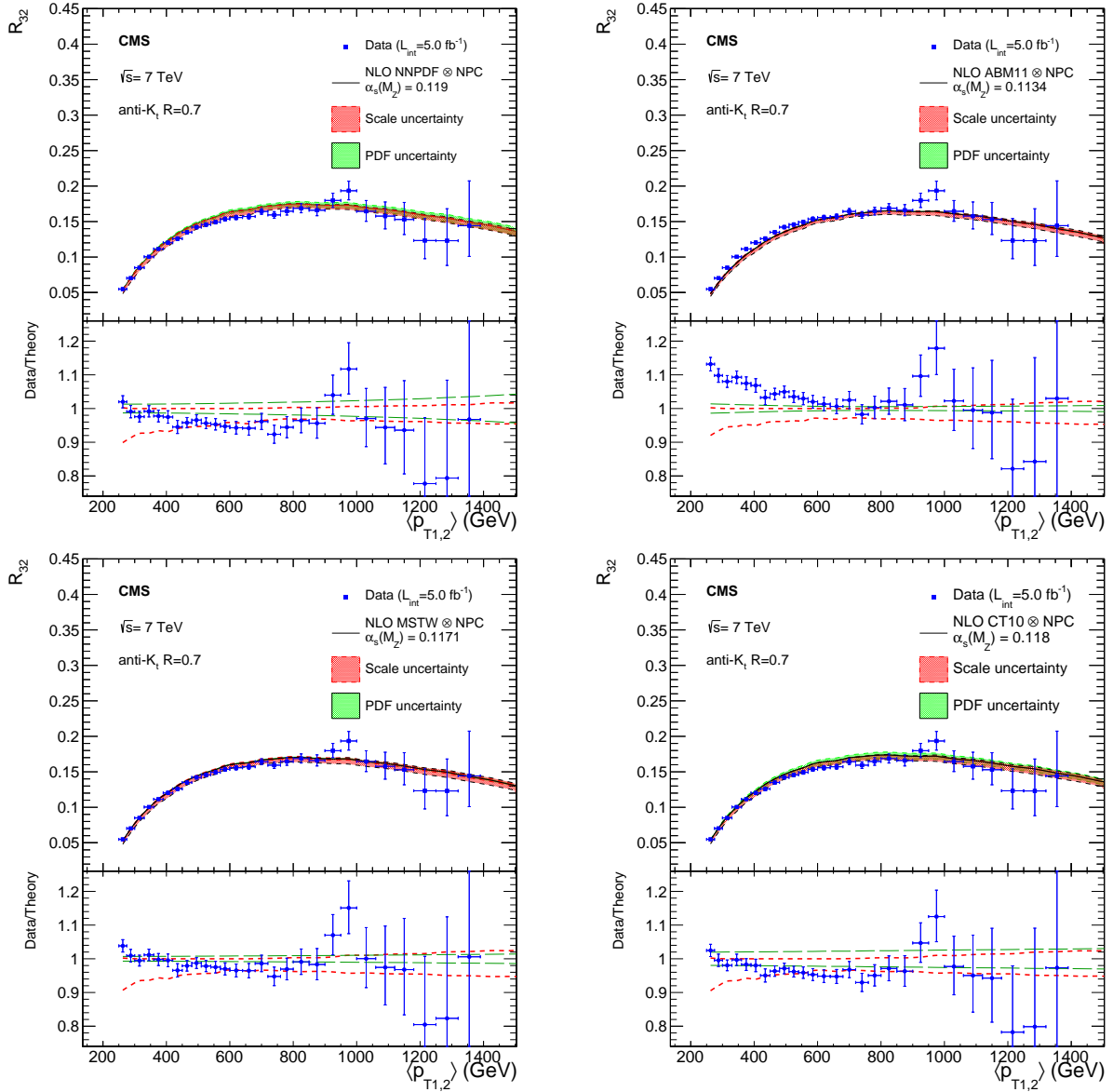
Figure 65: For scenario with jet $p_T > 150$ GeV and $|y| < 2.5$. Data over NLO theory predictions using the NNPDF2.1 (top left), the ABM11 (top right), the MSTW2008 (bottom left) and the CT10 (bottom right) PDF sets. On the top of each plot, the ratio R_{32} (solid circles) together with the NLO pQCD theoretical prediction (black line), the scale uncertainty (red band) and PDF uncertainty (green band). On the bottom of each plot, the Data/Theory ratio, the scale uncertainty (red dotted lines) and the PDF uncertainty (green dashed lines) bands.
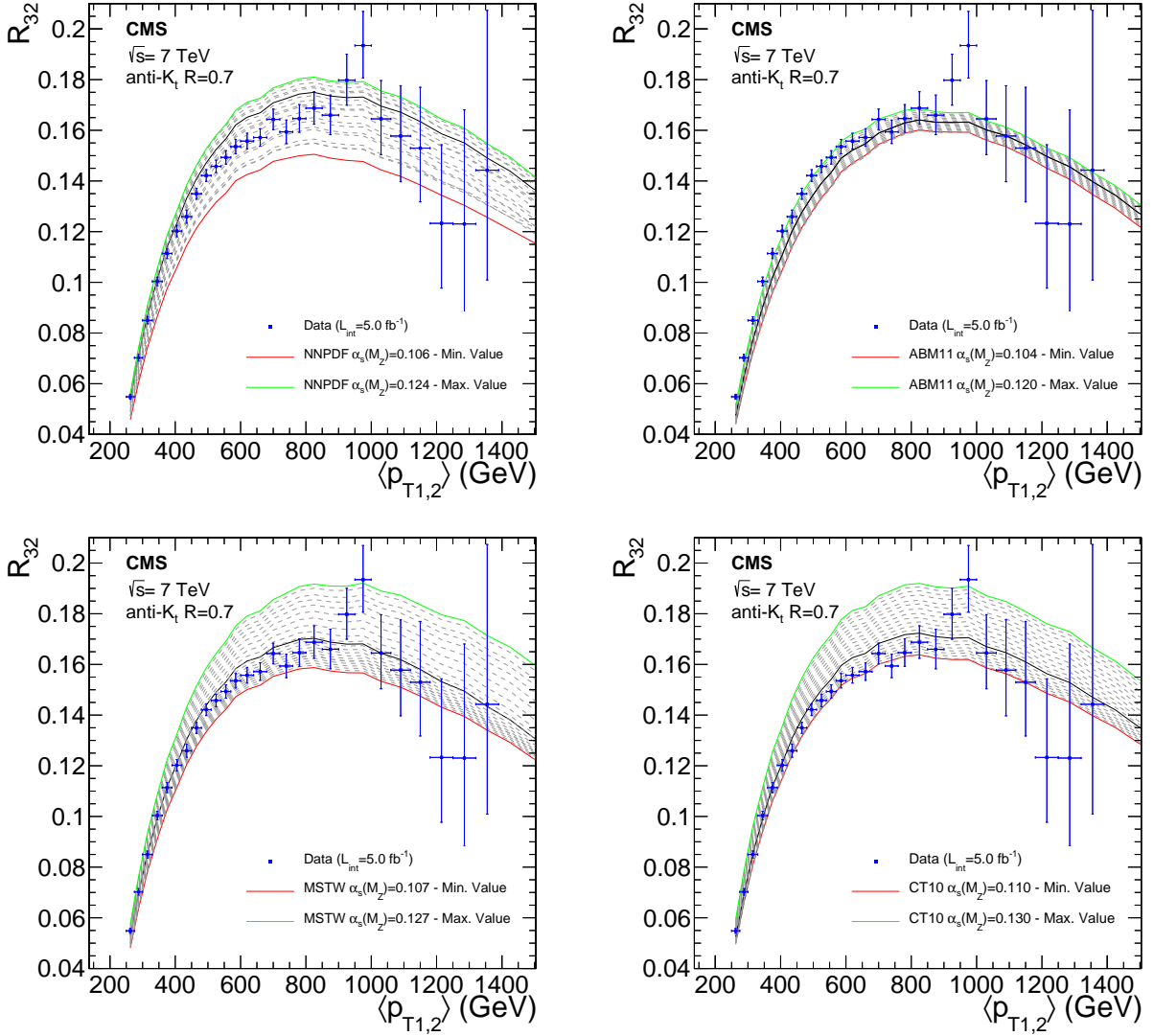
Figure 66: For scenario with jet $p_T > 150$ GeV and $|y| < 2.5$. The theoretical NLO calculations using the NNPDF2.1 (top left), the ABM11 (top right), the MSTW2008 (bottom left) and the CT10 (bottom right) PDF sets for various values of $\alpha_S(M_Z)$ together with the measurement R_{32}. The $\alpha_S(M_Z)$ has been varied in the range 0.106-0.124, 0.104-120, 0.107-0.127 and 0.110-0.130 for NNPDF2.1, ABM11, MSTW2008 and CT10 respectively, in bins of 0.001.

6.3   The running of α_S.

To investigate the running of the strong coupling, the fitted regions are split into bins of p_T and the fitting procedure is repeated in each of these bins. The inclusive jet cross section data are splitted in six separate regions while the R_{32} data in three regions.

The separate extractions of $\alpha_S(M_Z)$ from the inclusive jet cross section data are reported in Table 18 while the $\alpha_S(M_Z)$ values from the R_{32} are reported in Table 20. The experimental uncertainties for the obtained values are correlated.

These $\alpha_S(M_Z)$ determinations are then evolved back to the corresponding values $\alpha_S(Q)$. For the inclusive jet cross section theory the 2-loop solution to the renormalization group equation (RGE) is used since a NLO PDF used to extract the $\alpha_S(M_Z)$. For the R_{32} a 3-loop solution of the RGE is used since a NNLO PDF used to extract the $\alpha_S(M_Z)$. For each fit region the momentum scale Q is defined to be the cross section-weighted average. These values, derived again with the FASTNLO framework, are identical within about 1 GeV for different PDFs.

To emphasize that theoretical uncertainties limit the achievable precision, Tables 19 and 21 present the decomposition of the total uncertainty for the various bins in p_T ($\langle p_{\mathrm{T}1,2} \rangle$) into the experimental, PDF, NP, and scale(theory) components.

The extractions of $\alpha_S(Q)$ in separate ranges of Q as presented in tables 18 and 20. The values are shown in Figure 67 that presents the running of the strong coupling $\alpha_S(Q)$ (solid line) and its total uncertainty (band) as evolved from the CMS determination (inclusive jet cross section data), $\alpha_S(M_Z) = 0.1185^{+0.0065}_{-0.0041}$, using the 2-loop solution to the RGE, as before.

In the same figure the values of α_S at lower scales determined by the H1[56, 57], ZEUS[58], and D0[53, 54] Collaborations are shown for comparison. Recent CMS measurements, which are in agreement with the $\alpha_S(M_Z)$ determination of this study, are displayed as well. The results on α_S reported here are consistent with the energy dependence predicted by the RGE and extend the H1, ZEUS, and D0 results to the 1 TeV region for the first time.

Table 18: Determination of α_S in separate bins of jet p_T

p_T range (GeV)	Q (GeV)	$\alpha_S(M_Z)$	$\alpha_S(Q)$	No. of data points	χ^2/N_dof
114–196	136	$0.1172^{+0.0058}_{-0.0043}$	$0.1106^{+0.0052}_{-0.0038}$	20	6.2/19
196–300	226	$0.1180^{+0.0063}_{-0.0046}$	$0.1038^{+0.0048}_{-0.0035}$	20	7.6/19
300–468	345	$0.1194^{+0.0064}_{-0.0049}$	$0.0993^{+0.0044}_{-0.0034}$	25	8.1/24
468–638	521	$0.1187^{+0.0067}_{-0.0051}$	$0.0940^{+0.0041}_{-0.0032}$	20	10.6/19
638–905	711	$0.1192^{+0.0074}_{-0.0056}$	$0.0909^{+0.0042}_{-0.0033}$	22	11.2/21
905–2116	1007	$0.1176^{+0.0111}_{-0.0065}$	$0.0866^{+0.0057}_{-0.0036}$	26	33.6/25
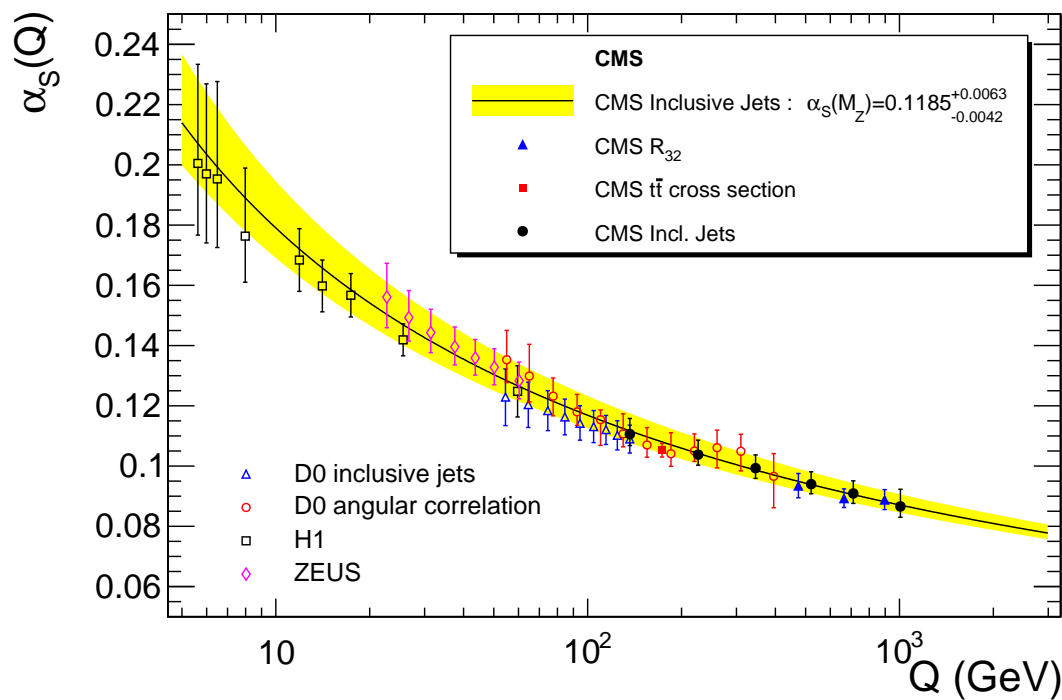
Figure 67: The strong coupling $\alpha_S(Q)$ (solid line) and its total uncertainty (band) evolved from the CMS determination $\alpha_S(M_Z) = 0.1185^{+0.0065}_{-0.0041}$ using a 2-loop solution to the RGE as a function of the momentum transfer $Q = p_T$. The extractions of $\alpha_S(Q)$ in six separate ranges of Q as presented in Table 18 are shown together with results from the H1[56, 57], ZEUS[58], and D0[53, 54] experiments at the HERA and Tevatron colliders. Recent other CMS measurements are displayed as well.

Table 19: Uncertainty composition for $\alpha_S(M_Z)$ from the determination of $\alpha_S(Q)$ in bins of p_T.

p_T range (GeV)	Q (GeV)	$\alpha_S(M_Z)$	exp.	PDF	NP	scale
114–196	136	0.1172	±0.0031	±0.0018	±0.0007	$^{+0.0045}_{-0.0022}$
196–300	226	0.1180	±0.0034	±0.0019	±0.0011	$^{+0.0048}_{-0.0025}$
300–468	345	0.1194	±0.0032	±0.0023	±0.0010	$^{+0.0049}_{-0.0027}$
468–638	521	0.1187	±0.0029	±0.0031	±0.0006	$^{+0.0052}_{-0.0027}$
638–905	711	0.1192	±0.0034	±0.0032	±0.0005	$^{+0.0057}_{-0.0030}$
905–2116	1007	0.1176	±0.0047	±0.0040	±0.0002	$^{+0.0092}_{-0.0020}$

Table 20: Determination of α_S in separate bins of jet $\langle p_{T1,2} \rangle$.

$\langle p_{T1,2} \rangle$ range (GeV)	Q (GeV)	$\alpha_S(M_Z)$	$\alpha_S(Q)$	No. of data points	χ^2/N_{dof}
420–600	474	0.1147 ± 0.0061	0.0936 ± 0.0041	6	4.4/5
600–800	664	0.1132 ± 0.0050	0.0894 ± 0.0031	5	5.9/4
800–1390	896	0.1170 ± 0.0058	0.0889 ± 0.0034	10	5.7/9

Table 21: Uncertainty composition for $\alpha_S(M_Z)$ from the determination of $\alpha_S(Q)$ in bins of $\langle p_{T1,2} \rangle$.

$\langle p_{T1,2} \rangle$ range (GeV)	Q (GeV)	$\alpha_S(M_Z)$	exp.	PDF	theory
420–600	474	0.1147	±0.0015	±0.0015	±0.0057
600–800	664	0.1132	±0.0018	±0.0025	±0.0039
800–1390	896	0.1170	±0.0024	±0.0021	±0.0048

7 Analysis at $\sqrt{s} = 8TeV$

This chapter describes the measurement of the dijet azimuthal decorrelations of the two jets with the largest transverse momenta, in pp collistions at $\sqrt{s} = 8TeV$ using the CMS detector at the LHC. The analysis is based on the full data set acquired during 2012 and corresponds to an integrated luminosity of $19.7 fb^{-1}$. The results are compared to next-to-leading-order QCD calculations and to simulations using various Monte Carlo event generators.

7.1 Introduction

Hadronic jets are the product of colored partons in the final state, as a consquence of the color confinement. In leading order perturbative quantum chromodynamics (pQCD) a two coloured final state partons give two balanced in p_T back to back jets. This in azimuthal decorrelation terms is translated as minimum decorrelation, $\Delta\phi_{Dijet} = |\phi_{jet1} - \phi_{jet2}|$, with $\Delta\phi_{Dijet} = \pi$. An emission of a third parton can lead to angles down to $\Delta\phi_{Dijet} = 2\pi/3$ while more partons in the final state lead to angle down to zero. Consequently this measurement probes multijet processes by measuring only the azimuthal angle of the two leading jets.

This analysis measures the normalized dijet cross section as a function of the dijet azimuthal angular separation in slices of $p_{T,max}$ which is defined as:

$$\frac{1}{\sigma_{Dijet}} \frac{d\sigma}{d\Delta\phi_{Dijet}} . \tag{89}$$

The normalization of the cross section leads to the reduction of various experimental and theoretical uncertainties.

7.2 The Azimuthal Decorrelations Measurement Overview

7.2.1 Event Selection and Reconstruction

This measurement uses data samples which were collected with single-jet high-level triggers (HLT). Four such HLT single-jet triggers were considered which require at least one jet in the event to have $p_T > 140, 200, 260,$ and $320\,GeV$. All except the highest-threshold trigger were prescaled during the 2012 run. The integrated luminosity $\mathcal{L}$ for each of the four trigger samples is shown in Table 22. For each of the triggers, the efficiency is estimated using lower-p_T-threshold triggers. The four jet trigger thresholds used ensure 100% trigger efficiency in the four jet samples for $200\,GeV < p_{T,max} < 300\,GeV$, $300\,GeV < p_{T,max} < 400\,GeV$, $400\,GeV < p_{T,max} < 500\,GeV$, and $p_{T,max} > 500\,GeV$.

Table 22: The integrated luminosity for each trigger sample considered in this analysis.

HLT p_T threshold (GeV)	140	200	260	320
$\mathcal{L}$ (fb^{-1})	0.06	0.26	1.06	19.7

The jets reconstructed using the PF technique and were clustered using the anti-k_T algorithm with the radius parameter set at $R = 0.7$. In order to suppress non-physical jets it is required that each jet should contain at least two particles, one of which is a charged hadron, and the jet energy fraction carried by neutral hadrons and photons should be less than 90%.

The energy of the reconstructed jets are corrected as described in subsection 5.2.1. These jet energy corrections are derived using simulated events, generated by PYTHIA 6.4.22 with tune Z2*[59] and processed through the CMS detector simulation based on GEANT4 [17], and in situ measurements with dijet, photon+jet, and Z+jet events. The jet energy corrections are applied to the jet four-momentum vector as a multiplicative factor. The multiplicative factor is in general smaller than 1.2, approximately uniform in η, with typical values of 1.1 for jets having $p_\mathrm{T} = 100\,\mathrm{GeV}$ and decreasing to 1.0 for higher values of p_T. Pileup effects are important only for jets with low p_T and become negligible for jets with $p_\mathrm{T} > 200\,\mathrm{GeV}$. The current measurement is therefore largely insensitive to pileup effects.

The two leading jets, which define $\Delta\phi_\mathrm{Dijet}$, are selected by considering all jets with $p_\mathrm{T} > 100\,\mathrm{GeV}$ and $|y| < 5$ in the event. Then events in which the two leading jets have $|y| < 2.5$ and the leading jet $p_\mathrm{T} > 200\,\mathrm{GeV}$, are selected. This two step selection in $|y|$ ensures that the event is not falsely redefined by looking at jets only at the region $|y| < 2.5$.

A variable, that separates events generated by hard QCD processes from events with large missing transverse energy ($\not{E}_\mathrm{T}$) in the final state, is the ratio of the $\not{E}_\mathrm{T}$ over the sum of the transverse energies in the event, $\not{E}_\mathrm{T} / \sum E_T$. The sum of the transverse energies is $\sum E_\mathrm{T} = \sum_i E_i \sin\theta_i$, and the missing transverse energy $\not{E}_\mathrm{T} = \sqrt{\left[\sum_i (E_i \sin\theta_i \cos\phi_i)\right]^2 + \left[\sum_i (E_i \sin\theta_i \sin\phi_i)\right]^2}$, where the summation is performed over all PF candidates in the event. Hard-QCD events contain relatively small $\not{E}_\mathrm{T}$, which originates from semi-leptonic decays of heavy vector bosons emitted by heavy quarks. On the other hand, larger $\not{E}_\mathrm{T}$ is expected for events with heavy vector bosons, at tree level, such as Z/W + jet(s), where W and Z decay into leptons and neutrinos. Figure 68 shows the distribution of the variable $\not{E}_\mathrm{T} / \sum E_T$ with $\pi/2 < \Delta\phi_\mathrm{Dijet} < \pi$ (left) and $0 < \Delta\phi_\mathrm{Dijet} < \pi/2$ (right), for events selected with the criteria described in the previous paragraph. The data (black points) are compared to simulated Monte-Carlo (MC) events (stacked), using the MADGRAPH event generator. Although the contribution from events with Z/W bosons plus jets is small in the region $\pi/2 < \Delta\phi_\mathrm{Dijet} < \pi$, this is not true for small $\Delta\phi_\mathrm{Dijet}$ values. To reduce the number of events with large $\not{E}_\mathrm{T}$, we reject events with $\not{E}_\mathrm{T} / \sum E_T > 0.1$, which correspond to 0.7% of the data sample.

Figure 69 shows the comparison of data (at detector level) with MC simulations of various contributions without any cut at $\not{E}_\mathrm{T} / \sum E_T$; such as QCD, Z+Jets, W+Jets, Drell-Yan, and $t\bar{t}$. The comparison shows that MADGRAPH gives a good description of data when various contributions are taken into account. The particular analysis though aims to deliver a QCD measurement, thus a cut is needed to reject processes other than hard QCD.

7.2.1.1   MC Shape Distortion Study

In order to study the impact of the cut $\not{E}_\mathrm{T} / \sum E_T > 0.1$, at the shape of the cross section the following study has been performed.

The Monte Carlo is reweighted in order to eliminate the discrepancy between data and MC in $\not{E}_\mathrm{T} / \sum E_T$. The spectrum of $\not{E}_\mathrm{T} / \sum E_T$ from the whole $\Delta\phi_\mathrm{Dijet}$ range has been derived from data and MC and the factors from the ratio Data/MC has been applied to the MC events. The reweighted spectra for the two regions are shown in figure 70.

The figure 71 shows in black point the reweighted QCD MC without any cut at $\not{E}_\mathrm{T} / \sum E_T$. The blue open circles show the QCD-QCD(Rej)+Bkg(Acc) where QCD(Rej) are the QCD MC events rejected and Bkg(Acc) are the "background"(ttbar, Z+Jets, W+Jets) events accepted by the cut. The bottom part of each plot shows the ratio of QCD-QCD(Rej)+Bkg(Acc) over QCD. This ratio
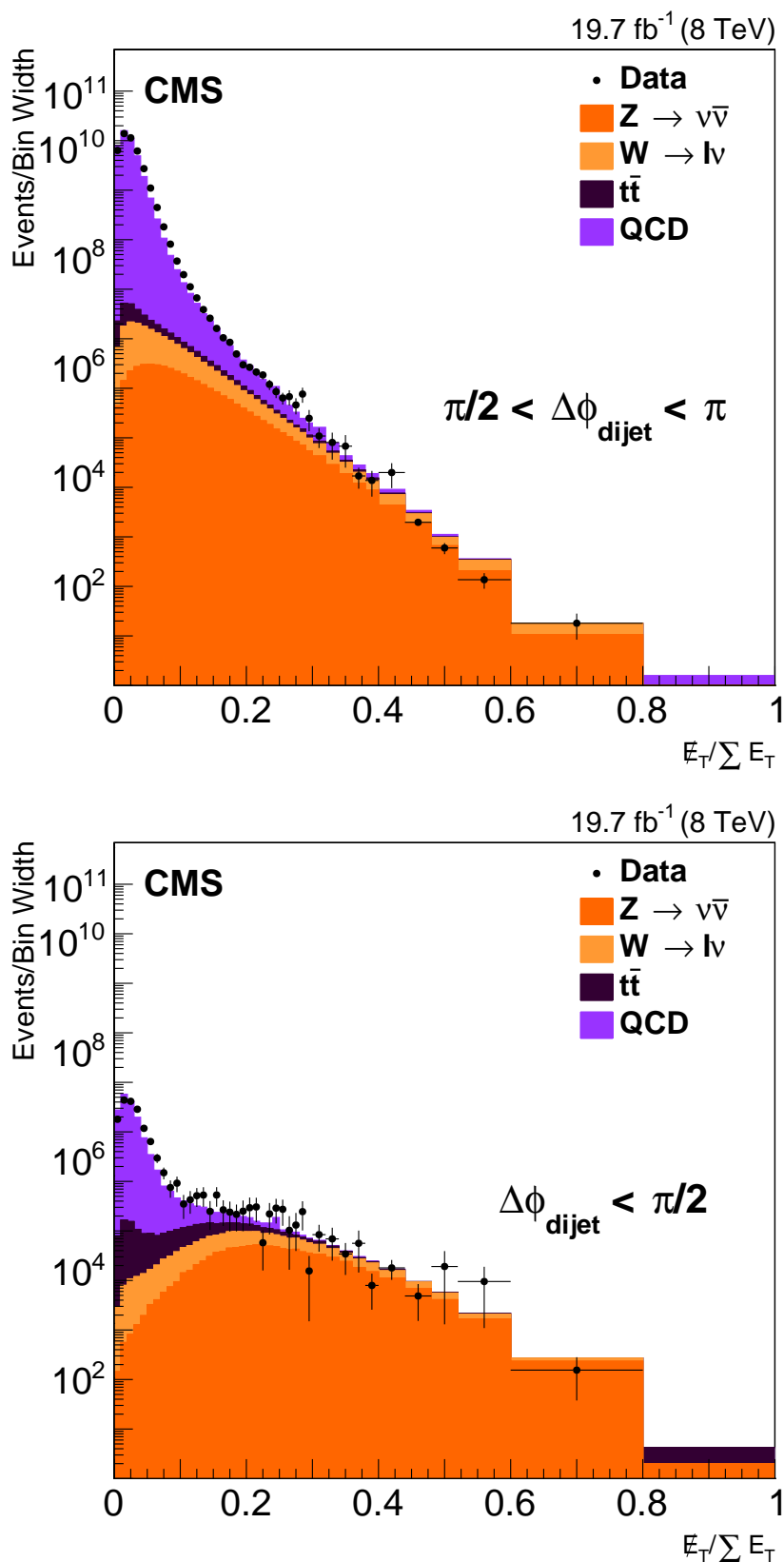
Figure 68: Distribution of $\not{E}_T / \sum E_T$ for data (black points) and simulated QCD and other processes with large $\not{E}_T$ (stacked), for $\pi/2 < \Delta\phi_{\text{Dijet}} < \pi$ (left) and $0 < \Delta\phi_{\text{Dijet}} < \pi/2$ (right). The main contribution of events with large $\not{E}_T$ in the final state is caused by processes like Z/W + jet(s) where $Z \to \nu\bar{\nu}$ and $W \to l\nu$.
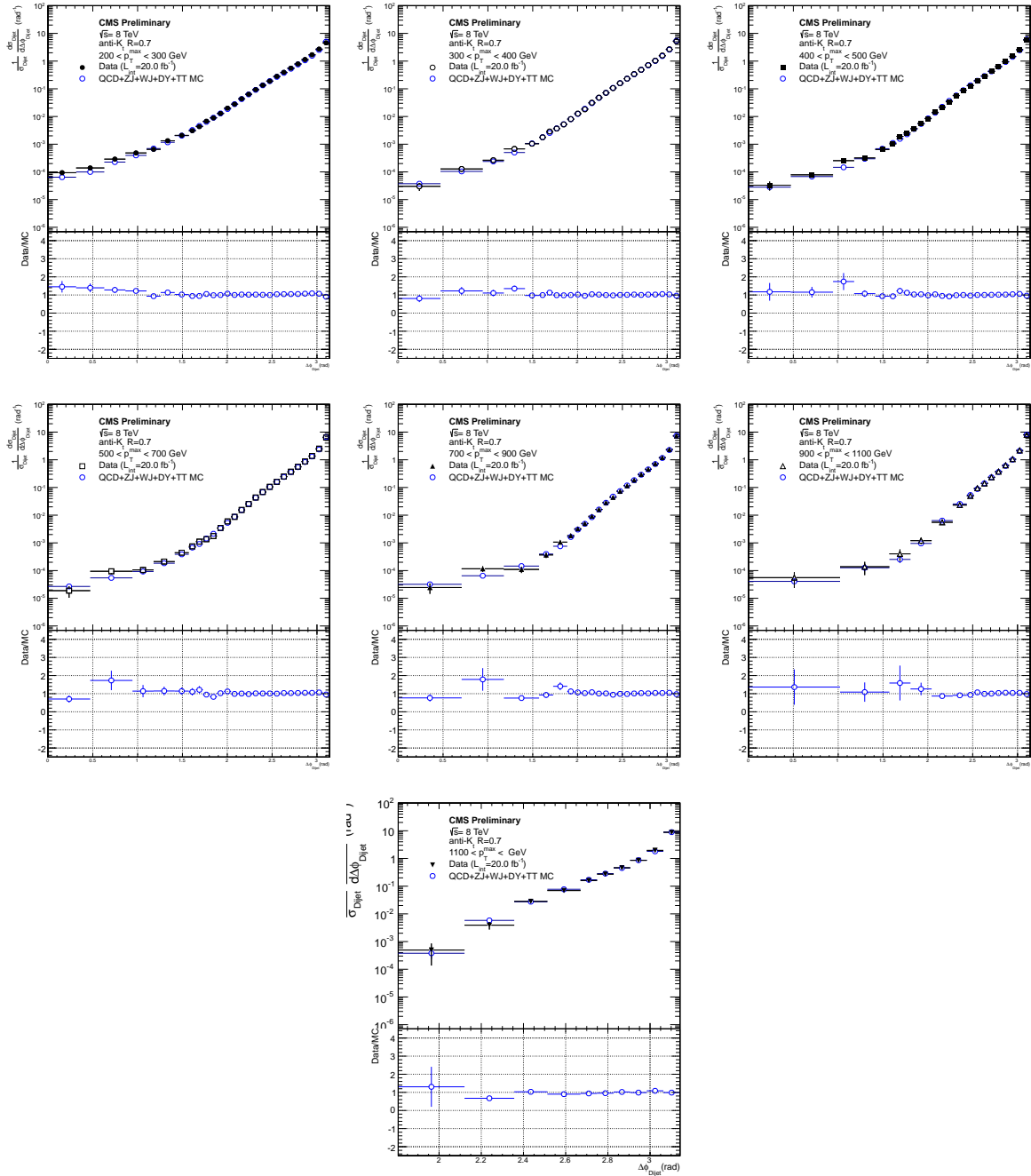
Figure 69: The differential dijet cross section in $\Delta\phi_{\text{Dijet}}$ for the seven $p_{\text{T,max}}$ regions, for various processes without cut at $\not{E}_T / \sum E_T$. Data over MC ratio (bottom of each plot).
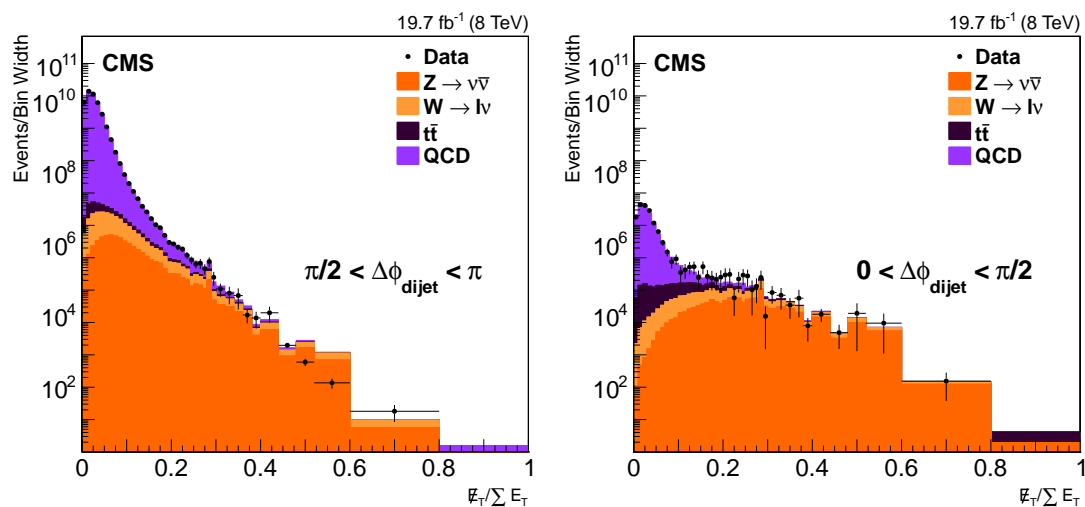
Figure 70: Reweighted $\not{E}_T / \sum E_T$ distributions for data (black points) and various MC samples(stacked) for $\pi/2 < \Delta\phi_{\text{Dijet}} < \pi$ (left) and $0 < \Delta\phi_{\text{Dijet}} < \pi/2$ (right).

shows the remaining shape distortion, where the rejected QCD is somewhat compensated by accepted "background". The ratio shows that the distorted points are all within the experimental uncertainties and the statistical uncertainty of the MC.

Figure 72 shows the same study without any reweighting of the MC. The results are almost identical with and without reweighting.

Figure 71: The differential dijet cross section in $\Delta\phi_{\mathrm{Dijet}}$ (top of each plot) for the seven $p_{\mathrm{T,max}}$ regions, for QCD Monte Carlo without cut at $\not{E}_T / \sum E_T$ and QCD - QCD(Rej.) + Bkg(Acc.). Cross section ratios (bottom of each plot) of [QCD - QCD(Rej.) + Bkg(Acc.)] over QCD. The Monte Carlo has been reweighted.

Figure 72: The differential dijet cross section in $\Delta\phi_{\text{Dijet}}$ (top of each plot) for the seven $p_{\text{T,max}}$ regions, for QCD Monte Carlo without cut at $\not{E}_T / \sum E_T$ and QCD - QCD(Rej.) + Bkg(Acc.). Cross section ratios (bottom of each plot) of [QCD - QCD(Rej.) + Bkg(Acc.)] over QCD.

7.2.2   Unfolding

The measured observables from various experiments cannot be compared directly to each other since each measurement is perturbed from different detector smearing effects. The measurements cannot be compared to theoretical predictions that do not simulate detector effects thus the unfolding method is used, which removes the detector effects from data and converts the measurement from detector to particle level.

The normalized dijet cross section differential in $\Delta\phi_{\text{Dijet}}$ has been unfolded using the inversion matrix method as is implemented by in the package ROOUNFOLD. The unfolding method takes as input the measured spectrum and the migration matrix derived from simulations. The output of the unfolding method is the unfolded spectrum and the covariance matrix of the unfolded spectrum.

The migration matrix can be derived using Monte Carlo simulations that contain information of the generated jets and the reconstructed jets with detector effects simulated. The lack of simulated events impels to the construction of a toy MC that allows the generation of a larger number of simulated events. The toy MC uses the generated level spectrum from PYTHIA6 with tune Z2* [60] and the smearing effects are taken into account using the $\Delta\phi_{\text{Dijet}}$ resolution. Figure 73 shows the resolution of $\Delta\phi_{\text{Dijet}}$ in bins of $p_{\text{T,max}}$, derived using PYTHIA6 TuneZ2* MC. Table 23 shows the results of the resolution studies, those values were used to construct the Toy MC.

Table 23: Summary of the $\Delta\phi_{\text{Dijet}}$ resolution studies.

$p_{\text{T,max}}$ (GeV)	(Gen_$\Delta\phi_{\text{Dijet}}$ - PF_$\Delta\phi_{\text{Dijet}}$)/Gen_$\Delta\phi_{\text{Dijet}}$ (%)
200-300	0.66
300-400	0.48
400-500	0.42
500-700	0.35
700-900	0.30
900-1100	0.27
1100-	0.25

Figure 74 shows the comparison of the spectrum derived from PYTHIA6 compared to the spectrum derived from the toy MC. A sanity check is shown in 74, where is shown that the toy MC spectra is almost identical to PYTHIA6, thus the underlying physical processes are propagated to the toy MC spectrum. The migration matrix, shown in figure 75, is constructed using the toy MC.

Using as inputs the migration matrix of Fig. 75 and the reconstructed spectrum shown in Fig 76(red), the unfolding method yielded the spectrum shown in Fig 76(blue). The particle level(unfolded) distributions compared to the detector level distributions differ by 3 to 4% for $\Delta\phi_{\text{Dijet}} < \pi/2$ and by less than 3% for $\pi/2 < \Delta\phi_{\text{Dijet}} < \pi$.
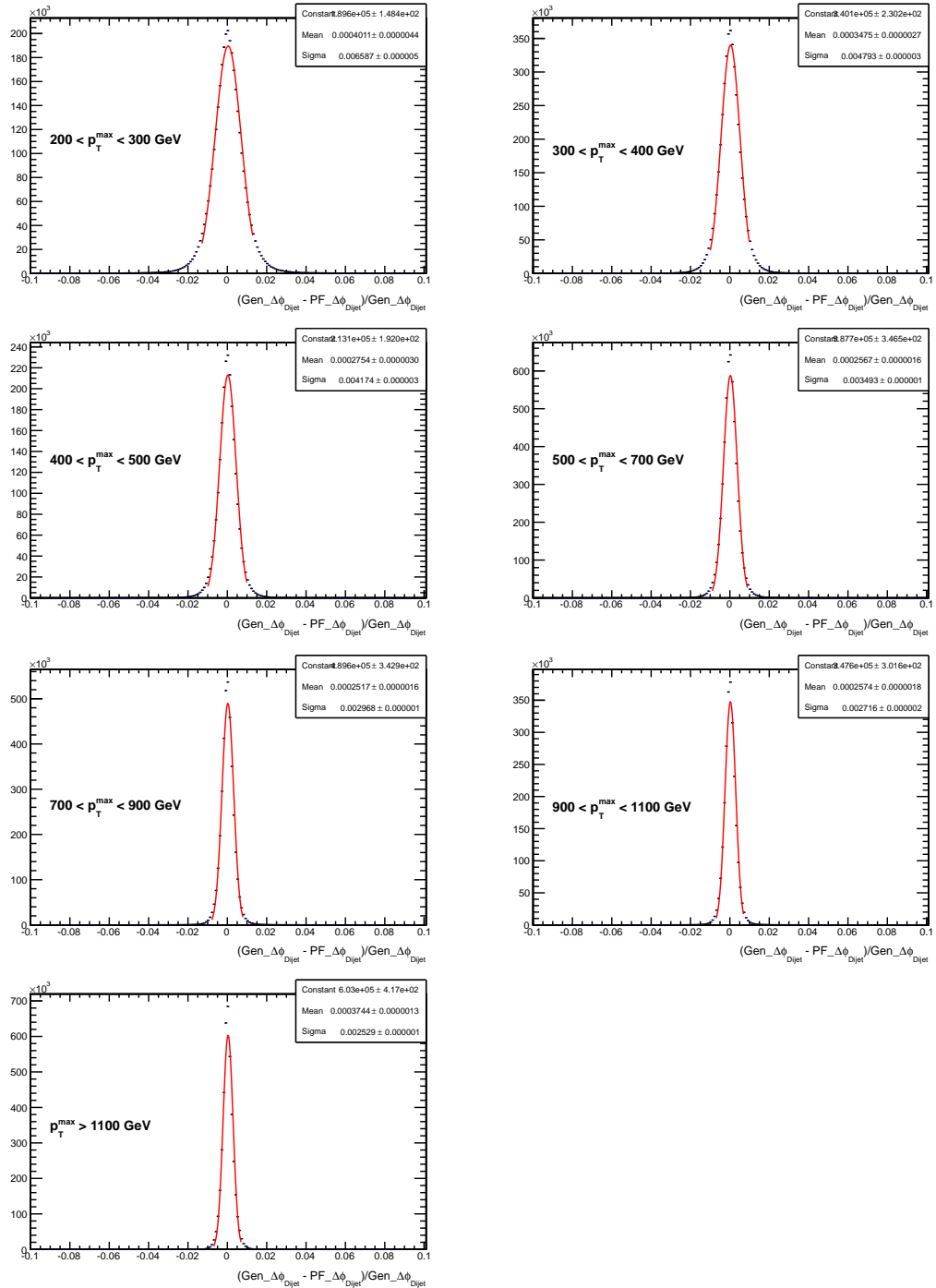
Figure 73: The $\Delta\phi_{\mathrm{Dijet}}$ resolution for each range of $p_{\mathrm{T,max}}$ used in this analysis.
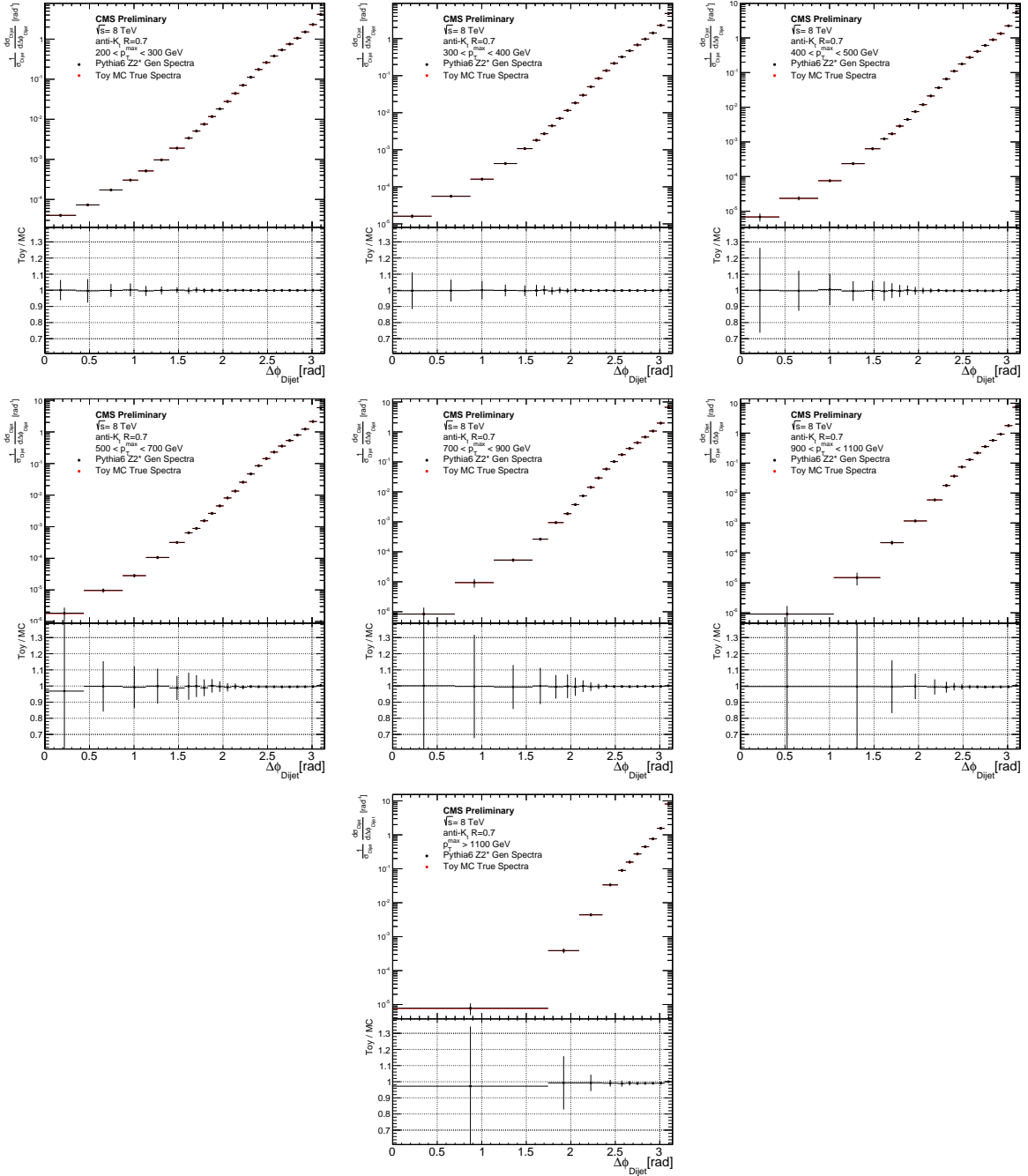
Figure 74: The normalized differential dijet cross section in $\Delta\phi_{\mathrm{Dijet}}$ (top of each plot) for the seven $p_{\mathrm{T,max}}$ regions, for the PYTHIA6 tune Z2* particle (GEN) level (black points) and for the Toy MC true level (red points). Ratios between the PYTHIA6 tune Z2* GEN Spectra and the Toy MC true spetra(bottom of each plot).
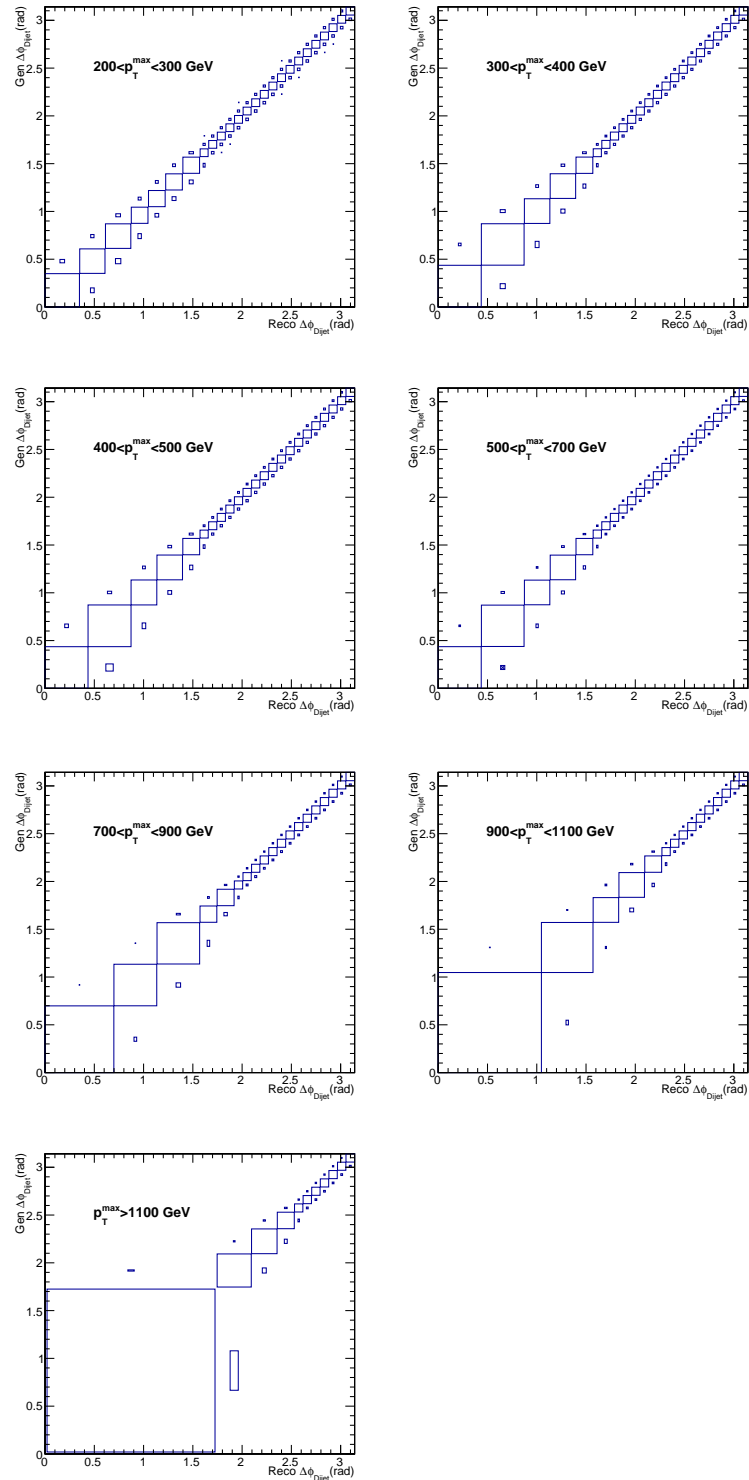
Figure 75: The responce matrices derived using a Toy MC which utilizes the true differential dijet cross sections in $\Delta\phi_{\text{Dijet}}$ (using GenJets) from PYTHIA6 tune Z2* MC.

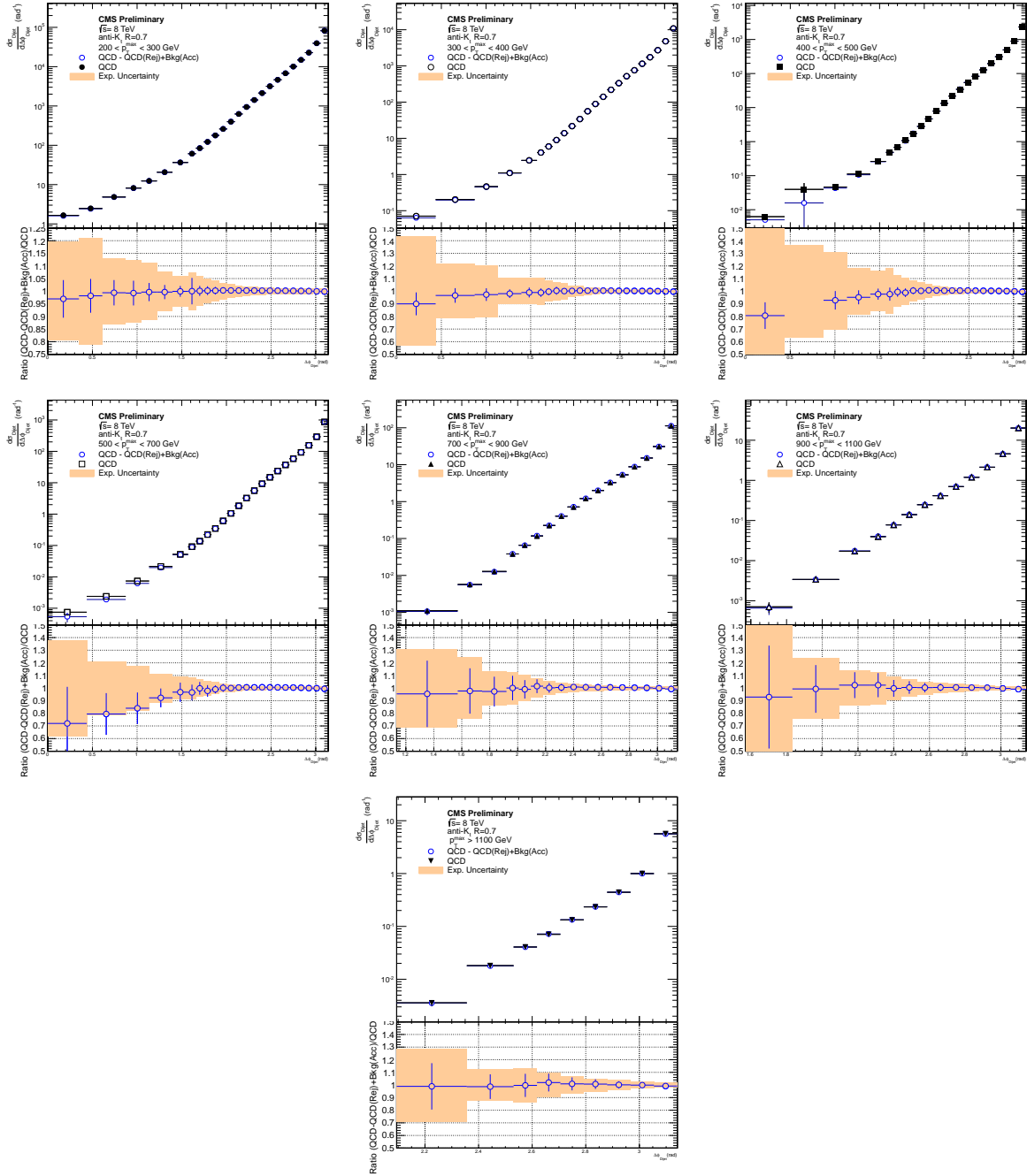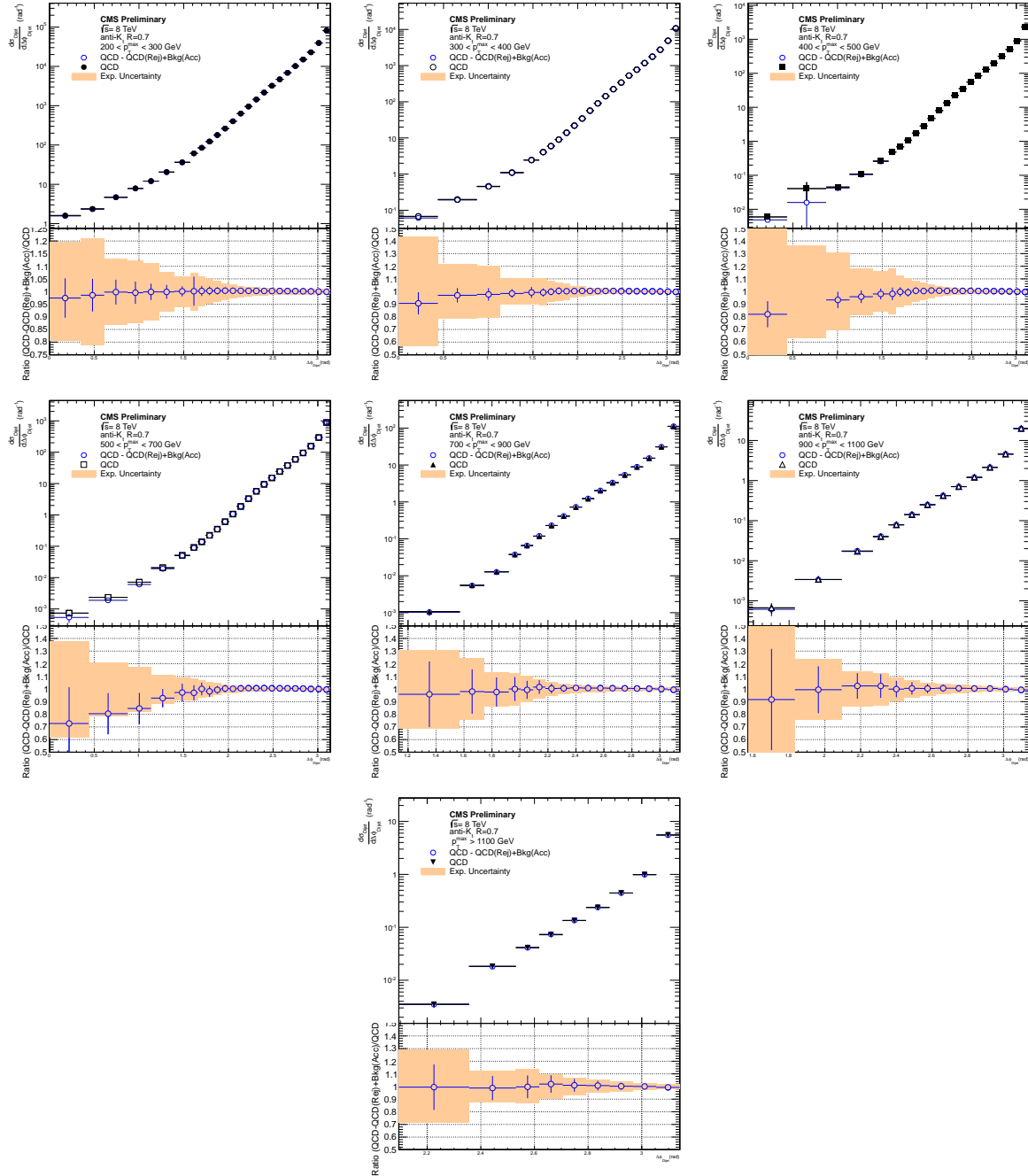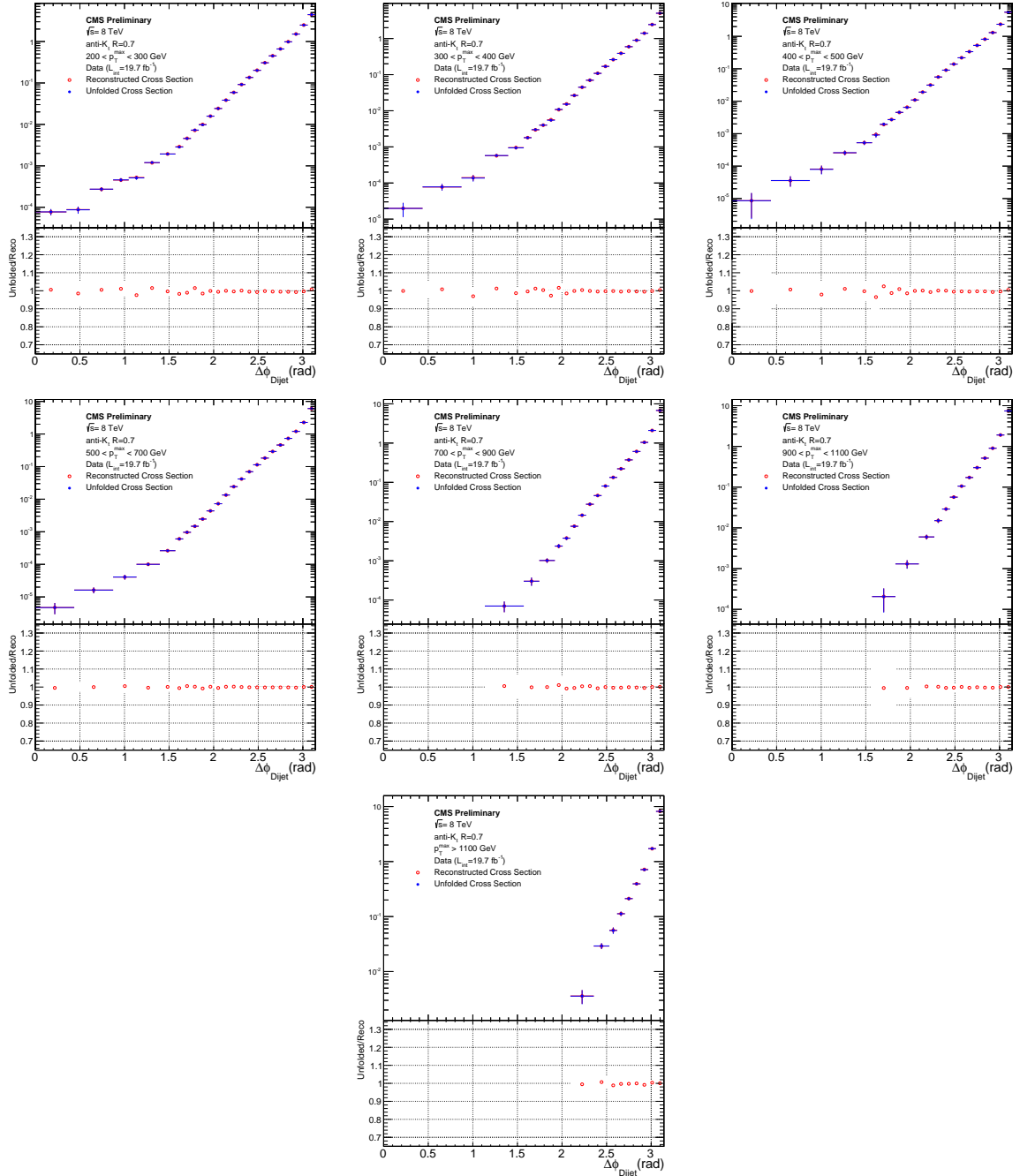Figure 76: The normalized differential dijet cross section in $\Delta\phi_{\text{Dijet}}$ (top of each plot) for the seven $p_{\text{T,max}}$ regions, for data at reconstruction (detector) level (open circles) and at stable-particle level (solid circles). Ratios between stable-particle level and reconstruction level (bottom of each plot). Response matrices derived from a Toy MC.

7.2.3 Systematic Uncertainties

The imprecise knowledge of the detector leads to the introduction of systematic uncertainties. The main uncertainties that affect the measurement of the normalized dijet cross section arise from:

- Jet energy scale uncertainties
- Unfolding
- Jet energy resolution

7.2.3.1 Jet energy scale uncertainties

The evaluation of the jet energy corrections described in chapter 5 is based on some assumptions and extrapolations that add an uncertainty to the corrections. The jet energy corrections used in the analysis are accompanied by twenty four mutually uncorrelated uncertainty sources. Each source represent a signed 1σ variation for each point in p_T and η.

The description of the sources and the way the have been calculated can be found in Ref. [61]. The important sources of the analysis are described below:

- AbsoluteStat, AbsoluteScale: these uncertainties for constant scale (AbsoluteScale) and p_T-dependent scale (AbsoluteStat) are extracted from a global fit to Z/gamma+jet and multijet data.

- AbsoluteMPFBias: additional constant scale uncertainty added for the biases of the MPF and p_T balanced methods coming from neutrinos and ISR outside of detector acceptance.

- Fragmentation: Based on Pythia6 Z2/Herwig++2.3 differences in fragmentation and underlying event (FullSim).

- SinglePionECAL, SinglePionHCAL: shape uncertainties for p_T-dependence considered from varation of single pion responses in ECAL and HCAL relative to the global fit reference of pT=208 GeV

- FlavorQCD: jet flavor. Based on Pythia6 Z2/Herwig++2.3 differences in uds/c/b-quark and gluon responses. It describes the uncertainty when extrapolating from the flavor composition in gamma/Z+jet events that are used to measure the absolute scale in data to the QCD mixture.

- RelativePtBB, RelativePtEC1 : these uncertainties arise as residual log-linear p_T dependence relative to the central fit (constant in BB, HF, log-linear in EC1, EC2 possibly due to radiation damage).

- RelativeFSR : this uncertainty arises from the eta-dependence uncertainty due to correction for final state radiation. Uncertainty increases toward HF, but is correlated from one region to the other.

- PileUpDataMC : rho-dependence of the data/MC difference observed in the data-based Random Cone method in Zero Bias data (RCZB). The L1 corrections assumes a scale factor constant in rho; take the variation of this data/MC scale factor within <rho> +/-RMS(rho).

- PileUpPtRef : the p_T dependent difference between the MC truth and the random cone offset in MC in the barrel could influence the global fit. This difference is propagated through a mock-up of Z/gamma+jet (L3Res) and dijet (L2Res) balancing machinery to estimate the remaining residual pileup uncertainty after L2L3Res.

- PileUpPtBB: this uncertainty arises from the observed variation of effective pile-up

versus p_T e.g. due to zero suppression effects.

The impact of the JES uncertainties at the measured quantity has been evaluated by varying each the p_T of each jet as: $p_{Tsource\pm} = p_T \pm \sigma_{source}$. The normalized dijet cross section evaluated for the two new samples with the shifted p_T; the envelope of the two is considered as the systematic uncertainty.

The uncertainty derived from one source (AbsoluteMPFBias) is shown in figure 77, it is observed that the uncertainty depends on $\Delta\phi_{\text{Dijet}}$. The resulting uncertainties in the normalised $\Delta\phi_{\text{Dijet}}$ dijet distributions range from 7% at $\Delta\phi_{\text{Dijet}} \approx 0$ via 3% at $\pi/2$ to 1% at π.
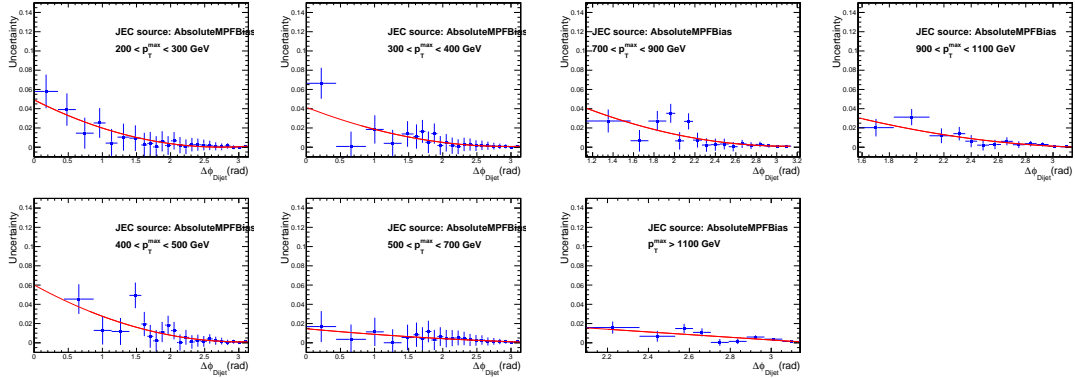
Figure 77: The systematic uncertainties on the normalized differential dijet cross section in $\Delta\phi_{\text{Dijet}}$ due to the AbsoluteMPFBias JES source uncertainty.

7.2.3.2   Unfolding

The unfolding method described in subsection 7.2.2 is based on the assumption that the MC and the resolution used to construct the migration matrix correspond to reality. Alternative Monte Carlos were used in order to evaluate the impact of the choice of the MC in the unfolded spectra. HERWIG++ and MADGRAPH events generators were also used to construct the migration matrix, the observed effect is less than 1%. The uncertainty due to the insufficient knowledge of the $\Delta\phi_{\text{Dijet}}$ resolution is estimated by varying the $\Delta\phi_{\text{Dijet}}$ resolution by $\pm 10\%$, which is a conservative estimate and is motivated by the observed difference between data and simulation in the jet $\Delta\phi_{\text{Dijet}}$ resolution [41]. The uncertainty due to the $\Delta\phi_{\text{Dijet}}$ variation is of the order of 1%.

7.2.3.3   Jet p_T resolution

The jet p_T resolution is responsible for migration of events between the $p_{T,max}$ bins, and is studied using the PYTHIA6 tune Z2* MC. The extracted p_T resolution does not describe the resolution derived from data thus the discrepancy between the two has to be take into account. The scale factors need to be applied to into account Data/MC resolution discrepancy are shown in table 24.

In order to evaluate the uncertainty due to the JER the cross sections were evaluated by smearing the generator level jets. Three samples were created by using the nominal JER and by varying it upwards and downwards according to the scale factors of table 24. Uncertainties evaluated by comparing the cross section obtained with the nominal value of the resolution with those where resolution varied up and down.

Table 24: The scale factors for the jet p_T resolution recommented by the Jet-MET.

$\lvert y \rvert$	c	c-up	c-down
0.0-0.5	1.079	1.105	1.053
0.5-1.1	1.099	1.127	1.071
1.1-1.7	1.121	1.150	1.092
1.7-2.3	1.208	1.254	1.162
2.3-2.8	1.254	1.316	1.192

Table 25 shows the systematic uncertainties from the three sources in the region below and above $\pi/2$. The systematic uncertainty due to the luminosity measurement is cancelled out since the dijet cross section is normalized to the total dijet cross section. Uncertainty due to pile-up effects was studied and found to be negligible since the analysis records high-p_T jets that are unlikely to arise pile-up interactions.

Table 25: The systematic uncertainties due to jet p_T resolution for the seven $p_{T,max}$ bins.

Source	$0 < \Delta\phi_{\text{Dijet}} < \pi/2$	$pi/2 < \Delta\phi_{\text{Dijet}} < \pi$
JES	7-3%	3-1%
Unfolding	1%	1%
JER	5-3%	3-0.5%

7.3   Comparison to Monte Carlo generators

PYTHIA6,PYTHIA8, and HERWIG++ are dijet leading order Monte Carlo generators that simulate higher order processes via the parton showers as described in subsection 4.8.4. Thus the dijet LO generators can yield more than two jets at the final states giving events with $\Delta\phi_{\text{Dijet}} < \pi$. The POWHEG framework provides a NLO dijet calculation and is interfaced with PYTHIA8 that simulates parton shower. MADGRAPH is the only LO matrix generator that produces from two to four partons in the final state, while parton shower is simulated by interfacing MADGRAPH to PYTHIA6.

Figures 78 and 79 show the comparison of data (black solid points) to the various MC generators. PYTHIA6,PYTHIA8, and HERWIG++ LO generators systematically overshoot data especially in the region below $5\pi/6$. Despite the fact that POWHEG is a dijet NLO generator interfaced to PYTHIA8 give similar results to PYTHIA8 alone. MADGRAPH interfaced to PYTHIA6 gives the best result throughout the $\Delta\phi_{\text{Dijet}}$ region.

Figure 78: The normalised dijet cross section differential in $\Delta\phi_{\text{Dijet}}$ for seven $p_{\text{T,max}}$ regions, scaled by multiplicative factors for presentation purposes. The error bars on the data points include statistical and systematic uncertainties. Overlaid on the data are predictions from the PYTHIA6, HERWIG++, PYTHIA8, MADGRAPH +PYTHIA6 and POWHEG +PYTHIA8 MC event generators.

Figure 79: Ratios of PYTHIA6, HERWIG++, PYTHIA8, MADGRAPH +PYTHIA6 and POWHEG +PYTHIA8 predictions to the normalised dijet cross section differential in $\Delta\phi_{\text{Dijet}}$, for all $p_{\text{T,max}}$ regions. The solid band indicates the total experimental uncertainty and the error lines on the MC points represent the statistical uncertainties of the simulated data.

7.4 Comparison to theoretical predictions

The theoretical predictions for the normalized differential dijet cross section in $\Delta\phi_{\text{Dijet}}$, are based on a 3-jet calculation at NLO. The correction of nonperturbative (NP) effects to account for multiparton interactions (MPI) and hadronization has been studied using event samples simulated with the PYTHIA6 tune Z2* and HERWIG++ tune 2.3 MC event generators. The corrections were found to be of the order of 1%, which is at the limit of the accuracy of the MC simulations. Therefore NP corrections are considered to be negligible and no such correction was applied to the pQCD predictions. The study is described in appendix C.

The theoretical calculations are performed using the NLOJET++ program version 4.1.3, within the framework of the FASTNLO package version 2.3.1. The differential cross section is calculated for 3-jet production at NLO, up to terms of order α_S^4 resulting into three or four partons in the final state. Thus the differential cross section is calculated at LO in the region $\pi/2 < \Delta\phi_{\text{Dijet}} < 3\pi/2$ where topologically at least four jets are required for $\Delta\phi_{\text{Dijet}} < 3\pi/2$ and at NLO in the region $\pi/3 < \Delta\phi_{\text{Dijet}} < \pi$. For consistency the normalization cross section for each slice in $p_{\text{T,max}}$ is derived as dijet cross section at LO in the region $\pi/2 < \Delta\phi_{\text{Dijet}} < 3\pi/2$ and at NLO in the region $\pi/3 < \Delta\phi_{\text{Dijet}} < \pi$. The bin at π cannot be calculated directly since higher order calculations and soft gluon radiation re-summation are required but cannot be handled by NLOJET++. The bin at π was calculated as the NLO dijet cross section within this bin. The number of flavors is set to five, the quarks are assumed to be massless, and the renormalisation and factorisation scales, μ_r and μ_f, are chosen to be equal to $p_{\text{T,max}}$. The parton density function (PDF) sets, with NLO evolutions, used for the calculations are tabulated in table 5.

The uncertainties due to renormalisation and factorisation scales are evaluated by varying the default choice of $\mu_r = \mu_f = p_{\text{T,max}}$ between $p_{\text{T,max}}/2$ and $2p_{\text{T,max}}$, simultaneously in the differential cross section and in the total cross section, in the following six combinations: $(\mu_r / p_{\text{T,max}}, \mu_f / p_{\text{T,max}})$ = (0.5,0.5), (0.5,1), (1,0.5), (1,2), (2,1) and (2,2). The PDF uncertainties are evaluated according to the prescriptions recommended for CT10 PDF set in Ref. [62] and described in subsection 4.9.3.

In figure 80 overlaid on the data are the results of the NLO calculations using the CT10-NLO PDF set. Figure 81 shows the ratio of the normalised differential dijet cross section in $\Delta\phi_{\text{Dijet}}$ over theory calculated using the CT10-NLO PDF set, together with the PDF and α_S (hatched area) and the scale (solid area) uncertainties. It is also shown, the ratio of theory calculated using alternative PDF sets over CT10, like ABM11 (dashed line), HERAPDF1.5 (dashed-three dotted line), MSTW2008 (dashed-dotted line), and NNPDF2.1 (dotted line).

Figure 82 shows the region $\Delta\phi_{\text{Dijet}} > 2\pi/3$ and figure 83 shows the k-factors of this region. Theory and data generally agree within the uncertainties for $\Delta\phi_{\text{Dijet}} > 2\pi/3$. Some differences are observed in the highest $p_{\text{T,max}}$ bin. Below the $\Delta\phi_{\text{Dijet}} = 2\pi/3$ region the tree level diagrams have four partons in the final state thus the NLO calculation becomes LO. This explains the differences between theoretical predictions and the steep increase of the scale uncertainties.

In order to quantify the agreement between data(D) and theory(T) and the coverage of the uncertainties the statistical pulls have been calculated. The pull is defined as:

$$p = \frac{D - T}{\sqrt{(\sigma_{exp}^2 + \sigma_{theory}^2)}} \qquad (90)$$

σ_{exp} is the total experimental uncertainty, both systematic and statistical. σ_{theory} is the quadratic
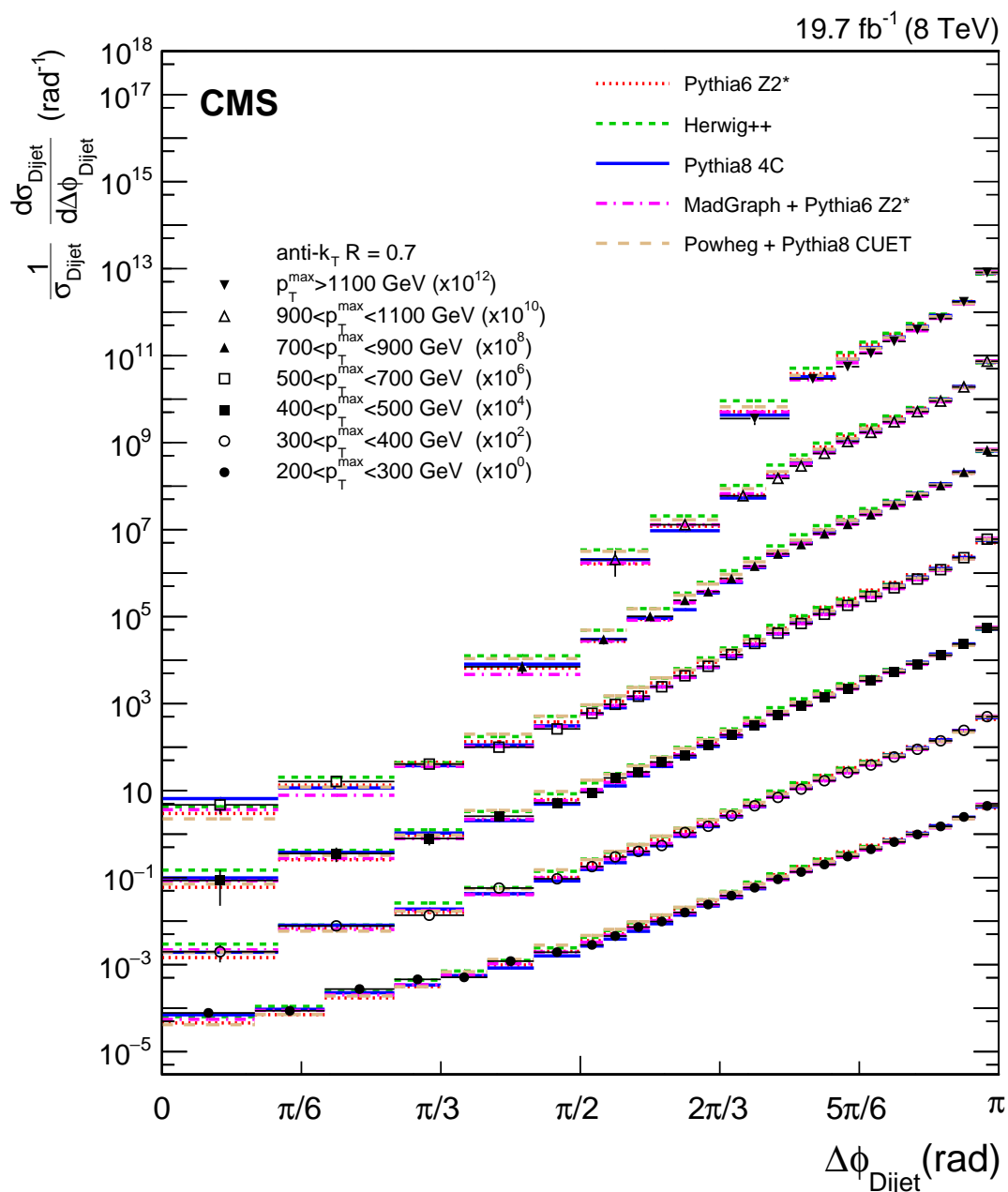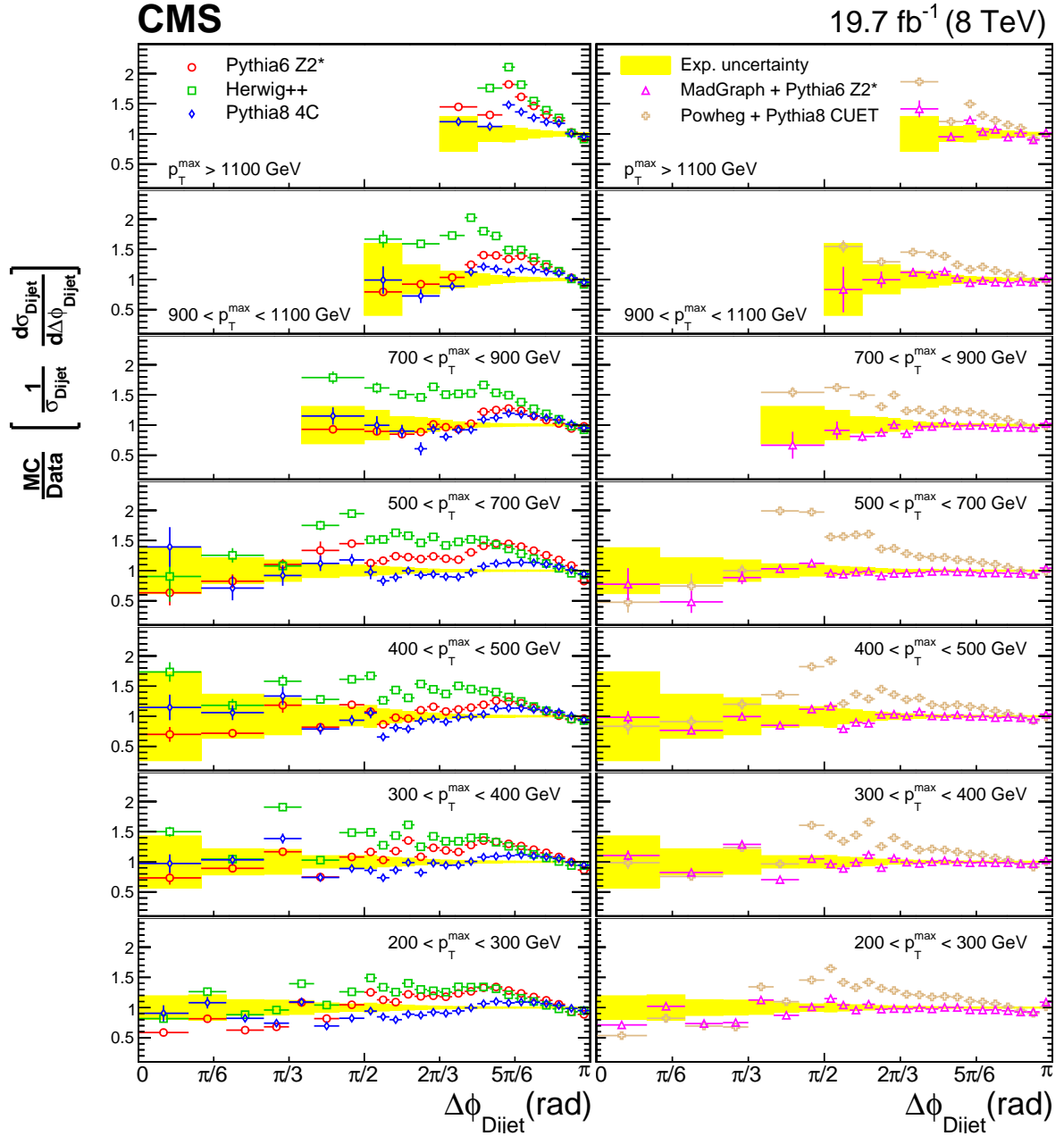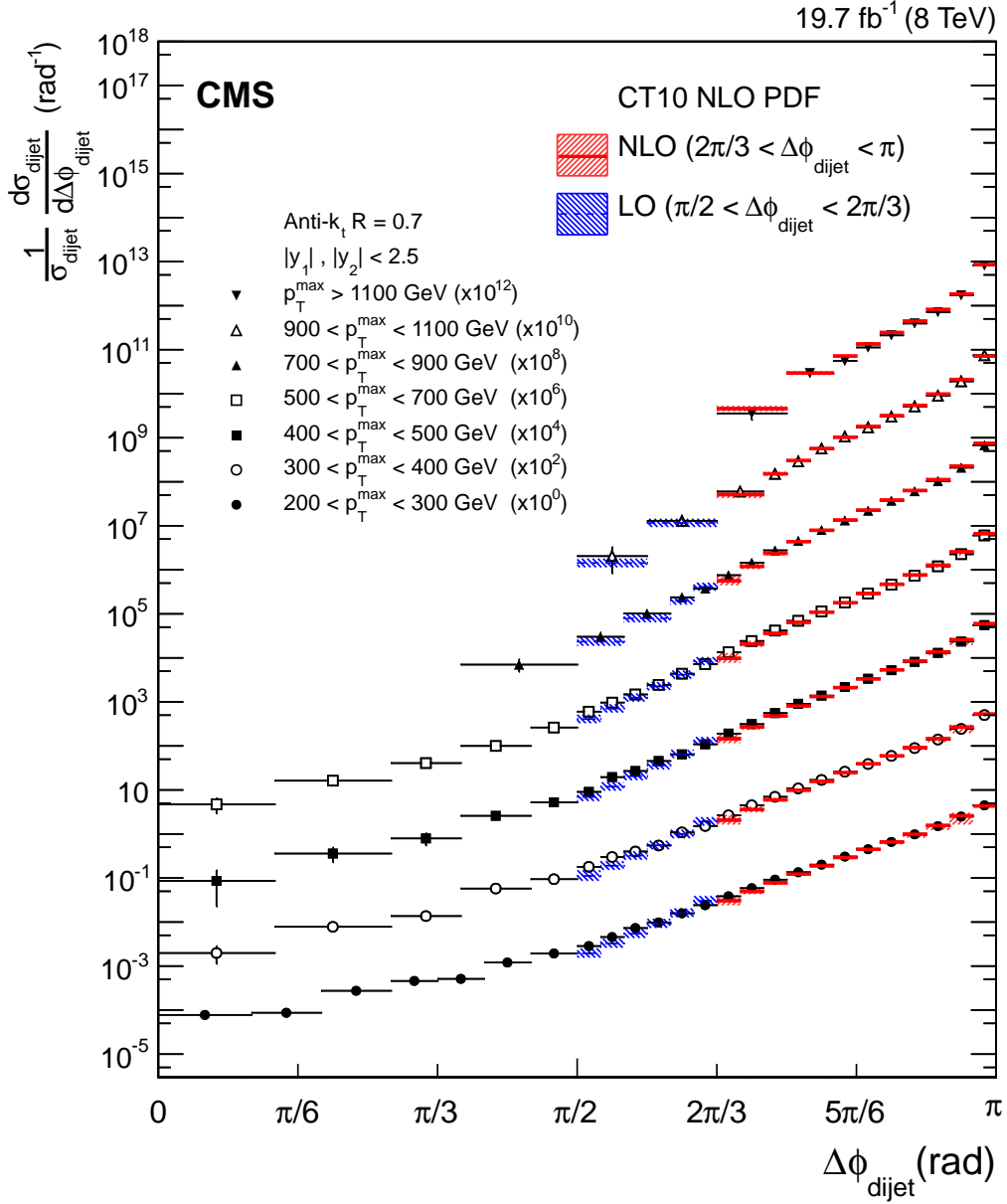
Figure 80: The normalised dijet cross section differential in $\Delta\phi_{\mathrm{Dijet}}$ for seven $p_{\mathrm{T,max}}$ regions, scaled by multiplicative factors for presentation purposes. The error bars on the data points include statistical and systematic uncertainties. Overlaid on the data(points) for $\Delta\phi_{\mathrm{Dijet}} > \pi/2$ are predictions from fixed-order calculations in pQCD (line) using the CT10 PDF set. PDF, α_S, and scale uncertainties are added quadratically to give the total theoretical uncertainty that is indicated by the hatched regions around the theory lines.
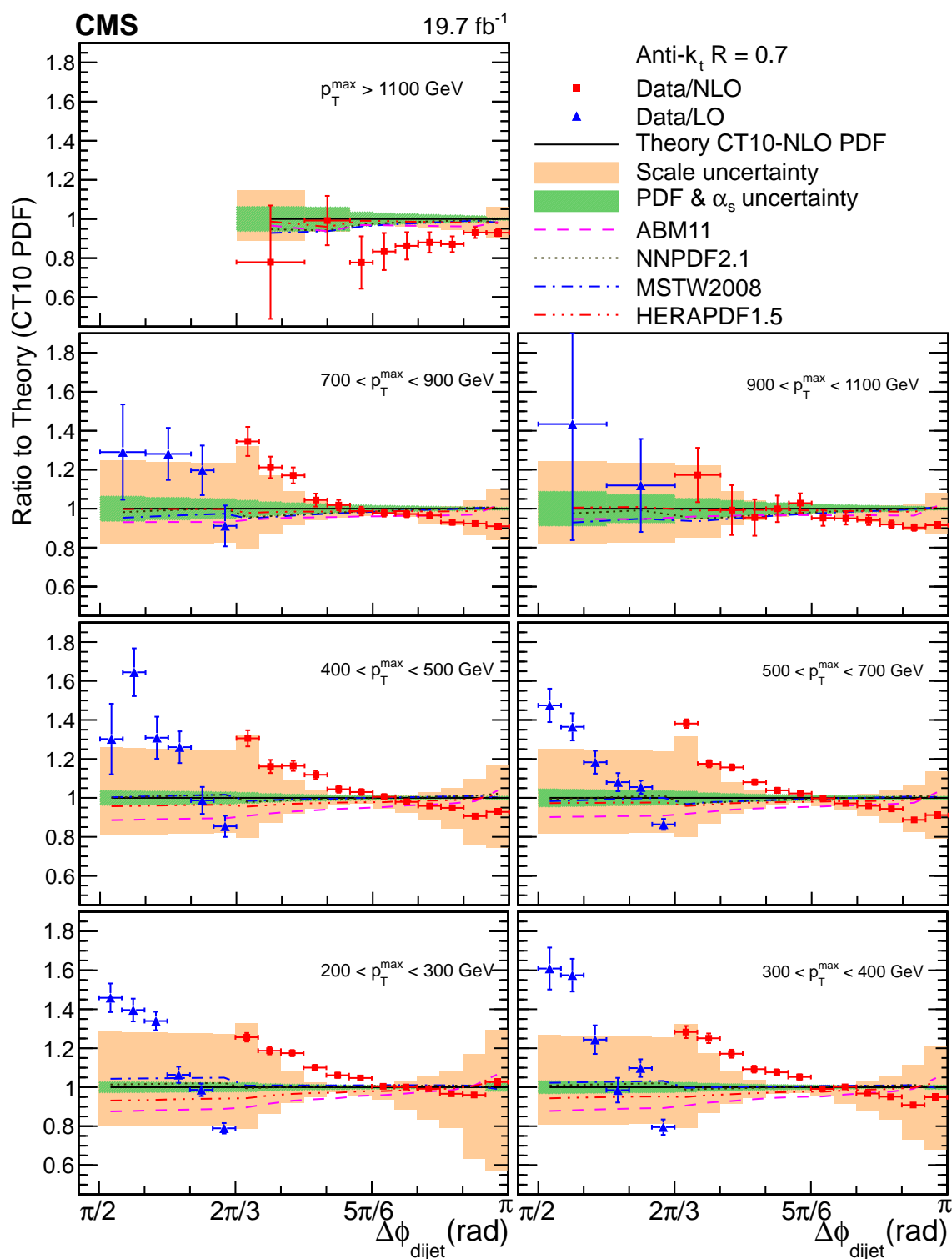
Figure 81: Ratios of the normalised dijet cross sections differential in $\Delta\phi_{\text{Dijet}}$ to fixed-order pQCD predictions using various PDF sets for all $p_{\text{T,max}}$ regions. The error bars on the data points represent the total experimental uncertainty. The uncertainties of the theoretical predictions due to the uncertainties of the PDFs, α_S, and scales are shown as bands.
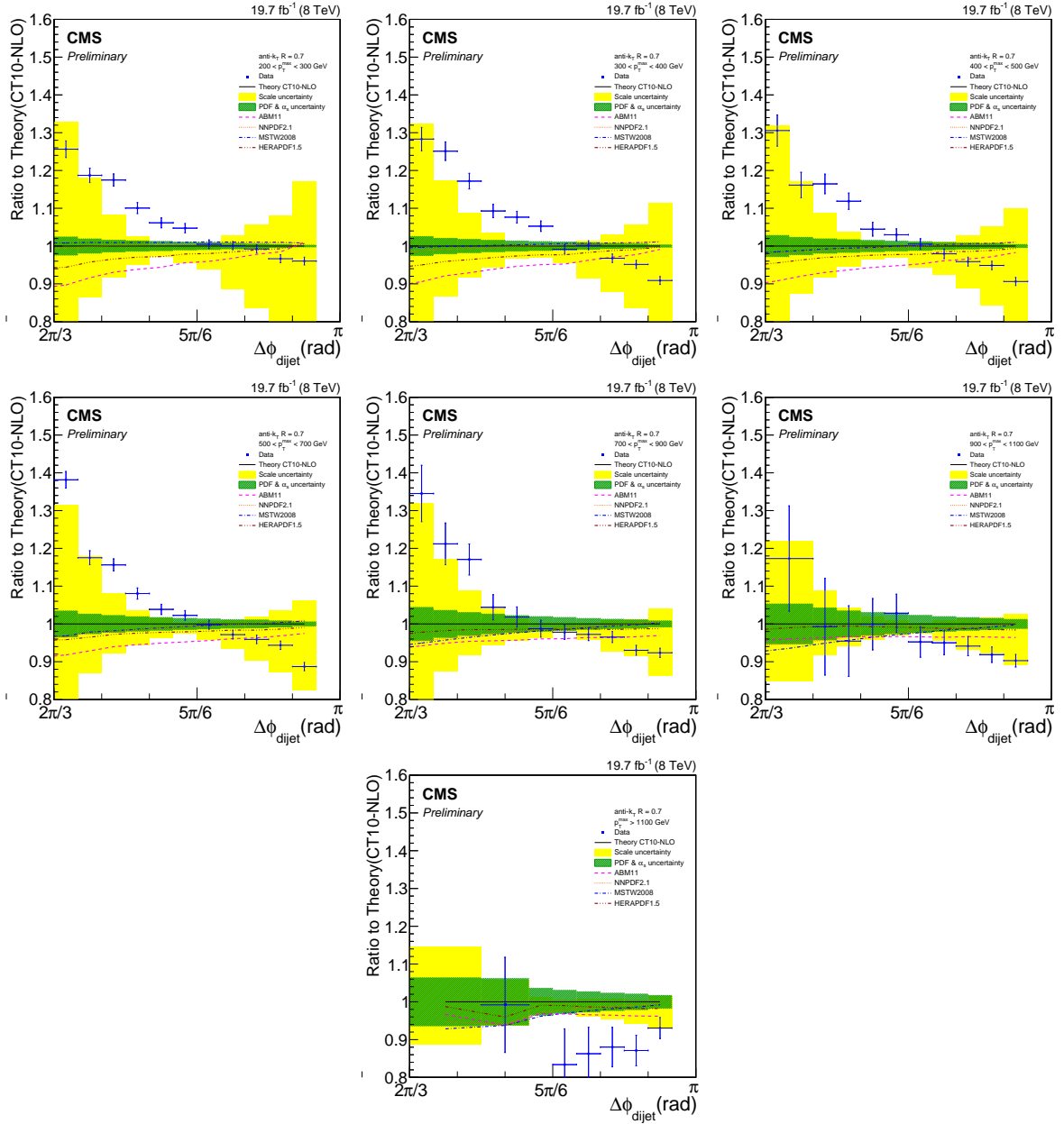
Figure 82: Ratio of the data to theory using the CT10-NLO PDF set for the five $p_{\mathrm{T,max}}$ bins starting from $\frac{2\pi}{3}$
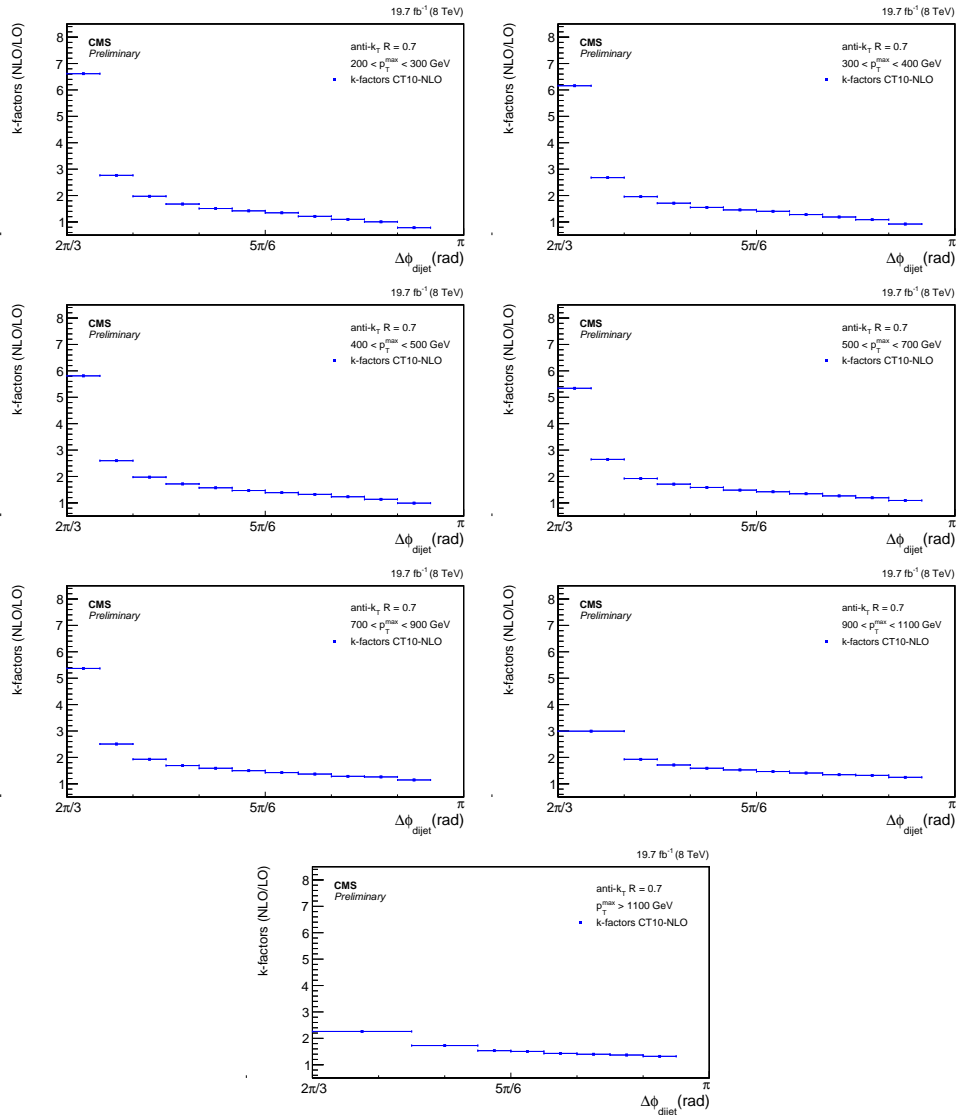
Figure 83: k-factors using the CT10-NLO PDF set for the five $p_{\text{T,max}}$ bins starting from $\frac{2\pi}{3}$

sum of scale, PDF and α_S uncertainty.

Figure 84 shows the pulls (in blue points) for the CT10-NLO PDF set. The black solid line shows the theoretical mean while the orange band shows the theoretical width of the pull distributions.

It is observed that in the region $5\pi/6 < \Delta\phi_{\text{Dijet}} < \pi$ that the pulls are close to one, except for the highest $p_{\text{T,max}}$ region. The region $2\pi/3 < \Delta\phi_{\text{Dijet}} < 5\pi/6$ exhibits the largest pulls due to the fact that the estimated theoretical uncertainties become very small. In the region $2\pi/3 < \Delta\phi_{\text{Dijet}} < \pi$ there is a tendency of larger pulls towards the smaller $\Delta\phi_{\text{Dijet}}$ region. The same pattern exists in the LO region but with less significance due to the large scale uncertainty.
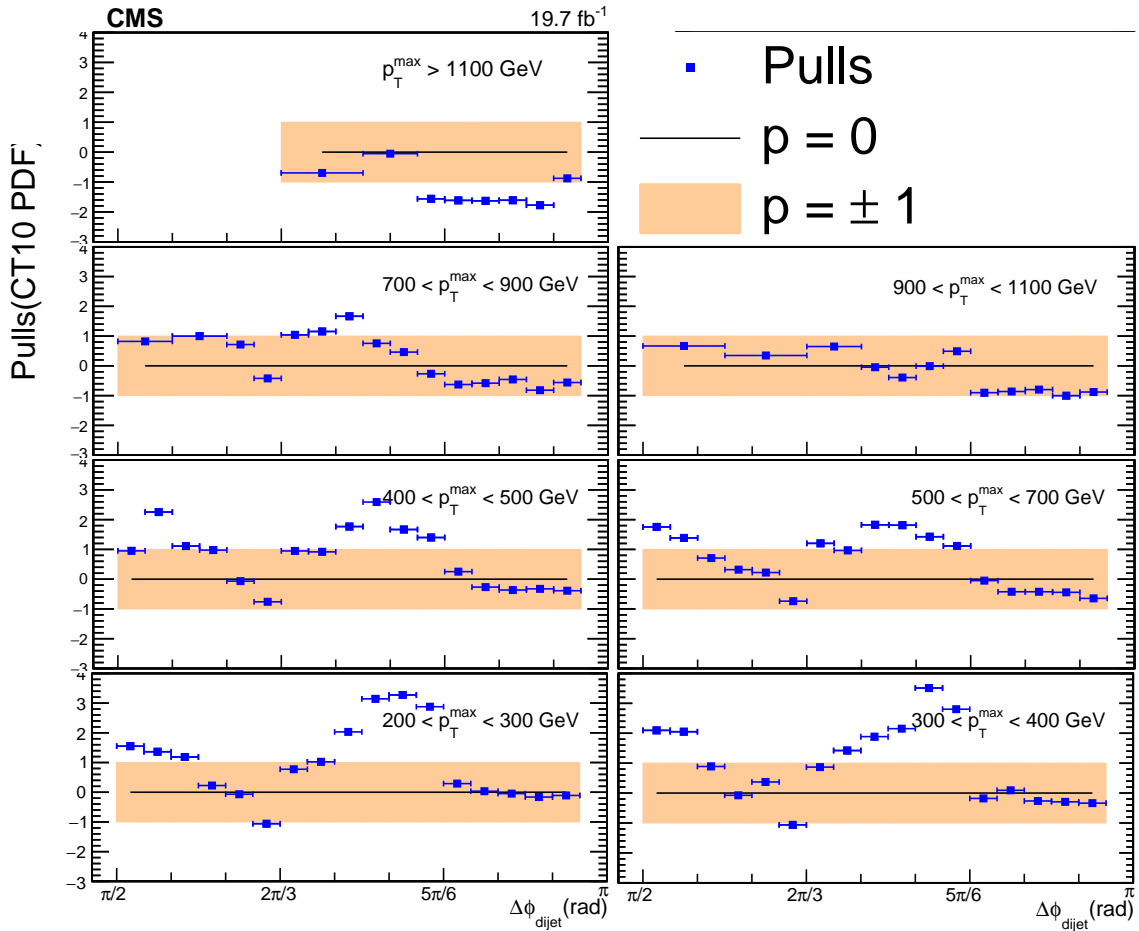
Figure 84: Pulls (blue points) for all $p_{\text{T,max}}$ regions using CT10 for the theoretical calculations.

Figure 85 shows that the proportion of the events with more than three jets is becoming significant for smaller $\Delta\phi_{\text{Dijet}}$ values. This explains why the description of data by theory is getting poorer as the $\Delta\phi_{\text{Dijet}}$ gets smaller and the fact that the k-factors (NLO/LO), shown in figure 83, are becoming larger.
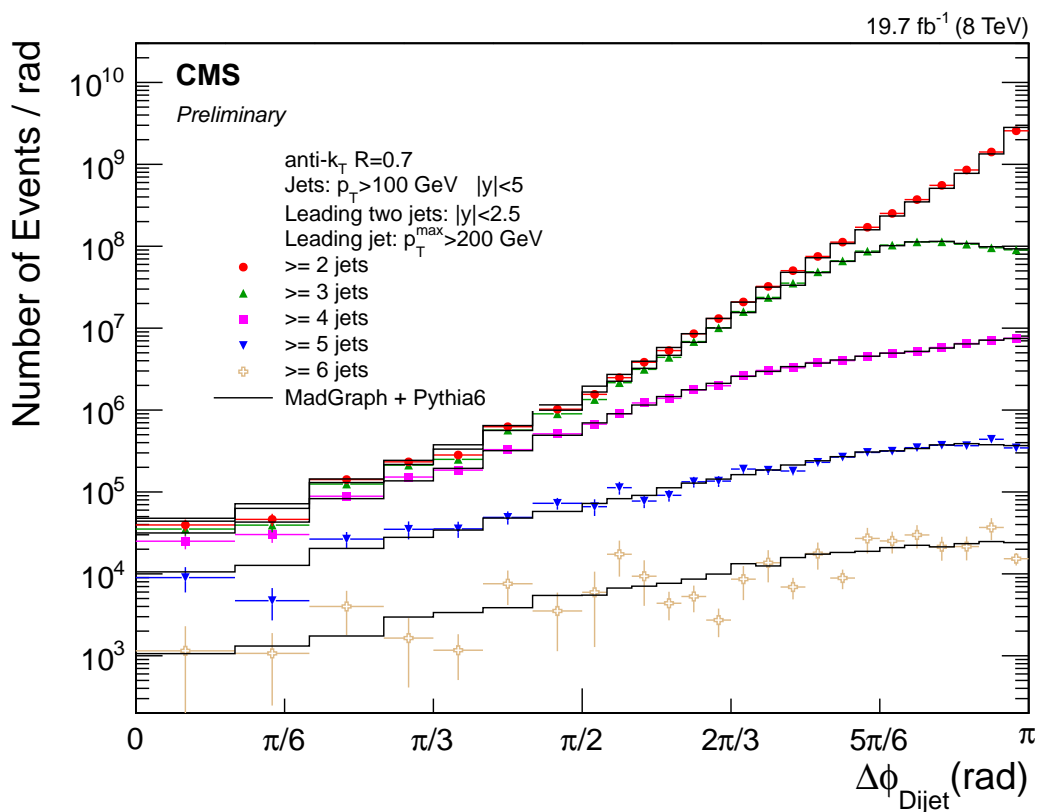
Figure 85: The $\Delta\phi_{\mathrm{Dijet}}$ distribution for events with at least 2, 3, 4, 5 and 6 jets with $p_{\mathrm{T}} > 100$ GeV and $|y| < 5$. The two leading jets, which define $\Delta\phi_{\mathrm{Dijet}}$, have $|y| < 2.5$ with the p_{T} of the leading one to be greater than 200 GeV.

7.5 Study of the sensitivity to alphas variations

A study of the sensitivity of the normalized differential cross section to $\alpha_S(M_Z)$ variation was performed in order to check the ability of extraction of the $\alpha_S(M_Z)$ from data. Figure 86 shows the sensitivity of the normalized differential cross section for all $p_{T,max}$ bins. The slope that is observed between data and theory makes the observable inappropriate for extraction of the $\alpha_S(M_Z)$ with a χ^2 fit.
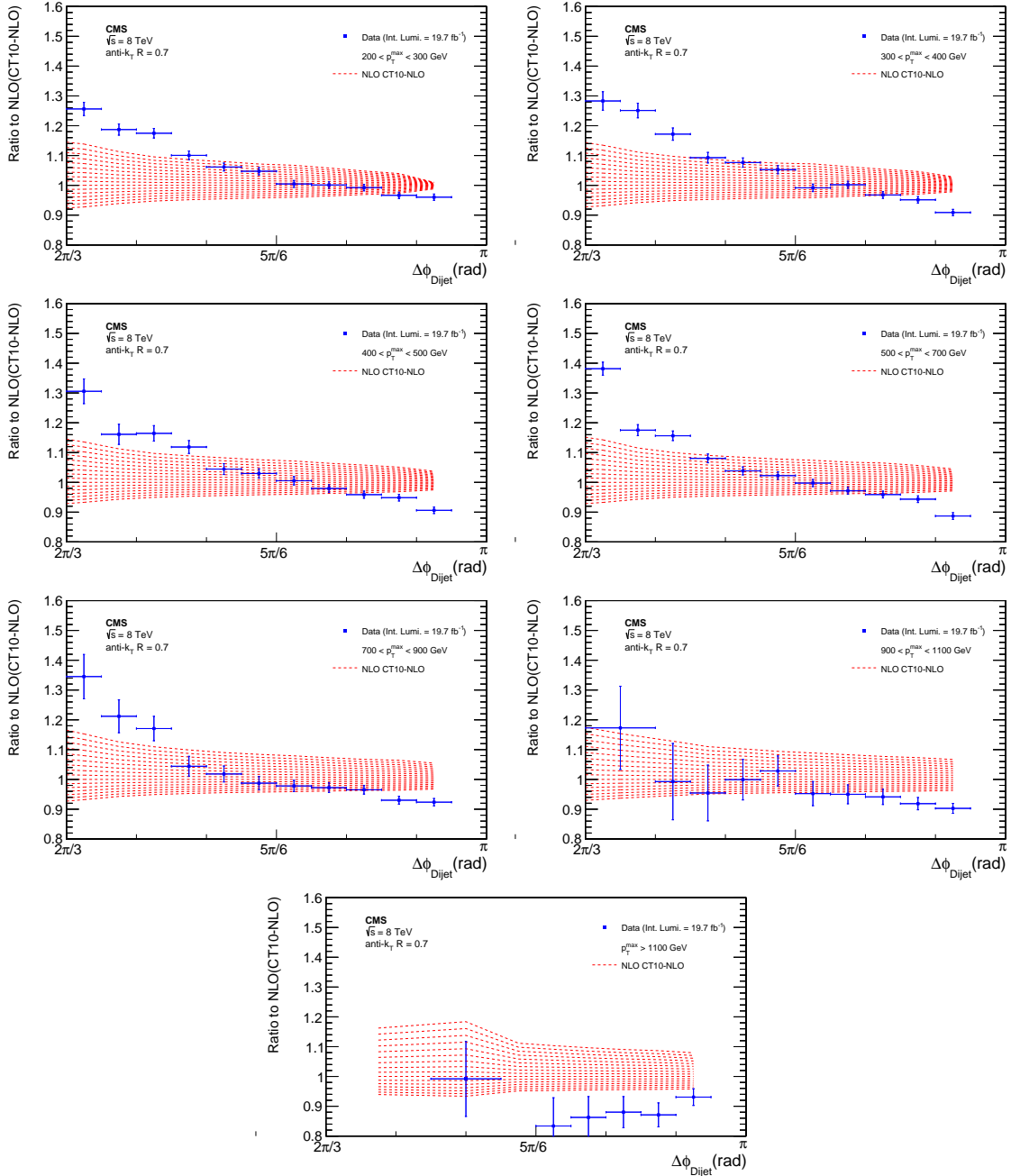
Figure 86: Sensitivity plots using CT10-NLO PDF set.

8 Summary

This thesis presented three analyses using data collected from the CMS detector during proton-proton collisions at $\sqrt{s} = 7$ TeV and $\sqrt{s} = 8$ TeV. All three analyses are studying events with jets in the final state.

The first analysis presented used the measurement from the inclusive jet cross sections in order to extract the strong coupling constant. The strong coupling constant from inclusive jet cross section has be determined to be

$$\alpha_S(M_Z) = 0.1185 \pm 0.0019\,(\text{exp.}) \pm 0.0028\,(\text{PDF}) \pm 0.0004\,(\text{NP})^{+0.0053}_{-0.0024}\,(\text{scale}) \qquad (91)$$

The second analysis is the measurement of the ratio of the inclusive $3-$jet cross section to $2-$jet cross section and the extraction of the strong coupling constant. The strong coupling constant from R_{32} has be determined to be

$$\alpha_S(M_Z) = 0.1148 \pm 0.0014(exp.) \pm 0.0018(PDF) \pm 0.0050(theory) \qquad (92)$$

The analysis of ratio 3jet to 2jet has been performed in order to derive a better measurement of $\alpha_S(M_Z)$ compared to the inclusive jet measurement, in terms of uncertainties. This hypothesis derived from the fact that the ratio cancels out both experimental and theoretical uncertainties. The results thought shows that only the PDF uncertainty was reduced significantly while experimental and theoretical uncertainties are similar. The experimental uncertainty is not reduced significantly since what is gained by the cancellation of the systematic uncertainties is lost by statistical uncertainties. The scale (theory) uncertainty of R_{32} can be reduced by choosing appropriate cuts at jets p_T but at the same time sensitivity on α_S variation is reduced rendering the observable useless for α_S extraction. Thus a compromise has to be done between the scale uncertainty reduction and the sensitivity to α_S variation. Furthermore the scale uncertainties of R_{32} are larger in the low-p_T region which contributes the most to the χ^2 fits due to the small experimental uncertainties.

Both values are consistent with the world average value of $\alpha_S(M_Z) = 0.1184 \pm 0.0007$. In both cases it seems that higher order calculations are needed in order to reduce the uncertainties of the extracted α_S values since the main uncertainty arises from the renormalization and factorization scale. Another way to reduce the uncertainties is the concoction of observables that are insensitive to higher order calculations and to the PDF of the proton.

The third analysis presented the measurement of the dijet azimuthal decorrelations. The observable found to be unsuitable for the extraction of the $\alpha_S(M_Z)$ but it lead to our better understanding of QCD processes. The fixed order pQCD calculation for three jet productions results four jets provide NLO prediction for the region $\Delta\phi_{\text{Dijet}} > 2\pi/3$ and LO prediction for the region $\Delta\phi_{\text{Dijet}} < 2\pi/3$. The NLO predictions describe the data within uncertainties down to $\Delta\phi_{\text{Dijet}} \approx 5\pi/6$, below that region theory deviates significantly since events with higher jet multiplicities are non-negligible. The same pattern can be seen in the LO order region where the four jet calculation can describe data around the region $\Delta\phi_{\text{Dijet}} \approx 2\pi/3$ but below that region calculations with additional jets are required.

The measurement of the dijet azimuthal decorrelations is also compared with various Monte Carlo generators matched to PS showed that LO and NLO calculations complemented with jets from PS. Among the LO generators PYTHIA8 gives the best description. The NLO generator POWHEG matched to PYTHIA8 gives the similar results to LO generators. The only MC

generator able to describe the data though the entire $\Delta\phi_{\text{Dijet}}$ regions is Madgraph, which generates four partons and uses PS from PYTHIA6. These comparisons emphasize the need of better multijet predictions.

References

[1] CMS Collaboration *Phys. Rev. Lett.* **106** (2011) 122003,
`doi:10.1103/PhysRevLett.106.122003`.

[2] ATLAS Collaboration *Phys. Rev. Lett.* **106** (2011) 172002,
`doi:10.1103/PhysRevLett.106.172002`.

[3] ALICE Collaboration, "The ALICE experiment at the CERN LHC", *JINST* **3** (2008)
S08002, `doi:10.1088/1748-0221/3/08/S08002`.

[4] LHCb Collaboration, "The LHCb Detector at the LHC", *JINST* **3** (2008) S08005,
`doi:10.1088/1748-0221/3/08/S08005`.

[5] TOTEM Collaboration, "The TOTEM experiment at the CERN Large Hadron Collider",
JINST **3** (2008) S08007, `doi:10.1088/1748-0221/3/08/S08007`.

[6] LHCf Collaboration, "The LHCf detector at the CERN Large Hadron Collider", *JINST* **3**
(2008) S08006, `doi:10.1088/1748-0221/3/08/S08006`.

[7] CMS Collaboration, "The CMS High Level Trigger", *Eur. Phys. J. C* **46** (2006) 605,
`doi:10.1140/epjc/s2006-02495-8`.

[8] F. Halzen and A. D. Martin, "Quark & Leptons: An Introductory Course In Modern
Particle Physics". John Wiley & Sons, 2008.

[9] D. Griffiths, "Introduction to Elementary Particles". Physics textbook. Wiley, 2008.

[10] M. Peskin and D. Schroeder, "An Introduction to Quantum Field Theory". Advanced
book classics. Addison-Wesley Publishing Company, 1995.

[11] M. Gell-Mann et al., "A schematic model of baryons and mesons", *Physics Letters* **8**
(1964), no. 3, 214–215.

[12] G. Zweig, "Origins of the quark model",.

[13] O. W. Greenberg, "Spin and unitary-spin independence in a paraquark model of baryons
and mesons", *Physical Review Letters* **13** (1964), no. 20, 598.

[14] B. Andersson, G. Gustafson, G. Ingelman, and T. Sjostrand, "Parton Fragmentation and
String Dynamics", *Phys. Rept.* **97** (1983) 31, `doi:10.1016/0370-1573(83)90080-7`.

[15] B. Andersson, G. Gustafson, and B. Soderberg, "A General Model for Jet Fragmentation",
Z. Phys. C **20** (1983) 317, `doi:10.1007/BF01407824`.

[16] G. Dissertori, I. Knowles, and M. Schmelling, "Quantum Chromodynamics: High Energy
Experiments and Theory". International series of monographs on physics. Clarendon
Press, 2003.

[17] GEANT4 Collaboration, "Geant4—a simulation tool kit", *Nucl. Instrum. Meth. A* **506**
(2003) 250, `doi:10.1016/S0168-9002(03)01368-8`.

[18] T. Sjöstrand, S. Mrenna, and P. Z. Skands, "PYTHIA 6.4 physics and manual", *JHEP* **05**
(2006) 026, `doi:10.1088/1126-6708/2006/05/026`, `arXiv:hep-ph/0603175`.

[19] T. Sjöstrand, S. Mrenna, and P. Z. Skands, "A Brief Introduction to PYTHIA 8.1", *Comput. Phys. Commun.* **178** (2008) 852, `doi:10.1016/j.cpc.2008.01.036`, `arXiv:0710.3820`.

[20] M. Bähr et al., "Herwig++ physics and manual", *Eur. Phys. J. C* **58** (2008) 639, `doi:10.1140/epjc/s10052-008-0798-9`, `arXiv:0803.0883`.

[21] S. Gieseke, P. Stephens, and B. Webber, "New formalism for QCD parton showers", *JHEP* **12** (2003) 045, `doi:10.1088/1126-6708/2003/12/045`, `arXiv:hep-ph/0310083`.

[22] J. Alwall et al., "MadGraph 5: going beyond", *JHEP* **06** (2011) 128, `doi:10.1007/JHEP06(2011)128`, `arXiv:1106.0522`.

[23] S. Mrenna and P. Richardson, "Matching matrix elements and parton showers with HERWIG and PYTHIA", *JHEP* **05** (2004) 040, `doi:10.1088/1126-6708/2004/05/040`, `arXiv:hep-ph/0312274`.

[24] S. Frixione, P. Nason, and C. Oleari, "Matching NLO QCD computations with Parton Shower simulations: the POWHEG method", *JHEP* **11** (2007) 070, `doi:10.1088/1126-6708/2007/11/070`, `arXiv:0709.2092`.

[25] S. Alioli, P. Nason, C. Oleari, and E. Re, "A general framework for implementing NLO calculations in shower Monte Carlo programs: the POWHEG BOX", *JHEP* **06** (2010) 043, `doi:10.1007/JHEP06(2010)043`, `arXiv:1002.2581`.

[26] S. Alioli, P. Nason, C. Oleari, and E. Re, "Jet pair production in POWHEG", `arXiv:1012.3380`.

[27] Z. Nagy, "Three-jet cross sections in hadron-hadron collisions at next-to-leading order", *Phys. Rev. Lett.* **88** (2002) 122003, `doi:10.1103/PhysRevLett.88.122003`, `arXiv:hep-ph/0110315`.

[28] Z. Nagy, "Next-to-leading order calculation of three-jet observables in hadron-hadron collisions", *Phys. Rev. D* **68** (2003) 094002, `doi:10.1103/PhysRevD.68.094002`, `arXiv:hep-ph/0307268`.

[29] D. Britzger, K. Rabbertz, F. Stober, and M. Wobisch, "New features in version 2 of the fastNLO project", `doi:10.3204/DESY-PROC-2012-02/165`, `arXiv:1208.3641`.

[30] "LHAPDF6: parton density access in the LHC precision era", `doi:10.1140/epjc/s10052-015-3318-8`, `arXiv:1412.7420`.

[31] S. Alekhin, J. Blumlein, and S. Moch, "Parton distribution functions and benchmark cross sections at next-to-next-to-leading order", *Phys. Rev. D* **86** (2012) 054009, `doi:10.1103/PhysRevD.86.054009`, `arXiv:1202.2281`.

[32] H.-L. Lai et al., "New parton distributions for collider physics", *Phys. Rev. D* **82** (2010) 074024, `doi:10.1103/PhysRevD.82.074024`, `arXiv:1007.2241`.

[33] H1 and ZEUS Collaboration, "Combined Measurement and QCD Analysis of the Inclusive e+- p Scattering Cross Sections at HERA", *JHEP* **1001** (2010) 109, `doi:10.1007/JHEP01(2010)109`, `arXiv:0911.0884`.

[34] A. D. Martin, W. J. Stirling, R. S. Thorne, and G. Watt, "Parton distributions for the LHC", *Eur. Phys. J. C* **63** (2009) 189, `doi:10.1140/epjc/s10052-009-1072-5`, `arXiv:0901.0002`.

[35] R. D. Ball et al., "Impact of Heavy Quark Masses on Parton Distributions and LHC Phenomenology", *Nucl. Phys. B* **849** (2011) 296, `doi:10.1016/j.nuclphysb.2011.03.021`, `arXiv:1101.1300`.

[36] CMS Collaboration, "Particle–Flow Event Reconstruction in CMS and Performance for Jets, Taus, and E_T^{miss}", CMS Physics Analysis Summary CMS-PAS-PFT-09-001, 2009.

[37] M. Cacciari, G. P. Salam, and G. Soyez, "The anti-k_t jet clustering algorithm", *JHEP* **04** (2008) 063, `doi:10.1088/1126-6708/2008/04/063`, `arXiv:0802.1189`.

[38] M. Cacciari, G. P. Salam, and G. Soyez, "FastJet User Manual", *Eur. Phys. J. C* **72** (2012) 1896, `doi:10.1140/epjc/s10052-012-1896-2`, `arXiv:1111.6097`.

[39] S. D. Ellis and D. E. Soper, "Successive combination jet algorithm for hadron collisions", *Phys. Rev.* **D48** (1993) 3160–3166, `doi:10.1103/PhysRevD.48.3160`, `arXiv:hep-ph/9305266`.

[40] M. Cacciari, G. P. Salam, and G. Soyez, "The anti-k_t jet clustering algorithm", *JHEP* **04** (2008) 063, `doi:10.1088/1126-6708/2008/04/063`, `arXiv:0802.1189`.

[41] CMS Collaboration, "Determination of jet energy calibration and transverse momentum resolution in CMS", *JINST* **6** (2011) P11002, `doi:10.1088/1748-0221/6/11/P11002`.

[42] CMS Collaboration, "Measurement of the ratio of the inclusive 3-jet cross section to the inclusive 2-jet cross section in pp collisions at $\sqrt{s}$ = 7 TeV and first determination of the strong coupling constant in the TeV range", *Eur. Phys. J. C* **73** (2013) 2604, `doi:10.1140/epjc/s10052-013-2604-6`, `arXiv:1304.7498`.

[43] CMS Collaboration, "Determination of Jet Energy Calibration and Transverse Momentum Resolution in CMS", *JINST* **6** (2011) P11002, `doi:10.1088/1748-0221/6/11/P11002`, `arXiv:1107.4277`.

[44] S. Agostinelli et al., "GEANT4: A Simulation toolkit", *Nuclear Instruments & Methods in Physics Research A* **506** (2003) 250, `doi:10.1016/S0168-9002(03)01368-8`.

[45] CMS Collaboration, "The fast simulation of the CMS detector at LHC", *J. Phys. Conf. Ser.* **331** (2011) 032049, `doi:10.1088/1742-6596/331/3/032049`.

[46] CMS Collaboration, "Absolute Calibration of the Luminosity Measurement at CMS: Winter 2012 Update", CMS Physics Analysis Summary CMS-PAS-SMP-12-008, 2012.

[47] J. Butterworth et al., "Les Houches 2013: Physics at TeV Colliders: Standard Model Working Group Report", `arXiv:1405.1067`.

[48] S. Dittmaier, A. Huss, and C. Speckner, "Weak radiative corrections to dijet production at hadron colliders", *JHEP* **1211** (2012) 095, `doi:10.1007/JHEP11(2012)095`, `arXiv:1210.0438`.

[49] CMS Collaboration, "Measurements of differential jet cross sections in proton-proton collisions at $\sqrt{s}$ = 7 TeV with the CMS detector", *Phys. Rev. D* **87** (2012) 12002, `doi:10.1103/PhysRevD.87.112002`.

[50] L. Lyons, A. J. Martin, and D. H. Saxon, "On the Determination of the *B* Lifetime by Combining the Results of Different Experiments", *Phys. Rev. D* **41** (1990) 982, `doi:10.1103/PhysRevD.41.982`.

[51] J. Beringer et al., "Review of Particle Physics (RPP)", *Phys. Rev. D* **86** (2012) 010001, `doi:10.1103/PhysRevD.86.010001`.

[52] CDF Collaboration, "Measurement of the strong coupling constant from inclusive jet production at the Tevatron $\bar{p}p$ collider", *Phys. Rev. Lett.* **88** (2002) 042001, `doi:10.1103/PhysRevLett.88.042001`, `arXiv:hep-ex/0108034`.

[53] D0 Collaboration, "Determination of the strong coupling constant from the inclusive jet cross section in $p\bar{p}$ collisions at sqrt(s)=1.96 TeV", *Phys. Rev. D* **80** (2009) 111107, `doi:10.1103/PhysRevD.80.111107`, `arXiv:0911.2710`.

[54] D0 Collaboration, "Measurement of angular correlations of jets at $\sqrt{s} = 1.96$ TeV and determination of the strong coupling at high momentum transfers", *Phys. Lett. B* **718** (2012) 56, `doi:10.1016/j.physletb.2012.10.003`, `arXiv:1207.4957`.

[55] B. Malaescu and P. Starovoitov, "Evaluation of the Strong Coupling Constant alpha-s Using the ATLAS Inclusive Jet Cross-Section Data", *Eur. Phys. J. C* **72** (2012) 2041, `doi:10.1140/epjc/s10052-012-2041-y`, `arXiv:1203.5416`.

[56] H1 Collaboration, "Jet Production in ep Collisions at High Q**2 and Determination of alpha(s)", *Eur. Phys. J. C* **65** (2010) 363, `doi:10.1140/epjc/s10052-009-1208-7`, `arXiv:0904.3870`.

[57] H1 Collaboration, "Jet Production in ep Collisions at Low Q**2 and Determination of alpha(s)", *Eur. Phys. J. C* **67** (2010) 1, `doi:10.1140/epjc/s10052-010-1282-x`, `arXiv:0911.5678`.

[58] ZEUS Collaboration, "Inclusive-jet photoproduction at HERA and determination of alphas", *Nucl. Phys. B* **864** (2012) 1, `doi:10.1016/j.nuclphysb.2012.06.006`, `arXiv:1205.6153`.

[59] CMS Collaboration, "Measurement of the underlying event activity at the LHC with $\sqrt{s}$ = 7 TeV and comparison with $\sqrt{s}$ = 0.9 TeV", *JHEP* **2011** (2011) `doi:10.1007/JHEP09(2011)109`.

[60] CMS Collaboration, "Study of the underlying event at forward rapidity in pp collisions at $\sqrt{s} = 0.9$, 2.76, and 7 TeV", *JHEP* **04** (2013) 072, `doi:10.1007/JHEP04(2013)072`, `arXiv:1302.2394`.

[61] CMS Collaboration, "Jet Energy Scale and Resolution in the 8 TeV pp data", CMS Physics Summary CMS-PAS-JME-13-004, 2013.

[62] J. Pumplin et al., "New generation of parton distributions with uncertainties from global QCD analysis", *JHEP* **07** (2002) 012, `doi:10.1088/1126-6708/2002/07/012`, `arXiv:hep-ph/0201195`.

A Extrapolation uncertainty

In some cases the PDF sets for various α_S provided by collaborations are not enough to give a full χ^2 parabola. In these cases the GRV running code used in order to calculate cross sections for lower α_S. These calculations performed specifically for the CT10-NLO for the two outermost rapidity bins.

In order to get a parabola wide enough allowing us to use the $\chi^2 + 1$ criterion to determine the uncertainties of $\alpha_S(M_Z)$ we calculated cross sections for three additional α_S values, 0.109, 0.110 and 0.111. The cross sections calculated using the GRV evolution code, for a given α_S using a CT10 PDF set with different α_S, are slightly different with the cross section calculated using the default evolution from CT10, which is HOPPET. This difference introduce some uncertainty on the final result, the determination of the uncertainty is described on the following paragraphs.

Using the PDF set with $\alpha_S(M_Z) = 0.112$, which is the lowest α_S provided by CT10, we calculated cross sections for 0.113, 0.114 and 0.115 α_S values. Then we recalculated cross sections with the same α_S values but using the corresponding PDF sets provided by CT. Comparing the two we assigned the maximum distance from one as uncertainty on cross section calculations. Assuming that the behavior around 0.112 with the same $\Delta\alpha_S$ is symmetric, we assigned the uncertainty derived from 0.113 to 0.111, from 0.114 to 0.110 and from 0.115 to 0.109.

Figure 87 shows the ratio

$$\frac{\sigma_{HOPPET}}{\sigma_{GRV}} \tag{93}$$

where σ_{GRV} is the cross section calculated using `CT10_as_0112.LHgrid` and GRV with $\alpha_S(M_Z)$ = 0.113 while σ_{HOPPET} is the cross section calculated using `CT10_as_0113.LHgrid`. The red dashed line shows the point with the maximum distance from one.
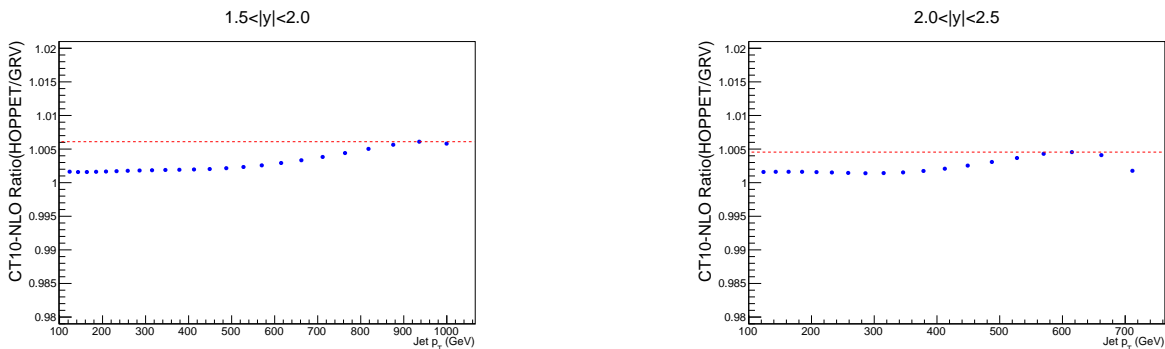

Figure 87: Ratio of cross sections using different evolutions.

Table 26 shows the uncertainties on each rapidity bin and on each PDF set.

Table 26: Uncertainties

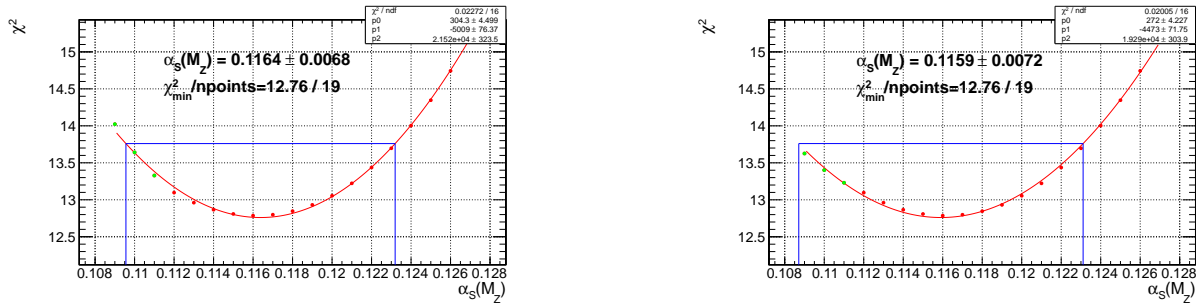| $|y|$ range	$\alpha_S(M_Z)$	Uncertainty (%)
$1.5 < |y| < 2.0$	0.113	1.5
$1.5 < |y| < 2.0$	0.114	1.1
$1.5 < |y| < 2.0$	0.115	0.6
$2.0 < |y| < 2.5$	0.113	1.1
$2.0 < |y| < 2.5$	0.114	0.8
$2.0 < |y| < 2.5$	0.115	0.4

Figure 88: χ^2 plots with shifted values. Left: cross sections shifted downwards. Right: cross sections shifted downwards. Green points are the points calculated with GRV.

In order to estimate the propagated uncertainty on the final result we shifted the cross sections upwards and downwards, i.e the cross section with $\alpha_S = 0.111$ shifted by $\pm 1.5\%$ in the $1.5 < |y| < 2.0$ region. Then we performed fits with the three additional points shifted upwards and downwards, the deviation from the non shifted fit assigned as the extrapolation uncertainty.

B   Chi-square Parabolas

This appendix includes all the χ^2 parabolas derived from the fits of the inlcusive jet cross section data, described in sub-section 6.1.
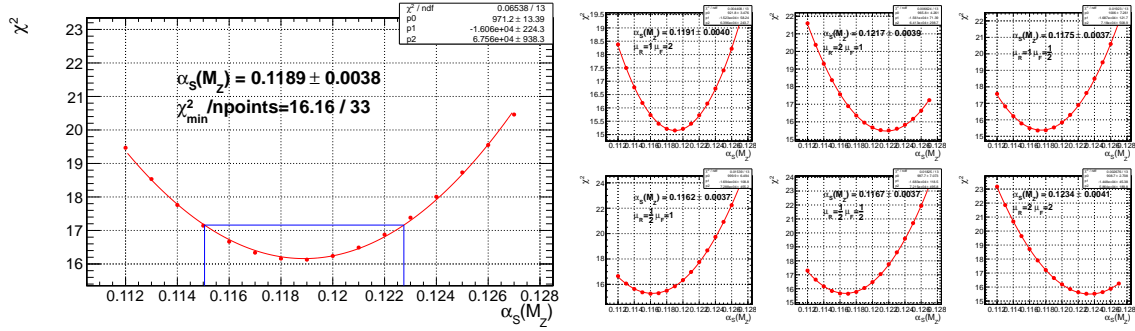
Figure 89: **For rapidity $|\mathbf{y}| < \mathbf{0.5}$.** On the left it is shown the χ^2 minimization with respect to $\alpha_S(M_Z)$ using the **CT10-NLO PDF** set. The experimental uncertainties are obtained from the $\alpha_S(M_Z)$ values for which χ^2 is increased by 1 with respect to the minimum value. At the right it is shown the χ^2 minimization by varying the scale between $p_T/2$ and $2p_T$ in six combinations.
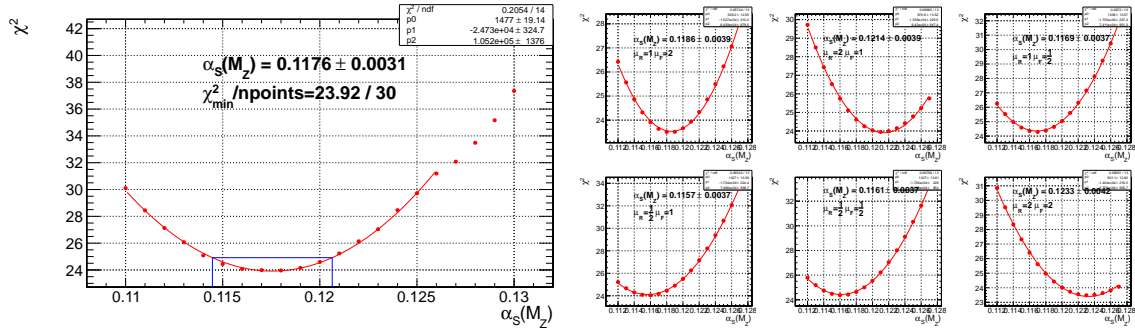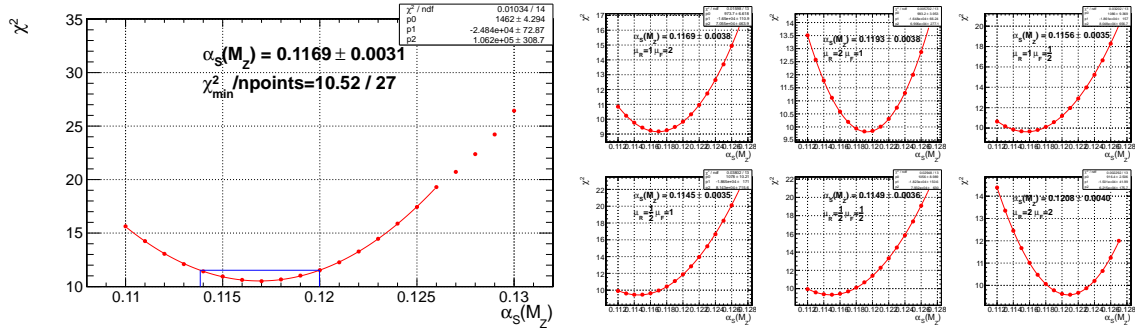

Figure 90: **For rapidity $\mathbf{0.5} < |\mathbf{y}| < \mathbf{1.0}$.** On the left it is shown the χ^2 minimization with respect to $\alpha_S(M_Z)$ using the **CT10-NLO PDF** set. The experimental uncertainties are obtained from the $\alpha_S(M_Z)$ values for which χ^2 is increased by 1 with respect to the minimum value. At the right it is shown the χ^2 minimization by varying the scale between $p_T/2$ and $2p_T$ in six combinations.
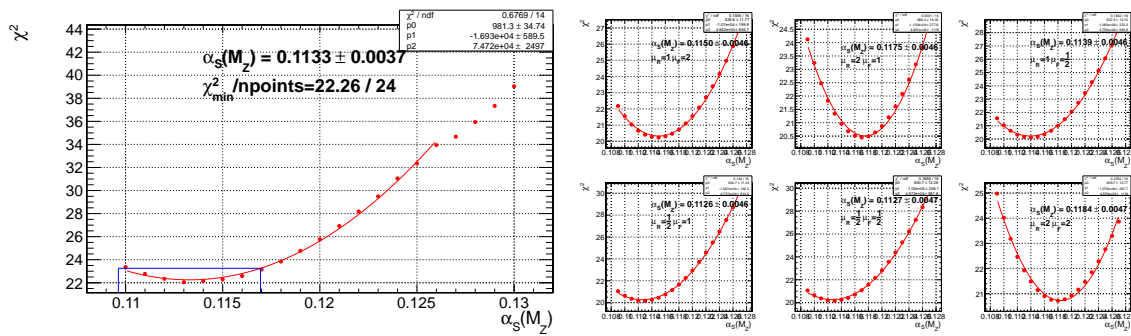

Figure 91: **For rapidity $\mathbf{1.0} < |\mathbf{y}| < \mathbf{1.5}$.** On the left it is shown the χ^2 minimization with respect to $\alpha_S(M_Z)$ using the **CT10-NLO PDF** set. The experimental uncertainties are obtained from the $\alpha_S(M_Z)$ values for which χ^2 is increased by 1 with respect to the minimum value. At the right it is shown the χ^2 minimization by varying the scale between $p_T/2$ and $2p_T$ in six combinations.
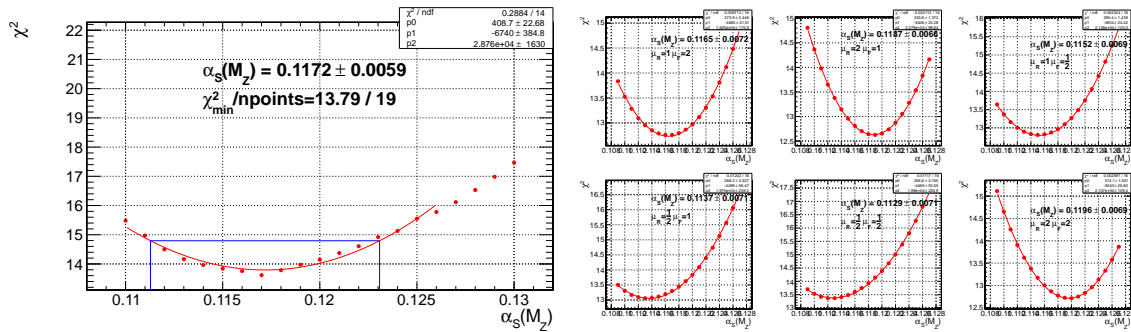
Figure 92: **For rapidity** $1.5 < |\mathbf{y}| < 2.0$. On the left it is shown the χ^2 minimization with respect to $\alpha_S(M_Z)$ using the **CT10-NLO PDF** set. The experimental uncertainties are obtained from the $\alpha_S(M_Z)$ values for which χ^2 is increased by 1 with respect to the minimum value. At the right it is shown the χ^2 minimization by varying the scale between $p_T/2$ and $2p_T$ in six combinations.
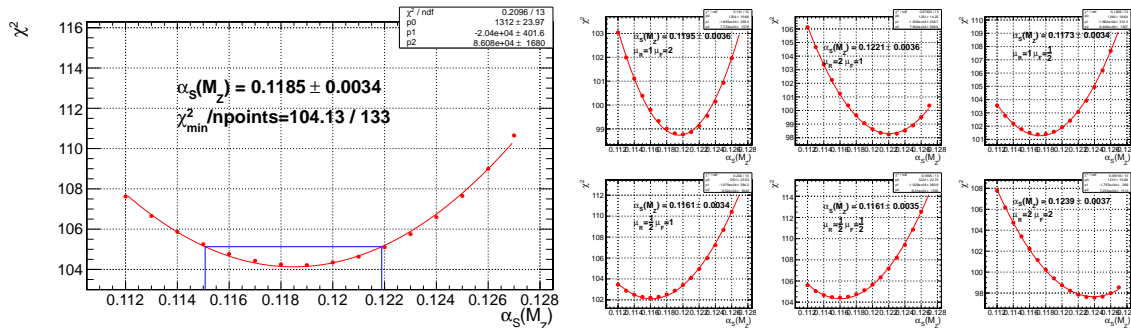

Figure 93: **For rapidity** $2.0 < |\mathbf{y}| < 2.5$. On the left it is shown the χ^2 minimization with respect to $\alpha_S(M_Z)$ using the **CT10-NLO PDF** set. The experimental uncertainties are obtained from the $\alpha_S(M_Z)$ values for which χ^2 is increased by 1 with respect to the minimum value. At the right it is shown the χ^2 minimization by varying the scale between $p_T/2$ and $2p_T$ in six combinations.
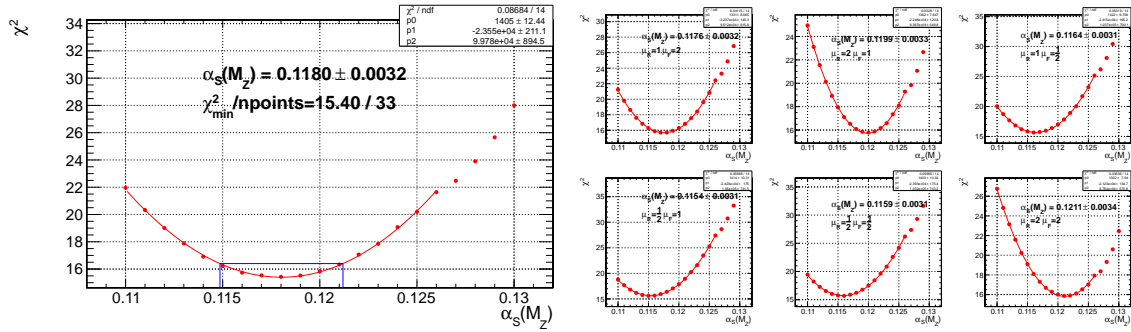

Figure 94: **ALL rapidity bins** $|\mathbf{y}| < 2.5$. On the left it is shown the χ^2 minimization with respect to $\alpha_S(M_Z)$ using the **CT10-NLO PDF** set. The experimental uncertainties are obtained from the $\alpha_S(M_Z)$ values for which χ^2 is increased by 1 with respect to the minimum value. At the right it is shown the χ^2 minimization by varying the scale between $p_T/2$ and $2p_T$ in six combinations.
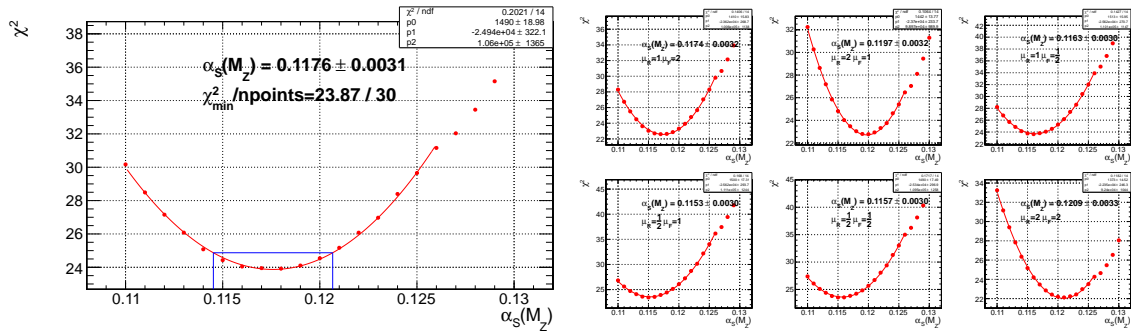
Figure 95: **For rapidity $|\mathbf{y}| < \mathbf{0.5}$.** On the left it is shown the χ^2 minimization with respect to $\alpha_S(M_Z)$ using the **CT10-NNLO PDF** set. The experimental uncertainties are obtained from the $\alpha_S(M_Z)$ values for which χ^2 is increased by 1 with respect to the minimum value. At the right it is shown the χ^2 minimization by varying the scale between $p_T/2$ and $2p_T$ in six combinations.
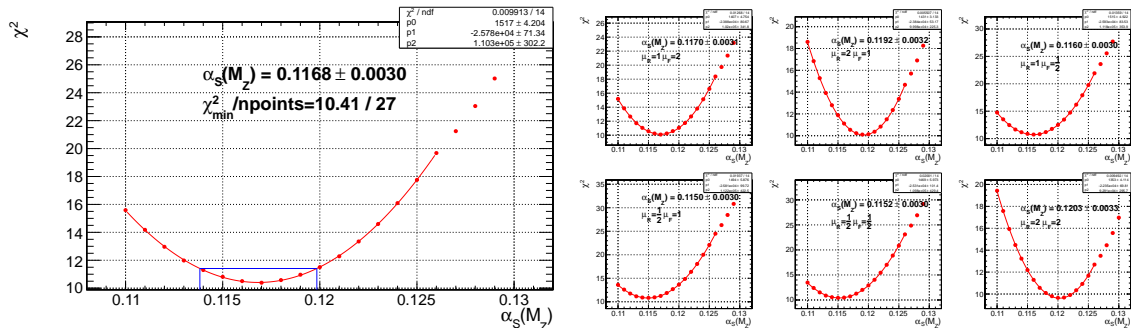

Figure 96: **For rapidity $\mathbf{0.5} < |\mathbf{y}| < \mathbf{1.0}$.** On the left it is shown the χ^2 minimization with respect to $\alpha_S(M_Z)$ using the **CT10-NNLO PDF** set. The experimental uncertainties are obtained from the $\alpha_S(M_Z)$ values for which χ^2 is increased by 1 with respect to the minimum value. At the right it is shown the χ^2 minimization by varying the scale between $p_T/2$ and $2p_T$ in six combinations.
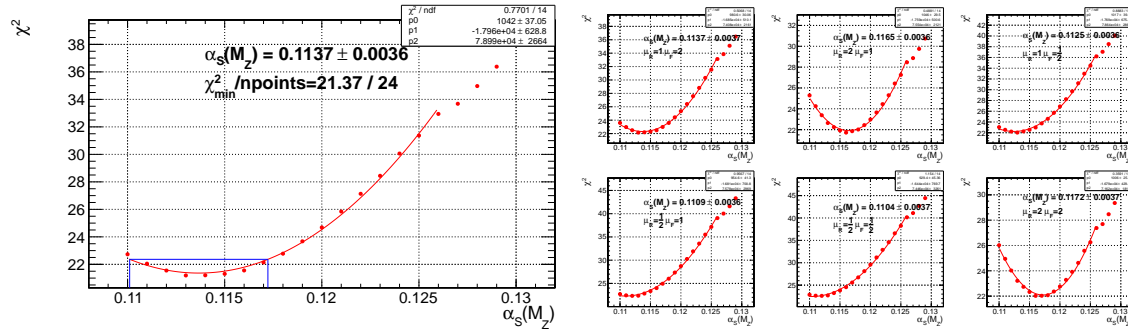

Figure 97: **For rapidity $\mathbf{1.0} < |\mathbf{y}| < \mathbf{1.5}$.** On the left it is shown the χ^2 minimization with respect to $\alpha_S(M_Z)$ using the **CT10-NNLO PDF** set. The experimental uncertainties are obtained from the $\alpha_S(M_Z)$ values for which χ^2 is increased by 1 with respect to the minimum value. At the right it is shown the χ^2 minimization by varying the scale between $p_T/2$ and $2p_T$ in six combinations.

Figure 98: **For rapidity $1.5 < |\mathbf{y}| < 2.0$**. On the left it is shown the χ^2 minimization with respect to $\alpha_S(M_Z)$ using the **CT10-NNLO PDF** set. The experimental uncertainties are obtained from the $\alpha_S(M_Z)$ values for which χ^2 is increased by 1 with respect to the minimum value. At the right it is shown the χ^2 minimization by varying the scale between $p_T/2$ and $2p_T$ in six combinations.
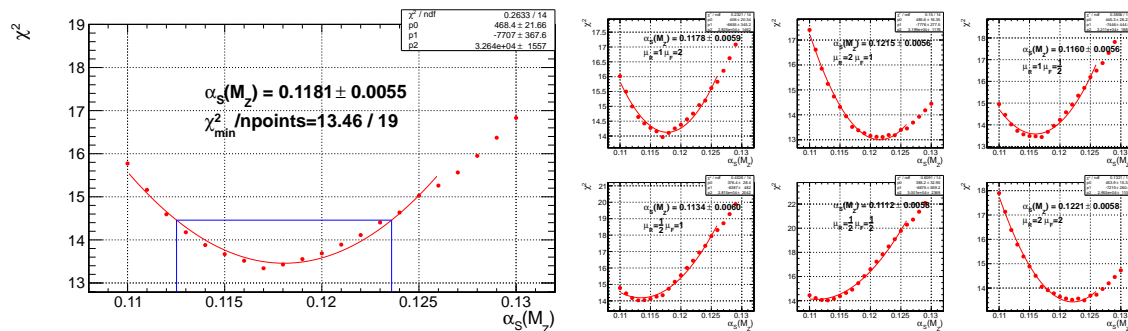

Figure 99: **For rapidity $2.0 < |\mathbf{y}| < 2.5$**. On the left it is shown the χ^2 minimization with respect to $\alpha_S(M_Z)$ using the **CT10-NNLO PDF** set. The experimental uncertainties are obtained from the $\alpha_S(M_Z)$ values for which χ^2 is increased by 1 with respect to the minimum value. At the right it is shown the χ^2 minimization by varying the scale between $p_T/2$ and $2p_T$ in six combinations.
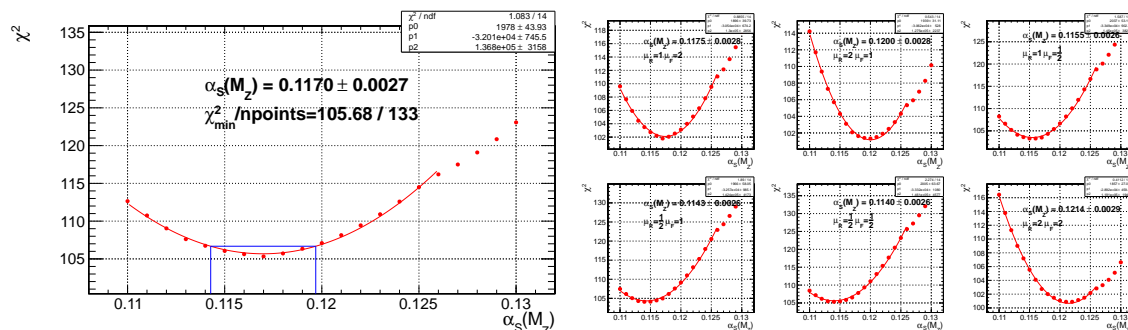

Figure 100: **ALL rapidity bins $|\mathbf{y}| < 2.5$**. On the left it is shown the χ^2 minimization with respect to $\alpha_S(M_Z)$ using the **CT10-NNLO PDF** set. The experimental uncertainties are obtained from the $\alpha_S(M_Z)$ values for which χ^2 is increased by 1 with respect to the minimum value. At the right it is shown the χ^2 minimization by varying the scale between $p_T/2$ and $2p_T$ in six combinations.
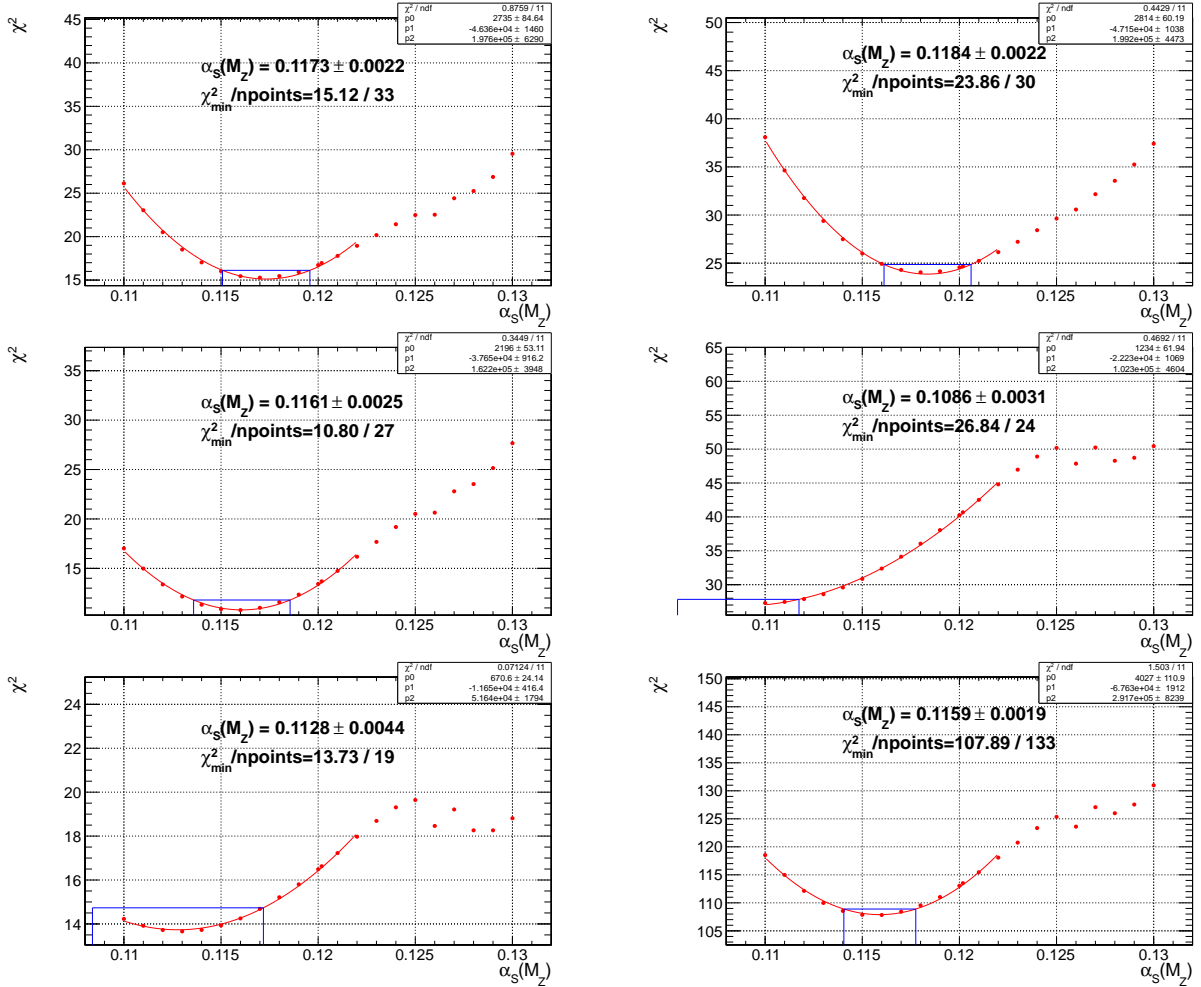
Figure 101: The χ^2 minimization with respect to $\alpha_S(M_Z)$ using the **MSTW2008-NLO PDF** set. The experimental uncertainties are obtained from the $\alpha_S(M_Z)$ values for which χ^2 is increased by 1 with respect to the minimum value. Top left: rapidity $|y| < 0.5$. Top right: rapidity $0.5 < |y| < 1.0$. Middle left: rapidity $1.0 < |y| < 1.5$. Middle right: rapidity $1.5 < |y| < 2.0$. Bottom left: rapidity $2.0 < |y| < 2.5$. Bottom right: all rapidity bins $|y| < 2.5$.

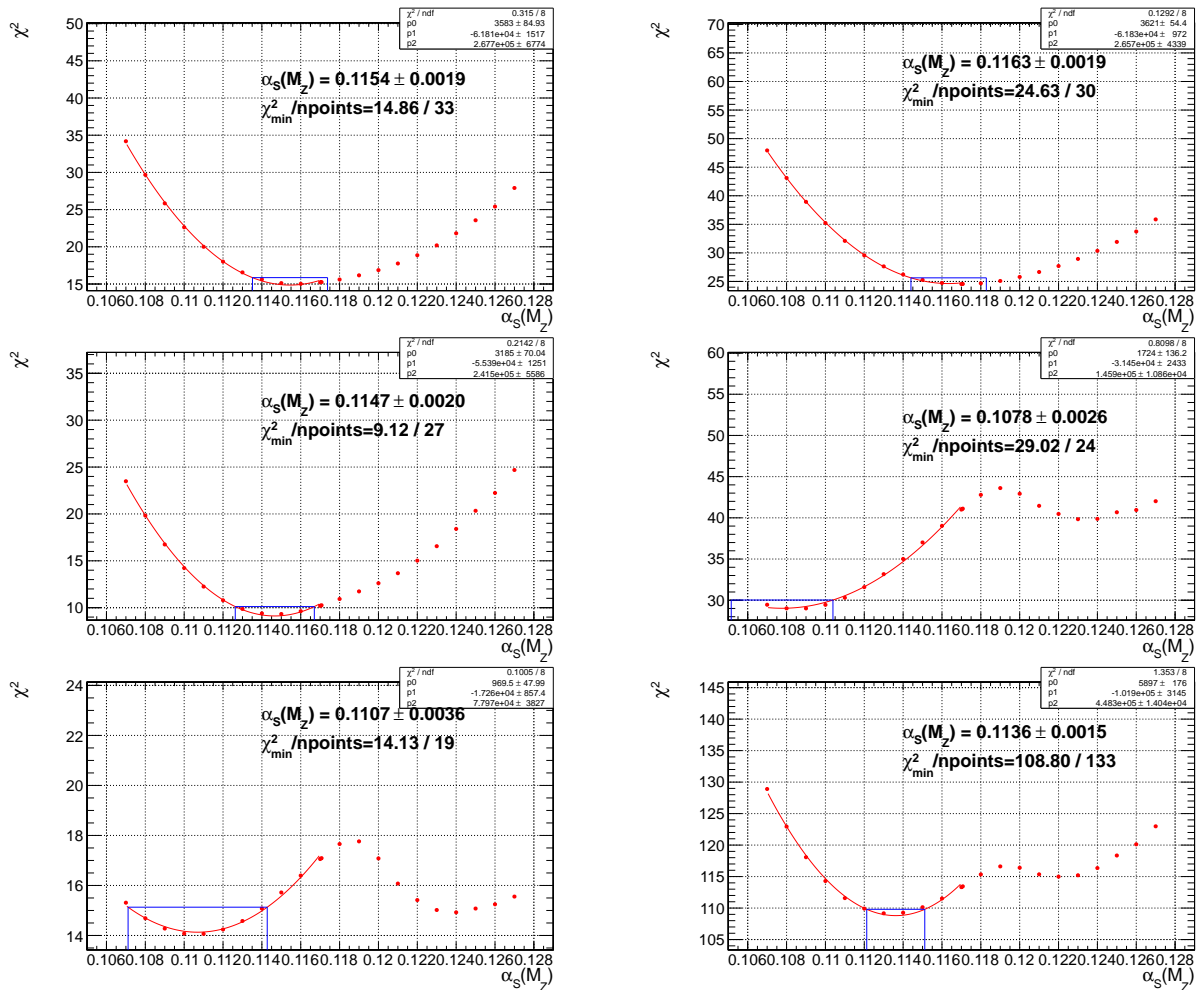Figure 102: The χ^2 minimization with respect to $\alpha_S(M_Z)$ using the **MSTW2008-NNLO PDF** set. The experimental uncertainties are obtained from the $\alpha_S(M_Z)$ values for which χ^2 is increased by 1 with respect to the minimum value. Top left: rapidity $|y| < 0.5$. Top right: rapidity $0.5 < |y| < 1.0$. Middle left: rapidity $1.0 < |y| < 1.5$. Middle right: rapidity $1.5 < |y| < 2.0$. Bottom left: rapidity $2.0 < |y| < 2.5$. Bottom right: all rapidity bins $|y| < 2.5$.

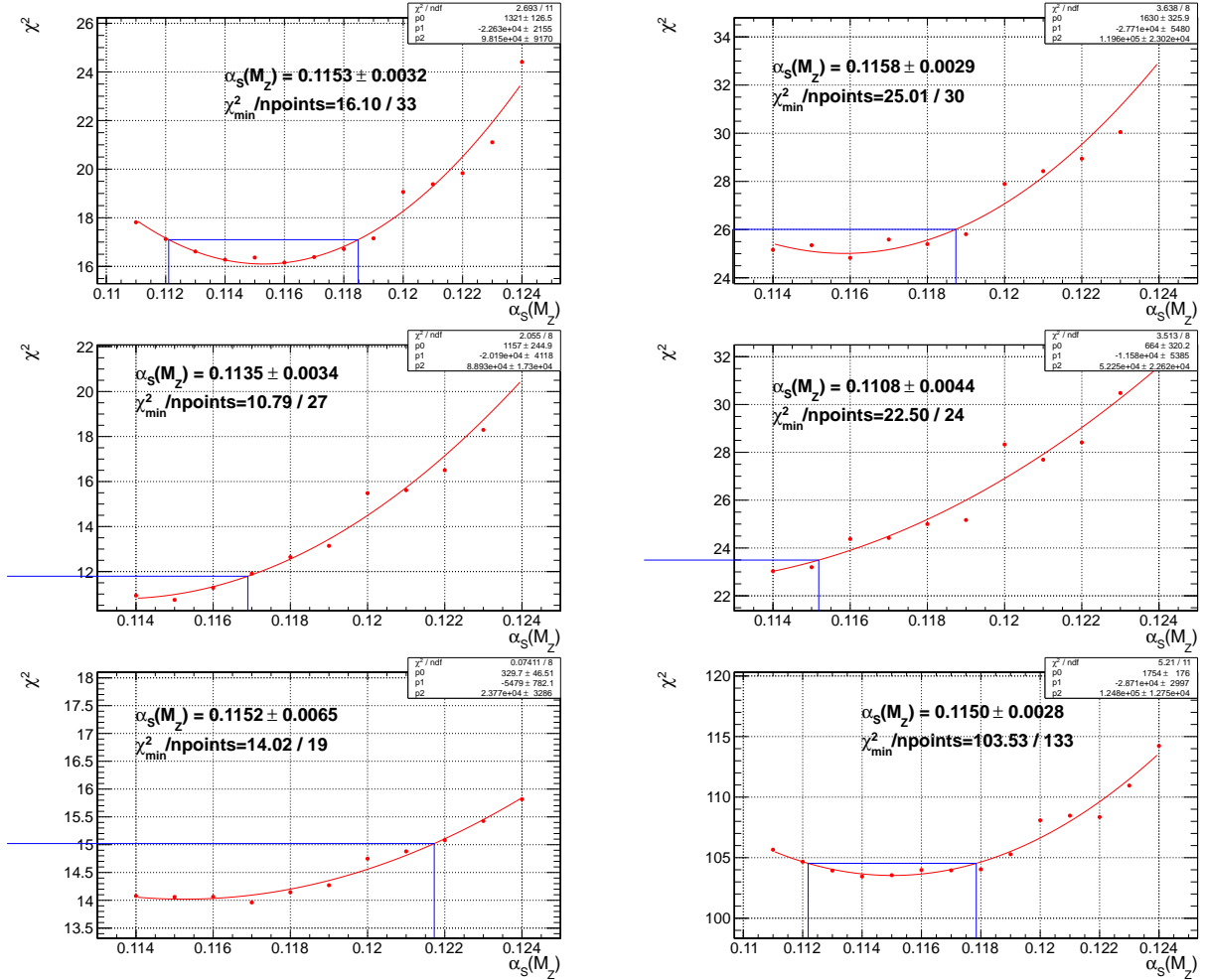Figure 103: The χ^2 minimization with respect to $\alpha_S(M_Z)$ using the **NNPDF2.1-NLO PDF** set. The experimental uncertainties are obtained from the $\alpha_S(M_Z)$ values for which χ^2 is increased by 1 with respect to the minimum value. Top left: rapidity $|y| < 0.5$. Top right: rapidity $0.5 < |y| < 1.0$. Middle left: rapidity $1.0 < |y| < 1.5$. Middle right: rapidity $1.5 < |y| < 2.0$. Bottom left: rapidity $2.0 < |y| < 2.5$. Bottom right: all rapidity bins $|y| < 2.5$.

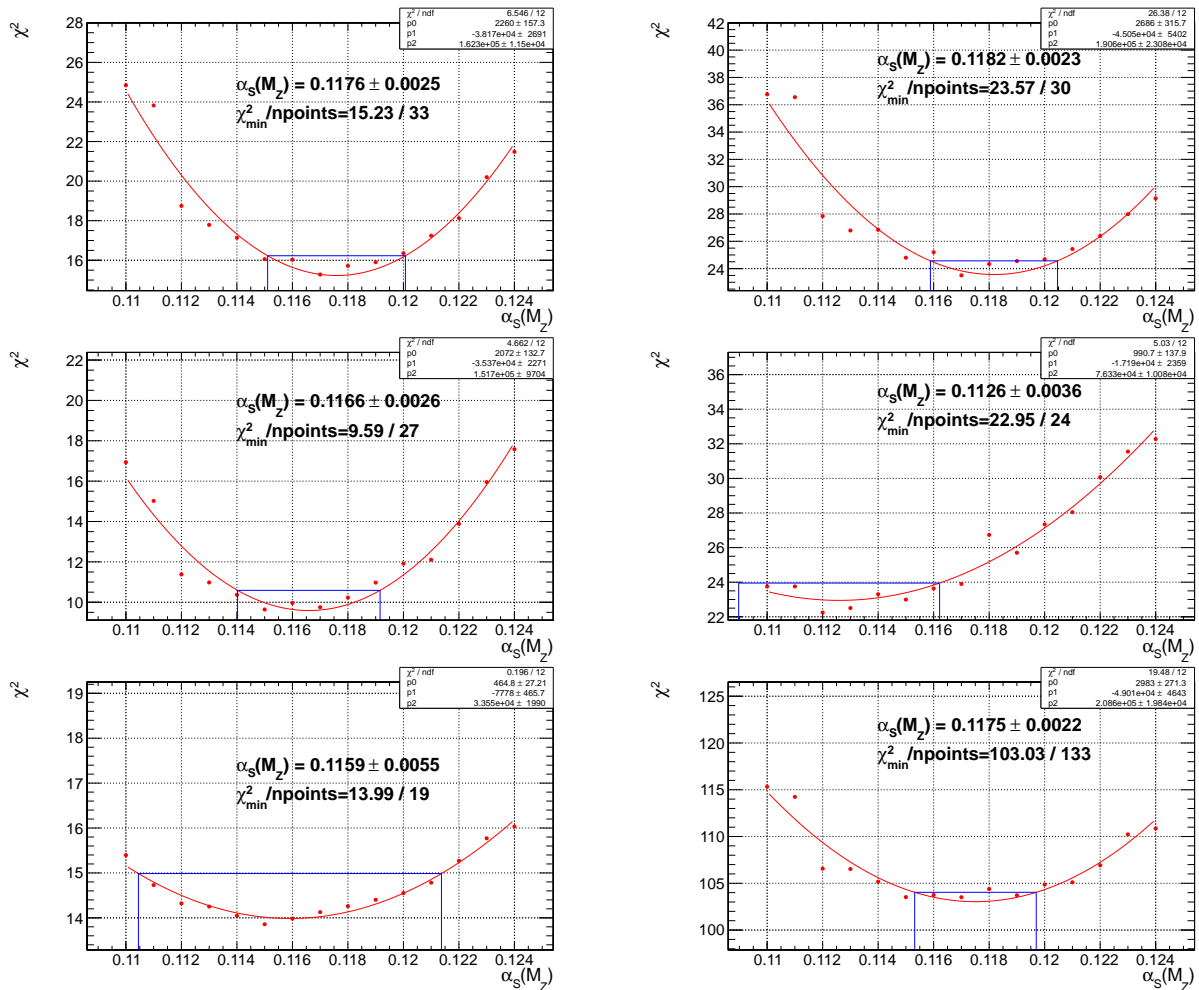Figure 104: The χ^2 minimization with respect to $\alpha_S(M_Z)$ using the **NNPDF2.1-NNLO PDF** set. The experimental uncertainties are obtained from the $\alpha_S(M_Z)$ values for which χ^2 is increased by 1 with respect to the minimum value. Top left: rapidity $|y| < 0.5$. Top right: rapidity $0.5 < |y| < 1.0$. Middle left: rapidity $1.0 < |y| < 1.5$. Middle right: rapidity $1.5 < |y| < 2.0$. Bottom left: rapidity $2.0 < |y| < 2.5$. Bottom right: all rapidity bins $|y| < 2.5$.

C   Non pertubative corrections for Azimuthal decorrelations

The pQCD calculations at NLO for this analysis were performed using the NLOJET++ program. These calculations do not include contributions from multiparton interactions and hadronization effects; the so called non perturbative(NP) effects. In order to compensate these effects, NP factors (C_{NP}) are calculated and applied as correction to theory as shown in Eq. (94):

$$\left(\frac{1}{\sigma_{Dijet}} \frac{d\sigma_{Dijet}}{d\Delta\phi_{Dijet}} \right)_{corrected} = C_{NP} \left(\frac{1}{\sigma_{Dijet}} \frac{d\sigma_{Dijet}}{d\Delta\phi_{Dijet}} \right)_{\text{NLOJET++}} \tag{94}$$

In order to calculate these factors MC generators were used with two different settings, the normal one and the $NO_{MPI} - NO_{HAD}$ setting. In the first case events were generated with all the contributions taken into account. In the second case events generated without hadronization and multiparton interactions taken into account. The ratio of the two different predictions are the NP correction factors.

In order to get an unbiased result two different MCs were used; PYTHIA6 tune Z2* and HERWIG++, using two different settings. But as it is shown in Fig 105 and Fig 106 the NP effects are negligible in the context of the current analysis.

The reason that NP effects are negligible in this analysis is that the measured differential cross section is normalized to the total cross section, thus any contribution to the differential cross section cancels out from the same contribution to the total cross section. In order to validate this argument, a study of the NP factors performed using the absolute differential cross section.

Fig 107 and Fig 108 show the NP correction factors for the various $p_{T,max}$ bins by using absolute cross sections. There is no obvious behavior of the NP corrections vs the $\Delta\phi_{Dijet}$ so one NP factor extracted per $p_{T,max}$ bin by fitting the function $y = a$. Fig 109 shows the NP correction factors derived using the p_T spectrum of the leading jet (top) and the factors using the the various $p_{T,max}$ bins for the absolute differential dijet cross section in $\Delta\phi_{Dijet}$ (bottom). The result is the same.

This study shows that NP corrections are important when dealing with absolute cross sections. In the case of the the normalised differential dijet cross section in $\Delta\phi_{Dijet}$ there is no need to apply any NP correction factor to compare theory to data.
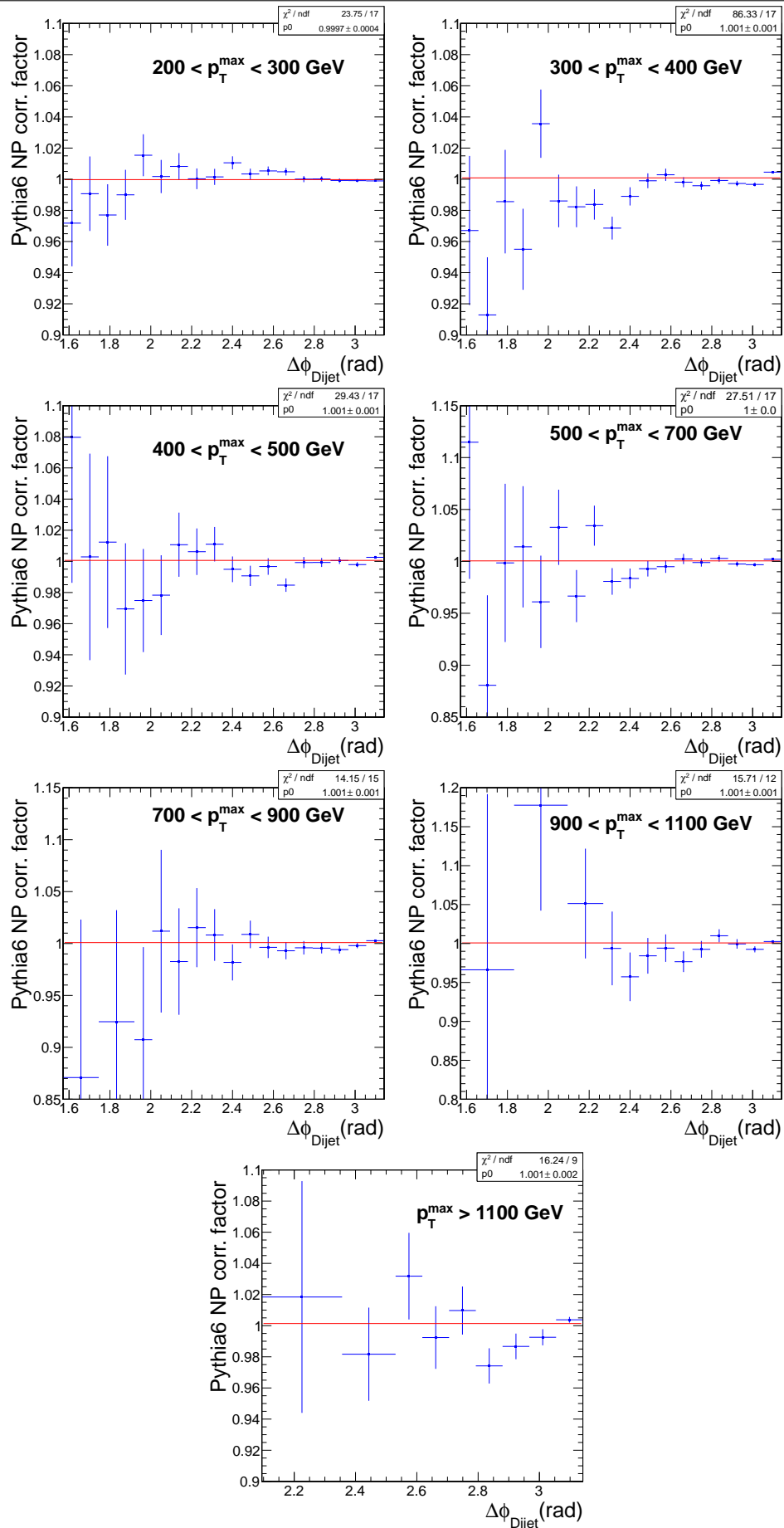
Figure 105: Non perturbative corrections for the normalised differential dijet cross section in $\Delta\phi_{\text{Dijet}}$ for all $p_{\text{T,max}}$ bins using PYTHIA6.
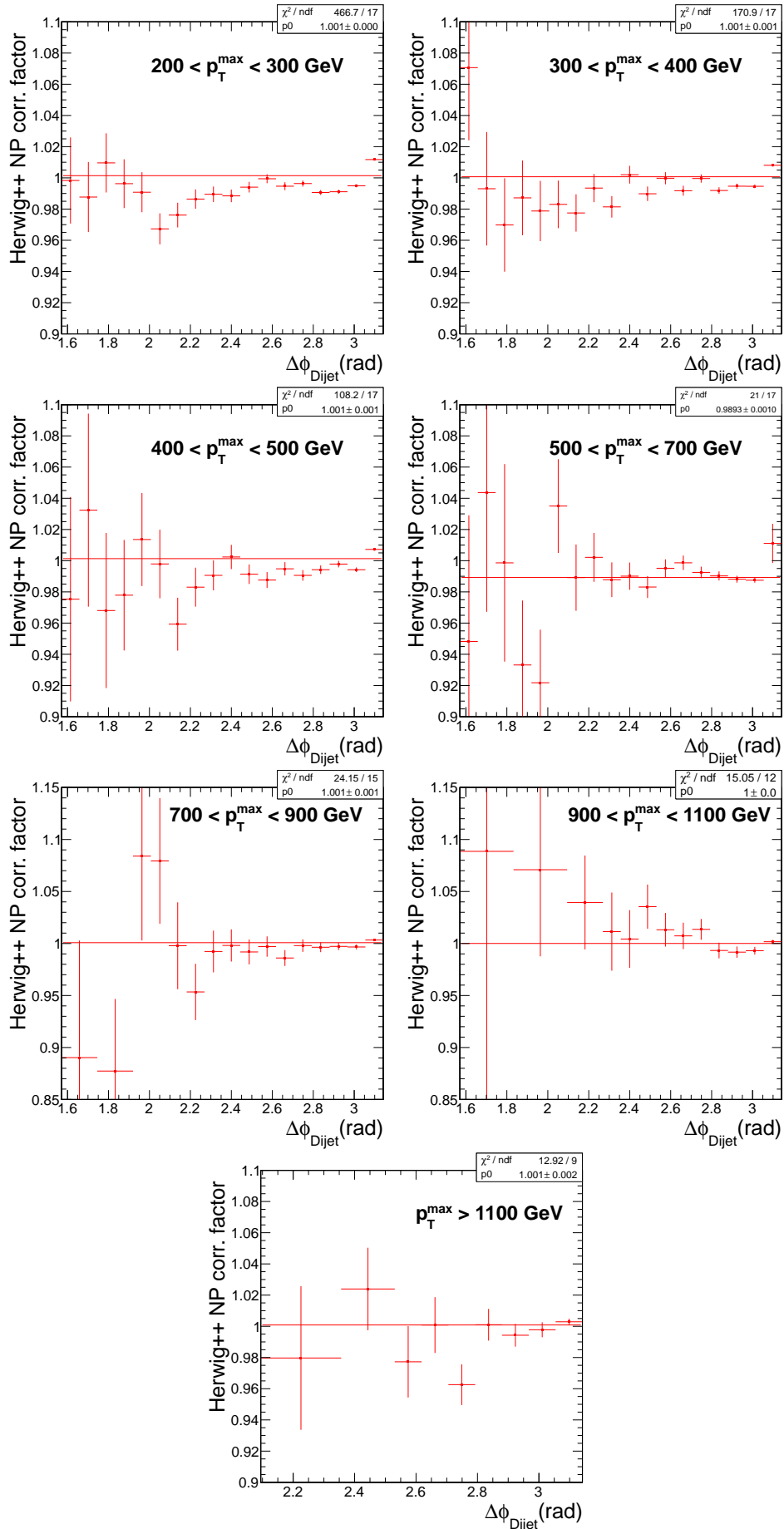
Figure 106: Non perturbative corrections for the normalised differential dijet cross section in $\Delta\phi_{\text{Dijet}}$ for all $p_{\text{T,max}}$ bins using HERWIG++.
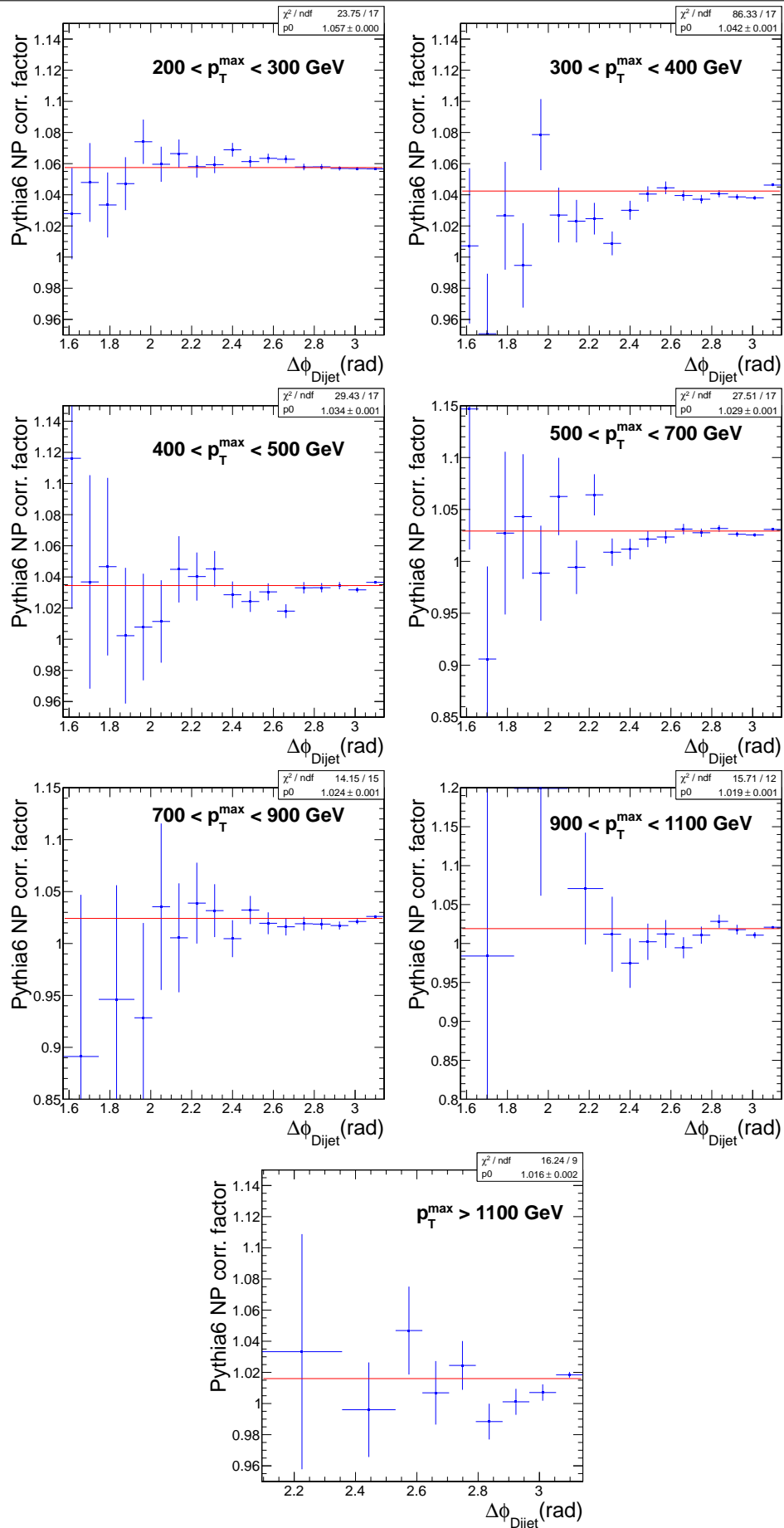
Figure 107: Non perturbative corrections for the absolute differential dijet cross section in $\Delta\phi_{\mathrm{Dijet}}$ for all $p_{\mathrm{T,max}}$ bins using PYTHIA6.
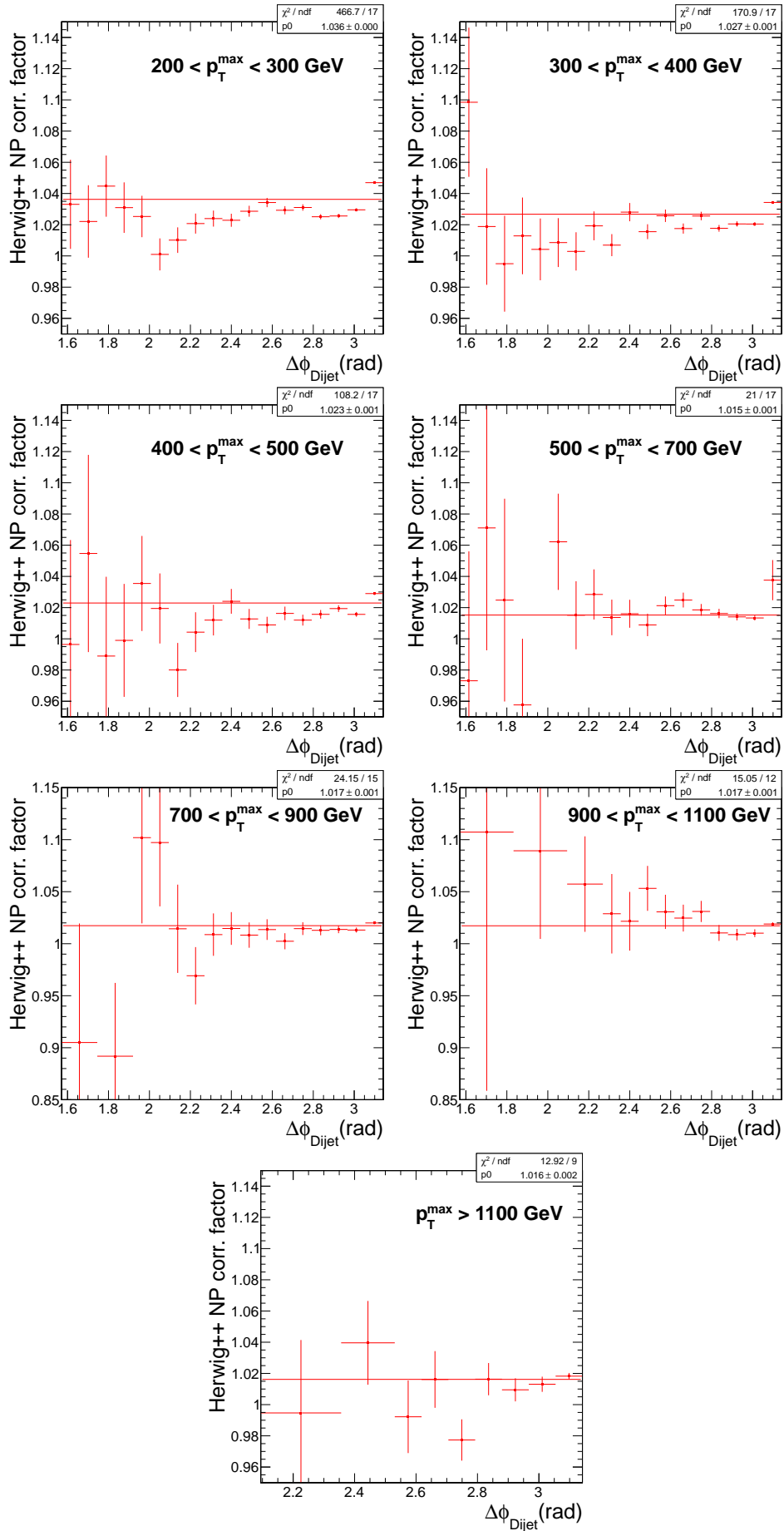
Figure 108: Non perturbative corrections for the absolute differential dijet cross section in $\Delta\phi_{\text{Dijet}}$ for all $p_{\text{T,max}}$ bins using HERWIG++.
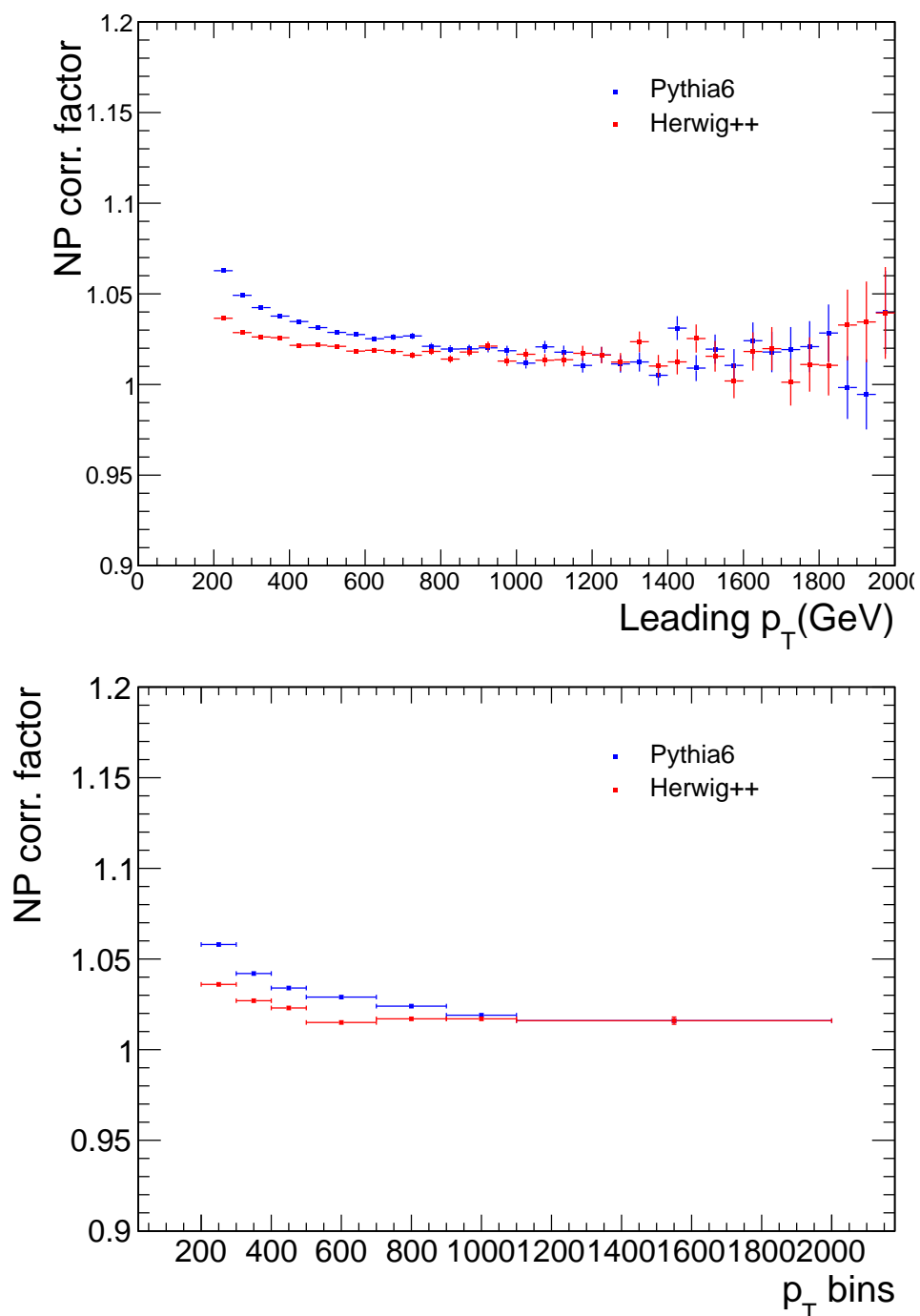
Figure 109: Non perturbative corrections derived using the p_T spectrum of the leading jet (top) and using the the various $p_{T,max}$ bins for the absolute differential dijet cross section in $\Delta\phi_{Dijet}$ (bottom).